

REPUBLIC of TURKEY
INONU UNIVERSITY
INSTITUTE of SCIENCE



Development of Ti-based Materials for Li-ion and Na-ion Batteries

Serkan DEMIREL

PhD Thesis

Physics Department

AGUST 2017

TURKİYE CUMHURİYETİ
İNÖNÜ ÜNİVERSİTESİ
FEN BİLİMLERİ ENSTİTÜSÜ

Li-iyon ve Na-iyon Piller İçin Ti-Bazlı Anot Materyallerinin Geliştirilmesi

Serkan DEMİREL

Doktora Tezi

Fizik Bölümü

Ağustos 2017

Title of Thesis : Development of Ti-based Materials for Li-ion and Na-ion Batteries

Prepared by : Serkan DEMIREL

Date : 25.08.2017

The thesis mentioned above is assessed by our jury, it was accepted as a PhD Thesis in Physics department.

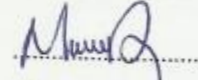
Examination Jury Members

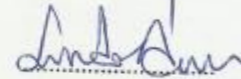
Supervisor : **Assoc. Prof. Serdar ALTIN**
Inonu University
Prof. Ali BAYRI
Inonu University
Prof. Yakup BALCI
Inonu University
Prof. Murat AYDIN
Adiyaman University
Assoc. Prof. Sevda AVCI
Istanbul Medeniyet University











Prof. Ibrahim ADIGUZEL

Institute President

Tezin Başlığı : Li-iyon ve Na-iyon Piller İçin Ti-Bazlı Anot Materyallerinin Geliştirilmesi

Tezi Hazırlayan : Serkan DEMİREL

Sınav Tarihi : 25.08.2017

Yukarıda adı geçen tez jürimizce değerlendirilerek Fizik Ana Bilim Dalında Doktora Tezi olarak kabul edilmiştir.

Sınav Jüri Üyeleri

Tez Danışmanı : Doç. Dr. Serdar ALTIN
İnönü Üniversitesi
Prof. Dr. Ali BAYRİ
İnönü Üniversitesi
Prof. Dr. Yakup BALCI
İnönü Üniversitesi
Prof. Dr. Murat AYDIN
Adıyaman Üniversitesi
Doç. Dr. Sevda AVCI
İstanbul Medeniyet Üniversitesi











Prof. Dr. İbrahim ADIGÜZEL

Enstitü Müdürü

HONOR CODE PLEDGE

This thesis entitled "Development of Ti-based Materials for Li-ion and Na-ion Batteries", which I have presented as a doctoral thesis, has been written by me without resorting to any means that contradicts with scientific ethic and traditions and I state that all sources that I used in the text and references are in the appropriate format and I pledge my honor.

Serkan DEMIREL



ONUR SÖZÜ

Doktora tezi olarak sunduđum 'Li-iyon ve Na-iyon Piller için Ti-Bazlı Anot Materyallerinin Geliştirilmesi' başlıklı bu çalışmanın bilimsel ahlak ve geleneklere aykırı düşecek bir yardıma başvurmaksızın tarafımdan yazıldığını ve yararlandığım bütün kaynakların, hem metin içinde hem de kaynakçada yönetimine uygun biçimde gösterilenlerden oluştuđunu belirtir, bunu onurumla doğrularım.

Serkan DEMİREL



ÖZET

Doktora Tezi

Li-iyon ve Na-iyon Piller İçin Ti-Bazlı Anot Materyallerinin Geliştirilmesi

Serkan DEMİREL

İnönü Üniversitesi

Fen Bilimleri Enstitüsü

Fizik Anabilim Dalı

146+xi sayfa

2017

Danışman: Doç. Dr. Serdar ALTIN

Bu doktora tez projesinde, Vanadyum katkılması ile Li-iyon ve Na-iyon piller için Titanyum bazlı anot malzemeleri incelenmiştir. Bu kapsamda, $\text{Li}_4\text{Ti}_{5-x}\text{V}_x\text{O}_{12}$, $\text{Li}_2\text{Ti}_{3-x}\text{V}_x\text{O}_7$, $\text{Li}_2\text{Ti}_{6-x}\text{V}_x\text{O}_{13}$, $\text{Na}_4\text{Ti}_{5-x}\text{V}_x\text{O}_{12}$, $\text{Na}_2\text{Ti}_{3-x}\text{V}_x\text{O}_7$ ve $\text{Na}_2\text{Ti}_{6-x}\text{V}_x\text{O}_{13}$ $x=(0, 0.025, 0.05, 0.1, 0.15)$ anot malzemeleri katı-hal reaksiyon ve iyon-değişim yöntemleri ile başarılı bir şekilde üretilmiştir. Anot malzemelerin yapısal özellikleri ve pil performansları detaylı bir şekilde incelenmiştir. XRD sonuçları, düşük seviyelerde V deęiřtirmesi ile ana fazların korunduęunu göstermiştir. Buna ek olarak Na-bazlı malzemelerde nano-tel oluşumu gözlemlenmiştir. Raman spektrum analizleri, 1000 döngü sonrasında pillerin anot malzemelerinin baę yapılarında deformasyon olduęunu göstermiştir.

Sonuç olarak, $\text{Li}_4\text{Ti}_5\text{O}_{12}$, $\text{Li}_2\text{Ti}_3\text{O}_7$ ve $\text{Na}_4\text{Ti}_5\text{O}_{12}$ anot malzemeleri ile üretilen pillerde, sistemlere yapılan düşük V katkılmaları ile pil ömrü ve pil kapasitelerinde artış sağlanmıştır.

Anahtar Kelimeler: Li-iyon, Na-iyon, Ex-situ, Vanadium, Titanium.

ABSTRACT

Ph.D. Thesis

Development of Ti-based Materials for Li-ion and Na-ion Batteries

Serkan DEMIREL

Inonu University
Institute of Science
Physics Department

146+xi pages

2017

Supervisor: Assoc. Prof. Serdar ALTIN

In this Ph.D. thesis project, Titanium-based anode materials for Li-ion and Na-ion batteries by vanadium doping in the system was investigated. $\text{Li}_4\text{Ti}_{5-x}\text{V}_x\text{O}_{12}$, $\text{Li}_2\text{Ti}_{3-x}\text{V}_x\text{O}_7$, $\text{Li}_2\text{Ti}_{6-x}\text{V}_x\text{O}_{13}$, $\text{Na}_4\text{Ti}_{5-x}\text{V}_x\text{O}_{12}$, $\text{Na}_2\text{Ti}_{3-x}\text{V}_x\text{O}_7$ and $\text{Na}_2\text{Ti}_{6-x}\text{V}_x\text{O}_{13}$ $x=(0, 0.025, 0.05, 0.1, 0.15)$ anode materials have been fabricated successfully via solid state reaction and ion exchange methods. The structural properties and battery performance of the anode were investigated in detail. XRD results of the samples showed that the main phase was protected for low V substitution in the system. In addition of this, It was observed a nanorod formation in Na-based anode materials. The structural properties of the anode materials after 1000 cycles of the battery cells were showed that the bound structure of the ions in the unit cell were deformed according to Raman spectra of the samples.

As a conclusion, it was found that the capacity and battery life of the cell fabricated by $\text{Li}_4\text{Ti}_5\text{O}_{12}$, $\text{Li}_2\text{Ti}_3\text{O}_7$ and $\text{Na}_4\text{Ti}_5\text{O}_{12}$ anode materials were improved by low level V-doping in the systems

Keywords: Li-ion, Na-ion, Ex-situ, Vanadium, Titanium.

ACKNOWLEDGMENTS

This study supported by TUBITAK the program of 2214-A International Scholarship Project, Inonu University Scientific Research Project Unit (IUBAP) project no: 2015/85, United States of America Air Force Office of Scientific Research (AFOSR) MURI FA9550-08-1-0407 and University of Illinois at Urbana-Champaign Materials Science and Engineering department. I would like to thank them for financial supports.

I would like to thank especially to my supervisor Assoc. Prof. Serdar ALTIN, who shows his incredibly passion, and energetic working afford during my Masters, PhD education and TUBITAK 2214-A project.

I would also like to thanks to Prof. Paul V. BRAUN from University of Illinois at Urbana-Champaign, USA, who provided the use of their laboratory for my TUBITAK 2214-A project studies.

I would also like to thank to my PhD committee advisors and my instructors Prof. Ali BAYRI, Prof. Yakup BALCI and Assist. Prof. Fatih BULUT, who educated me their valuable knowledge during my Master and PhD education life.

INDEX

	OZET.....	i
	ABSTRACT.....	ii
	ACKNOWLEDGEMENTS.....	iii
	INDEX.....	iv
	FIGURE LIST.....	vi
	TABLE LIST.....	x
	SYMBOLS AND ABBREVIATIONS.....	xi
1.	INTRODUCTION.....	1
2.	BATTERIES.....	3
2.1.	Primary Batteries.....	5
2.2.	Secondary Batteries.....	7
2.2.1.	Lithium Batteries.....	9
2.2.1.1.	Cathode Materials for Li-ion Battery.....	10
2.2.1.1.1.	LiCoO ₂ Cathode Material.....	10
2.2.1.1.2.	LiMn ₂ O ₄ Cathode Material.....	12
2.2.1.1.3.	LiFePO ₄ Cathode Material.....	13
2.2.1.2.	Anode Materials for Li-ion Battery.....	15
2.2.1.2.1.	Carbon based Anode Materials for Li-ion Batteries.....	15
2.2.1.2.2.	Transition Metals Anode Materials.....	16
2.2.1.2.3.	Titanium Oxide Based Anode Materials.....	18
2.2.1.2.3.1.	Li ₄ Ti ₅ O ₁₂ Anode Material for Li-ion Batteries.....	18
2.2.1.2.3.2.	Li ₂ Ti ₃ O ₇ Anode Material for Li-ion Batteries.....	21
2.2.1.2.3.3.	Li ₂ Ti ₆ O ₁₃ Anode Material for Li-ion Batteries.....	23
2.2.2.	Sodium Batteries.....	25
2.2.2.1.	Cathode Materials for Na-ion Batteries.....	25
2.2.2.1.1.	Layered Oxide Cathode Materials for Na-ion Battery.....	26
2.2.2.1.2.	Na _x CoO ₂ system for Na-ion Battery.....	27
2.2.2.1.3.	Na _x MnO ₂ system for Na-ion Battery.....	28
2.2.2.1.4.	Olivine NaFePO ₄ Cathode Material.....	30
2.2.2.2.	Anode Materials for Na-ion Batteries.....	31
2.2.2.2.1.	Carbon Based Anode Materials for Na-ion Batteries.....	32
2.2.2.2.2.	Sodium Metal Phosphate Anode Materials.....	32
2.2.2.2.3.	Titanium Oxide Based Anode Materials.....	34
2.2.2.2.3.1.	Na ₄ Ti ₅ O ₁₂ Anode Materials for Na-ion Batteries.....	34
2.2.2.2.3.2.	Na ₂ Ti ₃ O ₇ and Na ₂ Ti ₆ O ₁₃ Anode Materials for Na-ion Batteries.....	36
2.2.2.2.3.2.1.	Na ₂ Ti ₃ O ₇ system for Na-ion batteries.....	36
2.2.2.2.3.2.2.	Na ₂ Ti ₆ O ₁₃ system for Na-ion batteries.....	39
2.2.2.2.4.	Na-based Alloy Anode Materials.....	41
3.	PERFORMANCE PARAMETERS FOR BATTERIES.....	42
3.1.	Capacity.....	42
3.2.	Voltage.....	43
3.3.	Battery Life.....	45
4.	METHODOLOGY.....	47
4.1.	Sample Preparation.....	47

4.2.	X-ray Diffraction Analysis (XRD).....	47
4.3.	Scanning Electron Microscope Analysis (SEM).....	47
4.4.	Electrochemical Measurements.....	48
4.5.	Electrical Resistivity Measurements.....	49
5.	EXPERIMENTAL RESULTS.....	50
5.1.	DTA Results.....	50
5.2.	XRD Results.....	51
5.3.	Morphological Analysis.....	73
5.4.	Spectral Analysis.....	82
5.5.	Resistivity Analysis.....	95
5.6.	Battery Performance Analysis.....	100
6.	CONCLUSION.....	124
7.	REFERENCES.....	130
	RESUME.....	144

FIGURE LIST

Figure 2.1.	Baghdad battery in National Museum of Baghdad.....	3
Figure 2.2.	Volta battery.....	4
Figure 2.3.	Commercial battery types	5
Figure 2.4.	Primary type Alkaline-Manganese battery discharge curve	7
Figure 2.5.	Schematic of Lead-acid battery	8
Figure 2.6.	An example for layered structure system	10
Figure 2.7.	a) Charge-discharge characteristic of LiCoO_2 b) cyclic voltammetry characteristic of LiCoO_2	11
Figure 2.8.	Spinel crystal structure of LiMn_2O_4 system	12
Figure 2.9.	a) Charge-discharge characteristic b) cyclic voltammetry characteristic of LiMn_2O_4 system	13
Figure 2.10.	LiFePO_4 crystal structure	14
Figure 2.11.	a) LiFePO_4 charge-discharge curve. b) CV curve of LiFePO_4	14
Figure 2.12.	Structure of graphite.....	15
Figure 2.13.	Spinel type crystal structure of $\text{Li}_4\text{Ti}_5\text{O}_{12}$	18
Figure 2.14.	a) Charge-discharge characteristic of $\text{Li}_4\text{Ti}_5\text{O}_{12}$ b) Cyclic voltammetry characteristic of $\text{Li}_4\text{Ti}_5\text{O}_{12}$	19
Figure 2.15.	Crystal structure of $\text{Li}_2\text{Ti}_3\text{O}_7$	21
Figure 2.16.	Charge-discharge characteristic of $\text{Li}_2\text{Ti}_3\text{O}_7$	22
Figure 2.17.	Crystal structure of $\text{Li}_2\text{Ti}_6\text{O}_{13}$ system	23
Figure 2.18.	Charge-discharge characteristic of $\text{Li}_2\text{Ti}_6\text{O}_{13}$	24
Figure 2.19.	Layered structure for Na-ion cathode materials	26
Figure 2.20.	Voltage changes depend on Na concentration for Na_xCoO_2 cathode material	27
Figure 2.21.	Performance comparison between Li_xCoO_2 - Na_xCoO_2	27
Figure 2.22.	a) Tunneling Na_xMnO_2 structure, b) NaMnO_2 layered crystal structure,(Red; Oxygen, Turquoise; Manganese, Magenta; Sodium)	28
Figure 2.23.	Voltage changes depend on Na concentration for Na_xMnO_2 cathode material	29
Figure 2.24.	Olivine NaFePO_4 crystal structure and battery performance.....	30
Figure 2.25.	Crystal structure of NaFePO_4 system.....	31
Figure 2.26.	Na-ion battery performance of $\text{NaTi}_2(\text{PO}_4)_3$ system	33
Figure 2.27.	Crystal structure of $\text{NaTi}_2(\text{PO}_4)_3$	33
Figure 2.28	a) Crystal structure of $\text{Na}_4\text{Ti}_5\text{O}_{12}$ system, b) Charge-discharge characteristic of $\text{Na}_4\text{Ti}_5\text{O}_{12}$ system	35
Figure 2.29.	Battery performance of $\text{Na}_2\text{Ti}_3\text{O}_7$ system	37
Figure 2.30.	$\text{Na}_2\text{Ti}_3\text{O}_7$ and $\text{Na}_2\text{Ti}_6\text{O}_{13}$ crystal structures	38

Figure 2.31.	Battery performance of $\text{Na}_2\text{Ti}_6\text{O}_{13}$ system	40
Figure 3.1.	Variation of the voltage of battery cell electrodes according to the ratio of active substance	45
Figure 3.2.	Change of discharge time of battery voltage by temperature (T)	46
Figure 5.1.	DTA results of a) $\text{Li}_4\text{Ti}_5\text{O}_{12}$, $\text{Li}_2\text{Ti}_3\text{O}_7$ and $\text{Li}_2\text{Ti}_6\text{O}_{13}$, b) $\text{Na}_4\text{Ti}_5\text{O}_{12}$, $\text{Na}_2\text{Ti}_3\text{O}_7$ and $\text{Na}_2\text{Ti}_6\text{O}_{13}$	50
Figure 5.2.	XRD results of $\text{Li}_4\text{Ti}_{5-x}\text{V}_x\text{O}_{12}$ ($x=0, 0.025, 0.05, 0.1, 0.15$) powders	51
Figure 5.3.	XRD results of $\text{Li}_4\text{Ti}_{5-x}\text{V}_x\text{O}_{12}$ ($x=0, 0.025, 0.05, 0.1, 0.15$) electrodes after 1000 cycles.....	52
Figure 5.4.	Crystal parameter comparison of $\text{Li}_4\text{Ti}_{5-x}\text{V}_x\text{O}_{12}$ between before and after 1000 cycles.....	53
Figure 5.5.	Micro strain and crystallite sizes of $\text{Li}_4\text{Ti}_{5-x}\text{V}_x\text{O}_{12}$ between before and after 1000 cycles.....	54
Figure 5.6.	XRD results of $\text{Li}_2\text{Ti}_{3-x}\text{V}_x\text{O}_7$ ($x=0, 0.025, 0.05, 0.1, 0.15$) powders.	56
Figure 5.7.	XRD results of $\text{Li}_2\text{Ti}_{3-x}\text{V}_x\text{O}_7$ ($x=0, 0.025, 0.05, 0.1, 0.15$) electrodes after 1000 cycles.....	56
Figure 5.8.	$\text{Li}_2\text{Ti}_{3-x}\text{V}_x\text{O}_7$ a) a parameter results, b) b parameter results, c) c parameter results, d) crystal volume values, e) volume expansion rates.....	57
Figure 5.9.	Micro strain and crystallite sizes of $\text{Li}_2\text{Ti}_{3-x}\text{V}_x\text{O}_7$ between before and after 1000 cycles.....	58
Figure 5.10.	XRD results of $\text{Li}_2\text{Ti}_{6-x}\text{V}_x\text{O}_{13}$ ($x=0, 0.025, 0.05, 0.1, 0.15$) powders	59
Figure 5.11.	XRD results of $\text{Li}_2\text{Ti}_6\text{O}_{13}$ electrode after 1000 cycles.....	59
Figure 5.12.	a) Parameter a results, b) parameter b results, c) parameter c results, and d) crystal volume values of $\text{Li}_2\text{Ti}_{6-x}\text{V}_x\text{O}_{13}$	60
Figure 5.13.	Micro strain and crystallite sizes of $\text{Li}_2\text{Ti}_{6-x}\text{V}_x\text{O}_{13}$ between before and after 1000 cycles.....	60
Figure 5.14.	XRD results of $\text{Na}_4\text{Ti}_{5-x}\text{V}_x\text{O}_{12}$ ($x=0, 0.025, 0.05, 0.1, 0.15$) powders.....	62
Figure 5.15.	Ex-situ XRD results of $\text{Na}_4\text{Ti}_{5-x}\text{V}_x\text{O}_{12}$ ($x=0, 0.025, 0.05, 0.1, 0.15$) powders.....	62
Figure 5.16.	Crystal parameter comparison of $\text{Na}_4\text{Ti}_{5-x}\text{V}_x\text{O}_{12}$ between before and after 1000 cycles.....	63
Figure 5.17.	Micro strain and crystallite sizes of $\text{Na}_4\text{Ti}_{5-x}\text{V}_x\text{O}_{12}$ between before and after 1000 cycles.....	63
Figure 5.18.	XRD results of $\text{Na}_2\text{Ti}_{3-x}\text{V}_x\text{O}_7$ ($x=0, 0.025, 0.05, 0.1, 0.15$) powders	65
Figure 5.19.	Ex-situ XRD results of $\text{Na}_2\text{Ti}_{3-x}\text{V}_x\text{O}_7$ ($x=0, 0.025, 0.05, 0.1, 0.15$) powders.....	66
Figure 5.20.	Crystal parameter comparison of $\text{Na}_2\text{Ti}_{3-x}\text{V}_x\text{O}_7$ between before and after 1000 cycles.....	67

Figure 5.21.	Micro strain and crystallite sizes of $\text{Na}_2\text{Ti}_{3-x}\text{V}_x\text{O}_7$ between before and after 1000 cycles.....	68
Figure 5.22.	XRD results of $\text{Na}_2\text{Ti}_{6-x}\text{V}_x\text{O}_{13}$ ($x=0, 0.025, 0.05, 0.1, 0.15$) powders.....	69
Figure 5.23.	Ex-situ XRD results of $\text{Na}_2\text{Ti}_{6-x}\text{V}_x\text{O}_{13}$ ($x=0, 0.025, 0.05, 0.1, 0.15$) powders.....	70
Figure 5.24.	Crystal parameter comparison of $\text{Na}_2\text{Ti}_{6-x}\text{V}_x\text{O}_{13}$ between before and after 1000 cycles.....	71
Figure 5.25.	Micro strain and crystallite sizes of $\text{Na}_2\text{Ti}_{6-x}\text{V}_x\text{O}_{13}$ between before and after 1000 cycles.....	72
Figure 5.26.	SEM photographs of $\text{Li}_4\text{Ti}_{5-x}\text{V}_x\text{O}_{12}$ samples. a) $x=0$, b) $x=0.025$, c) $x=0.05$, d) $x=0.1$, e) $x=0.15$	74
Figure 5.27.	SEM photographs of $\text{Li}_2\text{Ti}_{3-x}\text{V}_x\text{O}_7$ samples. a) $x=0$, b) $x=0.025$, c) $x=0.05$, d) $x=0.1$, e) $x=0.15$	75
Figure 5.28.	SEM photographs of $\text{Li}_2\text{Ti}_{6-x}\text{V}_x\text{O}_{13}$ samples. a) $x=0$, b) $x=0.025$, c) $x=0.05$, d) $x=0.1$, e) $x=0.15$	77
Figure 5.29.	SEM photographs of $\text{Na}_4\text{Ti}_{5-x}\text{V}_x\text{O}_{12}$ samples. a) $x=0$, b) $x=0.025$, c) $x=0.05$, d) $x=0.1$, e) $x=0.15$	78
Figure 5.30.	SEM photographs of $\text{Na}_2\text{Ti}_{3-x}\text{V}_x\text{O}_7$ samples. a) $x=0$, b) $x=0.025$, c) $x=0.05$, d) $x=0.1$, e) $x=0.15$	80
Figure 5.31.	SEM photographs of $\text{Na}_2\text{Ti}_{6-x}\text{V}_x\text{O}_{13}$ samples. a) $x=0$, b) $x=0.025$, c) $x=0.05$, d) $x=0.1$, e) $x=0.15$	81
Figure 5.32.	Raman analysis of $\text{Li}_4\text{Ti}_{5-x}\text{V}_x\text{O}_{12}$ powder samples.....	83
Figure 5.33.	Ex-situ Raman analysis of $\text{Li}_4\text{Ti}_{5-x}\text{V}_x\text{O}_{12}$ electrodes after 1000 cycles.....	84
Figure 5.34.	Raman analysis of $\text{Li}_2\text{Ti}_{3-x}\text{V}_x\text{O}_7$ powder samples.....	85
Figure 5.35.	Ex-situ Raman analysis of $\text{Li}_2\text{Ti}_{3-x}\text{V}_x\text{O}_7$ electrodes after 1000 cycles.....	85
Figure 5.36.	Raman analysis of $\text{Li}_2\text{Ti}_{6-x}\text{V}_x\text{O}_{13}$ powder samples.....	87
Figure 5.37.	Ex-situ Raman analysis of $\text{Li}_2\text{Ti}_{6-x}\text{V}_x\text{O}_{13}$ electrodes after 1000 cycles.....	87
Figure 5.38.	Raman analysis of $\text{Na}_4\text{Ti}_{5-x}\text{V}_x\text{O}_{12}$ powder samples.....	89
Figure 5.39.	Ex-situ Raman analysis of $\text{Na}_4\text{Ti}_{5-x}\text{V}_x\text{O}_{12}$ electrodes after 1000 cycles.....	89
Figure 5.40.	Raman analysis of $\text{Na}_2\text{Ti}_{3-x}\text{V}_x\text{O}_7$ powder samples.....	91
Figure 5.41.	Ex-situ Raman analysis of $\text{Na}_2\text{Ti}_{3-x}\text{V}_x\text{O}_7$ electrodes after 1000 cycles.....	91
Figure 5.42.	Raman analysis of $\text{Na}_2\text{Ti}_{6-x}\text{V}_x\text{O}_{13}$ powder samples.....	93
Figure 5.43.	Ex-situ Raman analysis of $\text{Na}_2\text{Ti}_{6-x}\text{V}_x\text{O}_{13}$ electrodes after 1000 cycles.....	93

Figure 5.44.	CV measurements of the $\text{Li}_4\text{Ti}_{5-x}\text{V}_x\text{O}_{12}$ system. a) $x = 0$, b) $x = 0.025$, c) $x = 0.05$, and d) $x = 0.1$	101
Figure 5.45.	Battery performance of the $\text{Li}_4\text{Ti}_{5-x}\text{V}_x\text{O}_{12}$ system over 1000 cycles at 1C constant current.....	103
Figure 5.46.	Battery performance of $\text{Li}_4\text{Ti}_{5-x}\text{V}_x\text{O}_{12}$ system at different C rates...	104
Figure 5.47.	CV measurements of $\text{Li}_2\text{Ti}_{3-x}\text{V}_x\text{O}_7$ system where a) $x = 0$, b) $x = 0.025$, c) $x = 0.05$, d) $x = 0.1$, and e) $x = 0.15$	105
Figure 5.48.	Battery performance of the $\text{Li}_2\text{Ti}_{3-x}\text{V}_x\text{O}_7$ system at 1C rate up to 1000 cycles	107
Figure 5.49.	Battery performance at different C rates of the $\text{Li}_2\text{Ti}_{3-x}\text{V}_x\text{O}_7$ system	108
Figure 5.50.	CV measurements of the $\text{Li}_2\text{Ti}_6\text{O}_{13}$ system	109
Figure 5.51.	The battery performance of the $\text{Li}_2\text{Ti}_6\text{O}_{13}$ system at 1C rate up to 1000 cycles.....	110
Figure 5.52.	Different C rates battery performance of $\text{Li}_2\text{Ti}_6\text{O}_{13}$ system.....	111
Figure 5.53.	CV measurements of the $\text{Na}_4\text{Ti}_{5-x}\text{V}_x\text{O}_{12}$ system where a) $x = 0$, b) $x = 0.025$, c) $x = 0.05$, d) $x = 0.1$, and e) $x = 0.15$	112
Figure 5.54.	Battery performance of the $\text{Na}_4\text{Ti}_{5-x}\text{V}_x\text{O}_{12}$ system for 1C rate up to 1000 cycles.....	114
Figure 5.55.	Different C rates battery performance of $\text{Na}_4\text{Ti}_{5-x}\text{V}_x\text{O}_{12}$ system.....	115
Figure 5.56.	Cyclic voltammetry (CV) measurements of $\text{Na}_2\text{Ti}_{3-x}\text{V}_x\text{O}_7$ system. a) $x=0$, b) $x=0.025$, c) $x=0.05$, d) $x=0.1$, e) $x=0.15$	116
Figure 5.57.	The battery performance of the $\text{Na}_2\text{Ti}_{3-x}\text{V}_x\text{O}_7$ system for 1C rate up to 1000 cycles.....	118
Figure 5.58.	Different C rates battery performance of $\text{Na}_2\text{Ti}_{3-x}\text{V}_x\text{O}_7$ system.....	119
Figure 5.59.	CV measurements of the $\text{Na}_2\text{Ti}_{6-x}\text{V}_x\text{O}_{13}$ system where a) $x = 0$, b) $x = 0.025$, c) $x = 0.05$, d) $x = 0.1$, and e) $x = 0.15$	120
Figure 5.60.	Battery performance of the $\text{Na}_2\text{Ti}_{6-x}\text{V}_x\text{O}_{13}$ system for 1C rate up to 1000 cycles.....	122
Figure 5.61.	Different C rates battery performance of $\text{Na}_2\text{Ti}_{6-x}\text{V}_x\text{O}_{13}$ system....	123

TABLE LIST

Table 2.1.	Comparison of batteries.....	9
Table 2.2.	Experimental values of potential for the plateaus associated with reactions in binary transition metal compounds, M_aX_b	17
Table 3.1	Standard electrode potentials Some of the elements and compounds in liquid electrolyte at 298 K	44
Table 5.1.	Raman peaks definitions of $Li_4Ti_5O_{12}$ system.....	84
Table 5.2.	Raman peaks definitions of $Li_2Ti_3O_7$ system.....	86
Table 5.3.	Raman peaks definitions of $Li_2Ti_6O_{13}$ system.....	88
Table 5.4.	Raman peaks definitions of $Na_4Ti_5O_{12}$ system.....	90
Table 5.5.	Raman peaks definitions of $Na_2Ti_3O_7$ system.....	92
Table 5.6.	Raman peaks definitions of $Na_2Ti_6O_{13}$ system.....	94
Table 5.7.	Resistivity measurement results for $Li_4Ti_{5-x}V_xO_{12}$	95
Table 5.8.	Resistivity measurement results for $Li_2Ti_{3-x}V_xO_7$	96
Table 5.9.	Resistivity measurement results for $Li_2Ti_{6-x}V_xO_{13}$	97
Table 5.10.	Resistivity measurement results for $Na_4Ti_{5-x}V_xO_{12}$	98
Table 5.11.	Resistivity measurement results for $Na_2Ti_{3-x}V_xO_7$	98
Table 5.12.	Resistivity measurement results for $Na_2Ti_{6-x}V_xO_{13}$	99

SYMBOLS and ABBREVIATIONS

<i>T</i>	Temperature
<i>T_c</i>	Critic Temperature
<i>C</i>	Specific constant current value for charge/discharge process
<i>C_c</i>	Specific Capacity
<i>CV</i>	Cyclicvoltammetry or Cyclicvoltamogram
<i>CB</i>	Carbon Black
<i>PVDF</i>	Polyvinylidene fluoride
<i>F</i>	Faraday Constant
<i>R</i>	Gas Constant
<i>V</i>	Voltage
<i>E</i>	Electrode Potential
<i>Q</i>	Molar capacity
<i>I</i>	Current
<i>M</i>	Mass
<i>μ</i>	Mobility
<i>σ</i>	Electrical conductivity
<i>ρ</i>	Resistivity
<i>LTO</i>	Li ₄ Ti ₅ O ₁₂
<i>LCO</i>	LiCoO ₂

1. INTRODUCTION

To the present day, the use of underground energy sources without any consideration has been damaging the environment, environmental life, and human life. This situation has motivated humans to produce cleaner and more efficient energy sources. Especially nowadays, the development and adoption of electronic devices needs to be much more energy efficient.

Products such as electrical automobiles, laptops, cell phones, and any other portable devices need long-life energy storage systems and sources to simplify daily life and reduce environmental pollution.

One of the greatest discoveries in history is the lithium-ion (Li-ion) battery. It, along with its commercialisation in 1991, is of great importance in human history. Li-ion batteries, which are described as "secondary type batteries", offer a great advantage to the users because of their rechargeable features. They have taken their place in the technology with their high operating capacity, high operating voltage, and charge-discharge life. Nowadays, Li-ion batteries are used in devices such as mobile phones, computers, electric cars etc. However, Li-ion batteries also have some disadvantages. The most important of these is the cost of obtaining lithium element and reduced Li reserves.

To overcome these disadvantages, scientists work on alternative energy storage systems. In this context, sodium-ion (Na-ion) batteries have been discovered as an alternative energy storage system. Research results show that Na-ion batteries can be used instead of Li-ion batteries especially for stationary applications such as smart grid systems. In particular, these two elements have similar physical properties, and the Na is abundant in nature, and it is cheaper than Li. Environmentally friendly, easy to obtain, and low cost Na-ion batteries offer great advantages. On the other hand however, Na-ion batteries have some significant disadvantages compared to Li-ion batteries. The fact that the Na ion is heavier (larger atomic mass) and larger (greater atomic radius) than the Li ion results in significant disadvantages in battery performance. More specifically, a Li-ion battery has an average operating voltage of 3.04 V while the Na-ion battery has an average operating voltage of only 2.71 V.

Given the performance advantages and disadvantages of Li-ion and Na-ion batteries, consequently Na-ion batteries have been the subject of much performance boosting work and commercialisation efforts.

In this doctoral dissertation, performance upgrade studies of titanium (Ti) based anode materials have been conducted via vanadium (V) substitutions for both Li-ion and Na-ion batteries. In this context, the development of new generation Li-ion and Na-ion batteries, and their technological use, is evaluated in the experiments presented in this doctoral thesis.



2. BATTERIES

Batteries can generally be described as electrochemical power storage and usage systems [1]. This system is composed of at least two components, which react with each other to convert chemical energy into electrical energy via an electrochemical reaction [2]. The oldest battery known in the history is the Baghdad battery. It is believed to belong to the period from BC 250 to MS 224, and was introduced in 1935 by William Konig, director of the National Museum of Baghdad [3].



Figure 2.1. Baghdad battery in National Museum of Baghdad [4].

As seen in Figure 2.1, the Baghdad pylon has a positive and a negative pole when viewed from the outside. In general terms, a battery is composed of a negative electrode (anode), a positive electrode (cathode), and a fluid electrolyte which provides ionic conductivity [5]. A chemical reaction begins when these three components are combined. In this reaction, the active elements in the anode are ionised and move towards the cathode. During the ionization process, one or more electrons separates from the atom. This process reveals one ion and one or more free electrons [5]. The free electron moves to the conduction layers, and the ion moves from anode to cathode. Generally, this process is called the discharge process and the recharge process is reversible [5].

Until the Baghdad battery was recognised, the Volta battery was known as the first battery in history. It was discovered by Alexander Volta in 1799 and announced in 1800 [6].

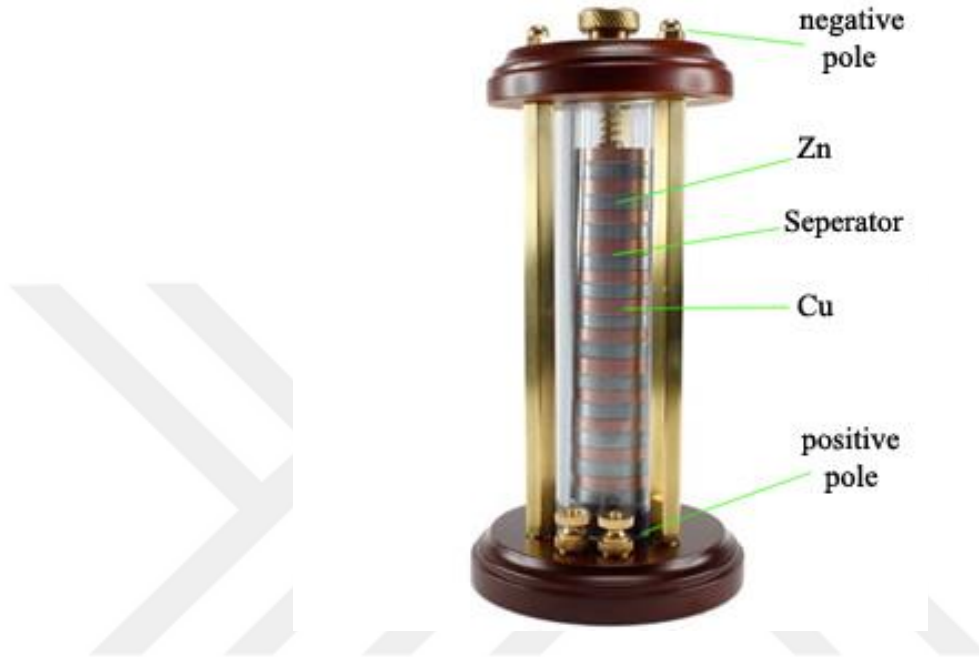


Figure 2.2. Volta battery [7].

Figure 2.2 shows a visual of a working Volta battery, which does not use a fluid electrolyte like the Baghdad battery. In the Volta battery there is a paper type separator layer that prevents shorting between the two metal plates acting as anode and cathode [8]. This separator layer allows the transfer of ions in terms of ionic conductivity, while preventing the electrons that break off the ions from transferring between the metal plates. Usually, batteries produced in the past have consisted of basic components such as anode, cathode, and electrolyte [5].



Figure 2.3. Commercial battery types [9].

Figure 2.3 shows the common commercial battery types [9]. Although the internal structures of these batteries are almost the same, their potentials are different in terms of their working voltage, working time, and shelf life [9]. The main reason for this is due to the structure of the electrode designs [9]. In the most general sense, the batteries are divided into two classes. These are called primary and secondary battery types [5]. The primary type batteries are non-rechargeable batteries and are therefore disposable. Secondary type batteries are rechargeable, so can be recharged and discharged over a specific lifetime period [5].

2.1. Primary Batteries

In the most general sense, the primary battery is a non-rechargeable and single-use battery [10]. They have high operating voltage, high capacity, and long shelf life. The adventure of the primary battery started with the Volta battery, which was discovered by A. Volta in 1799, when it attracted considerable attention. It began to be used in telegraph systems from 1830 [10]. Afterwards, research and development studies on batteries led to the discovery of the first high-current primary battery in 1870 [10]. The first production

of simple electric motors began after the high-current battery was discovered in 1870 [10]. In terms of commercialisation, although batteries firstly came to the attention of high-income people, over a very short time period batteries took their place in the markets. Nowadays, the primary type of non-rechargeable batteries are commercially effective, manufactured in varying sizes, and have different working potentials. The general internal structure of these batteries is composed of different types of anode (-) and cathode (+) materials [10,11].

In the case of a primary battery, the discharge reactions are not reversible because the reaction generally takes place in one direction. For example, the reactions occurring on a zinc-manganese (Zn-Mn) electrode [10] are:

reactions on cathode and obtained voltage amount:



reactions on anode and obtained voltage amount:



and general reaction in the battery:



In commercial and experimental research and development (R&D) studies, copper-zinc (Cu-Zn), nickel (Ni)-metal hydrate, carbon-zinc (C-Zn), alkaline-manganese, zinc-air, silver (Ag) oxide-zinc, lithium-manganese dioxide, lithium-carbon monofluoride, and lithium-thionyl chloride batteries can all be given as instances of primary battery types [5,10,12].

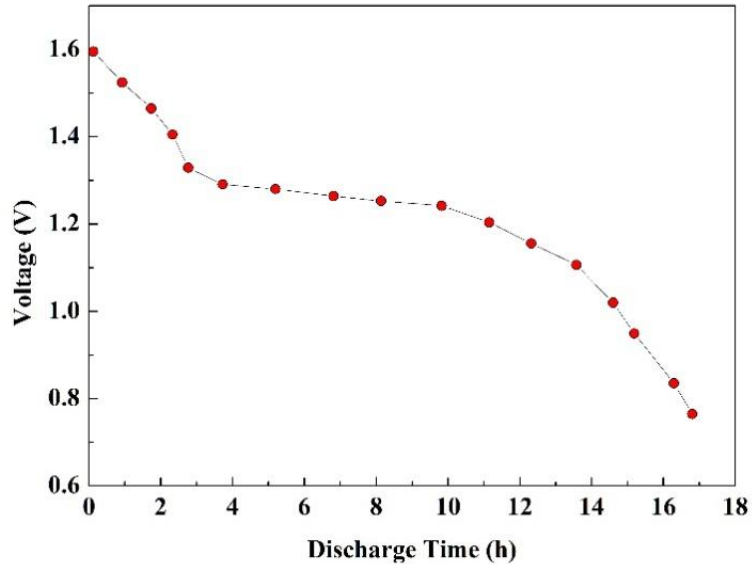


Figure 2.4. Primary type alkaline-manganese battery discharge curve [12].

Figure 2.4 shows an alkaline-manganese battery discharge characteristic curve. As can be seen from the figure, the primary batteries have good discharge capacity and long discharge time [12]. Usually, these characteristic properties are the common behavior for primary batteries.

2.2. Secondary Batteries

The story of secondary batteries, or rechargeable batteries, started with the discovery of the lead-acid battery in 1859 by French physicist Gaston Planté. This battery consists of lead-lead oxide (Pb-PbO, PbO₂, Pb₃O₄) electrodes and a sulphuric acid liquid electrolyte (H₂SO₄). Lead-acid batteries were first commercialised around 1900 and continuing to be used today [5,10,12]. The lead-acid batteries have received a great deal of attention due to their good working voltage (about 2V), long discharge-charge lifetime, and low production cost. This battery shows especially good discharge performance (~20 hours) under high discharge current (20 C) [5,10,12]. For that reason, this battery is used in electrical vehicles. On the other hand, lead-acid batteries have some disadvantages such as performance failure at low temperatures (< room temperature), heavy weight, and toxic and hazardous components [5,10,12].

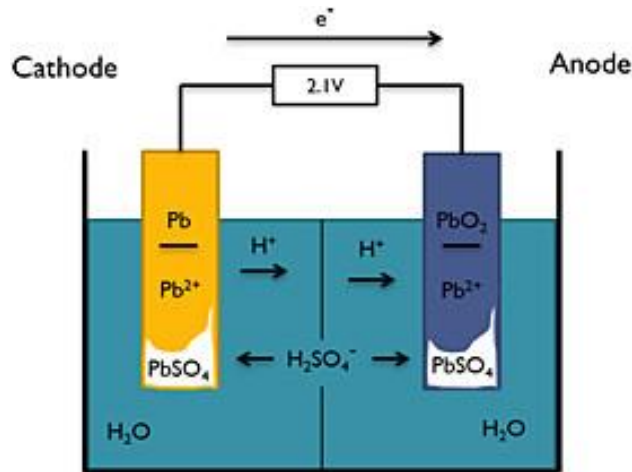


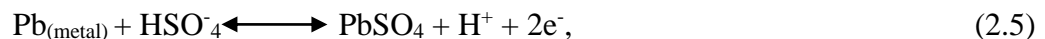
Figure 2.5. Schematic of a lead-acid battery [13].

Figure 2.5. shows the charge-discharge process of a lead-acid battery in a schematic fashion. The chemical reactions taking place in this battery can be described as [10,12]:

reaction in electrolyte:



reaction in negative electrode (anode):



reaction in positive electrode (cathode):



and total reaction:



For a secondary battery the charge-discharge process is repeatable until a specific lifetime. This type of battery always loses charge-discharge performances while waiting on the shelf or during charge-discharge cycling. This loss in performance is generally caused by electrode deformations, electrolyte deformations, and dendrite formation on electrode surfaces [5,10,12].

From the discovery of lead-acid secondary batteries to today, many secondary battery kinds have been discovered. These include secondary nickel-cadmium (Ni-Cd), silver oxide-zinc, lithium-manganese dioxide, lithium - vanadium oxide, lithium-polyaniline, lithium-carbon, lithium-LGH-vanadium oxide, lithium-polyacene, niobium (Nb) oxide - vanadium oxide, titanium oxide - manganese oxide lithium-metal, sodium-metal, and magnesium (Mg)-metal batteries [5,10,12].

Among these battery types, Li-ion batteries are the most attractive ones for technological evolution. Their discovery, and commercialisation in 1991, are of great importance in human history [14]. The first lithium based batteries were introduced in the 1960s and gained popularity in 1991 when they were commercialised by Sony with a LiCoO₂ cathode material [15]. This battery can, nowadays, be used as an energy source in almost all electronic devices. Lithium batteries are notable for both high energy density and high operating voltage. Especially for today's high-performance electrode, studies of this battery type have been increasing in number [10–12].

Table 2.1 Comparison of batteries [16].

	<i>Lead-acid</i>	<i>Ni-Cd</i>	<i>Ni-MH</i>	<i>Li-ion</i>	<i>Li-Poly</i>
<i>Voltage</i>	2	1.2	1.2	3.6-3.7	3.6-3.7
<i>Cycle life</i>	400	500-1000	400-1000	300-1000	300-1000
<i>Life (years)</i>	1	2	2	1+	1+
<i>Self-discharge rate</i>	%10	%30	%30	%3	%3
<i>Charging time (hours)</i>	8	1.5	4	2-6	2-6
<i>Safety</i>	No BMS	Good	Good	Poor	Average
<i>High temp performance</i>	Good	Good	Good	Average	Average
<i>Low temp performance</i>	Poor	Poor	Poor	Average	Average

2.2.1. Lithium Batteries

The secondary type lithium battery was discovered around 1960, and in 1991 Sony produced commercial Li-ion batteries with LiCoO₂ cathode materials [14,15]. Since then they have been used in almost every electronic device as energy storage and usage systems. There are many variant types of lithium battery, and they are popular, having

good working potentials and energy density values. In this context, high performance Li-ion battery electrodes and their investigations in the literature are discussed below.

2.2.1.1. Cathode Materials for Li-ion Batteries

Cathode materials, which create the positive pole of the battery, are the most important part of the system. To obtain high working voltage batteries, the cathode materials must have larger ionization voltages [10,12,17]. Nowadays, almost every electronic device needs a high working voltage and high working capacity. For these features, there are many cathode materials available. The materials can be separated from each other in terms of their structure and electrical and thermodynamics features. In the commercial field, LiCoO_2 and LiMn_2O_4 are the most commonly used Li-ion cathode materials, which we will now present [10,12,17].

2.2.1.1.1. LiCoO_2 Cathode Materials

LiCoO_2 is the most popular cathode material for Li-ion batteries. It has a layered crystal structure, and this layered structure enables the Li ions intercalate/deintercalated [10,12,18]. The Li^+ ions are bonded to the layers with weak Van der Waals forces and are able to move within the layers [18,19].

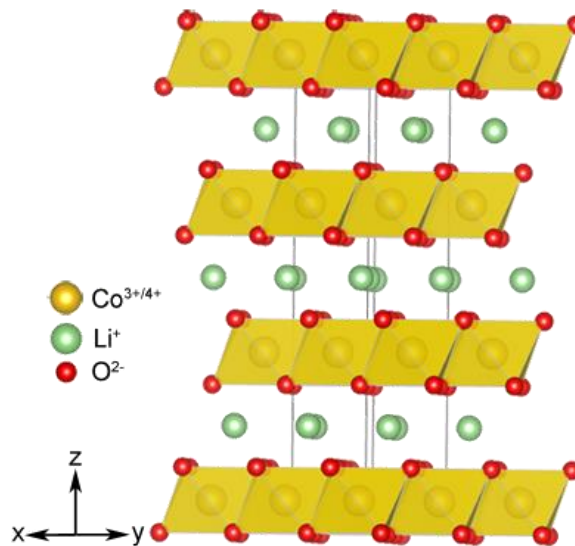


Figure 2.6. An example of a layered structure system [20].

Figure 2.6 shows the crystal structure of layered LiCoO_2 . In general, layered cathode materials consist of an ABC_2 type structure (A: alkaline earth metals, B: transition metals, C: metals or oxygen) [21], with the alkaline earth metals located between two similar transition metal oxide layers. The transition metal oxide layers have high electrical and thermal conductivity coefficients. On the other hand, the alkaline metal layers have insulator and low thermal conductivity coefficients [22]. In 1980, Goodegough discovered the cathode properties of LiCoO_2 [23], with crystal structure shown in Figure 2.6. In this structure the Li^+ ions are located between two CoO_2 layers. In 1991, Sony first produced commercial Li-ion batteries with LiCoO_2 cathode materials [24,25], and even today, LiCoO_2 /Carbon Li-ion batteries are still used in almost every electrical energy storage system.

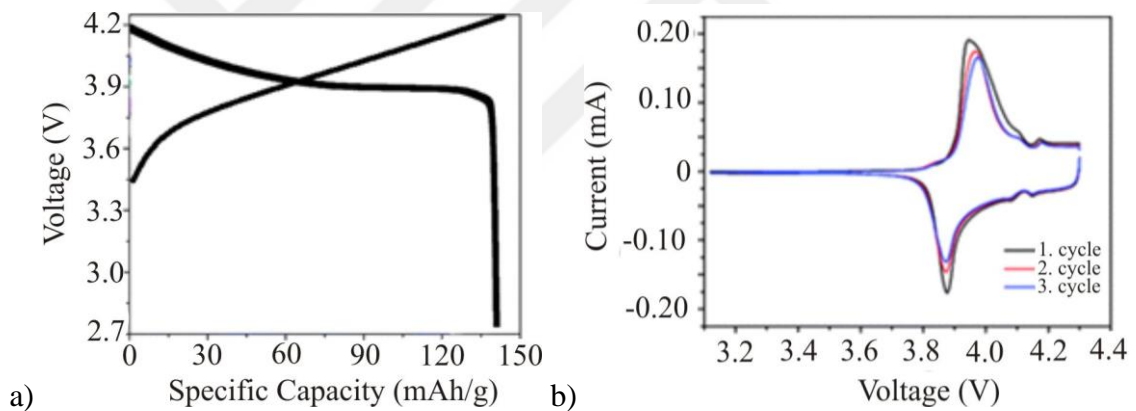


Figure 2.7. a) Charge-discharge and b) cyclic voltammetry characteristics of LiCoO_2 [10, 26].

Figure 2.7 shows the charge-discharge characteristics of LiCoO_2 , which has 274 mAh/g theoretical, and ~140 mAh/g experimental capacity values [27,28]. The open circuit voltage of LiCoO_2 is 3.9 V. Goodenough explained the effect of Li content in LiCoO_2 : when the amount of Li is reduced in this structure the open circuit voltage increases to 4.2 V at $\text{Li}_{0.5}\text{CoO}_2$ [23,27,28].

2.2.1.1.2. LiMn₂O₄ Cathode Material

Another popular battery cathode material is LiMn₂O₄ [29]. LiMn₂O₄ has low production cost and good environmental properties [29, 30]. Unlike the layered crystal structure of LiCoO₂, LiMn₂O₄ has a spinel type crystal structure [31].

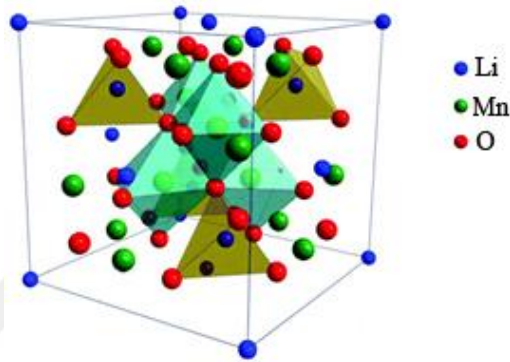


Figure 2.8. Spinel crystal structure of the LiMn₂O₄ system [32].

Figure 2.8 shows the spinel structure of the LiMn₂O₄ system. A three-dimensional (3D) spinel structure has some advantages for an electrode, such as high electron and ion flow and low internal electronic resistivity [33,34]. This structure also exhibits thermal stability. All of these advantages are desirable for battery systems [33,34]. LiMn₂O₄ was discovered by Thackeray et al. in 1986 [35]. Although the experimental capacity (~120 mAh/g) is 5–10% lower than that of LiCoO₂, LiMn₂O₄ has entered the literature as a cathode material with good performance.

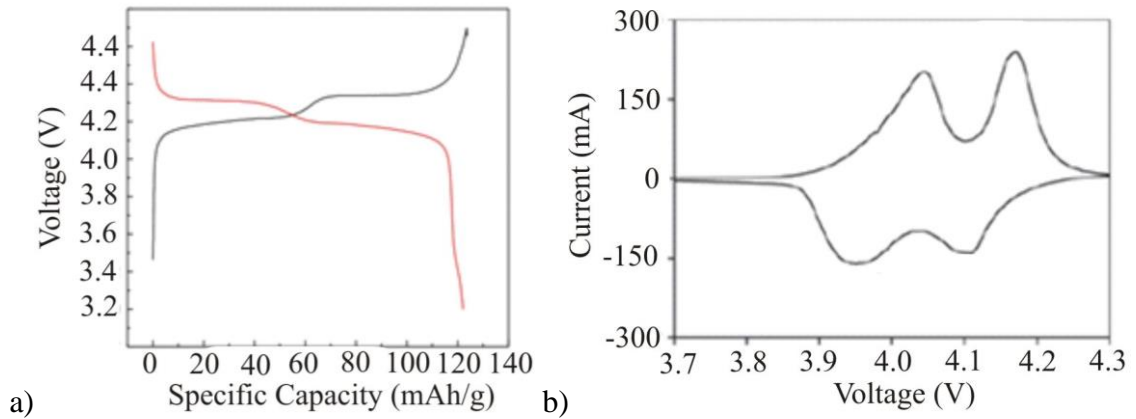


Figure 2.9. a) Charge-discharge and b) cyclic voltammetry characteristics of the LiMn_2O_4 system [36,37].

Figure 2.9 a) shows the charge-discharge characteristics of the LiMn_2O_4 system, which has 148 mAh/g theoretical, and ~120 mAh/g experimental, capacity between 4.4 and 3.0 V. Figure 2.9 b) shows the cyclic voltammetry (CV) results of LiMn_2O_4 [37,38]. As can be clearly seen in this figure, there are two different redox peaks for each electrode. The positive current peaks correspond to LiMn_2O_4 electrode redox peaks [38]. These redox peaks also affect the charge-discharge curves; as can be seen in Figure 2.9 a), there are two capacitance change steps for each charge and discharge curve [38]. For the discharge curve, the first down step approximately corresponds to the 4.17 V peak, while the second down step corresponds to the 4.04 V peak. These situations can be assumed to be similar for the negative CV region and charge curve [36–38].

2.2.1.1.3. LiFePO_4 Cathode Material

Iron (Fe) based cathode materials are very attractive for battery applications due to their natural abundance and low cost [39]. The LiFeO_2 compound can be described as the ideal low-cost battery [40]. However, the LiFeO_2 layered cathode material has some disadvantages due to Fe^{+3} reductions as the FeO_6 octahedral layers make very difficult the reduction of one electron from Fe^{3+} [40].

Thermally and mechanically stable LiFePO_4 has entered the scientific literature by Goodenough in 1996 [41]. LiFePO_4 is a type of LiMPO_4 compounds, where M is Fe, Co, Mn, or Ni. LiFePO_4 also has better battery performance than other compositions [42].

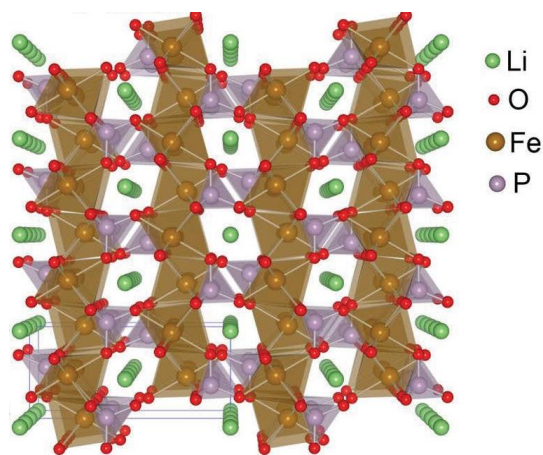


Figure 2.10. LiFePO₄ crystal structure [43].

LiFePO₄ has the close packed hexagonal crystal structure with Li-ions moving along one direction in the channels of the structure (Figure 2.10) [43]. Furthermore, this structure provides high diffusion routes for ions. A higher diffusion rate means high charge-discharge capacity at high currents [43].

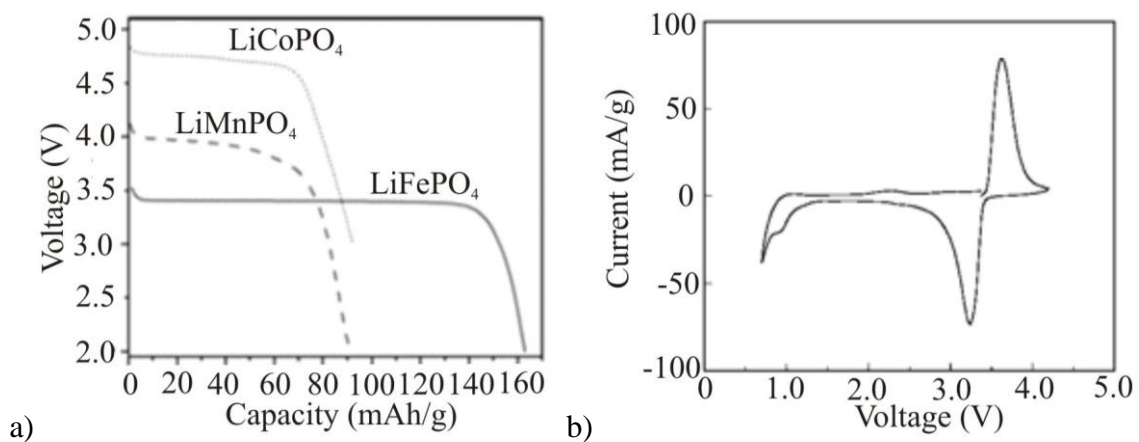


Figure 2.11. a) LiFePO₄ charge-discharge curve. b) CV curve of LiFePO₄ [5,44].

Figure 2.11 shows the charge-discharge curve of a LiFePO₄/C battery. LiFePO₄ has ~160 mAh/g capacity value and ~ 3.55 V long discharge plateau. Figure 2.11 also shows that LiFePO₄ has better battery performance than Mn and cobalt (Co) based

compounds [43,44]. On the other hand, LiFePO_4 has a lower voltage plateau than LiMnPO_4 (4.13 V), despite Fe being to the right of Mn in the periodic table.

2.2.1.2. Anode Materials for Li-ion Batteries

The anode material (negative pole during discharge) is another important component of a battery. For a high working voltage battery, the anode materials have to have lower ionization voltages [45]. Normally, the total battery working potential is equal to the anode and cathode ionization voltage difference. There are many anode materials for Li-ion batteries, which can be classified as metal-oxide, carbon based, and alloys [43]. We will now present the most popular anode materials for Li-ion batteries.

2.2.1.2.1. Carbon based Anode Materials for Li-ion Batteries

Carbon based (graphite) compounds can be described as the most attractive anode materials for Li-ion batteries [46]. Graphite has a good charge-discharge performance and low production cost, making it attractive for Li-ion batteries. Graphite has a theoretical capacity of 372 mAh/g and Li ions can bond with six C atoms in the LiC_6 formation [44,47].

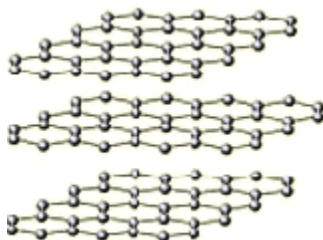
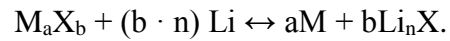


Figure 2.12. Structure of graphite [48].

Figure 2.12 shows the graphite structure, which is hexagonal two dimensional (2D). In this structure, one Li ion can bond with six C atoms [47]. Graphite anode materials have ~300 mAh/g experimental capacity and a ~0.1V plateau voltage. Because of this, graphite is one of the most selected anode materials for commercial applications.

2.2.1.2.2. Transition Metals Anode Materials

Transition metals anode materials can be a good alternative to carbon based materials. These anode materials can transfer from two to six electrons, according to the reactions below [49]:



Here, M is a transition metal, X is an anion, and n is the formal oxidation state of X [50]. Transition metal anode materials can consist of oxide and non-oxide alloys. In the above reaction, the X can be oxygen (O), sulphur (S), nitrogen (N), phosphorous (P), and fluorine (F).

Table 2.2 Experimental values of potential for the plateaus associated with reactions in binary transition metal compounds of the type M_aX_b [44].

M	X = O		X = S		X = N		X = P		X = F	
	Phase	E_{conv}/V	Phase	E_{conv}/V	Phase	E_{conv}/V	Phase	E_{conv}/V	Phase	E_{conv}/V
Cr	Cr ₂ O ₃	0.2	CrS	0.85	CrN	0.2			CrF ₃	1.8 ^[c]
Mn	MnO ₂	0.4	MnS	0.7			MnP ₄	0.2 ^[d]		
	Mn ₂ O ₃	0.3								
	MnO	0.2								
Fe	Fe ₂ O ₃	0.8	FeS ₂	1.5			FeP ₂	0.3	FeF ₃	2.0 ^[c]
	Fe ₃ O ₄	0.8	FeS	1.3	Fe ₃ N	0.7	FeP	0.1		
	FeO	0.75								
Co	Co ₃ O ₄	1.1	CoS ₂	1.65-1.3 ^[b]	CoN	0.8	CoP ₃	0.3	CoF ₂	2.2 ^[c]
	CoO	0.8	Co _{0.92} S	1.4	Co ₃ N	1.0				
			Co ₉ S ₈	1.1						
Ni	NiO	0.6	NiS ₂	1.6	Ni ₃ N	0.6	NiP ₃	0.7	NiF ₂	1.9 ^[c]
			NiS	1.5			NiP ₂	0.5-0.3 ^[b]		
			Ni ₃ S ₂	1.4			Ni ₃ P	Slope ^[a]		
Cu	CuO	1.4	CuS	2.0-1.7 ^[b]	Cu ₃ N		CuP ₂	0.7	CuF ₂	3.0
	Cu ₂ O	1.4	Cu ₂ S	1.7			Cu ₃ P	0.8		
Mo	MoO ₃	0.45	MoS ₂	0.6						
	MoO ₂	Slope ^[a]								
W			WS ₂	0.8-0.6 ^[b]						
Ru	RuO ₂	0.9								

a) Slope indicates the absence of a distinct voltage plateau in the electrochemical profile.

b) Two plateaus were observed in the electrochemical profile.

c) Data collected for nanocomposites with carbon at 70 °C.

d) Conversion of Li₇MnP₄ to Li₃P and Mn.

Table 2.2 shows the experimental working voltage values of transition metal anode materials. As we see in the table, each transition metal anode material has a low working voltage, and this situation is very good for a battery. Also, Table 2.2 shows that the oxide transition metal compounds have lower voltages than other types of combinations; in addition, those transition metal oxides have average capacity values of 600–900 mAh/g [44]. These capacity values apply to the very first charge-discharge

cycles. After a few cycles these oxide compounds have dramatically reduced capacity values during the long charge-discharge process [44,49].

2.2.1.2.3. Titanium Oxide Based Anode Materials

Titanium oxide based anode materials can provide an alternative to carbon and transition metal anode materials. They include different compositions such as $\text{Li}_4\text{Ti}_5\text{O}_{12}$, $\text{Li}_2\text{Ti}_3\text{O}_7$, and $\text{Li}_2\text{Ti}_6\text{O}_{13}$ [51]. These materials constitute a part of the work presented in this Ph.D. thesis.

2.2.1.2.3.1. $\text{Li}_4\text{Ti}_5\text{O}_{12}$ Anode Material for Li-ion Batteries

$\text{Li}_4\text{Ti}_5\text{O}_{12}$ (LTO) is the most attractive anode material for Li-ion batteries, and it is used in some commercial batteries. $\text{Li}_4\text{Ti}_5\text{O}_{12}$ can also be used as the anode material in supercapacitors, Li-ion capacitors, and hybrid supercapacitors [51, 52]. $\text{Li}_4\text{Ti}_5\text{O}_{12}$ has a low working potential around 1.5 V, a high discharge capacity ~ 175 mAh/g, and a stable long charge-discharge cycle life. All of these excellent properties are due to the spinel type cubic crystal structure [53].

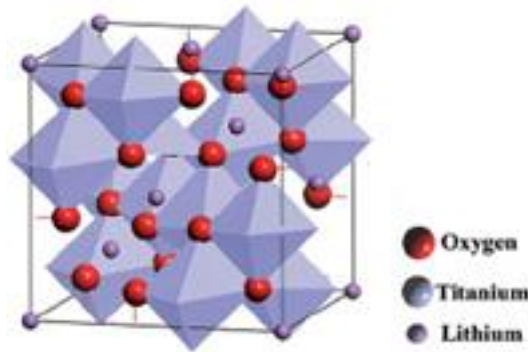


Figure 2.13. Spinel type crystal structure of $\text{Li}_4\text{Ti}_5\text{O}_{12}$ [53].

Figure 2.13 shows the spinel type crystal structure of the $\text{Li}_4\text{Ti}_5\text{O}_{12}$ system. In this system, there are two lithium ions at 8a and 16c sites, with atoms ionizing and moving during the charge-discharge process. The $\text{Li}_4\text{Ti}_5\text{O}_{12}$ system also has zero microstrain in its crystal structure [53], ensuring a stable crystal structure which is reflected in the long battery life [51–53].

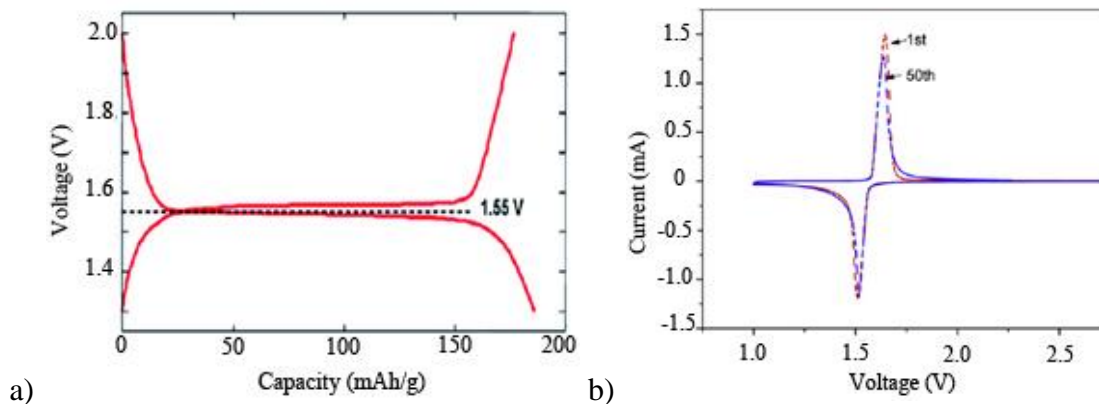


Figure 2.14. a) Charge-discharge characteristics of $\text{Li}_4\text{Ti}_5\text{O}_{12}$ b) CV characteristics of $\text{Li}_4\text{Ti}_5\text{O}_{12}$ [54, 55].

Figure 2.14 shows the charge-discharge and CV characteristics of the $\text{Li}_4\text{Ti}_5\text{O}_{12}$ system. It is clear from Figure 2.14a) that $\text{Li}_4\text{Ti}_5\text{O}_{12}$ has a long capacity plateau during the charge-discharge process [54]. This system has ~ 170 mAh/g discharge capacity between 1.0 and 2.0 V [54]. Figure 2.14 b) shows the CV characteristics of the system. $\text{Li}_4\text{Ti}_5\text{O}_{12}$ (LTO) has a redox reaction at 1.55V where Li^+ ions separate from the crystal structure [55]. Another redox reaction occurs at 1.5V, and this peak corresponds to the counter electrode reaction [55].

Researchers have been working to improve the electrochemical performance of the LTO system. To achieve this, different types of synthesis methods have been used such as solid state reaction, spray paralysis, sol-gel, molten salt, micro wave and electrodeposition [51–57]. LTO has insulator like electrical conductivity behavior. For a battery electrode, high resistivity effects the battery performance negatively. To handle this problem, researchers have been working on decreasing the grain size. The LTO electrode's battery performance improves when the grain size is lower than $1 \mu\text{m}$, because of the reduction in the mean ion path. A short ion path leads to low electrical resistance and has a positive effect on battery performance [53–57].

Researchers have also been trying some element doping/substitution in the LTO system in an effort to improve battery performance. Scandium (Sc), silver (Ag), copper

(Cu), vanadium (V), magnesium (Mg), zinc (Zn), nitrogen (N), cobalt (Co), manganese (Mn), calcium (Ca), strontium (Sr), etc. doping or substitutions improves the battery capacity as a result of the enhancement in electrical conductivity [58]. Battery capacity increases by around 5–20 mAh/g.

Morphological treatments are another way to improve battery performance. Thin films, porosity control, nanorods, etc. can be a better way to upgrade battery performance than substitution methods. Thin film and porosity control in particular can improve the capacity to around 1000 mAh/g. In this context, we now summarise some work from the literature on $\text{Li}_4\text{Ti}_5\text{O}_{12}$.

In 2015 Ge et al. studied the mesoporous $\text{Li}_4\text{Ti}_5\text{O}_{12}$ system [59]. Morphological characterizations showed that the synthesised materials have ~5 nm non-ordered pore sizes [59]. Mesoporous $\text{Li}_4\text{Ti}_5\text{O}_{12}$ was synthesised via the hydrothermal method in this study. The electrochemical results showed that mesoporous $\text{Li}_4\text{Ti}_5\text{O}_{12}$ materials have 169 mAh/g at 1 C current rate and 140 mAh/g at 30 C [59]. In 2016 Zeng et al. studied a nano-tin (Sn), antimony (Sb), and bismuth (Bi) embedded $\text{Li}_4\text{Ti}_5\text{O}_{12}$ composite [60]. The morphological studies showed that the materials consisted of ~10 nm particles [60]. The C was used as anode material in this work. Under 200 mA constant current rate, $\text{Li}_4\text{Ti}_5\text{O}_{12}/\text{Sn}/\text{C}$, $\text{Li}_4\text{Ti}_5\text{O}_{12}/\text{Sb}/\text{C}$, and $\text{Li}_4\text{Ti}_5\text{O}_{12}/\text{Bi}/\text{C}$ have 718.4, 678.2, and 597.8 mAh/g discharge capacity values, respectively [60]. Tran et al. have also studied the $\text{Li}_4\text{Ti}_5\text{O}_{12}$ anode material. Spinel $\text{Li}_4\text{Ti}_5\text{O}_{12}$ was synthesised at nano sizes by a solution route using LiOH and $\text{Ti}(\text{OBU})_4$ [61]. The morphological characterizations showed that $\text{Li}_4\text{Ti}_5\text{O}_{12}$ was in the spinel phase with homogenous nanoparticles around 100 nm [61]. In this work, $\text{Li}_4\text{Ti}_5\text{O}_{12}$ showed good battery performance of 160 mAh/g at a rate of C/10, as well as good specific capacities of 120, 110, and 100 mAh/g at high rates of C, 5 C and 10 C, respectively [61]. In 2017, Tang et al. studied carbon coated $\text{Li}_4\text{Ti}_5\text{O}_{12}$ material [62]. In this work $\text{Li}_4\text{Ti}_5\text{O}_{12}$ was synthesised via an in-situ lithium-doped Ti based metal-organic framework precursor with thermal annealing [62]. The annealing temperature was between 800 and 900 °C. Battery performance tests showed that the carbon coated $\text{Li}_4\text{Ti}_5\text{O}_{12}$ battery has 181 and 150 mAh/g discharge capacity after 1000 cycles, under 1000 and 2000 mA current rates, respectively [62]. Again in 2017, Jingyuan et al. studied

a Fe_3O_4 nanoparticle coated $\text{Li}_4\text{Ti}_5\text{O}_{12}$ nanowires synthesized via a hydrothermal synthesis method [63]. In this study, Li metal was used as an anode material [63]. The results showed that the Fe_3O_4 nanoparticle coated $\text{Li}_4\text{Ti}_5\text{O}_{12}$ nanowires have 780 mAh/g discharge capacity under 1C current rate for the first cycle [63].

2.2.1.2.3.1. $\text{Li}_2\text{Ti}_3\text{O}_7$ Anode Material for Li-ion Batteries

The $\text{Li}_2\text{Ti}_3\text{O}_7$ system is another important anode material in titanium oxide based battery cells. Although $\text{Li}_2\text{Ti}_3\text{O}_7$ has 198 mAh/g theoretical capacity, it is known that the system has ~140 mAh/g experimental discharge capacity [64]. Although $\text{Li}_2\text{Ti}_3\text{O}_7$ has good capacity and working potential values, the capacity of the cell decreases dramatically after repeated cycling. In other words, $\text{Li}_2\text{Ti}_3\text{O}_7$ has higher capacity fading than $\text{Li}_4\text{Ti}_5\text{O}_{12}$ [64–66].

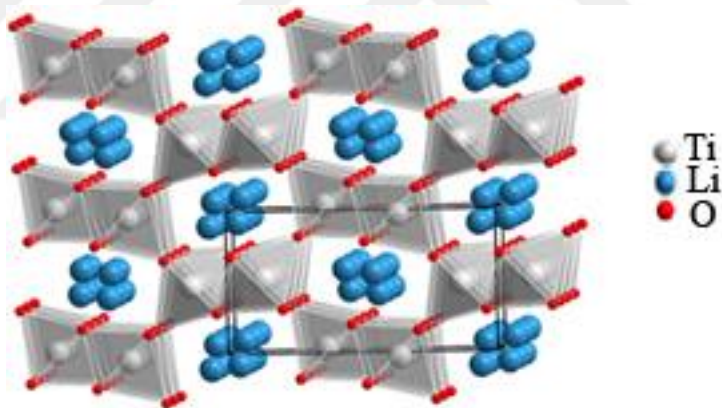


Figure 2.15. Crystal structure of $\text{Li}_2\text{Ti}_3\text{O}_7$ [66].

$\text{Li}_2\text{Ti}_3\text{O}_7$ has an octahedral crystal structure [65] as shown in Figure 2.15. The Li ions move along one direction in the lattice [65,66]. The $\text{Li}_2\text{Ti}_3\text{O}_7$ system is in the Pbnm space group, and has $a = 5.016 \text{ \AA}$, $b = 9.543 \text{ \AA}$, and $c = 2.945 \text{ \AA}$ crystal parameters [64–66].

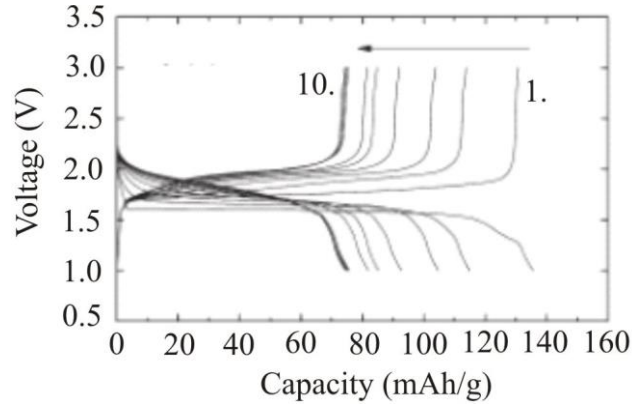


Figure 2.16. Charge-discharge characteristics of $\text{Li}_2\text{Ti}_3\text{O}_7$ [67].

Figure 2.16 shows the charge-discharge characteristics of the $\text{Li}_2\text{Ti}_3\text{O}_7$ system. It has a wide plain plateau at 1.55V, similar to $\text{Li}_4\text{Ti}_5\text{O}_{12}$ [67]. On the other hand, $\text{Li}_2\text{Ti}_3\text{O}_7$ shows a microstrain in the crystal structure unlike microstrain-free $\text{Li}_4\text{Ti}_5\text{O}_{12}$. The mechanism of the fast capacity fade in $\text{Li}_2\text{Ti}_3\text{O}_7$ was not explained.

The capacity fade in the cell fabricated with $\text{Li}_2\text{Ti}_3\text{O}_7$ is attributed to the crystal structure stabilization problem during the charge-discharge process [10,12]. During cycling, Li^+ intercalation/deintercalation affects the microstrain and crystal structure leading to a change in the volume and the symmetry [10, 12, 24]. Volume expansion rate is very effective in the battery life [10, 12, 24]. Therefore, substitution or structural modification studies in $\text{Li}_2\text{Ti}_3\text{O}_7$ are important for both the explanation of the mechanism and technological applications [10, 12, 24]. Although the $\text{Li}_2\text{Ti}_3\text{O}_7$ system is classified as a titanium-oxide based material, there are only a limited number of studies in the literature [referans]. Hence, it is important to investigate the $\text{Li}_2\text{Ti}_3\text{O}_7$ system thoroughly. Studies from the literature are summarized below.

In 2006, Thournout et al. studied Fe and Ni substituted $\text{Li}_2\text{Ti}_3\text{O}_7$ materials (instead of Ti) synthesised by a quenching process via the solid state reaction method [68]. The electrochemical results showed that the capacity of pure $\text{Li}_2\text{Ti}_3\text{O}_7$ was ~105 mAh/g, the Fe substituted $\text{Li}_2\text{Ti}_3\text{O}_7$ was ~98mAh/g, and the Fe/Ni substituted $\text{Li}_2\text{Ti}_3\text{O}_7$ was 68 mAh/g [68]. In 2006, Ma and Noguchi studied temperature effects on battery performance for the $\text{Li}_2\text{Ti}_3\text{O}_7$ system synthesized by a solid state reaction process [69]. The electrochemical

measurements were conducted at room temperature, 40, 50, and 70 °C. They found that the batteries had capacities of 140 mAh/g, 163 mAh/g, 158 mAh/g, and 120 mAh/g at room temperature, 40, 50, and 70 °C, respectively [69]. In 2010, Villevieille et al. studied carbon modified $\text{Li}_2\text{Ti}_3\text{O}_7$ materials under different gas conditions [70]. A half-cell was prepared for electrochemical measurements [70]. The capacity measurements were conducted at a C/10 rate and the obtained capacity values were 150, 140, 140, and 160 mAh/g for Ar, Ar/H₂, N₂, and N₂/H₂ gases, respectively [70]. In 2015, Gan et al. studied the synthesis conditions of the $\text{Li}_2\text{Ti}_3\text{O}_7$ system [71], and found that the sintering temperature is very important. In this study, the $\text{Li}_2\text{Ti}_3\text{O}_7$ materials were synthesised under vacuum conditions, and pure $\text{Li}_2\text{Ti}_3\text{O}_7$ can be synthesised at a minimum temperature of 700 °C [71]. The electrochemical measurement of the cell revealed ~120 mAh/g discharge capacity under a 1C current rate [71].

2.2.1.2.3.2. $\text{Li}_2\text{Ti}_6\text{O}_{13}$ Anode Material for Li-ion Batteries

Nowadays, commercial batteries for high technology applications should have a long lifetime (above 1000 cycles) with high crystalline stability. Ti based battery cells have longer battery life than the other oxide batteries [51]. $\text{Li}_2\text{Ti}_6\text{O}_{13}$ is another kind of titanium oxide based anode material [51]. It has a long charge-discharge cycle life (average 1000 cycle) and low discharge capacity around 30 mAh/g [51,72].

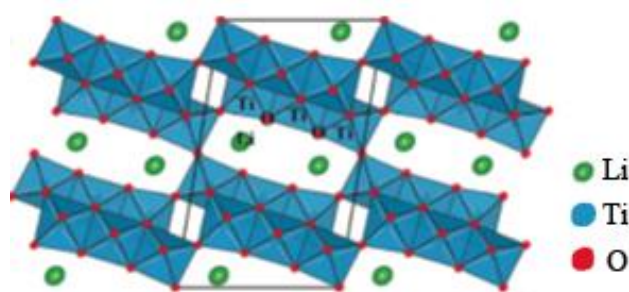


Figure 2.17. Crystal structure of $\text{Li}_2\text{Ti}_6\text{O}_{13}$ system [73].

Figure 2.17 shows the crystal structure of the $\text{Li}_2\text{Ti}_6\text{O}_{13}$ system, where the system has monoclinic crystal structure and Li^+ ions move in a tunnel like structure along one

direction [73]. The $\text{Li}_2\text{Ti}_6\text{O}_{13}$ system is in the $C2/m$ space group, and lattice parameters are reported as $a = 15.3065 \text{ \AA}$, $b = 3.74739 \text{ \AA}$, and $c = 9.1404 \text{ \AA}$ [73].

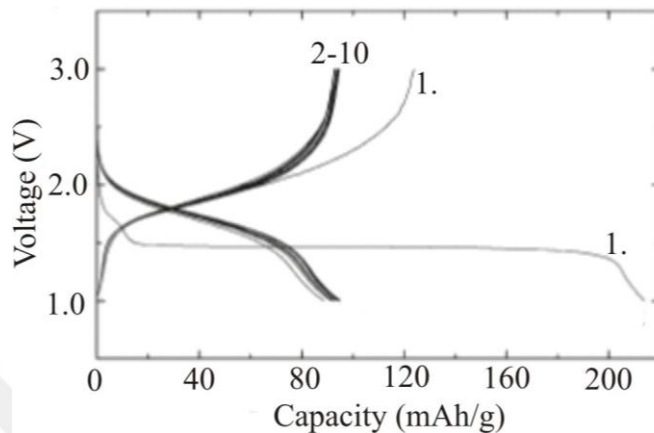


Figure 2.18. Charge-discharge characteristic of $\text{Li}_2\text{Ti}_6\text{O}_{13}$ [73].

Figure 2.18 shows the $\text{Li}_2\text{Ti}_6\text{O}_{13}$ system charge-discharge characteristics. It is seen from the figure that the capacity of the first cycle is $\sim 210 \text{ mAh/g}$, but it decreases to $\sim 90 \text{ mAh/g}$ under 0.1C . The voltage plateau characteristics is another important quantity for $\text{Li}_2\text{Ti}_6\text{O}_{13}$ anode material. The first cycle of the $\text{Li}_2\text{Ti}_6\text{O}_{13}$ battery has a long voltage plateau at $\sim 1.5 \text{ V}$; the voltage loses the plateau behavior and decreases with increasing capacity as seen in Figure 2.18 [73]. Even though $\text{Li}_2\text{Ti}_6\text{O}_{13}$ has a stable cycle life, there is an obstacle to its synthesis because it cannot have a direct synthesis method. The ion exchange method can be used. $\text{Na}_2\text{Ti}_6\text{O}_{13}$ or $\text{K}_2\text{Ti}_6\text{O}_{13}$ are used for ion exchange to synthesize $\text{Li}_2\text{Ti}_6\text{O}_{13}$ [73,74].

It should be noted that $\text{Li}_2\text{Ti}_6\text{O}_{13}$ is not much studied in the literature. Hence, it needs further investigation to improve battery applications. In this context, some important studies in the literature about $\text{Li}_2\text{Ti}_6\text{O}_{13}$ are now presented. In 2015, Zhang et al. studied $\text{Na}_2\text{Ti}_6\text{O}_{13}$ and $\text{Li}_2\text{Ti}_6\text{O}_{13}$ systems which were synthesised by the ion-exchange method described in Ref [75]. The electrochemical measurements showed that the $\text{Li}_2\text{Ti}_6\text{O}_{13}$ had $\sim 190 \text{ mAh/g}$ and $\sim 150 \text{ mAh/g}$ for the first and second cycles, respectively [75]. In 2011, Katoka et al. studied the $\text{Li}_2\text{Ti}_6\text{O}_{13}$ system produced via an ion-exchange method and found that $\text{Li}_2\text{Ti}_6\text{O}_{13}$ has $\sim 210 \text{ mAh/g}$ capacity in first cycle; the capacity

reduced to ~90mAh/g under 0.1C current rate for the second cycle [76]. $\text{Li}_2\text{Ti}_6\text{O}_{13}$ had long plateau at ~1.5 V for the first cycle [76]. In 2011, Pérez-Flores et al. studied Li insertion behavior of the $\text{Li}_2\text{Ti}_6\text{O}_{13}$ system. The $\text{Li}_2\text{Ti}_6\text{O}_{13}$ materials were synthesised from $\text{Na}_2\text{Ti}_6\text{O}_{13}$ via an ion-exchange method [77]. This study showed a dramatic drop in capacity over the first five cycles. At C/12 current rate, the obtained capacity values were 250 mAh/g and 150 mAh/g for first and fifth cycles, respectively [77].

2.2.2. Sodium Batteries

Nowadays, Li-ion batteries are the best candidates for energy storage systems due to their domination in commercial electronic devices; however, limited lithium reserves on earth, and the cost of lithium production, are major problems for the future of Li-ion batteries [23,78,79]. In addition, lithium carbonate presents a high level of environmental risk for living things [80]. Scientists have been working to find environmentally friendly new battery materials which have higher efficiency and lower production cost. In the past decade, Na based batteries have come to attention due to their eco-friendly and low cost properties. The properties of Na-ion battery electrodes and their investigations in the literature are summarized below.

2.2.2.1. Cathode Materials for Na-ion Batteries

The cathode material is an important part of Li-ion batteries as well as Na-ion ones. Na-ion batteries are considered as alternative for Li-ion batteries due to their natural abundance and low production cost when compared to Li-ion batteries. It is expected that Na-ion batteries must have high working voltage and high capacity value cathode materials for commercialization in the market. But, the studies in the literature about Na-ion batteries show that it has lower battery performance when compared to Li-ion batteries. It is foresight that Na-ion batteries will be replaced with Li-ion batteries in the market in the next future. In this section, we investigate the Na- cathode materials with high performances.

2.2.2.1.1. Layered Oxide Cathode Materials for Na-ion Batteries

Generally, the layered oxide cathode materials have the formula AMO_2 ($A = Li, Na; M = Co, Mn, Ni,$ and their combinations) [81,82]. Li based layered structures are known with their high energy density. A good battery performance was therefore expected from the Na based cathodes with similar crystalline properties. Nowadays, researchers have focused on these types of structures for development and improvement of Na-ion batteries.

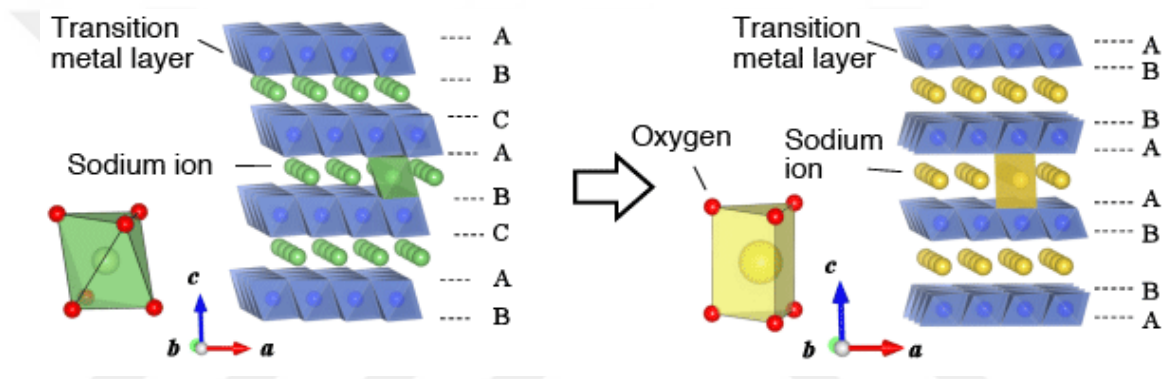


Figure 2.19. Layered structure of Na-ion cathode materials [83].

Figure 2.19 shows the layered crystalline structure of Na-ion cathode materials. In this layered structure, the Na ions are located between the oxidised transition metal layers of MO_6 ($M = Co, Mn,$ or Ni). These layers are very important for the diffusion of Na ions during the charge and discharge processes. The Na-ions in the lattice are weakly bound to oxygen atoms. These bonds provide Na^+ ion insertion/disinsertion during the charge-discharge process — the rechargeable property of battery cells. Figure 2.19 also shows the stacking of layers in the structure, which can be different for different materials. These differences are named as P2 (as ABBA stacks), P3 (as ABBCCA stacks), and O3 (as ABCABC stacks) phases [84–87].

2.2.2.1.1.1. Na_xCoO_2 system for Na-ion Batteries

In 1993, Doeff et al. discovered P2-type Na_xCoO_2 which has the working potential of 2.8 V [88]. After this initial discovery, studies showed that batteries based on Na_xCoO_2 have ~130 mAh/g capacity values between 2.0–3.5 V [43,88].

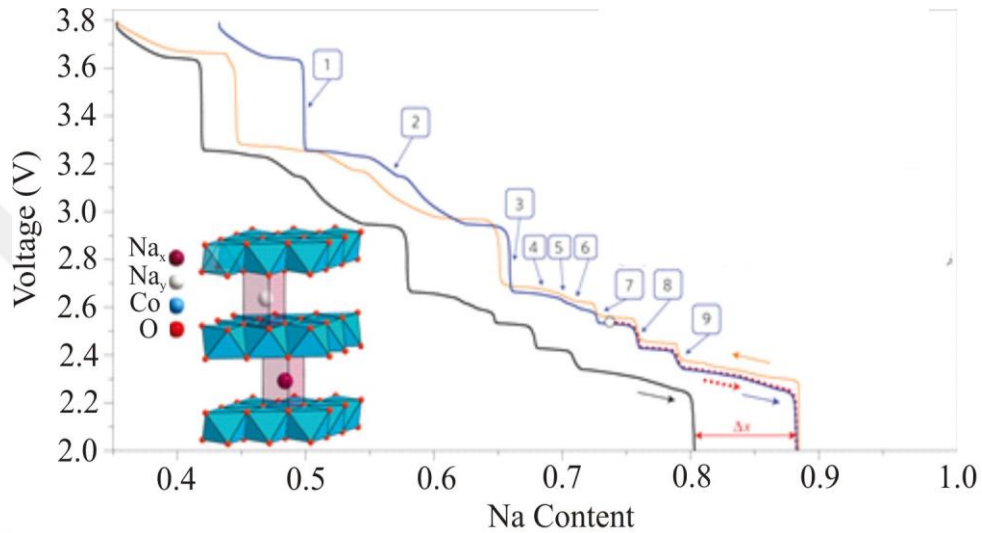


Figure 2.20. Voltage change dependence of Na concentration in Na_xCoO_2 cathode material [89].

Figure 2.20 shows how the voltage depends on Na concentration in Na_xCoO_2 . The step-like behavior in the CV graph is related to Na diffusion at the different sites of the lattice; detailed information can be found in Ref. [89].

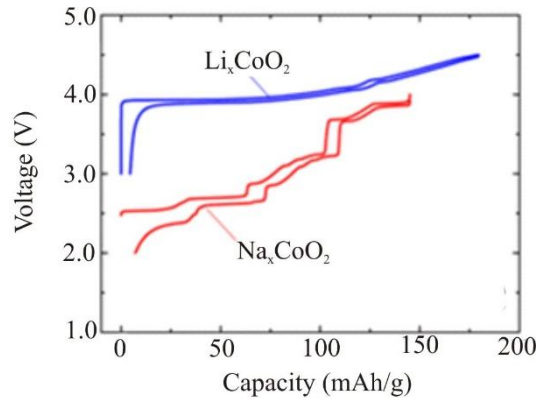


Figure 2.21. Performance comparison between Li_xCoO_2 and Na_xCoO_2 [90].

Figure 2.21 shows the battery performance comparison between Li_xCoO_2 and Na_xCoO_2 batteries. Although these two materials have the same crystal structure, the battery performance differs. In addition to this, Na_xCoO_2 does not show the stable plateau of the capacity during charge-discharge due to the different Na-sites in the lattice.

2.2.2.1.1.2. Na_xMnO_2 system for Na-ion Battery

Another important cathode material for rechargeable batteries is Na_xMnO_2 . It has a different type of crystal structure compared to the layered Na_xCoO_2 system [91]. It is reported that the crystal structure is strongly dependent on Na content in the lattice, and that the lattice symmetry also changes with the amount of Na in Na_xMnO_2 where x is 0.2, 0.40, 0.44, 0.70, and 1 [43,91]. $x = 1$ phase has a layered structure, which is the crucial property for the cathode materials of rechargeable batteries [43].

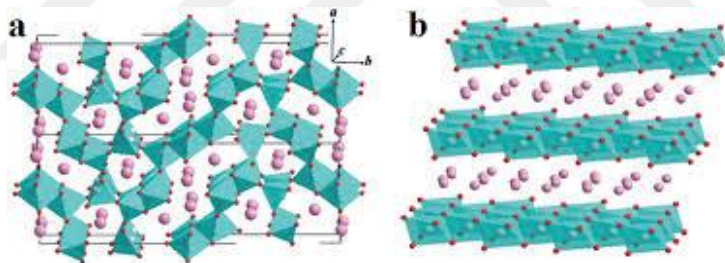


Figure 2.22. a) Tunneling structure of Na_xMnO_2 , b) NaMnO_2 layered crystal structure. Red: O, turquoise: Mn, magenta: Na. [92].

Figure 2.22 shows the different types of crystal structures of Na_xMnO_2 . It has a monoclinic crystal structure, which assists tunneling, as it can be extended along the c axis and the Na^+ ions move in the spaces between the MnO_6 layers [92].

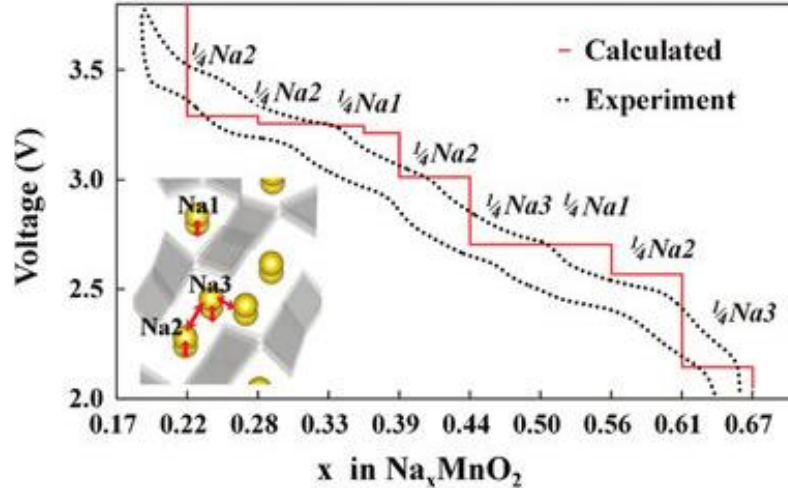


Figure 2.23. Voltage change dependence of Na concentration for Na_xMnO_2 cathode material [93].

Figure 2.23 shows the theoretical and experimental discharge characteristics of the battery, which is fabricated from Na_xMnO_2 cathode materials, as a function of Na concentration. The Na_xMnO_2 system has a step-like charge-discharge characteristics, same as Na_xCoO_2 . In the steps in Figure 2.23, it can be noted that the oxidative reduction potential of Na1 and Na2 atoms is greater than that of the Na3 atom [94].

The Na-ion battery has a voltage range of 2–3.6 V for the cell fabricated with Na_xMnO_2 cathode material [81]. The capacity of these batteries increases from 120 mAh/g to 200 mAh/g with increasing Na concentration. Furthermore, when the Na content is between $x = 0.8$ –1 for Na_xMnO_2 , ~200 mAh/g capacity is obtained [43]. On the other hand, the battery performance can be improved for batteries with lower Na concentrations by using a different synthesis method. The $x = 0.44$ phase can be synthesized in nanowire form, and the Na-ion battery which is fabricated from these nanowires has approximately 200 mAh/g capacity [87]. However, a Na-ion battery produced from the bulk form of $\text{Na}_{0.44}\text{MnO}_2$ has an average capacity of just 120–140 mAh/g [43]. So, $\text{Na}_{0.44}\text{MnO}_2$ in the form of nanowires is a good candidate for Na-ion batteries. However, $\text{Na}_{0.44}\text{MnO}_2$ nanorod batteries have just a ~50 charge-discharge cycle life which can be explained by decomposition of the nanowires during cycles of the batteries [34].

2.2.2.1.2. Olivine NaFePO₄ Cathode Material

Another remarkable material including Na-ions as cathode materials is phosphate based. It is well known that the phosphate based cathode materials have higher working voltage and capacity than the other oxide cathode materials, and these advantages of the Na-P-O based materials are of great interest in battery studies.

Morean et al. produced NaFePO₄ and Na_{0.7}FePO₄ phase as cathode materials and the Na-ion batteries which is fabricated from these materials have showed a capacity of ~154 mAh/g value as seen in the figure 2.24 [95]. In the other studies, it was observed that the batteries fabricated by using Na-Fe-P-O have the capacity values between 140 and 160 mAh/g. [95–97].

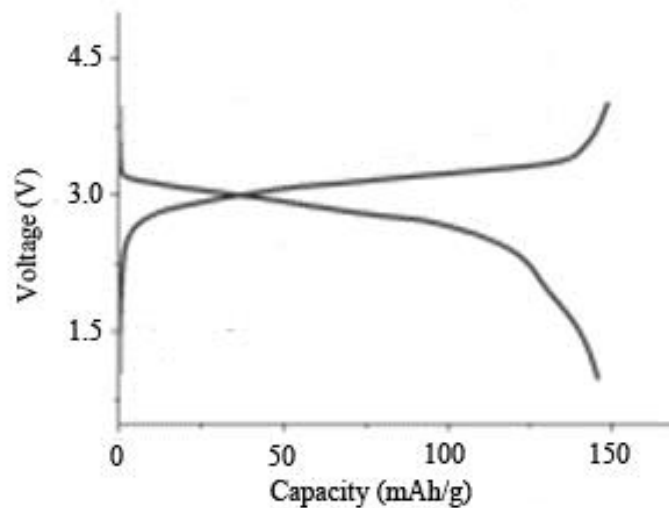


Figure 2.24. Olivine NaFePO₄ battery performance [95].

The Na-ion batteries which are produced using NaFePO₄ cathode material have a great advantage compared to the layered Na-Mn-O and Na-Co-O batteries; the characteristic property of the battery fabricated using NaFePO₄ is 130 mAh /g capacity between 3.2 and 2.8V. So, it can be concluded that NaFePO₄ batteries show stable performance compared to Na-Mn-O and Na-Co-O batteries [95–97]. This stable battery performance is related to the structural stability of the cell during the charge and discharge processes, which can provide non-deformed crystal structure over 1000 cycles; this is better than any of the other batteries [95–97].

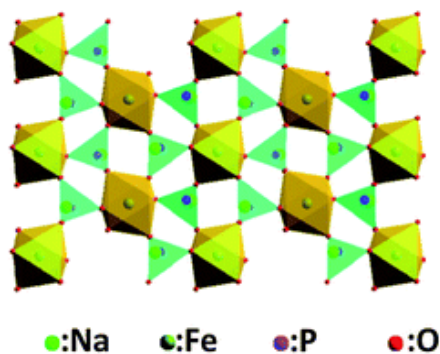


Figure 2.25. Crsytal structure of NaFePO₄ system [98].

Figure 2.25 shows the crystal structure of the NaFePO₄ system. The orthorhombic crystal structure consists of a Na, FeO₆, and PO₄ substructure that has better stability during charge-discharge due to the similar structures of the subsystems [99].

2.2.2.2. Anode Materials for Na-ion Batteries

Although Na metal is not a good anode material for Na-ion batteries, Na metal is a common choice for scientific research. The batteries which are fabricated using Na metal exhibit a short lifetime of the cell since it is easily oxidises during charge/discharge, causing a loss of the battery properties from the cell structures. The other important problem is the working temperature of the battery fabricated from Na anode materials. The melting temperature of Na is 97.7 °C. The environmental temperature is the crucial factor that leads to irregularities in battery performance [100]. In the selection of anode materials for Na-ion batteries, it should be noted that the anode material must have a low ionization potential and large volume of the unit cell for ion intercalation/deintercalation. The most suitable anode materials with these properties are carbon and titanium based compounds [101–103].

2.2.2.2.1. Carbon Based Anode Materials

For carbon based anodes, graphite is the most preferred material in terms of commercial production and scientific research. Although graphite is the most common anode material for Li-ion batteries, it cannot be used in Na-ion batteries since it doesn't exhibit battery properties, which results in no voltage in the cell [104–106]. This can be explained by the Na⁺ ions having a larger ionic radius than the Li⁺ ions preventing Na⁺ ion diffusion to the graphite layers [107]. Although graphite based anodes do not have battery properties, scientists have been trying to develop different forms of carbon for Na-ion battery applications [43,104-107]. It was found that petroleum-coke carbon, which is a hard carbon, was observed to have anodic performance in a cell; hard carbon has a theoretical capacity of 335 mAh/g, a promising result for future battery technology [43]. Doeff et al. experimentally observed the battery performance of the cell which is fabricated by hard carbon as 85mAh/g, the highest value of the carbon based anodes for Na-ion batteries [108].

2.2.2.2.2. Sodium Metal Phosphate Anode Materials

In 2011, Park and colleagues discovered that NaTi₂(PO₄)₃ could be used as an anode in Na-ion battery cells [109]. The NaTi₂(PO₄)₃ system has a voltage of 2.1 V and it has a two-step voltage change as seen in Figure 2.25. The experimental studies have shown that the NaTi₂(PO₄)₃ system has 123 mAh/g average capacity, which is very promising for future studies.

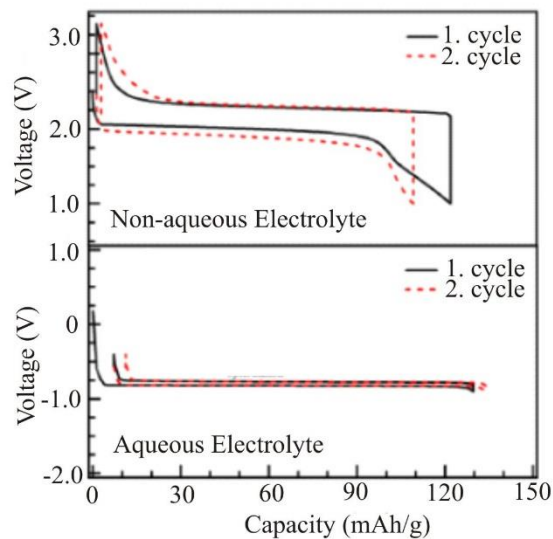


Figure 2.26. Na-ion battery performance of the $\text{NaTi}_2(\text{PO}_4)_3$ system [110].

From Figure 2.26 we see that $\text{NaTi}_2(\text{PO}_4)_3$ has a long stable voltage plateau during the charge-discharge process [110]. When compared to the batteries fabricated using layered Na-Co-O and Na-Mn-O, $\text{NaTi}_2(\text{PO}_4)_3$ is more stable. However, one disadvantage is its higher anodic voltage of 2.1 V; more studies are required to overcome this obstacle [110].

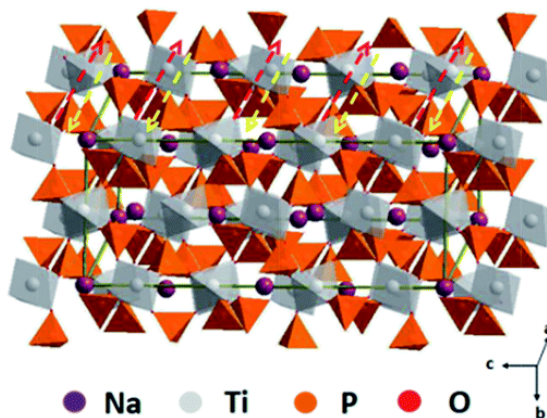


Figure 2.27. Crystal structure of $\text{NaTi}_2(\text{PO}_4)_3$ [111].

Stable battery performance is related to the crystal structure of the electrode materials. Figure 2.27 shows the trigonal crystal structure of the $\text{NaTi}_2(\text{PO}_4)_3$ system, which consists of TiO_6 and PO_4 substructures. The Ti-O and P-O bonds cause the formation of empty channels with widths up to 108 Å; Na^+ ions can diffuse easily in these channels during intercalation/deintercalation [111].

2.2.2.2.3. Titanium Oxide Based Anode Materials

Studies of sodium-metal oxide anode material for the new generation Na-ion batteries are important for future technologies. Titanium based anode materials were seen to play a crucial role in the Na-ion battery studies. Three different types of Ti based anode materials, $\text{Na}_4\text{Ti}_5\text{O}_{12}$, $\text{Na}_2\text{Ti}_3\text{O}_7$, and $\text{Na}_2\text{Ti}_6\text{O}_{13}$ will be examined in the following sections.

2.2.2.2.3.1. $\text{Na}_4\text{Ti}_5\text{O}_{12}$ Anode Materials for Na-ion Batteries

Li based electrode materials have similar structure to Na based electrode materials for rechargeable batteries; examples include $\text{Li}_4\text{Ti}_5\text{O}_{12}$ and $\text{Na}_4\text{Ti}_5\text{O}_{12}$. The $\text{Na}_4\text{Ti}_5\text{O}_{12}$ system has attracted attention as an anode material due to its high theoretical capacity of 340 mAh/g [112]. In addition, $\text{Na}_4\text{Ti}_5\text{O}_{12}$ anode material has different intrinsic characteristic properties when compared to other anode materials, so that it can be used as an anode electrode in Li-ion batteries as well as in Na-ion ones [113]. When it is used in Li-ion batteries, the capacity is 110 mAh/g, a good result when compared to other Li anodes. Another advantage of $\text{Na}_4\text{Ti}_5\text{O}_{12}$ is the synthesis in the form of nano-sized structures [43].

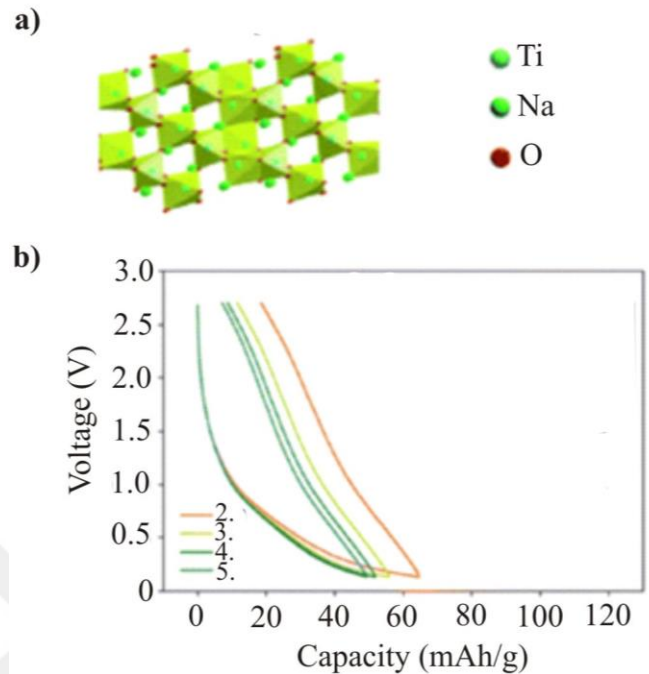


Figure 2.28 a) Crystal structure and b) charge-discharge characteristics of the Na₄Ti₅O₁₂ system [114].

Figure 2.28 a) shows the Na₄Ti₅O₁₂ crystal structure and the charge-discharge characteristics of the cell. Na₄Ti₅O₁₂ has a monoclinic crystal structure, which is different from Li₄Ti₅O₁₂. Na₄Ti₅O₁₂ system is in the P3 space group, and lattice parameters are $a = b = 5.31997 \text{ \AA}$ and $c = 9.5567 \text{ \AA}$. This monoclinic structure consists of TiO₆ substructures and weakly bound Na ions in the lattice [114, 130]. The Na-ions were placed between TiO₆ regions, and this structure is called the tunneling structure. It should be noted that Na₄Ti₅O₁₂ has strain-type crystal structure which can cause deformation during the charge and discharge processes.

Although Na₄Ti₅O₁₂ has 340 mAh/g theoretical capacity, experimentally the obtained capacity value is ~60 mAh/g, which is low enough for commercialization [115]. So Na₄Ti₅O₁₂ as an anode material has some advantages as well as some disadvantages. The most important disadvantage is its short lifetime during charge-discharge compared to the other anode materials. It can be explained by deformation of the crystal structure due to a possible increase in the microstrain [43,113]. Another important observation for

$\text{Na}_4\text{Ti}_5\text{O}_{12}$ is the anisotropic crystal structure as seen in Figure 2.28 b); it is predicted that this high anisotropy in the lattice can cause the capacity of the cell to decrease [43]. According to Naeyaert et al., $\text{Na}_4\text{Ti}_5\text{O}_{12}$ has anisotropic crystal structure volume changes during cycles of the battery. During the first cycle, 64% volume change of the cell was observed which prevents the Na ion diffusion during intercalation/deintercalation [115]. So, we see that the stability of the crystal structure of $\text{Na}_4\text{Ti}_5\text{O}_{12}$ during intercalation/deintercalation is the most effective problem of this material. Hence, much more investigation of this material is needed for it to be useful in battery applications. In addition to this, cyclic voltammetry results were not found in the literature for $\text{Na}_4\text{Ti}_5\text{O}_{12}$ anode materials. Some studies of $\text{Na}_4\text{Ti}_5\text{O}_{12}$ are given below.

In 2012, Hee Woo et al. synthesised nano-sized and bulk $\text{Na}_4\text{Ti}_5\text{O}_{12}$ with different lattice symmetry by an ion-exchange method using $\text{Li}_4\text{Ti}_5\text{O}_{12}$ [116]. The capacities of the trigonal, monoclinic and nano-sized phase of $\text{Na}_4\text{Ti}_5\text{O}_{12}$ are reported as ~40 mAh/g, ~60 mAh/g, and ~100 mAh/g, respectively [116].

In 2014, Naeyaert et al. investigated the structural and electrochemical properties of $\text{Na}_4\text{Ti}_5\text{O}_{12}$ materials synthesised via solid state reaction method [115]. They found that the monoclinic $\text{Na}_4\text{Ti}_5\text{O}_{12}$ system has 64% structure volume change during the Na^+ intercalation/deintercalation process [115]. The obtained discharge capacity value of the cell is ~65 mAh/g.

2.2.2.3.1. $\text{Na}_2\text{Ti}_3\text{O}_7$ and $\text{Na}_2\text{Ti}_6\text{O}_{13}$ Anode Materials for Na-ion Batteries

$\text{Na}_2\text{Ti}_3\text{O}_7$ and $\text{Na}_2\text{Ti}_6\text{O}_{13}$ are other titanium oxide based anode materials for rechargeable batteries. Basically, $\text{Na}_2\text{Ti}_3\text{O}_7$ and $\text{Na}_2\text{Ti}_6\text{O}_{13}$ anode materials have the same monoclinic crystalline structure. These two materials have some advantages as well as some disadvantages according to their electrochemical properties as summarized in the following subsections.

2.2.2.2.3.1.1. $\text{Na}_2\text{Ti}_3\text{O}_7$ System for Na-ion Batteries

It is very important that a good anode material should have a high electrochemical capacity for low voltages (0–2 V). $\text{Na}_2\text{Ti}_3\text{O}_7$ has a theoretical capacity of 311 mAh/g,

which is the preferable value for commercial products [117]. Although experimental measurements are still far from the theoretical value, it is believed that researchers will reach the theoretical value in the near future. $\text{Na}_2\text{Ti}_3\text{O}_7$ anode material synthesised via hydrothermal method is found to have a capacity value of 188 mAh/g after 100 cycles [117,118]. On the other hand, the capacity value of $\text{Na}_2\text{Ti}_3\text{O}_7$, synthesized via solid state reaction method is only 75 mAh/g [95,117,118]. So, it should be noted that the battery performance of the fabricated cell is very sensitive to the synthesis method, and we hope that the theoretical value of capacity will be reached with new or modified synthesis methods.

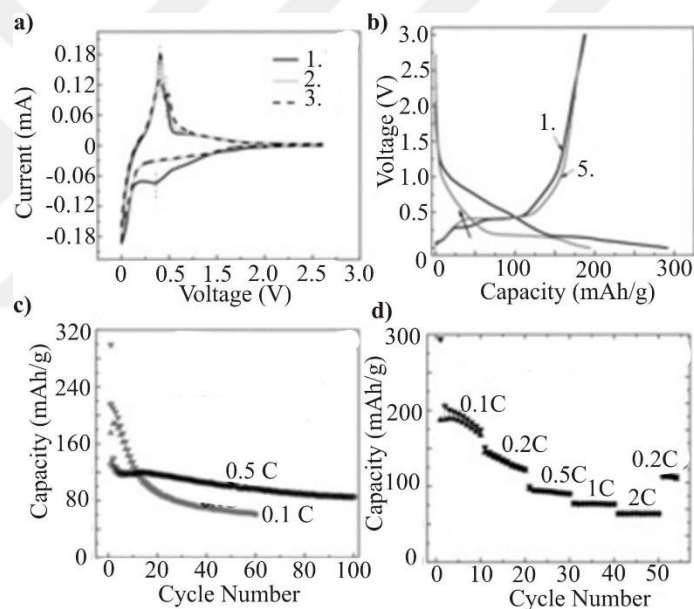


Figure 2.29. Battery performance of $\text{Na}_2\text{Ti}_3\text{O}_7$ system [118].

Figure 2.29 a) shows the CV curve of the $\text{Na}_2\text{Ti}_3\text{O}_7$ system [118]. There is one anodic peak in the graph. The voltage-capacity behavior of $\text{Na}_2\text{Ti}_3\text{O}_7$ reveals a big capacity fade during cycling of the cell (Figure 2.29 b) [118]. This result can be explained by the anisotropic structure of the unit cell, which is similar to the $\text{Na}_4\text{Ti}_5\text{O}_{12}$ system. $\text{Na}_2\text{Ti}_3\text{O}_7$ has an open circuit voltage of 0.3 V, which is the expected value for anode materials; $\text{Na}_2\text{Ti}_3\text{O}_7$ is therefore an ‘ultra-low voltage’ anode material.

The $\text{Na}_2\text{Ti}_3\text{O}_7$ system has a monoclinic crystal structure and the Na ions move in one dimension. Furthermore, the $\text{Na}_2\text{Ti}_3\text{O}_7$ anode material has low electrical conductivity and a short diffusion path for Na ions since they can be obtained in nano-sized wires and granular formation. So, $\text{Na}_2\text{Ti}_3\text{O}_7$ is potentially a great candidate for use as an anode material in Na-ion batteries [84,87,117].

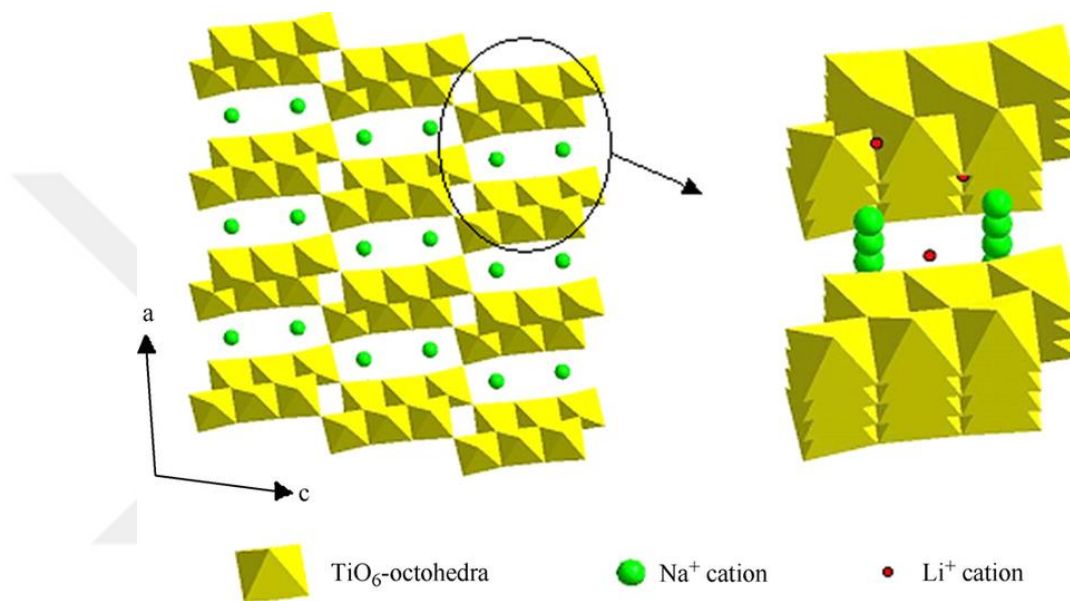


Figure 2.30. $\text{Na}_2\text{Ti}_3\text{O}_7$ and $\text{Na}_2\text{Ti}_6\text{O}_{13}$ crystal structures [119].

Figure 2.30 shows the crystal structure of the $\text{Na}_2\text{Ti}_3\text{O}_7$ system in the P121/m1 space group. The crystal parameters of $\text{Na}_2\text{Ti}_3\text{O}_7$ are reported as $a = 8.571 \text{ \AA}$, $b = 3.804 \text{ \AA}$, and $c = 9.135 \text{ \AA}$ [117, 131], and the Na ions in the unit cell were located between TiO_6 octahedral layers. Some literature works for $\text{Na}_2\text{Ti}_3\text{O}_7$ are given below.

In 2013, Pan et al. studied sodium storage and transport properties in layered $\text{Na}_2\text{Ti}_3\text{O}_7$ systems [118]. The $\text{Na}_2\text{Ti}_3\text{O}_7$ was synthesised via the solid state reaction method and the electrochemical measurements were conducted between 0 and 3 V. The capacity value of the cell fabricated with $\text{Na}_2\text{Ti}_3\text{O}_7$ as an anode was found to be $\sim 188 \text{ mAh/g}$ for 0.1C current rate [118].

In 2015, Man et al. have synthesised sheet-like $\text{Na}_2\text{Ti}_3\text{O}_7$ materials and the sample has been synthesised with colloidal carbon spheres which have $\sim 2 \text{ micron}$ sizes and the

detailed production method can be seen in Ref [120]. The electrochemical measurements show that the initial cycle capacities is obtained as 191/424, 171/364, 136/276, 126/248 and 104/206 mAh/g (charge capacity/discharge capacity) for 0.1, 0.2, 1, 2 and 5 C constant current, respectively [120].

In 2016, Zhou et al. studied the fabrication of $\text{Na}_2\text{Ti}_3\text{O}_7$ nanowires made via solvothermal synthesis [121]. This synthesis method provides both nanowire and 3D porous structure. In the study, $\text{Na}_2\text{Ti}_3\text{O}_7$ nanowires reach ~450 mAh/g discharge capacity, and the capacity value decreases to 150 mAh/g with increasing cycle numbers [121].

In 2017, Ding et al. studied $\text{Na}_2\text{Ti}_3\text{O}_7$, synthesised via solid state reaction method, for Na-ion batteries. The electrochemical tests were carried out with a graphite counter electrode. The reported discharge capacity is ~100 mAh/g for 100 mA constant current rate [122].

2.2.2.2.3.1.2. $\text{Na}_2\text{Ti}_6\text{O}_{13}$ System for Na-ion Batteries

Another Na based anode material is the $\text{Na}_2\text{Ti}_6\text{O}_{13}$ system, which is similar to $\text{Na}_2\text{Ti}_3\text{O}_7$ in terms of crystal structure and anode performance. The most important advantage of the $\text{Na}_2\text{Ti}_6\text{O}_{13}$ system is its high cycling life of the cell [89,92]. Rudola and colleagues studied $\text{Na}_2\text{Ti}_6\text{O}_{13}$ material for battery applications in 2013; the produced battery cell was used over 5000 cycles which was the stuffing-discharge life, and they found that the decrease in electrochemical capacity is about 5mAh/g, indicating that this material is promising for the future [123]. Figure 2.29 also shows $\text{Na}_2\text{Ti}_6\text{O}_{13}$ crystal structure in the $C2/m$ space group with lattice parameters of $a = 1.51310$ nm, $b = 0.37450$ nm, and $c = 0.91590$ nm [124].

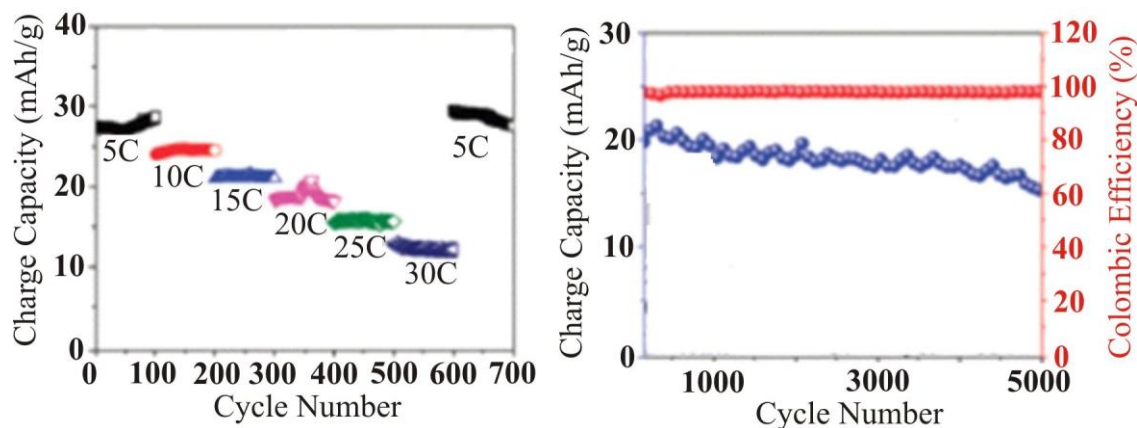


Figure 2.31. Battery performance of $\text{Na}_2\text{Ti}_6\text{O}_{13}$ [123].

Figure 2.31 shows the battery performance of $\text{Na}_2\text{Ti}_6\text{O}_{13}$. Even though $\text{Na}_2\text{Ti}_6\text{O}_{13}$ has a stable charge-discharge characteristics, the capacity values are very low for technological and commercial applications [123]. This material has ~ 35 mAh/g capacity for a 1C current rate. On the other hand, $\text{Na}_2\text{Ti}_6\text{O}_{13}$ has a stable cycle life. The capacity retention is reported as 85% for 5000 cycles [123].

$\text{Na}_2\text{Ti}_6\text{O}_{13}$ can easily be synthesised in nano-size structures with the solid state reaction method. As mentioned before, it is well known that nano-sized rods and granular structures provide great advantages in battery construction, and so it was expected that the nano-sized $\text{Na}_2\text{Ti}_6\text{O}_{13}$ will be used in Na-ion batteries after many studies focusing on how to improve the capacity [85, 94].

In 2014, Shen and Wagemaker studied Na dependence in the $\text{Na}_{2+x}\text{Ti}_6\text{O}_{13}$ system prepared via solid state reaction method with ball mill [125]. The electrochemical test was conducted under C/10 current rate and in the voltage range of 2.5–0.3 V [125]. The electrochemical performance results showed that $\text{Na}_2\text{Ti}_6\text{O}_{13}$ has a capacity of 170 mAh/g for the first cycle, and it then decreases to 50 mAh/g at the second cycle [125].

In 2016, Li et al. studied nanorods of the $\text{Na}_2\text{Ti}_6\text{O}_{13}$ system [126] which were synthesised via solid state reaction method with different annealing temperatures. The obtained results showed that nanorods of $\text{Na}_2\text{Ti}_6\text{O}_{13}$ have a battery capacity of 175 mAh/g at the first cycle and 90 mAh/g at the second one [126].

In 2017, Rambabu et al. fabricated thin films of the $\text{Na}_2\text{Ti}_6\text{O}_{13}$ system [127] synthesised via the plasma laser deposition method. The electrochemical measurements yielded capacity values of 73 mAh/g for first cycle and 48 mAh/g for the second one [127].

2.2.2.2.4. Na based Alloy Anode Materials

Another focus of research on anode materials for the new generation of Na-ion batteries is the Na based alloys. It is well known that Na can be easily alloyed with many common metals such as tin (Sn), germanium (Ge), lead (Pb) and antimony (Sb), and it was found that they have high capacity values compared to the oxide anodes [43,128]. The alloys $\text{Na}_{15}\text{Sn}_4$, Na_3Sb , Na_3Ge , and $\text{Na}_{15}\text{Pb}_4$ have capacities of 847 mAh/g, 660 mAh/g, 1108 mAh/g, and of 484 mAh/g, respectively [43,128]. Although Na based alloys exhibit high capacity values, the major disadvantage of these alloys can be a decrease of the capacity by 90% after 160 cycles [43,128]. Another problem is the oxidation of the anodes during cycling of the battery cells [43,128]. Because of these reasons, Na-alloys need more investigation to overcome their problems for use in commercial applications.

3. PERFORMANCE PARAMETERS FOR BATTERIES

The production of the electrodes is the first stage in battery studies; the second important stage is understanding of the phenomena of the batteries for their characterization. For this purpose, we briefly review the important parameters for batteries.

3.1. Capacity

The capacity of a battery can be defined as the amount of load ions that the battery can store. The most commonly used unit of capacity is the ampere-hour, but different units can be used such as W-h (Watt-hour) and kW-h (kilowatt-hour) [5,10,12,129]. The meaning of those units is obtained current or power within an hour during potential generation [5,10,12,129].

It is important to estimate the theoretical capacity of the designed cell; it can be calculated as the molar weight of the active electrode material in electrode construction [5,10,12,129]. Molar capacity is the amount of electrification that occurs with an electrochemical reaction. This value is denoted by Q and given by:

$$Q = xnF \quad (3.1)$$

where x is the number of moles of reactant entering the selected electro active fraction, n is the number of electron transfers per mole in the reaction, and F is the Faraday constant [5,10,12,129]. The mass of the electroactive component is given as:

$$M = xM_r \quad (3.2)$$

where M is the bulk mass of the electro-active component and M_r is the molecular mass of the component. The capacity value of the cell can also be given as Ah/kg or Ah/g and the mass in the active materials should be found in the electrodes. This capacity is called 'specific capacity', and is calculated from [5,10,12,129]:

$$C_c = nF/M \quad (3.3)$$

The specific capacity is calculated by multiplying by the mass of the electro-active component entering the reaction in the battery cell [5,10,12,129]. In practice, the real

situation is different from the above equations so that the theoretical calculated values cannot be reached practically [5,10,12,129]. Possible explanations for this are:

- It may be due to the electrolyte, current conducting materials, coating on the battery, etc, in addition to the type of active material.
- It may also be due to undesired (between the electroactive material and the electrolyte) and incomplete (between the cathode and the electroactive material) reactions. Undesirable reactions also affect the charge discharge time, and hence the capacity of the battery, because the resulting internal resistance change also affects the current drawn from the battery cell.

3.2. Voltage

The theoretical standard potential of a battery cell, $E^0(\text{cell})$, can be calculated as the potential difference occurring in the electrochemical reaction. This value can be found from the difference between the standard electrode potential of the cathode and the anode [5,10,12,129]:

$$E^0(\text{Cathode}) - E^0(\text{Anode}) = E^0(\text{cell}) \quad (3.4)$$

To calculate the cell potential, the values of the reduction reactions must be known at standard environmental conditions (298 Kelvin temperature and 1 atmosphere pressure are considered normal environmental conditions) [5,10,12,129]. Table 3.1 shows the standard electrode potentials which are used for the anode and cathode of battery cells [5,10,12,129].

Table 3.1 Standard electrode potentials. Some of the elements and compounds are liquid electrolytes at 298 K [12].

Reaction	Electrode Potential (V)
$\text{Li}^+ + \text{e}^- \rightarrow \text{Li}$	-3.10
$\text{Na}^+ + \text{e}^- \rightarrow \text{Na}$	-2.71
$\text{Mn}^{2+} + 2\text{e}^- \rightarrow \text{Mn}$	-1.18
$\text{Cd}(\text{OH})_2 + 2\text{e}^- \rightarrow \text{Cd} + 2\text{OH}^-$	-0.82
$\text{Zn}^{2+} + 2\text{e}^- \rightarrow \text{Zn}$	-0.76
$\text{Cd}^{2+} + 2\text{e}^- \rightarrow \text{Cd}$	-0.40
$\text{Ni}^{2+} + 2\text{e}^- \rightarrow \text{Ni}$	-0.26
$2\text{H}^+ + 2\text{e}^- \rightarrow \text{H}_2$	0.00
$\text{Cu}^{2+} + \text{e}^- \rightarrow \text{Cu}^+$	+0.16
$\text{Cu}^{2+} + 2\text{e}^- \rightarrow \text{Cu}$	+0.34
$2\text{AgO} + \text{H}_2\text{O} + 2\text{e}^- \rightarrow \text{Ag}_2\text{O} + 2\text{OH}^-$	+0.64
$\text{Fe}^{3+} + \text{e}^- \rightarrow \text{Fe}^{2+}$	+0.77
$\text{Hg}^{2+} + 2\text{e}^- \rightarrow \text{Hg}$	+0.80
$\text{Ag}^+ + \text{e}^- \rightarrow \text{Ag}$	+0.80
$2\text{Hg}^{2+} + 2\text{e}^- \rightarrow \text{Hg}_2^{2+}$	+0.91
$\text{O}_2 + 4\text{H}^+ + 4\text{e}^- \rightarrow 2\text{H}_2\text{O}$	+1.23
$\text{ZnO} + \text{H}_2\text{O} + 2\text{e}^- \rightarrow \text{Zn} + 2\text{OH}^-$	+1.26
$\text{PbO}_2 + \text{SO}_4^{2-} + 4\text{H}^+ + 2\text{e}^- \rightarrow \text{PbSO}_4 + 2\text{H}_2\text{O}$	+1.70
$\text{F}_2 + 2\text{e}^- \rightarrow 2\text{F}^-$	+2.87

The potential of the battery does not remain constant during discharge due to various factors such as ion amount change and/or chemical reactions continuing through the electrodes during discharge [5,10,12,129]. For this reason, the variable cell potential can be determined by the Nernst equation:

$$E = E^0 - RT \ln W \quad (3.5)$$

where R is the Boltzmann constant, T is the ratio of the temperature (Kelvin), and W is amount of unreacted ions in the active material [5,10,12,129]. For example,



when the reaction starts in the battery the Nernst equation can be written as:

$$E = E^0 - RT \ln (m_A / m_{A^{+2}}). \quad (3.7)$$

The Nernst equation is also a time-varying equation since the amount of $\ln W$ may change via time-dependent chemical reactions, changing the value of the cell potential (self-cathodic, anodic, or electrolytic reactions) [5,10,12,129]. This change can be seen in Figure 3.1.

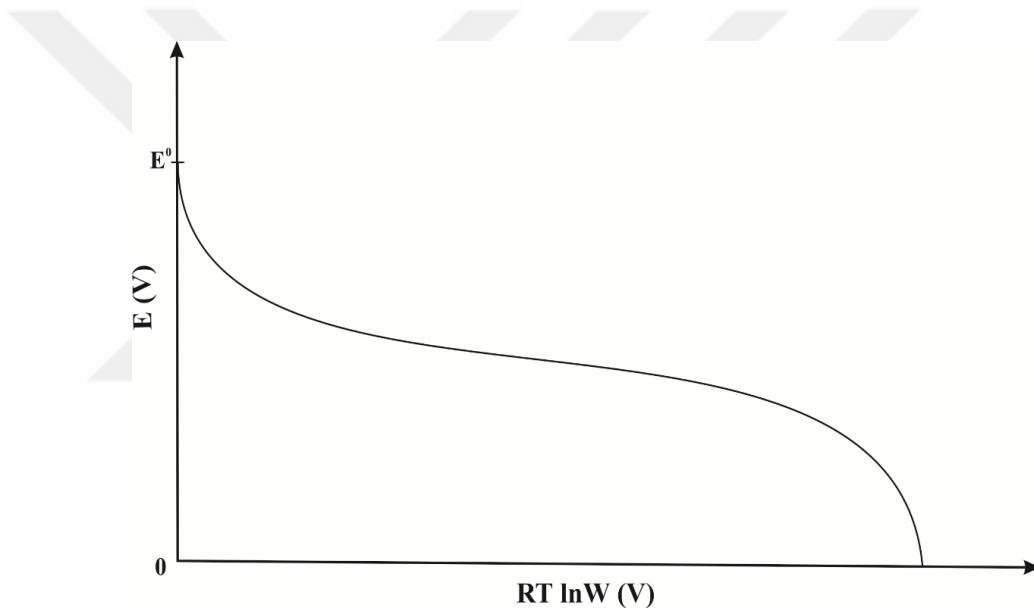


Figure 3.1. Variation of the voltage of battery cell electrodes according to the ratio of the active substance [12].

3.3. Battery Life

The "cycle" can be defined as the total time spent during a single charge and discharge for a rechargeable battery. The battery life can be defined as the sum of these cycles during active use of the battery. The number of cycles for rechargeable batteries can vary from 500 to 1000 cycles. The internal components of the battery cell and the environmental conditions can also affect the cycle number or the lifetime of the battery. Each produced battery has a certain operating temperature range due to the characteristics

of the components, thus the chemical reaction between the electrolyte and the electrodes which causes the decrease in lifetime of the cell (Figure 3.2) [13,14]. As an example, nickel-metal-hydride (NiMH) batteries lose 60% of their capacity when working at 60°C [15].

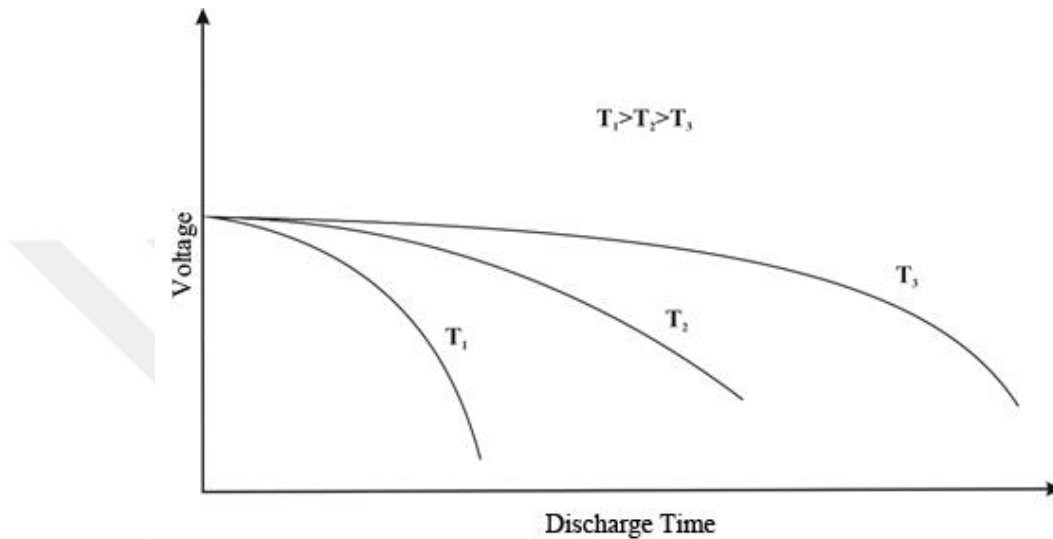


Figure 3.2 Change of discharge time of battery voltage with temperature (T) [12].

Another reason for the decrease in the lifetime of the cell is the strain effect on the electrode active substances [5,10,12,129]. During fabrication of the active material of the cell, the internal strain in the crystal structure can change. Furthermore, the microstrain can be caused by crystal structure deformations which affect the movement of ions in the structure [12]. In addition to these factors, internal pressure during charging/discharging at high potential or current, and settlement-separation reactions of the active material, can be important parameters affecting the battery performance of the cell [5,10,12,129].

4. METHODOLOGY

4.1. Sample Preparation

$\text{Li}_4\text{Ti}_{5-x}\text{V}_x\text{O}_{12}$, $\text{Li}_2\text{Ti}_{3-x}\text{V}_x\text{O}_7$, $\text{Li}_2\text{Ti}_{6-x}\text{V}_x\text{O}_{13}$, $\text{Na}_4\text{Ti}_{5-x}\text{V}_x\text{O}_{12}$, $\text{Na}_2\text{Ti}_{3-x}\text{V}_x\text{O}_7$ and $\text{Na}_2\text{Ti}_{6-x}\text{V}_x\text{O}_{13}$ anode materials have been synthesized via a solid state reaction method; $x = (0, 0.025, 0.05, 0.1, \text{ and } 0.15)$. Synthesis of the anode active materials was carried out with 99% purity Li_2CO_3 , Na_2CO_3 , TiO_2 , and V_2O_5 . Double heat treatment cycles were applied to the fabrication of $\text{Li}_4\text{Ti}_{5-x}\text{V}_x\text{O}_{12}$ and $\text{Na}_2\text{Ti}_{3-x}\text{V}_x\text{O}_7$ powders. On the first heat treatment, samples were heated to 800 °C in air for 16 hours to remove carbonates from the structure. A second heat treatment was then applied to the obtained final powders under the same conditions. A similar fabrication method was used for $\text{Na}_4\text{Ti}_{5-x}\text{V}_x\text{O}_{12}$ and $\text{Na}_2\text{Ti}_{6-x}\text{V}_x\text{O}_{13}$, powders at 600 °C and 1100 °C, respectively. The ion-exchange method was used for the fabrication of $\text{Li}_2\text{Ti}_{6-x}\text{V}_x\text{O}_{13}$. In this method, $\text{Na}_2\text{Ti}_6\text{O}_{13}$ powders were put into molten salt LiNO_3 at 360 °C for six hours where Li and Na ions were exchanged. The differential thermal analysis (DTA) of the unreacted powders was measured using a Netzsch DTA system. The measurement was conducted at 10 °C/min constant heating rate and from room temperature up to 900 °C.

4.2. X-ray Diffraction Analysis (XRD)

The crystal structural analysis of the materials was determined using X-ray diffraction (XRD), a method based on Bragg reflections. X-ray analysis of the prepared samples was performed using $\text{CuK}\alpha$ ($\lambda = 1.5405 \text{ \AA}$) radiation with a Siemens Bruker D5000 computer-controlled X-ray diffractometer at the University of Illinois at Urbana-Champaign Materials Research Laboratory. The measurements were taken at a constant scanning rate of $2^\circ/\text{min}$ at $2\theta = 2\text{--}80^\circ$. The crystal parameters of the samples were determined by comparing MDI Jade 9.0 Crystal Refinement program results with reference data.

4.3. Scanning Electron Microscope Analysis (SEM)

Electron microscopy is based on the principle that an electron beam accelerated under high voltage is reflected from a sample surface to obtain information about the

sample. As a result of the non-elastic interference of the high-energy beam electrons with the outer orbiting electrons of the atoms in the sample, low-energy Auger electrons are generated. Again, as a result of the interaction with the orbital electrons, the electrons break off from their orbit or decrease in energy, move to the surface of the sample, and accumulate on it. These electrons are defined as secondary electrons. The electron beam focusing on the sample surface can also generate elastic interactions with sample atoms. The electrons formed in this way are called backscattered electrons, and the amount of backscattered electrons is proportional to the atomic number of the sample. In other words, data from these scattering events are collected with the aid of a detector and a sample surface image is obtained.

In addition, the non-elastic interactions between the sample atoms and the electron beam are characteristic of X-rays and continuous bonds in the sample. For energy dispersive X-ray analysis (EDX), the electron beam from the filament interacts with the atoms on the sample surface, resulting in X-rays at different wavelengths. These are scattered over each element at different wavelengths and angles. The determination of the phases and % atomic distributions in the structure using these X-rays was performed using a Bruker detector combined with a Leo Evo-40xVP system.

For the surface morphology analysis, a JEOL 6060LV general purpose SEM at the University of Illinois at Urbana-Champaign Materials Research Laboratory was used. A back scattering detector (BSD) with 3 nm separation power was used, as well as a secondary electron (SE) detector at 30 kV acceleration voltage and 4.5 nm in XVP mode separation power, a 0.2–30 kV acceleration voltage range, and a magnification of 7 to 1,000,000 times.

4.4. Electrochemical Measurements

To perform electrochemical characterization of the battery cell, pure Li and Na metals were used as the counter electrode. $\text{Li}_4\text{Ti}_{5-x}\text{V}_x\text{O}_{12}$, $\text{Li}_2\text{Ti}_{3-x}\text{V}_x\text{O}_7$, $\text{Li}_2\text{Ti}_{6-x}\text{V}_x\text{O}_{13}$, $\text{Na}_4\text{Ti}_{5-x}\text{V}_x\text{O}_{12}$, $\text{Na}_2\text{Ti}_{3-x}\text{V}_x\text{O}_7$, and $\text{Na}_2\text{Ti}_{6-x}\text{V}_x\text{O}_{13}$ $x = (0, 0.025, 0.05, 0.1, \text{ and } 0.15)$ electrodes were mixed by polyvinylidene fluoride (PVDF) and carbon black (CB) at the rates of 70:15:15 for CR2032 coin cells, since the resistivity values of Ti based electrodes

were higher than those of the other electrodes. The coin cells were pressed in an Ar gas filled glove by Vigor. The electrochemical measurements of the cell were performed using a Bio-logic VPM3 for charge-discharge and CV testing. Charge-discharge measurements were done at 0.2, 0.5, 1, and 2C rates in the voltage range 0.5–2 V. CV measurements were taken at 0.1 mV constant voltage scanning rate in the 0.1–2 V range.

4.5. Electrical Resistivity Measurements

The resistivity measurements of the cell and raw-electrodes were conducted at the University of Illinois at Urbana-Champaign Materials Research Laboratory. The measurements were taken at room temperature by an Agilent DC Benchtop 2 Point Probe Station system. The resistivity of samples was determined from:

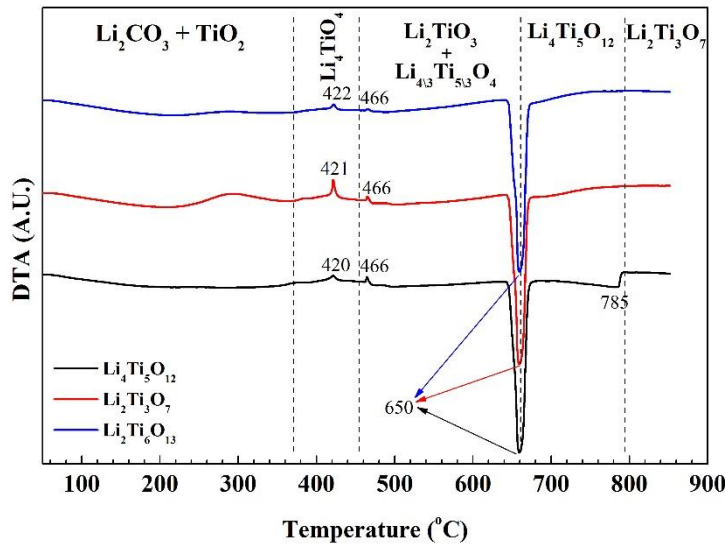
$$\rho = \frac{R \cdot A}{L}$$

where ρ is resistivity, R is resistance, A is the cross section, and L is the distance between the contact points.

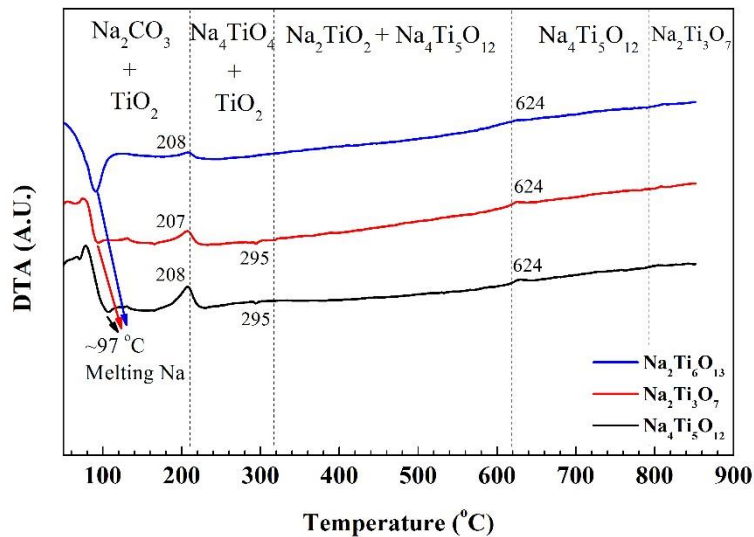
5. EXPERIMENTAL RESULTS

5.1. DTA Results

The DTA analysis is one of the techniques that gives a deep negative peak in the graph which depends on the endothermic and exothermic reactions in the sample. So it is important to find out the temperature dependence of the reactions of the powders. In addition to this, the phase formation temperature of the pre-mixed powders can easily be determined by DTA analysis.



a)



b)

Figure 5.1. DTA results of a) $\text{Li}_4\text{Ti}_5\text{O}_{12}$, $\text{Li}_2\text{Ti}_3\text{O}_7$, and $\text{Li}_2\text{Ti}_6\text{O}_{13}$; b) $\text{Na}_4\text{Ti}_5\text{O}_{12}$, $\text{Na}_2\text{Ti}_3\text{O}_7$, and $\text{Na}_2\text{Ti}_6\text{O}_{13}$.

The DTA analysis was performed on the pre-mixed raw powders for the fabrication of $\text{Li}_4\text{Ti}_5\text{O}_{12}$, $\text{Li}_2\text{Ti}_3\text{O}_7$, $\text{Li}_2\text{Ti}_6\text{O}_{13}$, $\text{Na}_4\text{Ti}_5\text{O}_{12}$, $\text{Na}_2\text{Ti}_3\text{O}_7$, and $\text{Na}_2\text{Ti}_6\text{O}_{13}$ compositions by using the starting materials Li_2CO_3 , Na_2CO_3 , and TiO_2 obtained from Alpha Aesar. The obtained DTA curves of the samples are given in Figure 5.1. The phase formation temperatures of $\text{Li}_4\text{Ti}_5\text{O}_{12}$ and $\text{Na}_2\text{Ti}_3\text{O}_7$ were determined to be at around 800 °C, the temperature of the $\text{Na}_4\text{Ti}_5\text{O}_{12}$ phase is at about 600 °C, and $\text{Li}_2\text{Ti}_3\text{O}_7$ and $\text{Na}_2\text{Ti}_6\text{O}_{13}$ can be fabricated at 1100 °C which is higher than the upper limit of our system. The other peaks on the DTA curves are related to decomposition, unwanted phases, and evaporation of the carbonate in the systems.

5.2. XRD Results

In this study, the XRD investigation are carried out in two parts; the first part includes the as prepared samples before they are used as an anode material in the battery cell and the second part concerns the samples which are cycled for 1000 times in the cell.

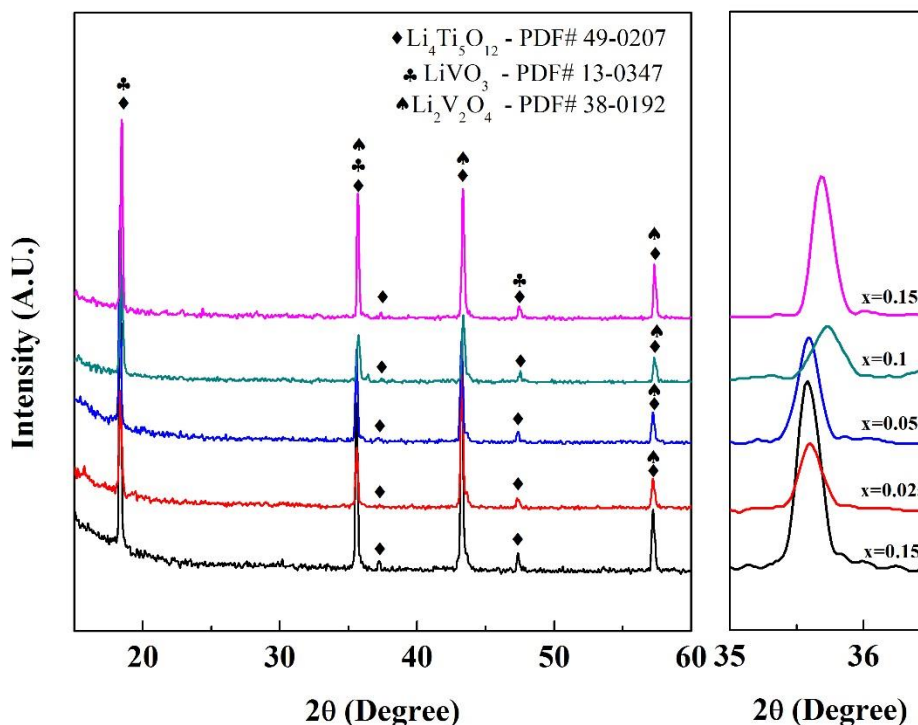


Figure 5.2. XRD results of $\text{Li}_4\text{Ti}_{5-x}\text{V}_x\text{O}_{12}$ ($x = 0, 0.025, 0.05, 0.1, \text{ and } 0.15$) powders.

XRD results of the as prepared powders are given in Figure 5.2. Three different phases are observed with increasing vanadium content in the structure, such as $\text{Li}_4\text{Ti}_5\text{O}_{12}$, LiVO_3 , and $\text{Li}_2\text{V}_2\text{O}_4$ phases. The XRD analysis of the unsubstituted samples shows that $\text{Li}_4\text{Ti}_5\text{O}_{12}$ is synthesized successfully without any impurity phases. The vanadium substitution in the system causes the formation of impurity phases in the structure after $x = 0.1$. It should be noted that the samples where V substituted with $x = 0-0.15$ does not change the main phase of $\text{Li}_4\text{Ti}_5\text{O}_{12}$. Although the XRD peak of the secondary phases such as LiVO_3 and $\text{Li}_2\text{V}_2\text{O}_4$ are overlapping with the diffraction pattern, we see in the peaks at around 36° that the impurity phases are formed for $x \geq 0.1$ value as shown in the right panel of Figure 5.2. This graph also shows the successful V substitution for $x < 0.1$: the peak shifts to the right indicating successful substitutions and the shift to higher angle in the XRD peaks is attributed to substitution of smaller ions in the structure. The cell and lattice parameters of the samples were calculated using Rietvelt refinement methods as shown in Figure 5.4.

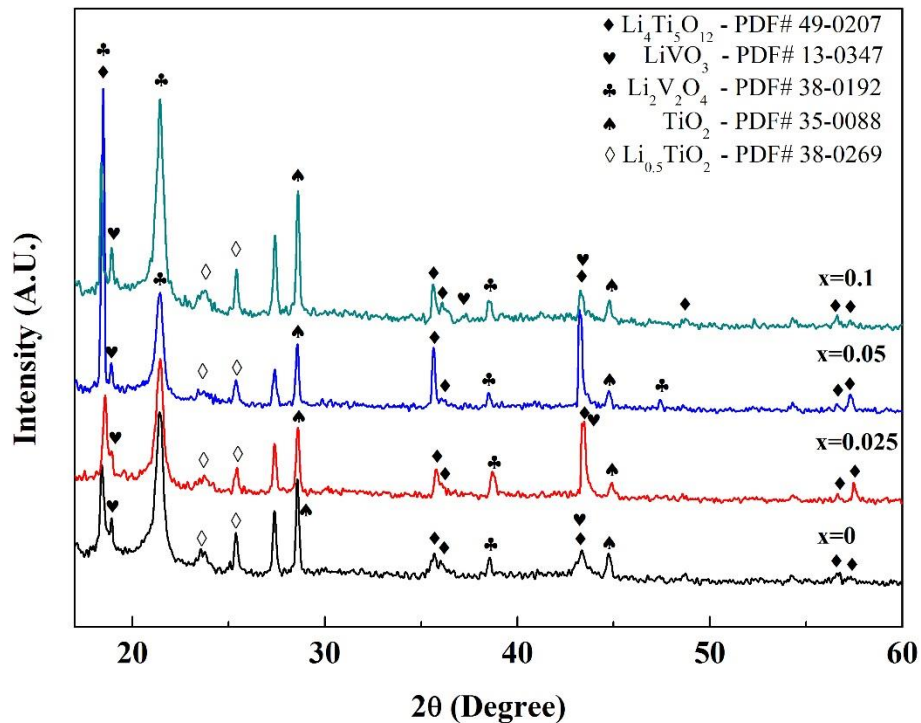


Figure 5.3. XRD results of $\text{Li}_4\text{Ti}_{5-x}\text{V}_x\text{O}_{12}$ ($x = 0, 0.025, 0.05, 0.1$, and 0.15) electrodes after 1000 cycles.

For an octahedral environment, the radii of Ti^{4+} and V^{5+} ions are given as 0.6 pm and 0.54 pm, respectively. When V ions were substituted with Ti in the structure, a decrease of the lattice volume until solubility limit of the V ions is expected. In $\text{Li}_4\text{Ti}_5\text{O}_{12}$ the decrease of the volume which is calculated from the XRD pattern up to $x = 0.1$ supports the discussion above, as seen in Figure 5.4.

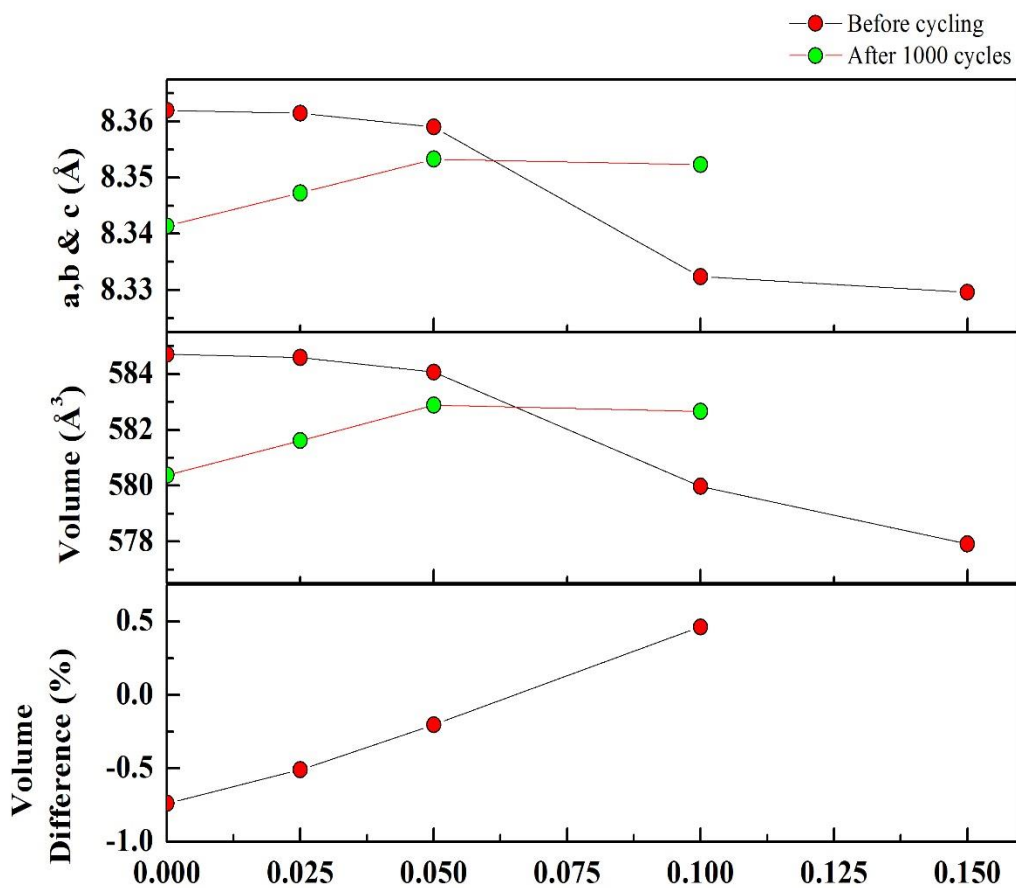


Figure 5.4. Crystal parameter comparison of $\text{Li}_4\text{Ti}_{5-x}\text{V}_x\text{O}_{12}$ before and after 1000 cycles.

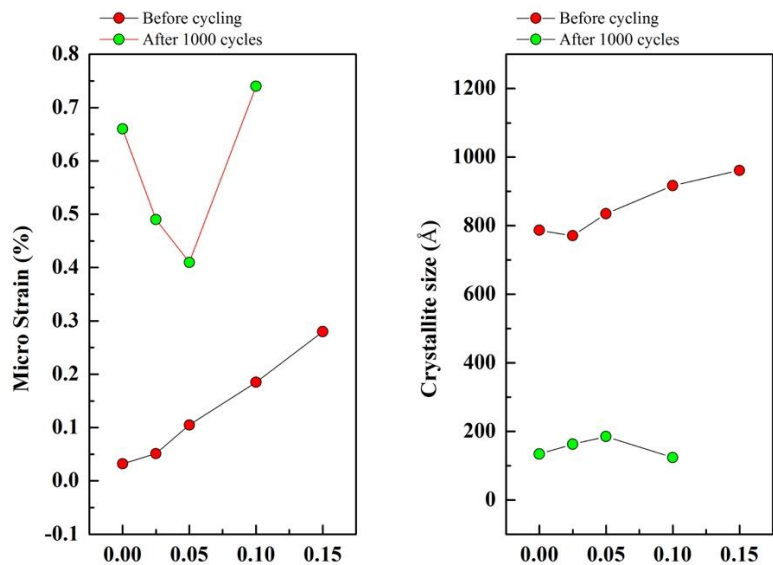


Figure 5.5. Microstrain and crystallite sizes of $\text{Li}_4\text{Ti}_{5-x}\text{V}_x\text{O}_{12}$ before and after 1000 cycles.

The calculated microstrain and crystallite size of the unsubstituted samples are given in Figure 5.5. Although the microstrain value is almost zero, the strain increases with increasing V content. It can be predicted that the shrinkage of the lattice may cause an increase in the strain in the samples. The increase of the crystallite size is related to the increase of the stability of the samples.

Deformation of the lattice during cycling of the battery is the main reason for the decrease in battery performance [5,10]. For this purpose, the structural deformation of the electrode after 1000 cycles is investigated. Figure 5.3 shows the ex-situ XRD results of V-substituted $\text{Li}_4\text{Ti}_5\text{O}_{12}$ anode electrodes. It should be noted that the sample with $x = 0.15$ did not show any battery performance and so its XRD pattern at 1000 cycles was not measured. The XRD pattern of the ex-situ data has two different structures. One is a broad halo due to non-crystalline phases such as CB and PVDF in the electrode and the second is the crystalline phase of the active materials. No peaks belonging to the Al substrate in the electrodes are observed. After 1000 cycles, the main phase of the pure sample is determined to be $\text{Li}_4\text{Ti}_5\text{O}_{12}$. The TiO_2 , $\text{Li}_{0.5}\text{TiO}_2$, $\text{Li}_2\text{V}_2\text{O}_4$, and LiVO_3 impurity phases are observed for increasing V content in the electrodes. It can be concluded that the cycling

of the electrode causes the deformation of the lattice and the formation of the TiO_2 phase, since many of the Li-ions do not come back to the electrode during the cycling process of the cell.

Figures 5.4 and 5.5 shows the crystal parameters, volume changes, microstrain, and crystallite size values of the samples which are charged/discharged 1000 cycles. Microstrain values reduce until $x = 0.05$ substitutions and then increase. In addition, the microstrain values increase with increasing V substitutions. One can understand from Figure 5.3 that the impurity phases are dominant for $x \geq 0.1$ and it can be predicted that the increase of the microstrain is related to the impurity phases.

XRD patterns of $\text{Li}_2\text{Ti}_{3-x}\text{V}_x\text{O}_7$ samples where $x = 0, 0.025, 0.05, 0.1, \text{ and } 0.15$ are given in Figure 5.6. $\text{Li}_2\text{Ti}_3\text{O}_7$ (where $x = 0$) samples without any impurity phases are synthesized successfully. When the V ions are substituted into the system, the impurity phase of $\text{Li}_2\text{V}_2\text{O}_4$ for $x \geq 0.025$ appears in the samples. The solubility limit of V in $\text{Li}_2\text{Ti}_3\text{O}_7$ is therefore determined as $x \leq 0.025$.

Figure 5.7 shows the ex-situ XRD results of $\text{Li}_2\text{Ti}_3\text{O}_7$ anode electrodes after 1000 cycles. The main phase of $\text{Li}_4\text{Ti}_5\text{O}_{12}$ is not changed in the pure samples. The broad halo is due to CB and PVDF and the Ti_6O_{11} and $\text{Li}_{0.5}\text{TiO}_2$ impurity phases are determined in the electrodes. For $\text{Li}_4\text{Ti}_5\text{O}_{12}$, it can be seen that some part of the Li-ions do not return to the sites in the crystal structure, so the reason for the capacity fade could be due to non-returned Li-ions in the battery cell.

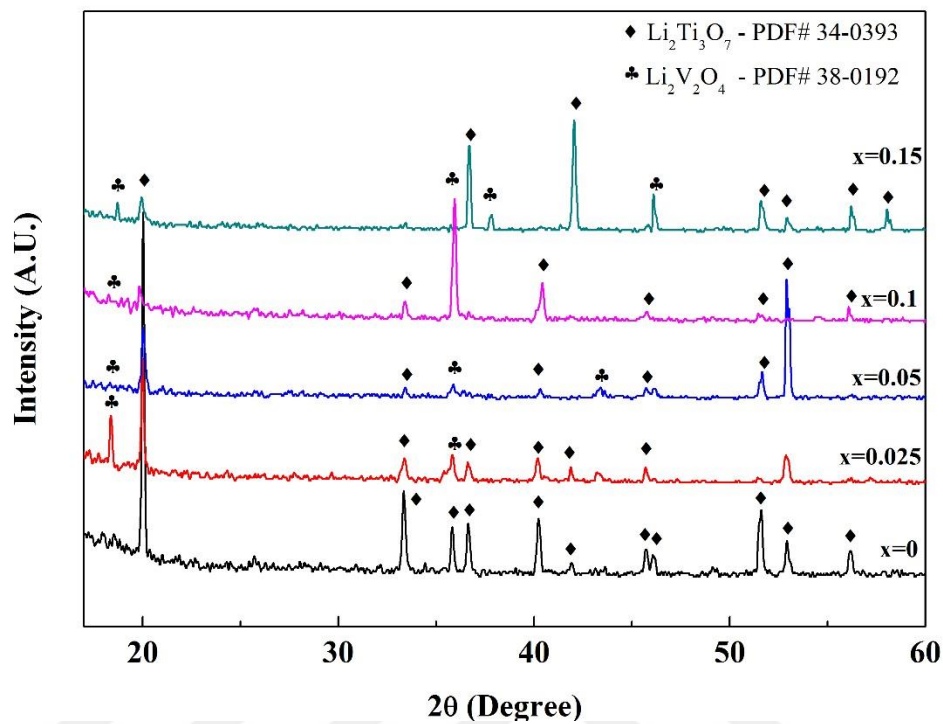


figure 5.6. XRD results of $\text{Li}_2\text{Ti}_{3-x}\text{V}_x\text{O}_7$ ($x = 0, 0.025, 0.05, 0.1, \text{ and } 0.15$) powders.

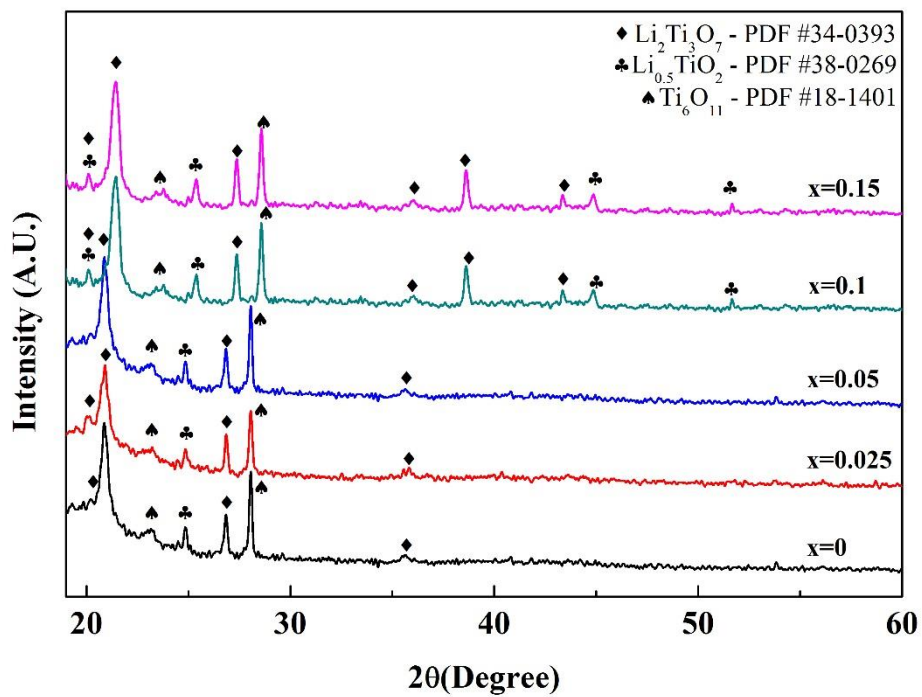


Figure 5.7. XRD results of $\text{Li}_2\text{Ti}_{3-x}\text{V}_x\text{O}_7$ ($x = 0, 0.025, 0.05, 0.1, \text{ and } 0.15$) electrodes after 1000 cycles.

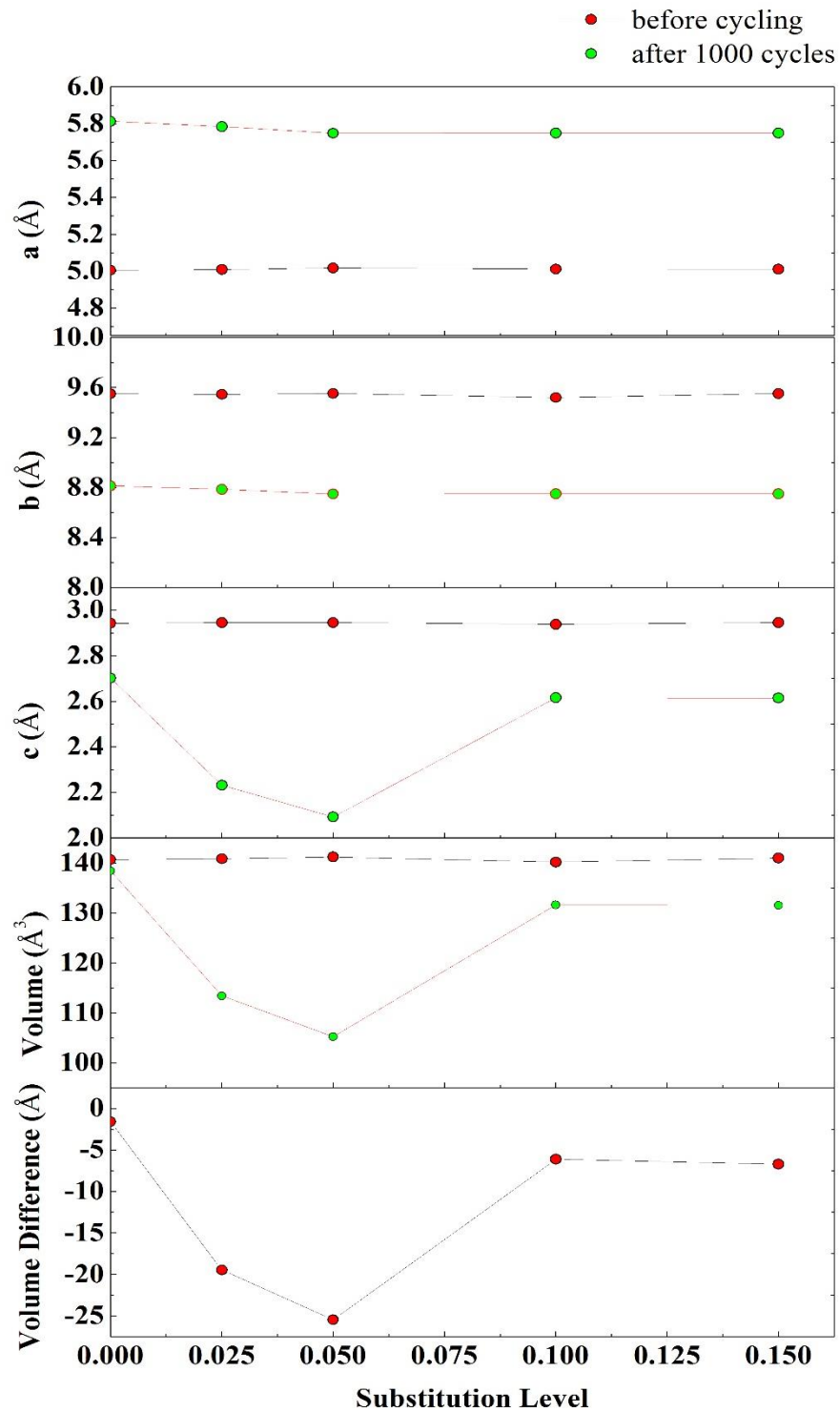


Figure 5.8. V content dependence of the cell parameters for $\text{Li}_2\text{Ti}_{3-x}\text{V}_x\text{O}_7$.

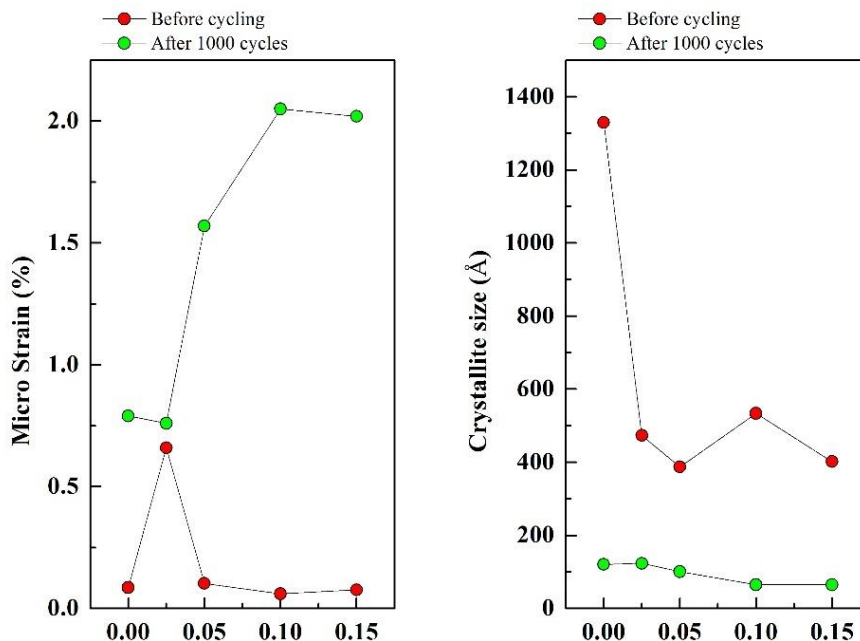


Figure 5.9. Microstrain and crystallite sizes of $\text{Li}_2\text{Ti}_{3-x}\text{V}_x\text{O}_7$ before and after 1000 cycles.

Figures 5.8 and 5.9 show the changes in the crystal parameters, volume, microstrain, and crystallite size of $\text{Li}_2\text{Ti}_{3-x}\text{V}_x\text{O}_7$. According to Rietveld refinement, $\text{Li}_2\text{Ti}_{3-x}\text{V}_x\text{O}_7$ ($x = 0, 0.025, 0.05, 0.1, \text{ and } 0.15$) samples show orthorhombic crystal structure; the a and b parameters of the samples are almost the same with increasing V content while the c parameters decrease until a certain value and then increase. The change of the lattice volume is related to the valence state of the main phase and impurity phases in the samples. The microstrain value of the $\text{Li}_2\text{Ti}_3\text{O}_7$ phase implies almost zero strain, as expected, and it increases with increasing V substitution for $x \leq 0.025$. After this value the microstrain started to rise again. After 1000 cycles the microstrain values of the electrodes increase. The change of the microstrain in the samples is related to volume changes of the lattice and impurity phases in the samples.

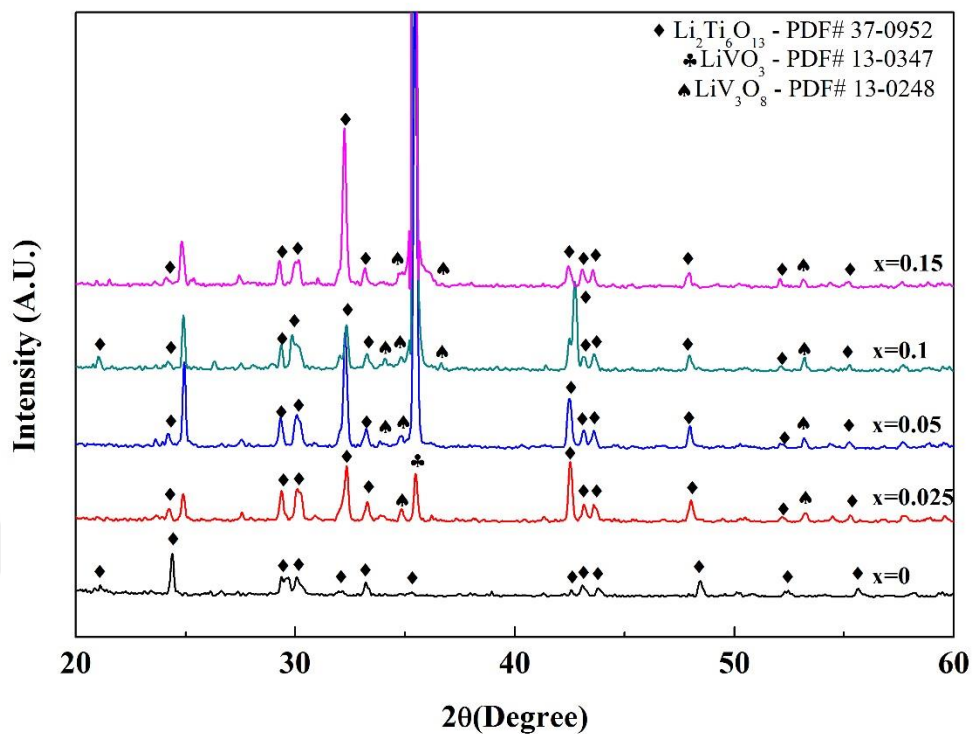


Figure 5.10. XRD results of $\text{Li}_2\text{Ti}_{6-x}\text{V}_x\text{O}_{13}$ ($x = 0, 0.025, 0.05, 0.1, \text{ and } 0.15$) powders.

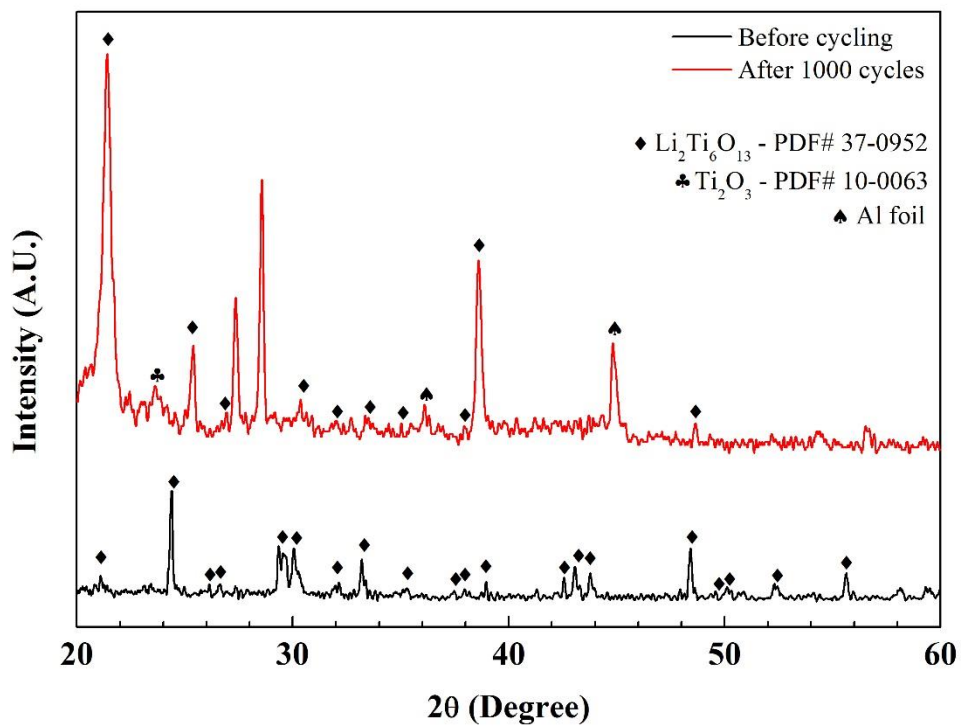


Figure 5.11. XRD results of the $\text{Li}_2\text{Ti}_6\text{O}_{13}$ electrode after 1000 cycles.

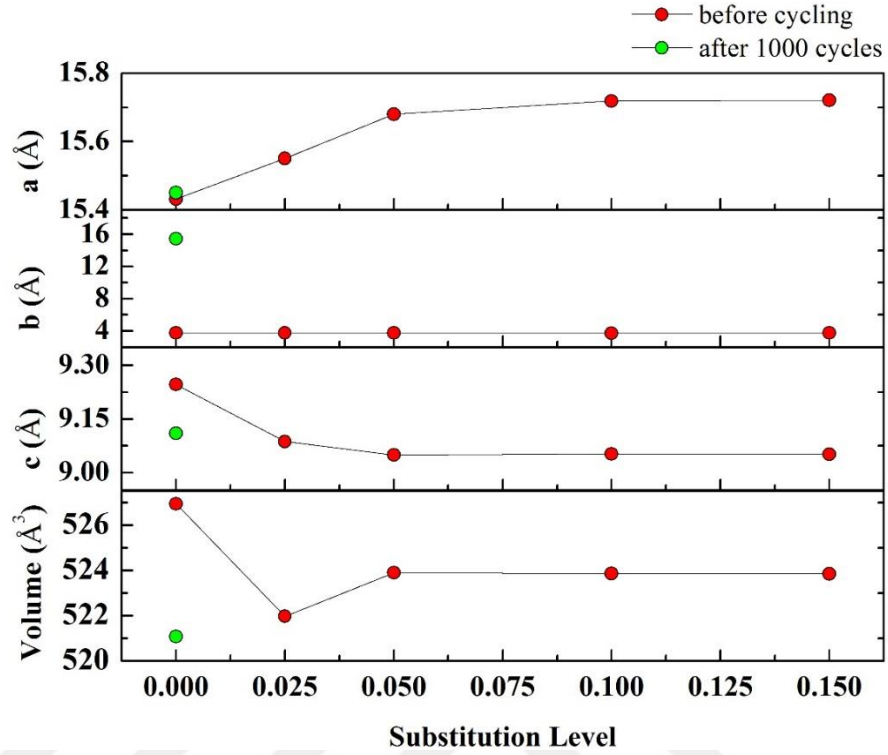


Figure 5.12. V content dependence of the cell parameters for of $\text{Li}_2\text{Ti}_{6-x}\text{V}_x\text{O}_{13}$.

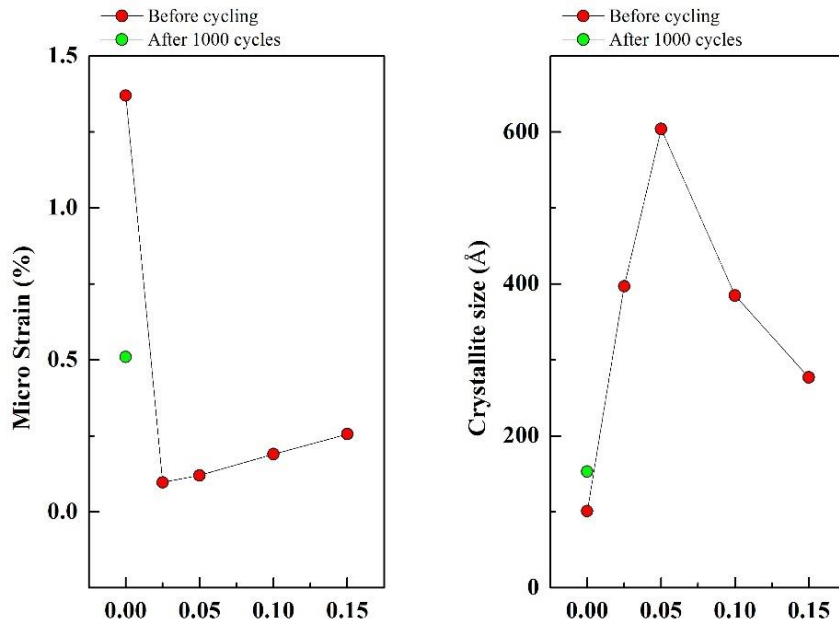


Figure 5.13. Microstrain and crystallite sizes of $\text{Li}_2\text{Ti}_{6-x}\text{V}_x\text{O}_{13}$ before and after 1000 cycles.

Another important Li-Ti-O phase for battery applications is $\text{Li}_2\text{Ti}_6\text{O}_{13}$. XRD patterns from $\text{Li}_2\text{Ti}_{6-x}\text{V}_x\text{O}_{13}$ samples (where $x = 0, 0.025, 0.05, 0.1, \text{ and } 0.15$) are shown in Figure 5.10. The pure sample shows only peaks of the $\text{Li}_2\text{Ti}_6\text{O}_{13}$ phase without any impurities. Increasing V content in the structure causes the formation of LiVO_3 and LiV_3O_8 phases for $x \geq 0.025$ substitutions. Although the main phase does not change by substitution, the impurity phases become the main phase with increasing substitution levels.

Figure 5.11 shows the ex-situ XRD results of an anode electrode after 1000 cycles. As stated in the battery performance section, the impurity phases in $\text{Li}_2\text{Ti}_6\text{O}_{13}$ cause decrease in the battery properties. Although the main phase ($\text{Li}_2\text{Ti}_6\text{O}_{13}$) does not change after 1000 cycles, the Ti_2O_3 impurity phase is observed in the samples.

Figure 5.12 and 5.13 shows the crystal parameters, volume changes, microstrain, and crystallite sizes for the samples. According to Rietveld refinement, $\text{Li}_2\text{Ti}_{6-x}\text{V}_x\text{O}_{13}$ ($x = 0, 0.025, 0.05, 0.1, \text{ and } 0.15$) samples have a monoclinic crystal structure; the a parameters increased and the c parameters decreased. The crystal volume of the cell was decreased with V substitutions for $x \leq 0.025$ and the lattice volume was not changed for $x \geq 0.025$. We can conclude that the stable volume of the cell is related to the solubility limit of the V ions in the structure. Figure 5.12 also shows the change of the crystal volume depending on V substitutions. According to these results, the volume expansion rates were calculated as -1.11% for a pure $\text{Li}_2\text{Ti}_6\text{O}_{13}$ sample.

Figure 5.13 shows the microstrain values of $\text{Li}_2\text{Ti}_{6-x}\text{V}_x\text{O}_{13}$ ($x = 0, 0.025, 0.05, 0.1, \text{ and } 0.15$) samples. V substitution causes a decrease in the microstrain for $x \leq 0.025$, although it then increases with increasing V content. After 1000 cycles the microstrain values of the electrodes decrease. In addition, the crystallite size of the samples increases with increasing V substitutions for $x \leq 0.05$. However, after $x = 0.05$ the crystallite size starts to decrease.

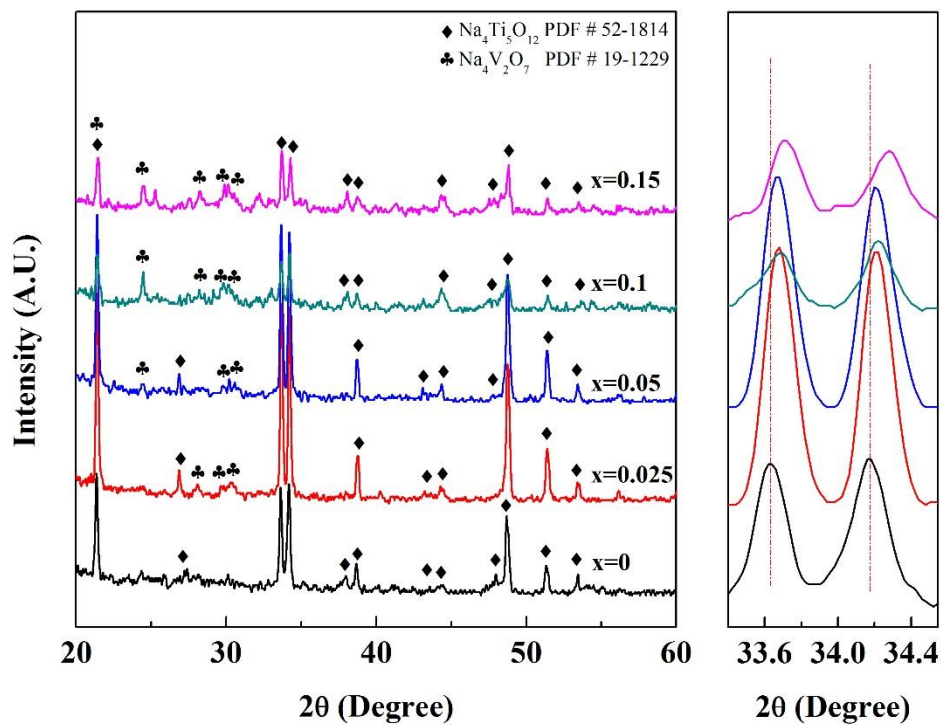


Figure 5.14. XRD results of $\text{Na}_4\text{Ti}_{5-x}\text{V}_x\text{O}_{12}$ ($x = 0, 0.025, 0.05, 0.1, \text{ and } 0.15$) powders.

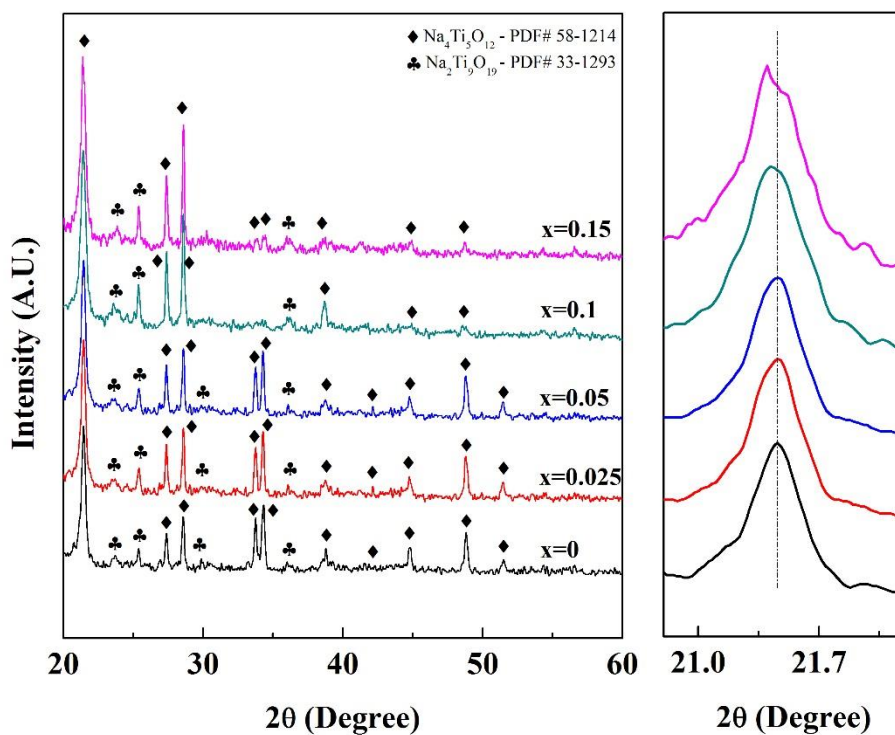


Figure 5.15. Ex-situ XRD results of $\text{Na}_4\text{Ti}_{5-x}\text{V}_x\text{O}_{12}$ ($x = 0, 0.025, 0.05, 0.1, \text{ and } 0.15$) powders.

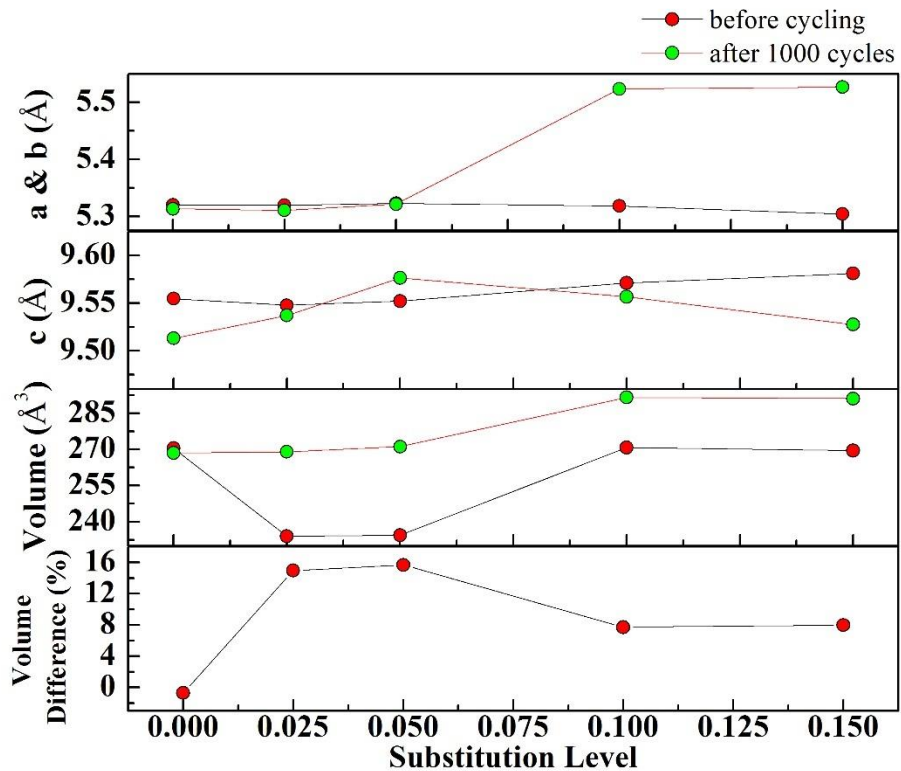


Figure 5.16. Crystal parameter comparison of $\text{Na}_4\text{Ti}_{5-x}\text{V}_x\text{O}_{12}$ before and after 1000 cycles.

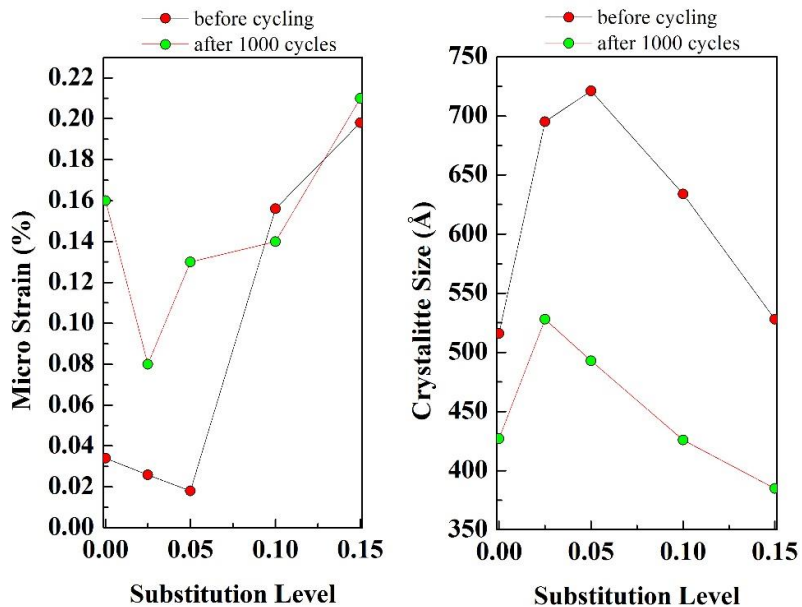


Figure 5.17. Microstrain and crystallite sizes of $\text{Na}_4\text{Ti}_{5-x}\text{V}_x\text{O}_{12}$ before and after 1000 cycles.

In the last decade, the Na based batteries have been alternatives of rechargeable batteries due to their natural abundance and they have nature friendly properties. So, Na-Ti-O based oxide materials have come to be regarded as good anode materials for rechargeable batteries.

The XRD measurements of $\text{Na}_4\text{Ti}_{5-x}\text{V}_x\text{O}_{12}$ ($x = 0, 0.025, 0.05, 0.1, \text{ and } 0.15$) samples are shown in Figure 5.14. The structural analysis of the pure sample shows $\text{Na}_4\text{Ti}_5\text{O}_{12}$ as the main phase for $x = 0$. The V substitution in the system causes formation of some impurity phases such as $\text{Na}_4\text{V}_2\text{O}_7$. No impurity phases are observed for $x \leq 0.05$, which means the solubility limit of the V ions in the $\text{Na}_4\text{Ti}_5\text{O}_{12}$. $\text{Na}_4\text{V}_2\text{O}_7$ impurity phase is only observed for $x \geq 0.05$ and the main phase remains same for all V contents. The peaks shift to the right indicating successful substitutions for Ti^{5+} with V^{4+} . In addition, the lattice volume decreases until $x = 0.05$, and the volume increases giving a stable value for increasing V level. These changes in the unit cell volume can be due to two reasons; one is the ionic radii difference between V^{4+} and Ti^{5+} , and second one is the formation of the impurity phases.

Figure 5.15 shows the ex-situ XRD results of anode electrodes after 1000 cycles. The main phase of the unsubstituted sample is $\text{Na}_4\text{Ti}_5\text{O}_{12}$. $\text{Na}_2\text{Ti}_9\text{O}_{19}$ phase appears in the V substituted samples as an impurity phase. This impurity phase becomes dominant for $0.1 \leq x \leq 0.15$. Figure 5.15 also shows the small angle peak shifting to the left; these peak shifts appear with $x = 0.1$ and 0.15 substitution levels. The lower angle change of the XRD peak is related to a change of the valence state of V ions from $5+$ to $4+$.

Figures 5.16 and 5.17 show the crystal parameters, volume changes, microstrain, and crystallite sizes upon V substitution. According to Rietveld refinements, $\text{Na}_4\text{Ti}_{5-x}\text{V}_x\text{O}_{12}$ ($x = 0, 0.025, 0.05, 0.1, \text{ and } 0.15$) samples have a monoclinic structure, and the a, b, and c parameters change by V doping and cycling of the electrodes. V substitutions between $x = 0.1$ and 0.15 cause abnormal changes in the crystal parameters. This situation can be due to the impurity phases and ionic radii difference between V and Ti ions in the lattice. The ionic radius difference of the ions in the crystal structure is also responsible for the changes in microstrain. The value of the volume expansions increases to 15% with $x = 0.05$ substitution level. Low level volume expansions, for example, <7% are the

most desired for the Li-ion batteries because of the increasing microstrain. It should be noted that Na-electrode materials have high microstrain due to the larger radii of the Na ions compared to Li electrodes. According to Figure 5.17, although the volume expansion rate increases, the microstrain values decrease after 1000 cycles for $x = 0.025$.

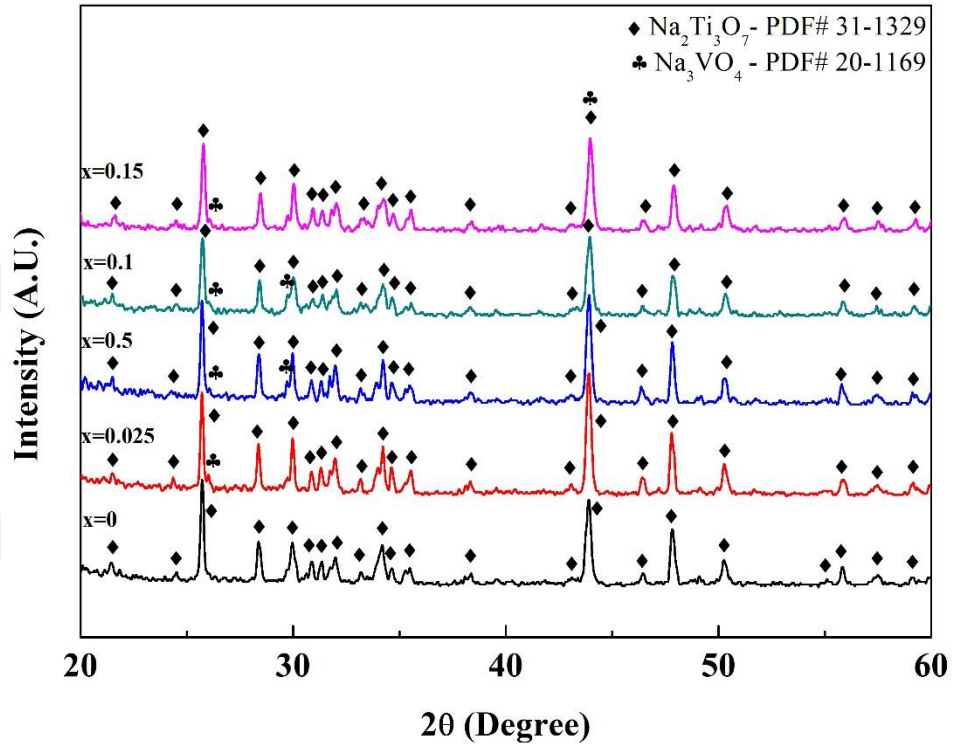


Figure 5.18. XRD results of $\text{Na}_2\text{Ti}_{3-x}\text{V}_x\text{O}_7$ ($x = 0, 0.025, 0.05, 0.1, \text{ and } 0.15$) powders.

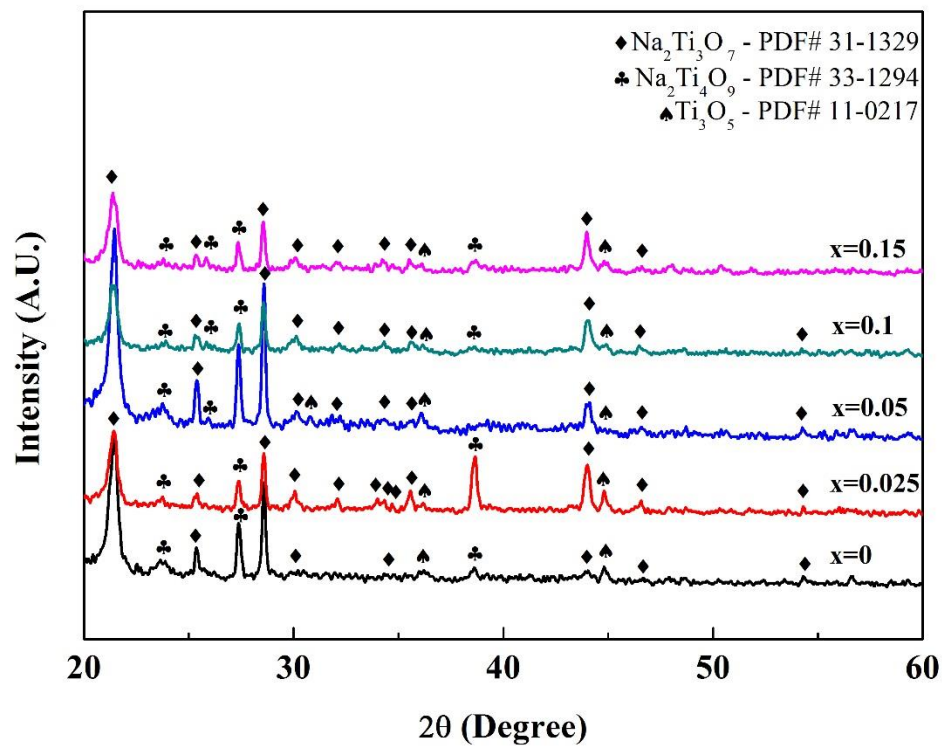


Figure 5.19. Ex-situ XRD results of $\text{Na}_2\text{Ti}_{3-x}\text{V}_x\text{O}_7$ ($x = 0, 0.025, 0.05, 0.1, \text{ and } 0.15$) powders.

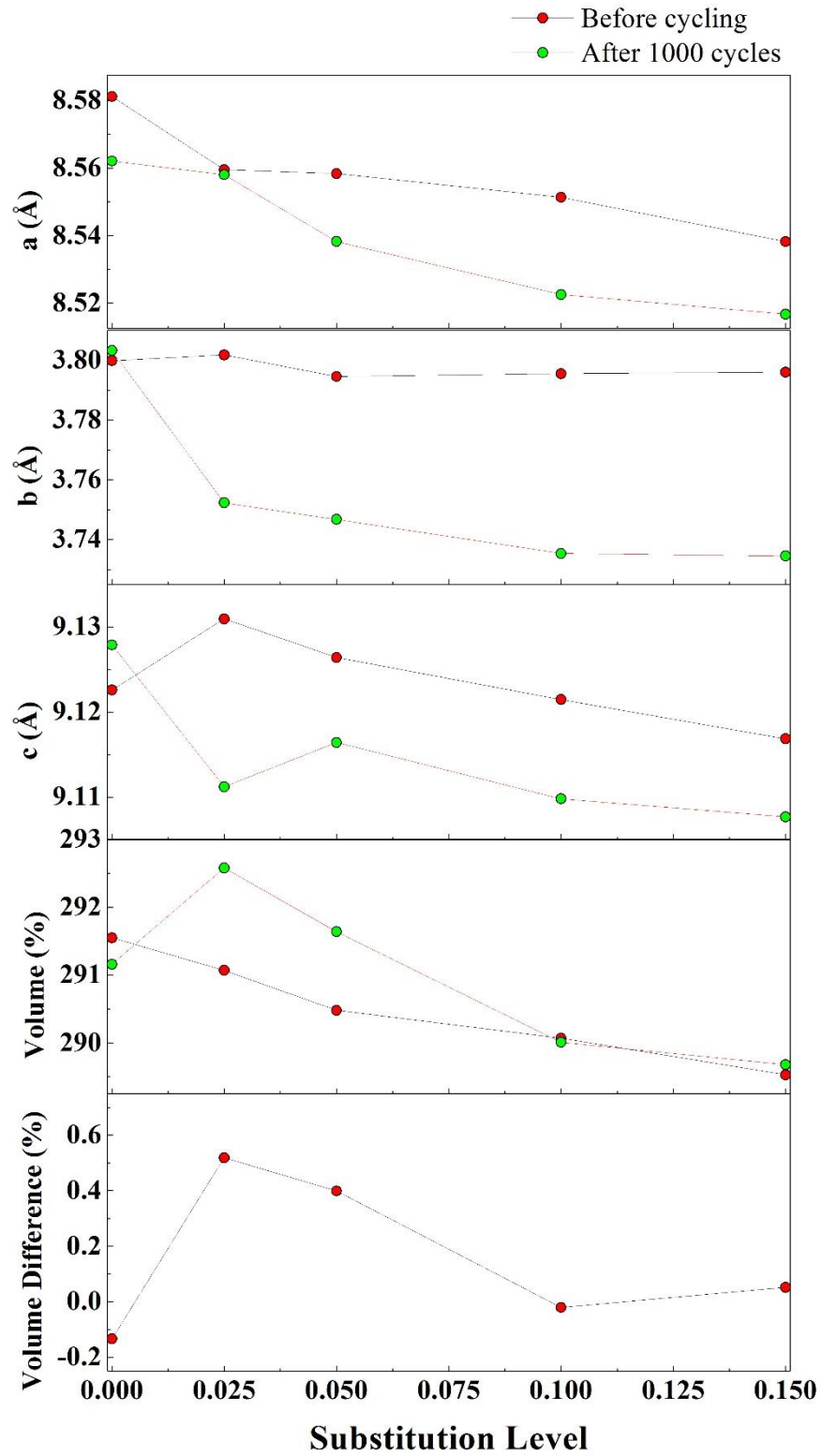


Figure 5.20. Crystal parameter comparison of $\text{Na}_2\text{Ti}_{3-x}\text{V}_x\text{O}_7$ before and after 1000 cycles.

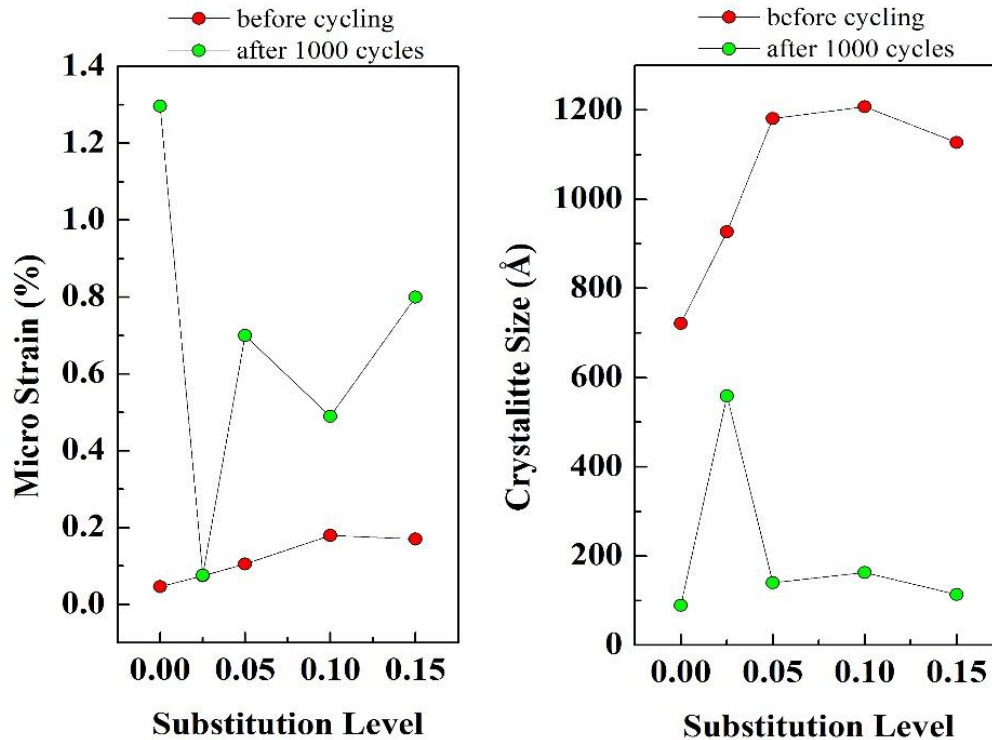


Figure 5.21. Microstrain and crystallite sizes of $\text{Na}_2\text{Ti}_{3-x}\text{V}_x\text{O}_7$ before and after 1000 cycles.

The XRD patterns of $\text{Na}_2\text{Ti}_{3-x}\text{V}_x\text{O}_7$ ($x = 0, 0.025, 0.05, 0.1, \text{ and } 0.15$) samples are shown in Figure 5.18. The unsubstituted samples are obtained without any impurity phases, and the main phase is $\text{Na}_2\text{Ti}_3\text{O}_7$ as expected. Although the vanadium substitution in the system causes the formation of the impurity phase for $x \geq 0.1$ levels of substitution (such as Na_3VO_4), the main phase remains the same for all samples substituted with V. The solubility limit of V ions in $\text{Na}_2\text{Ti}_3\text{O}_7$ is determined as $x \leq 0.1$.

Figure 5.19 shows the ex-situ XRD results of anode electrodes after 1000 cycles. It is clear that the main phase of $\text{Na}_2\text{Ti}_3\text{O}_7$ does not change in the structure. In addition, the Ti_3O_5 and $\text{Na}_2\text{Ti}_4\text{O}_9$ impurity phases are observed in the structure above 1000 cycles. The impurity phases become dominant for $x \geq 0.05$ compared to lower doping levels.

Figures 5.20 and 5.21 show the crystal parameters, volume changes, microstrain, and crystallite sizes of the samples. According to Rietveld refinement, $\text{Na}_2\text{Ti}_{3-x}\text{V}_x\text{O}_7$ ($x = 0, 0.025, 0.05, 0.1, \text{ and } 0.15$) samples have a monoclinic structure and the calculated a, b

and *c* parameters decrease with increasing V content in the structure. The crystal volume decrease with increasing V content, the obtained changes are just 0–1%. Figure 5.21 shows the microstrain and crystallite size results. According to these results, all V substitutions cause increase of both microstrain and crystallite size. On the other hand, after 1000 cycles with *x* = 0.025 substitution, a smaller microstrain value is obtained than that of the other substitution levels or the pure sample.

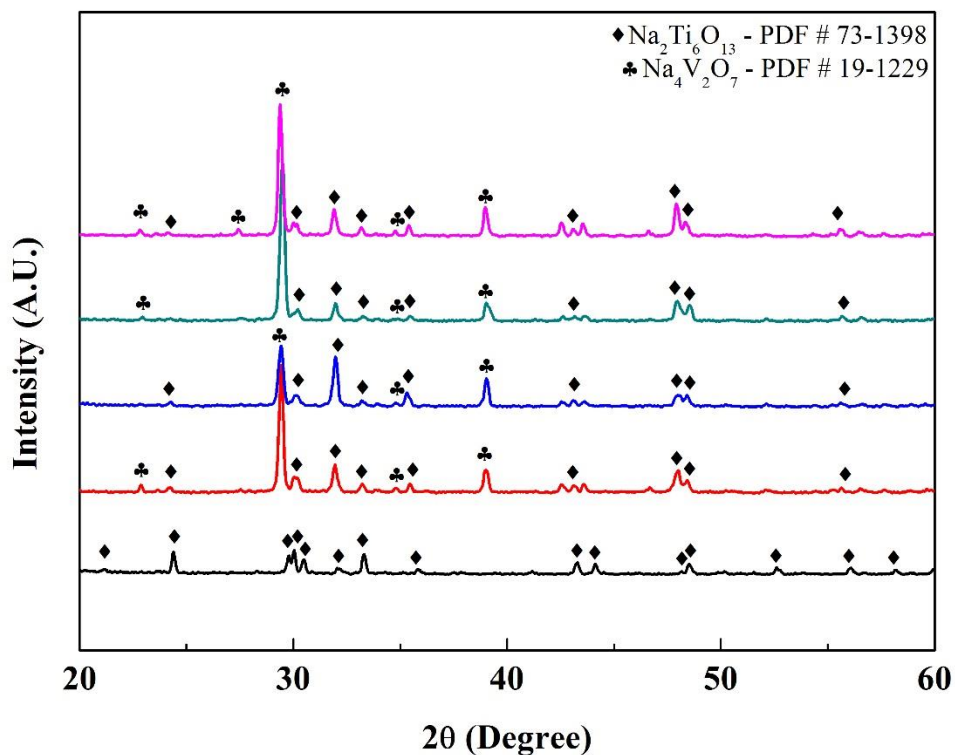


Figure 5.22. XRD results of $\text{Na}_2\text{Ti}_{6-x}\text{V}_x\text{O}_{13}$ ($x = 0, 0.025, 0.05, 0.1, \text{ and } 0.15$) powders.

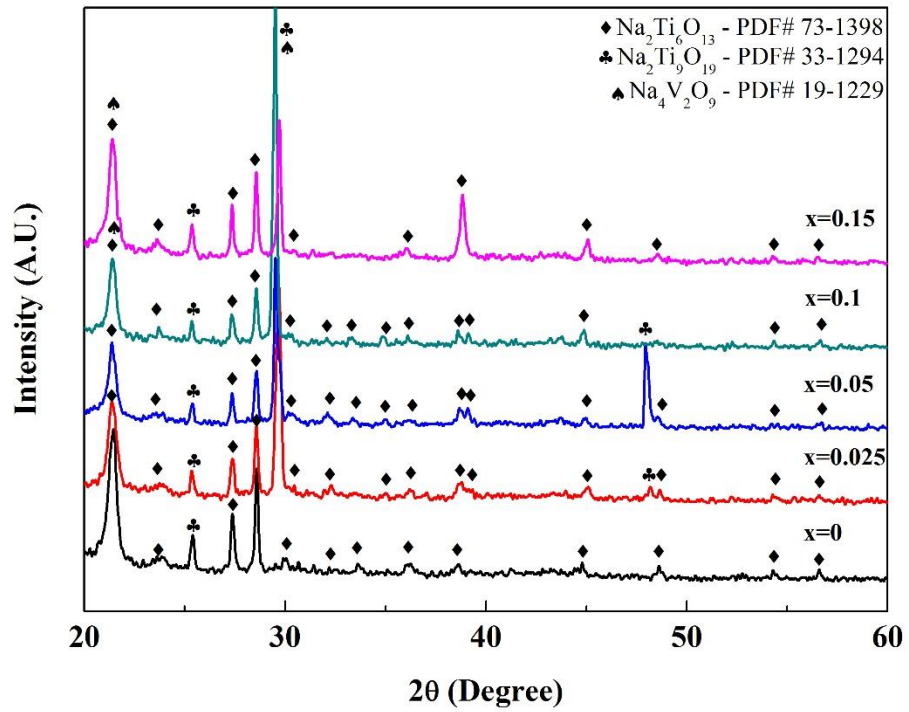


Figure 5.23. Ex-situ XRD results of $\text{Na}_2\text{Ti}_{6-x}\text{V}_x\text{O}_{13}$ ($x = 0, 0.025, 0.05, 0.1, \text{ and } 0.15$) powders.

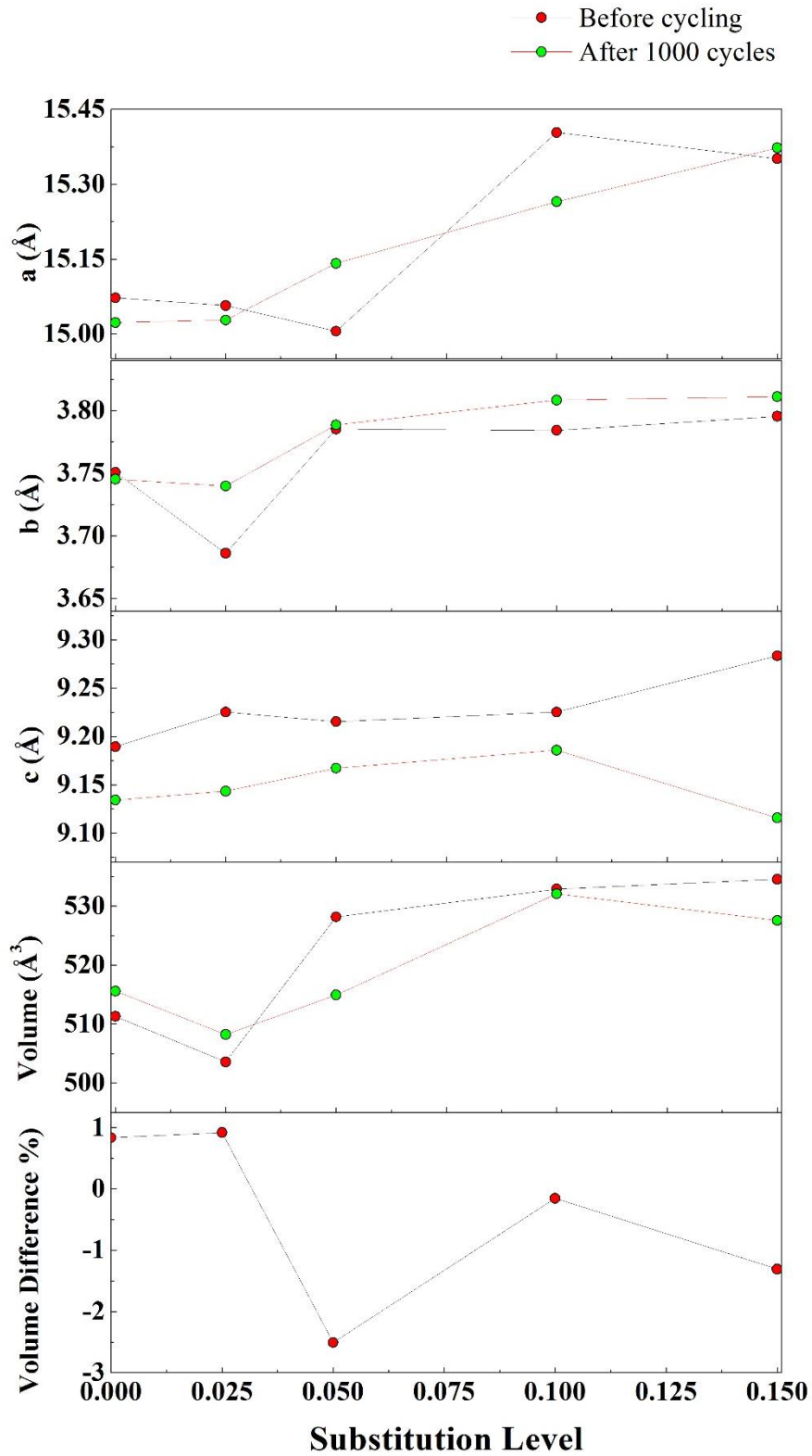


Figure 5.24. Comparison of crystal parameters of $\text{Na}_2\text{Ti}_{6-x}\text{V}_x\text{O}_{13}$ before and after 1000 cycles.

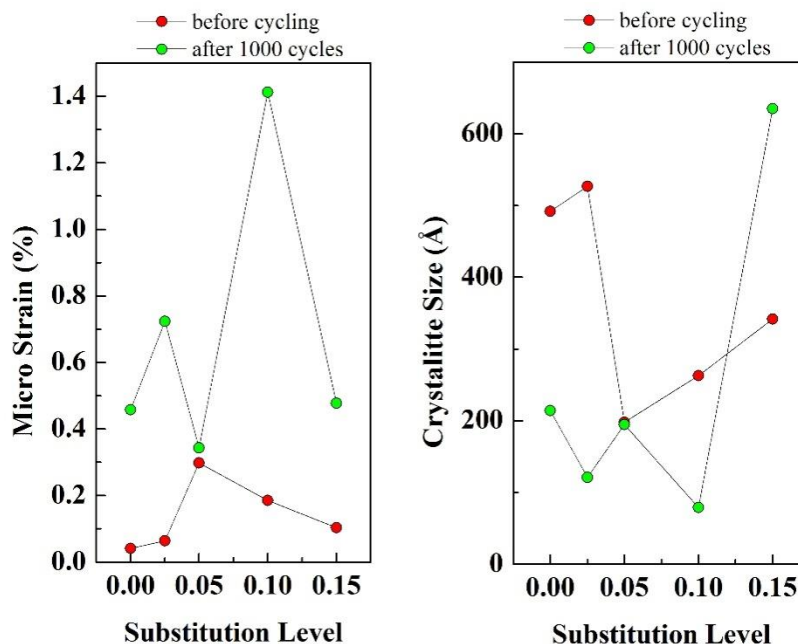


Figure 5.25. Microstrain and crystallite sizes of $\text{Na}_2\text{Ti}_{6-x}\text{V}_x\text{O}_{13}$ before and after 1000 cycles.

The XRD patterns of $\text{Na}_2\text{Ti}_{6-x}\text{V}_x\text{O}_{13}$ ($x = 0, 0.025, 0.05, 0.1, \text{ and } 0.15$) samples are given in Figure 5.22. The XRD pattern of the pure sample exhibits no impurity phases and is well matched with $\text{Na}_2\text{Ti}_6\text{O}_{13}$ phase. When the V content in the samples increases, an impurity phase of $\text{Na}_4\text{V}_2\text{O}_7$ is observed in the structure for $x \geq 0.025$, which is the lowest substitution level in this study. The main phase of the samples remains unchanged for all substitution levels.

Figure 5.23 shows the ex-situ XRD results of anode electrodes after 1000 cycles. The main phase of $\text{Na}_2\text{Ti}_6\text{O}_{13}$ does not change after 1000 cycles and $\text{Na}_4\text{V}_2\text{O}_7$ and $\text{Na}_2\text{Ti}_9\text{O}_{19}$ impurity phases are observed. Furthermore, the $\text{Na}_2\text{Ti}_9\text{O}_{19}$ impurity phase becomes dominant for $x = 0.025$ and 0.05 levels.

Figures 5.24 and 5.25 show the crystal parameters, volume changes, microstrain, and crystallite sizes. According to Rietveld refinements, $\text{Na}_2\text{Ti}_{6-x}\text{V}_x\text{O}_{13}$ ($x = 0, 0.025, 0.05, 0.1, \text{ and } 0.15$) samples have a monoclinic structure, and the a, b, and c parameters change with increasing V content as seen in the figure. According to volume expansion rates, the crystal volume decreases after $x = 0.25$ level of V substitution. According to

microstrain calculations, all V substituted samples show higher microstrain than that of the pure sample. However, crystallite sizes decrease for $x = 0.05$ and higher levels of V substitution. On the other hand, after 1000 cycles we did not obtain any regular increase or decrease in the microstrain and crystallite sizes of the electrodes. This situation can be explained by assuming that the V substitution causes instability of the samples.

5.3. Morphological Analysis

The morphological surface analysis of the as-prepared samples, and after 1000 cycles, were investigated with the SEM. Before SEM analysis, the samples were washed with dimethyl carbonate (DMC) in an Ar gas filled glove box. Cycling of the battery can cause changes of the surface morphology of the electrodes since the Li/Na intercalation and deintercalation in the grains causes deformation and re-organization of the structure. So, SEM is a powerful tool for determination of this kind of change in the electrodes.

Figure 5.26 shows SEM photographs of $\text{Li}_4\text{Ti}_{5-x}\text{V}_x\text{O}_{12}$ samples with different V contents. According to the surface morphology, unsubstituted and V substituted samples are formed in a granular structure and the increasing V content causes the tight connection of the grains. The grain sizes in the samples increase with increasing substitution levels. SEM images of the 1000-cycled electrodes show that the samples have a conducting problem compared to the as-prepared samples. The coating layer on the surface of the electrodes is formed by interactions of diffused ions in electrolyte and electrode; these cause deformation in the structure and the formation of new phases on the surface of the electrodes [solid electrolyte interface (SEI) layers] during Li/Na intercalation and deintercalation in the cell. So, an unwanted coating layer on the electrodes has non-conducting properties leading to worse SEM images than that of the as-prepared samples. Furthermore, the SEI layers also cause a deterioration of the battery performance. There is no SEM image for the $x = 0.15$ sample since no voltage was measured.

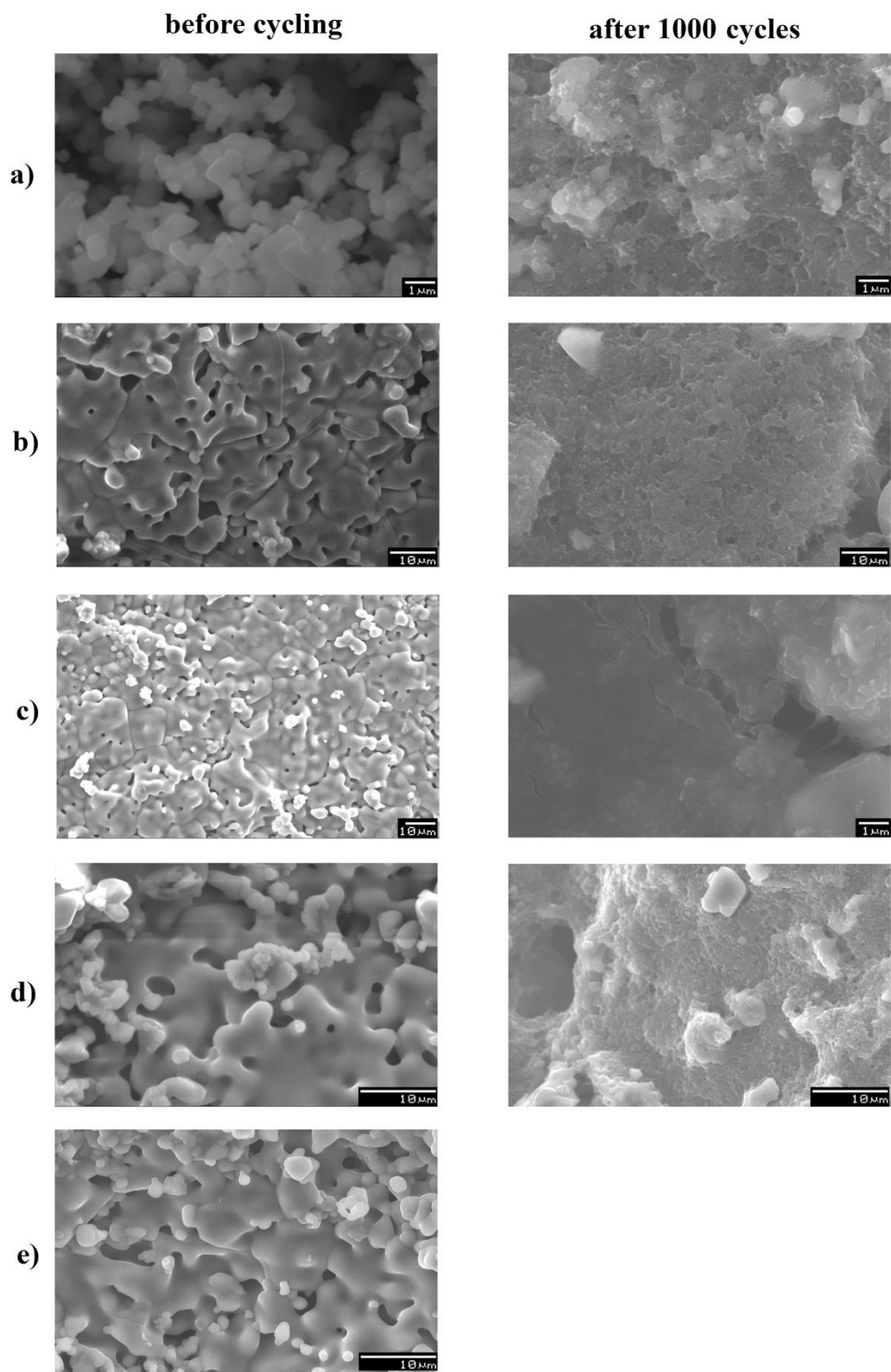


Figure 5.26. SEM photographs of $\text{Li}_4\text{Ti}_{5-x}\text{V}_x\text{O}_{12}$ samples. a) $x = 0$, b) $x = 0.025$, c) $x = 0.05$, d) $x = 0.1$, and e) $x = 0.15$.

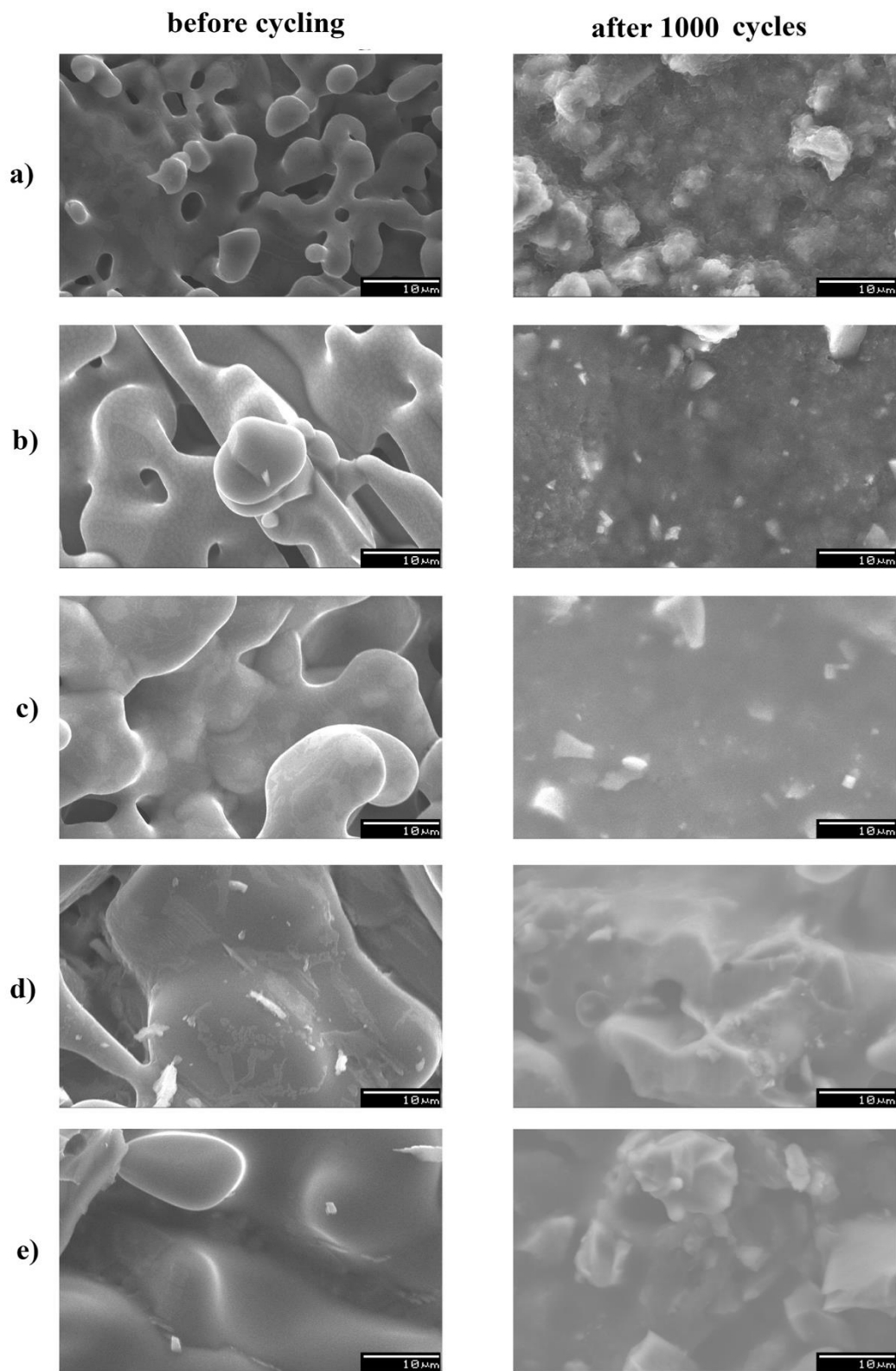


Figure 5.27. SEM photographs of $\text{Li}_2\text{Ti}_{3-x}\text{V}_x\text{O}_7$ samples. a) $x = 0$, b) $x = 0.025$, c) $x = 0.05$, d) $x = 0.1$, and e) $x = 0.15$.

Figure 5.27 shows SEM images of $\text{Li}_2\text{Ti}_{3-x}\text{V}_x\text{O}_7$ samples. The surface morphology of the unsubstituted sample shows an almost granular structure, as observed in $\text{Li}_4\text{Ti}_5\text{V}_x\text{O}_{12}$. When the V content increases, it is clear that the grain sizes in the samples increase and tightly connected grains are observed. Furthermore, the surface structure of the V unsubstituted samples exhibit partial formation of the melting phase. After 1000 cycles, the SEI layers are formed as a coating layer on the electrode surface as in $\text{Li}_4\text{Ti}_5\text{O}_{12}$. The clarity of the SEM images of the V substituted samples are worse than that of the as-prepared samples. It can be predicted that the change of the surface morphology after 1000 cycles of the battery cell is directly related to battery performance.

Figure 5.28 shows the SEM analysis of $\text{Li}_2\text{Ti}_{6-x}\text{V}_x\text{O}_{13}$ samples. According to the surface morphology of the sample, two types of grain formation are observed; one is a granular structure and the other is the base structure. The differences in the surface of the $\text{Li}_2\text{Ti}_6\text{O}_{13}$ pure samples may be due to the formation process of the $\text{Li}_2\text{Ti}_6\text{O}_{13}$ phase (ion-exchange process). It can be suggested that Na based impurity phases (the base materials for the ion-exchange mechanism of $\text{Li}_2\text{Ti}_6\text{O}_{13}$) can behave as nucleation centres for phase formation. As seen in the surface analysis of the V substituted samples, nanowire formations are observed. As stated above, the granular type grains have higher surface energy than the base type grains due to higher surface area. The growth point of the nanowire should be formed in this metastable region of the surface. It is clear that V doping in $\text{Li}_2\text{Ti}_6\text{O}_{13}$ causes the formation of nanowires which can play a catalytic role for nanorod formation, in that it can decrease the required energy of formation and accelerate nanorod growth. Another possible scenario for the formation of nanorods may be the Na-rich composition. As seen in the study of $\text{Na}_{0.44}\text{MnO}_2$ and $\text{Na}_2\text{Ti}_6\text{O}_{13}$ phases, the Na-rich phase in the structure causes nanowire formation [123, 144]. However, the nanowires started to decompose for $x \geq 0.1$. This may be due to the impurity phases in the structure as seen in the XRD section: the impurity phases are dominant after $x = 0.1$.

After 1000 cycles, we obtained battery performance from only the pure sample. The batteries which were fabricated using V substituted materials didn't show any voltage and cycling properties. So, only the pure sample surface change after 1000 cycles is presented. It can be seen from the surface of the electrode that deformation of the grains is observed and it is related to the deterioration of cycling properties of the cell.

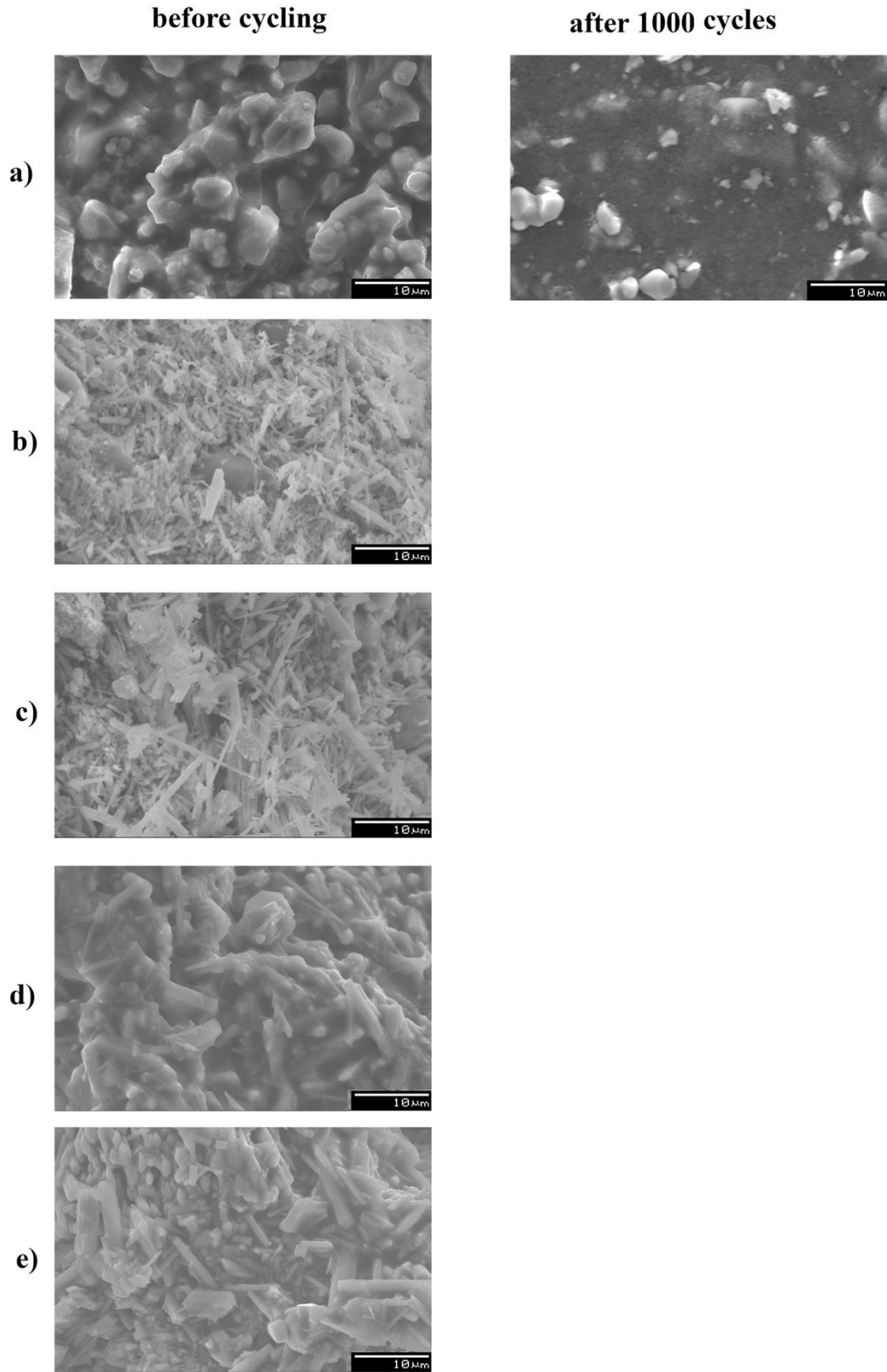


Figure 5.28. SEM photographs of $\text{Li}_2\text{Ti}_{6-x}\text{V}_x\text{O}_{13}$ samples. a) $x = 0$, b) $x = 0.025$, c) $x = 0.05$, d) $x = 0.1$, and e) $x = 0.15$.

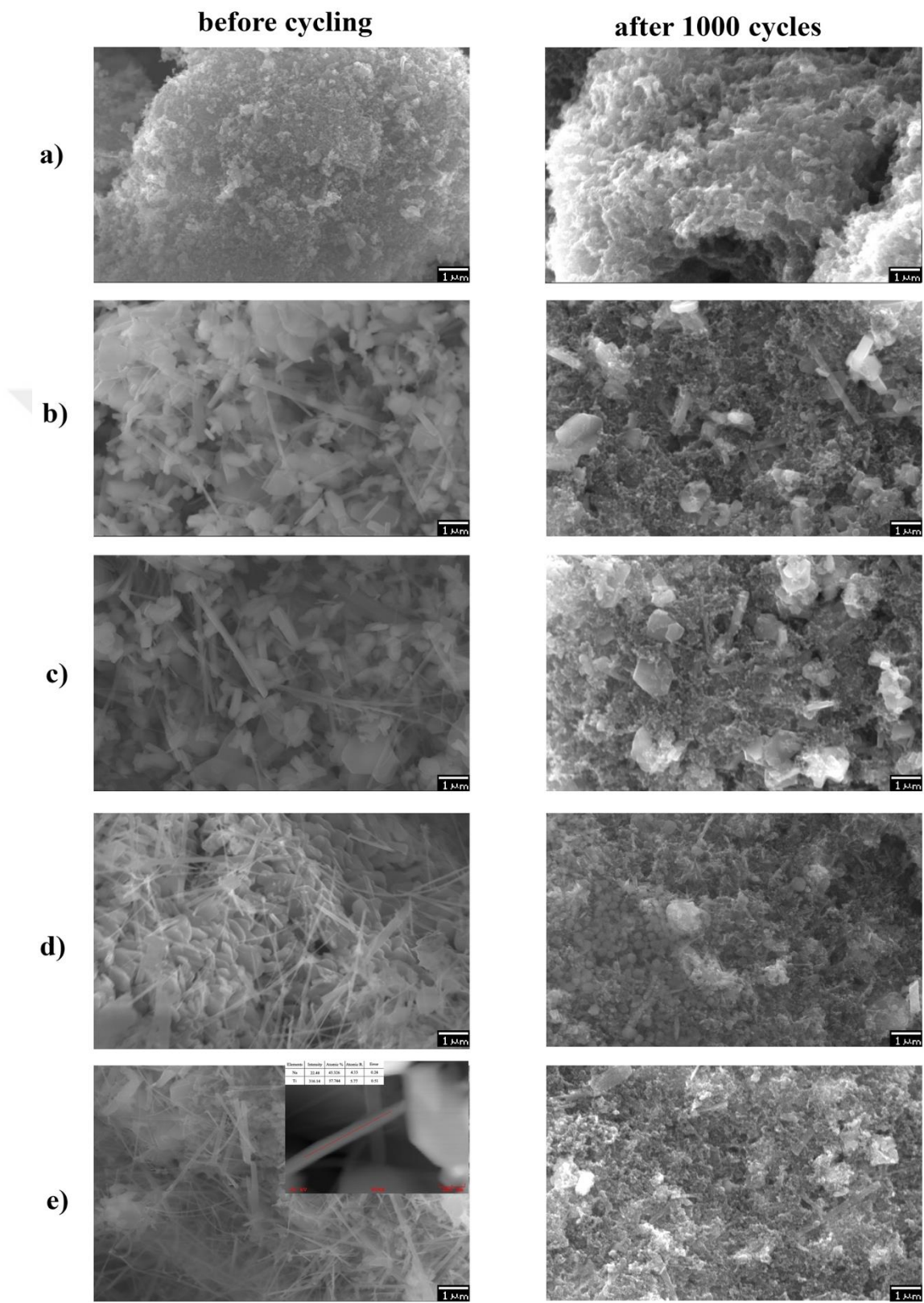


Figure 5.29. SEM photographs of $\text{Na}_4\text{Ti}_{5-x}\text{V}_x\text{O}_{12}$ samples. a) $x = 0$, b) $x = 0.025$, c) $x = 0.05$, d) $x = 0.1$, and e) $x = 0.15$.

Figure 5.29 shows SEM images of $\text{Na}_4\text{Ti}_{5-x}\text{V}_x\text{O}_{12}$ samples. The pure samples have plate-like and rod-like grains and the grains are randomly bound to the others. When the V ions are substituted into samples, rod-like grains start to grow in one direction for the formation of the nanowires. The plate-like grains are tightly connected to others. As stated before, The V ions in the structure play a catalytic role for the formation of the nanowires. The numbers of nanowires on the surface increase with increasing V content in the samples.

There is more SEI formation on the $\text{Na}_4\text{Ti}_5\text{O}_{12}$ electrode after 1000 cycles. On the other hand, SEI layers decrease with increasing V compared to pure $\text{Na}_4\text{Ti}_5\text{O}_{12}$ electrodes. Figures 5.29 b) and c) show the $x = 0.025$ and $x = 0.05$ substitution levels. At these levels, the SEI layers become lower and thinner than pure samples. In contrast, for $x = 0.1$ and $x = 0.15$ the SEI layers get a little thicker than for $x = 0.025$ and $x = 0.05$ substitution levels.

Figure 5.29 also shows the structural changes in the nanorods after 1000 cycles. Some parts of the nanowires disappear and new small point-type grains are observed on the bigger ones. We can conclude that the point type grain formation is one of the reasons for the decrease in battery performance.

Figure 5.30 shows SEM photographs of $\text{Na}_2\text{Ti}_{3-x}\text{V}_x\text{O}_7$ samples. The rod-like and plate-like grains are observed for the unsubstituted sample, rod-like grains grow in the form of nanowires, and plate-like grains disappear with increasing V content. According to these SEM photos and the $\text{Na}_4\text{Ti}_{5-x}\text{V}_x\text{O}_{12}$ morphological analysis, similar results can be expected for $\text{Na}_2\text{Ti}_{3-x}\text{V}_x\text{O}_7$ samples. Nanorods started to form on the material surface with V substitution. A random orientation of the nanowires is observed with a porous structure. The number of nanowires and their thicknesses increase with increasing V content. According to EDX analysis, V ions are not diffused to the structure of the nanowire, supporting the idea of a catalytic role for V ions in the structure. After 1000 cycles the surface morphology of the electrodes shows point-like grain formation on the nanowires. We can conclude that intercalation and deintercalation of Na ions formed the clusters as seen in the figure. $\text{Na}_2\text{Ti}_{3-x}\text{V}_x\text{O}_7$ nanorods show less decomposition compared to $\text{Na}_4\text{Ti}_{5-x}\text{V}_x\text{O}_{12}$ phases after 1000 cycles, since the batteries fabricated with $\text{Na}_2\text{Ti}_{3-x}\text{V}_x\text{O}_7$ nanorods are more stable.

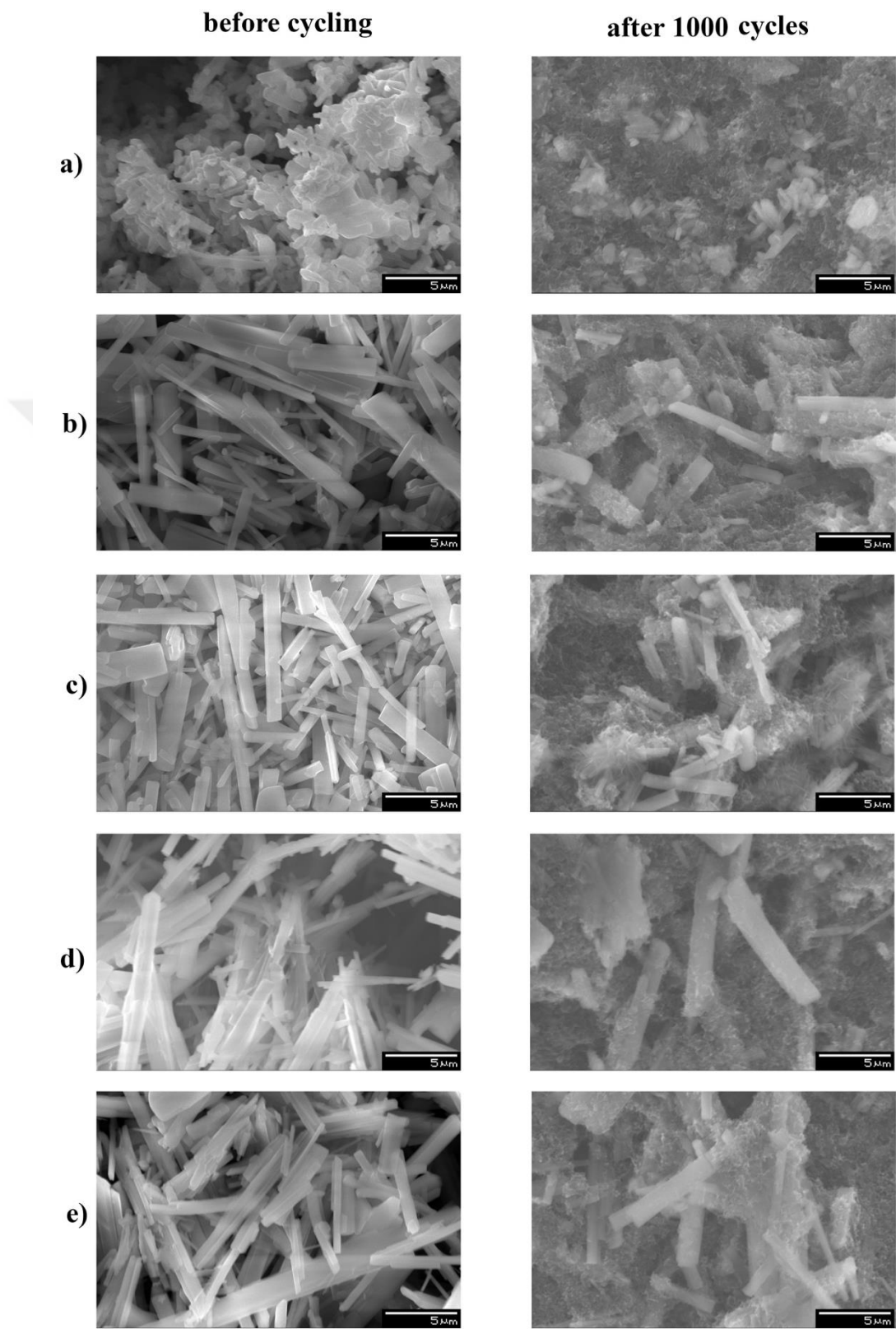


Figure 5.30. SEM photographs of $\text{Na}_2\text{Ti}_{3-x}\text{V}_x\text{O}_7$ samples. a) $x = 0$, b) $x = 0.025$, c) $x = 0.05$, d) $x = 0.1$, and e) $x = 0.15$.

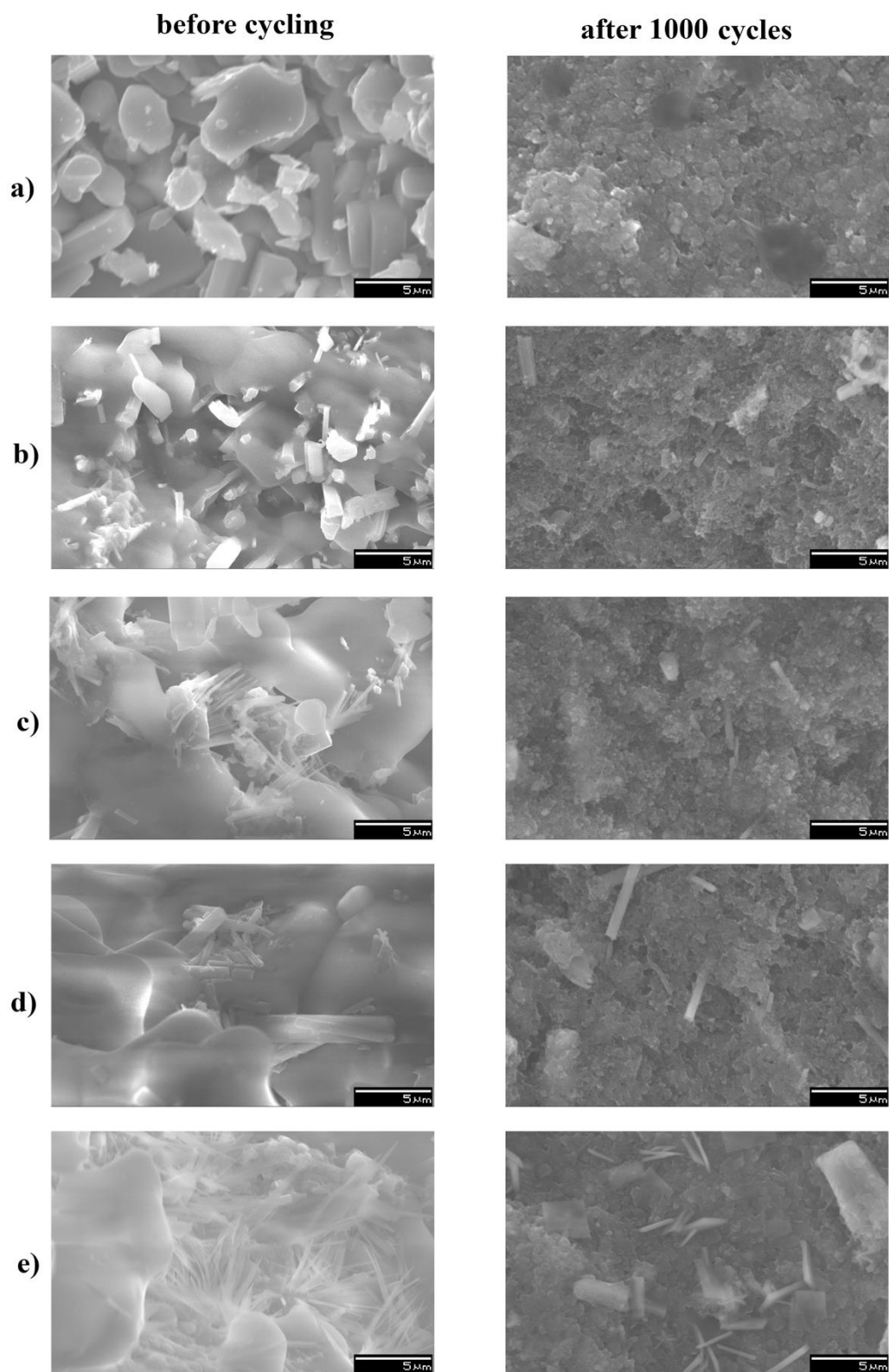


Figure 5.31. SEM photographs of $\text{Na}_2\text{Ti}_{6-x}\text{V}_x\text{O}_{13}$ samples. a) $x = 0$, b) $x = 0.025$, c) $x = 0.05$, d) $x = 0.1$, and e) $x = 0.15$.

Figure 5.31 shows SEM photographs of the $\text{Na}_2\text{Ti}_{6-x}\text{V}_x\text{O}_{13}$ samples. We observe that the pure samples have plate-like and rod-like grains, and the plate-like grains are tightly bound to each other. When V ions are substituted, the rod-like grains disappear and the plate-like grains are combined with each other for the formation of bigger grains than observed in the pure sample. So, the grain sizes increase with increasing substitution levels. On the other hand, we rarely observe the formation of nanowires from grains on the surface. The numbers of nanowires are less than observed in other samples. After 1000 cycles, the SEI layers and point-like grain formation is observed for all samples. The deformation of the grains and the formation of the SEI layer in $\text{Na}_2\text{Ti}_{6-x}\text{V}_x\text{O}_{13}$ electrodes can be related to the decrease of the battery performance of the cell.

5.4. Spectral Analysis

Raman spectroscopy is a powerful method to investigate the change of the vibrational modes of the bonds in the electrode material during charge, discharge, and V doping. The structural stability of the sample which is used as an electrode in the battery cell has a crucial influence on the battery lifetime. For this purpose, the pure and 1000 cycled samples were investigated.

The Raman spectra of the $\text{Li}_4\text{Ti}_{5-x}\text{V}_x\text{O}_{12}$ powders with $x = 0-0.15$ are shown in Figure 5.32. Six Raman active modes are observed in the spectra and V doping does not change any vibrational modes. It is predicted that the vibrational modes belong to V bonding is below the resolution limit of the device, since the doping levels in the samples are as low as $x = 0-0.15$. The vibrational modes of $\text{Li}_4\text{Ti}_5\text{O}_{12}$ samples are given in Table 5.1. Half of the Raman active modes are due to Li-O vibrations and the other parts are due to Ti-O. Although a small peak shift is observed in the spectra when V ions are substituted, as seen in the figure, the main structure of the Raman peaks does not change by the substitutions.

Figure 5.33 shows the ex-situ Raman spectra after 1000 cycles of the battery cell. It is clear that the intensity and the resolution of the Raman spectra are worse than that of the as-prepared powders. The ion insertion-exertion process during charge-discharge causes a change in the unit cell, and the structure through which the ions are extracted in

the lattice induce the change in the modes. The deformation of the vibrational modes directly affects battery performance. According to the ex-situ XRD results, there is a new type of impurity phase formation for $x = 0.15$. The peaks at 155 and 195 cm^{-1} are the different modes of the O-Ti-O bonds which may be due to the impurity phases [12].

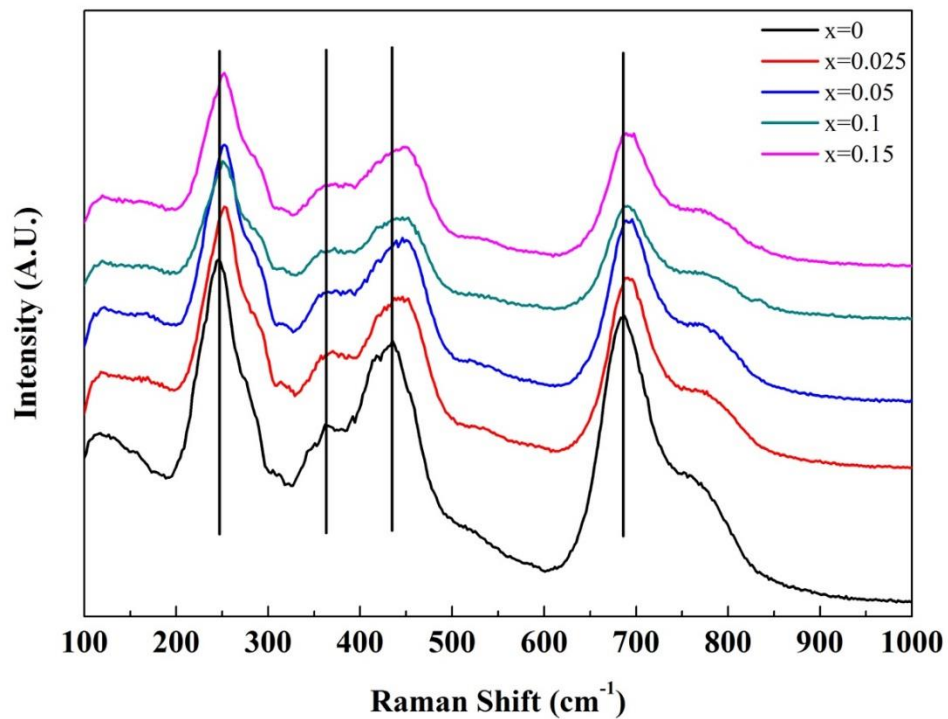


Figure 5.32. Raman analysis of $\text{Li}_4\text{Ti}_{5-x}\text{V}_x\text{O}_{12}$ powder samples.

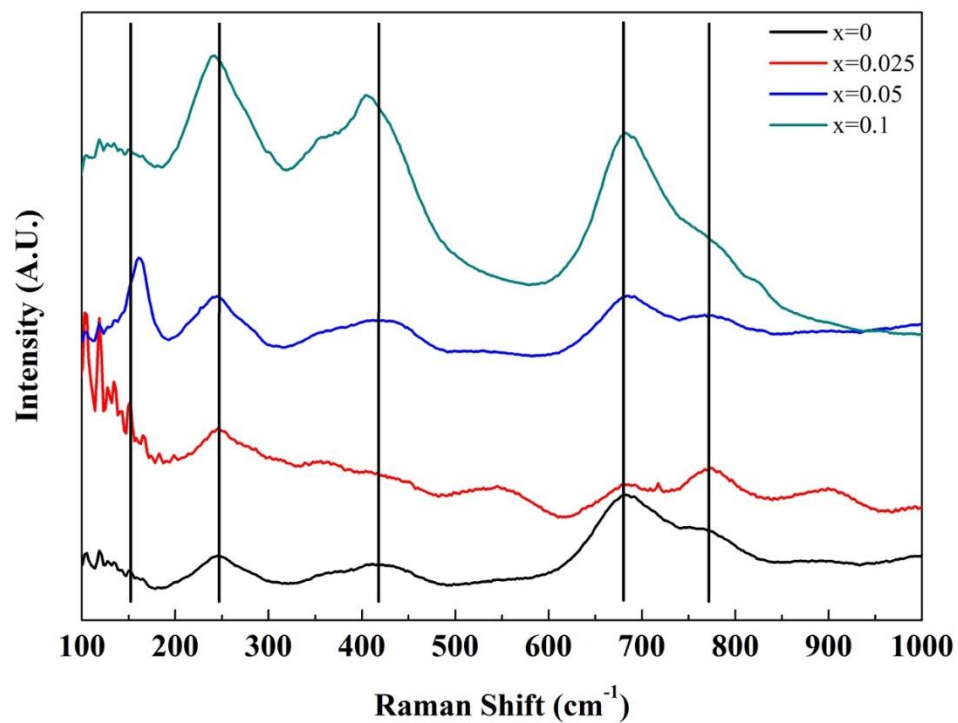


Figure 5.33. Ex-situ Raman analysis of $\text{Li}_4\text{Ti}_{5-x}\text{V}_x\text{O}_{12}$ electrodes after 1000 cycles.

Table 5.1. Raman peak definitions for the $\text{Li}_4\text{Ti}_5\text{O}_{12}$ system.

<i>Peak (nm)</i>	<i>Bonds</i>	<i>Reference</i>
120	O-Ti-O	[132]
244	O-Li-O	[132]
367	Li-O in LiO_4	[133]
437	Li-O in LiO_6	[133]
686	Ti-O in TiO_2	[134]
770	Ti-O in TiO_2	[134]

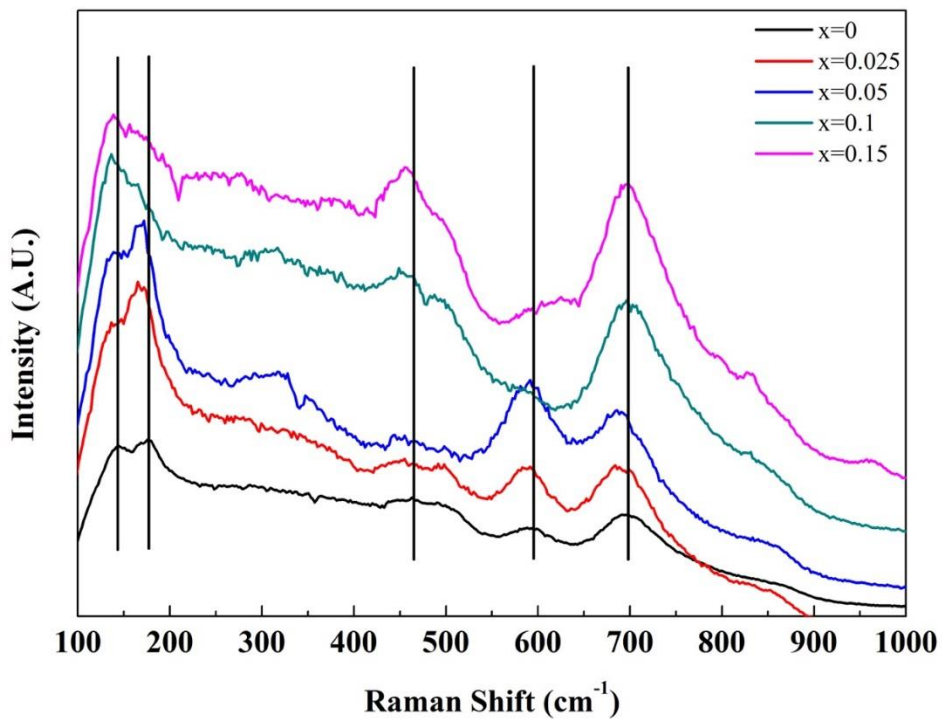


Figure 5.34. Raman analysis of $\text{Li}_2\text{Ti}_{3-x}\text{V}_x\text{O}_7$ powder samples.

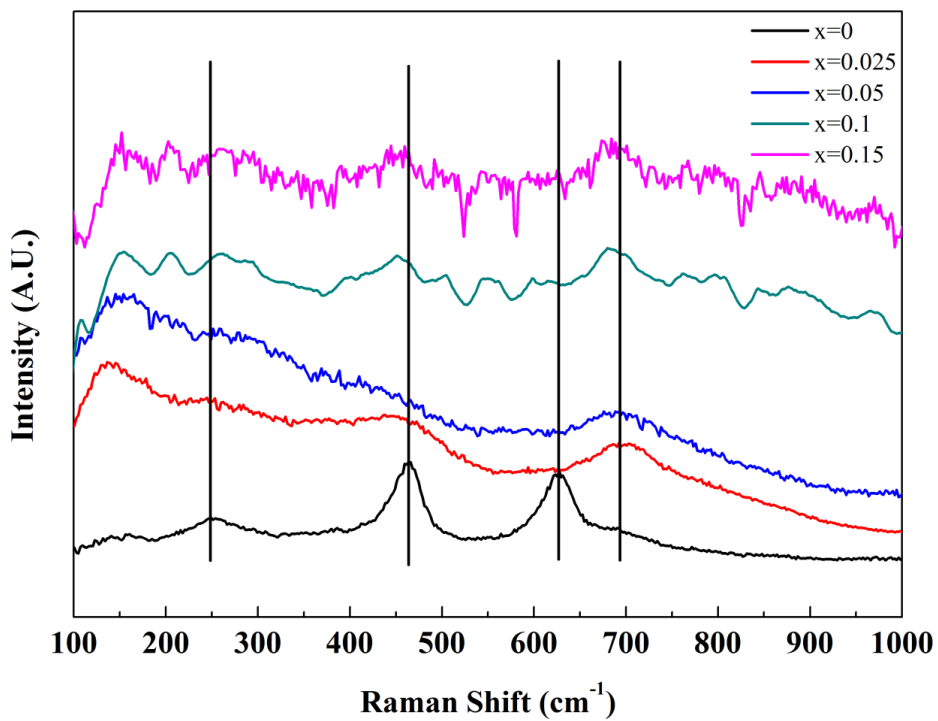


Figure 5.35. Ex-situ Raman analysis of $\text{Li}_2\text{Ti}_{3-x}\text{V}_x\text{O}_7$ electrodes after 1000 cycles.

Table 5.2. Raman peak definitions of the $\text{Li}_2\text{Ti}_3\text{O}_7$ system.

<i>Peak (nm)</i>	<i>Bonds</i>	<i>Reference</i>
125	O-Ti-O	[132]
174	O-Li-O	[132]
466	Li-O in LiO_6	[133]
595	Li-O in LiO_6	[133]
696	Ti-O in TiO_2	[134]

Raman spectra of $\text{Li}_2\text{Ti}_{3-x}\text{V}_x\text{O}_7$ samples are given in Figure 5.34 and the peak wavelengths are presented in Table 5.2. Five different Raman active modes are observed in the spectra. The increasing V doping level causes a fluctuation of the Raman peaks around the peak value of the unsubstituted samples since the impurity phases (as seen in the XRD section) cause a change in the vibration modes.

Figure 5.35 shows the ex-situ Raman spectra of the samples after 1000 cycles of the battery cell. It is easily seen from the figure that the vibration modes change drastically with cycling of the cell. The vibrations decrease or disappear because ion diffusion causes a change of the unit cell and/or the formation of new unwanted phases in the structure.

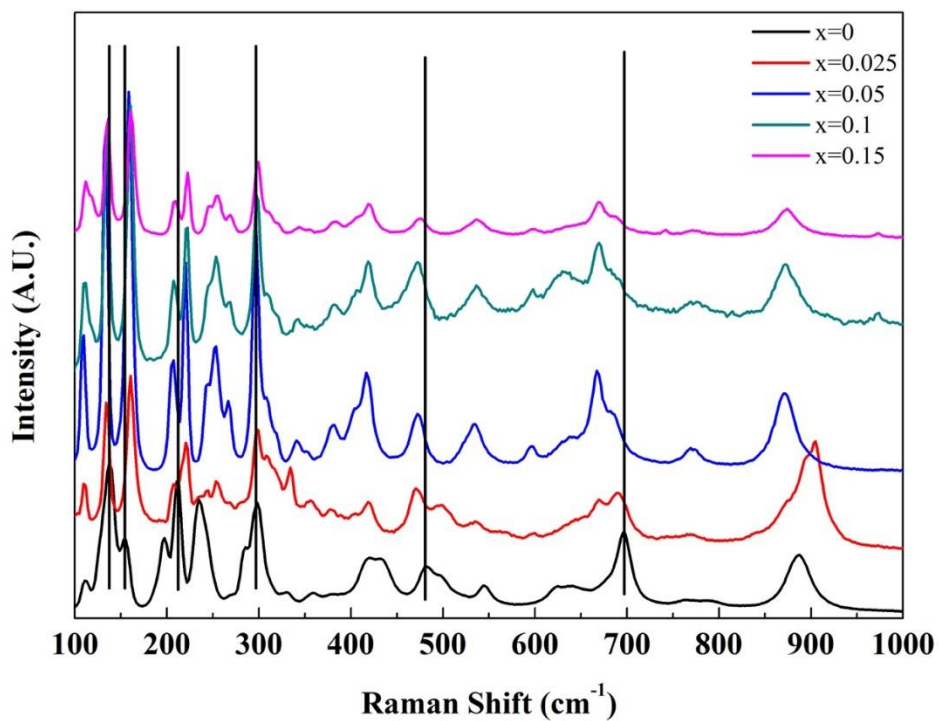


Figure 5.36. Raman analysis of $\text{Li}_2\text{Ti}_{6-x}\text{V}_x\text{O}_{13}$ powder samples.

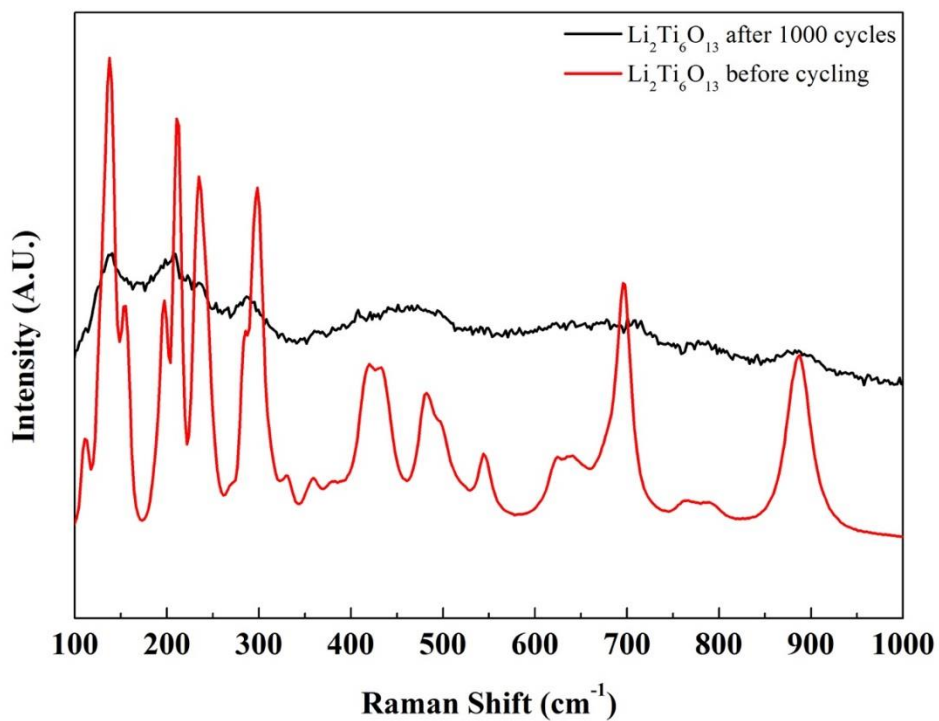


Figure 5.37. Ex-situ Raman analysis of $\text{Li}_2\text{Ti}_{6-x}\text{V}_x\text{O}_{13}$ electrodes after 1000 cycles.

Table 5.3. Raman peaks assignments for the $\text{Li}_2\text{Ti}_6\text{O}_{13}$ system

<i>Peak (nm)</i>	<i>Bounds</i>	<i>reference</i>
125	O-Ti-O	[132]
138	O-Ti-O	[132]
205	O-Li-O	[132]
241	Li-O-Ti	[135, 136]
315	Li-O-Ti	[135, 136]
426	Ti-O-Ti	[137]
490	Ti-O in TiO_2	[138]
643	Ti-O in TiO_2	[134]
692	Ti-O in TiO_2	[139], [142]
892	Ti-O in TiO_2	[134]

Figure 5.36 shows that $\text{Li}_2\text{Ti}_{6-x}\text{V}_x\text{O}_{13}$ powder has 10 different Raman active modes, the details are listed in Table 5.3. V doping in the $\text{Li}_2\text{Ti}_6\text{O}_{13}$ phase changes the Raman active modes so that some of the Raman peaks are shifted, some disappear, and some new peaks are observed. Those peak shifts and intensity increases originate from bond expansion with vanadium substitutions.

Figure 5.37 shows the ex-situ Raman spectra of the as-prepared powder and electrodes after 1000 cycles. The resolution and intensity of the peaks decrease due to the deformation of the structure during the ion insertion-extraction process of the battery cell. Because the V substituted samples didn't show battery properties, we didn't measure 1000 cycle data for them.

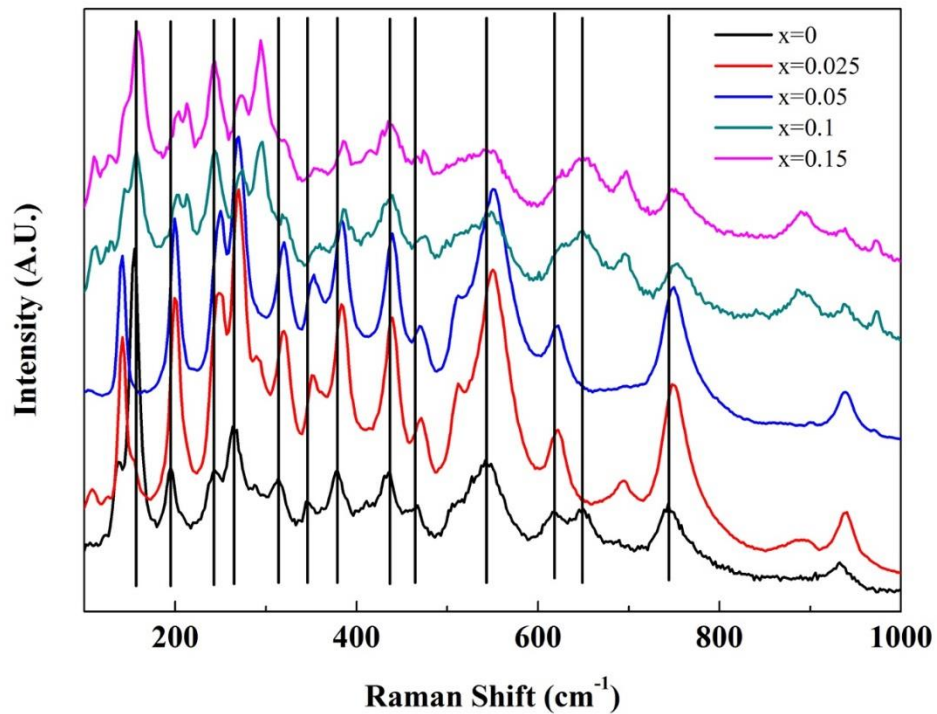


Figure 5.38. Raman analysis of $\text{Na}_4\text{Ti}_{5-x}\text{V}_x\text{O}_{12}$ powder samples.

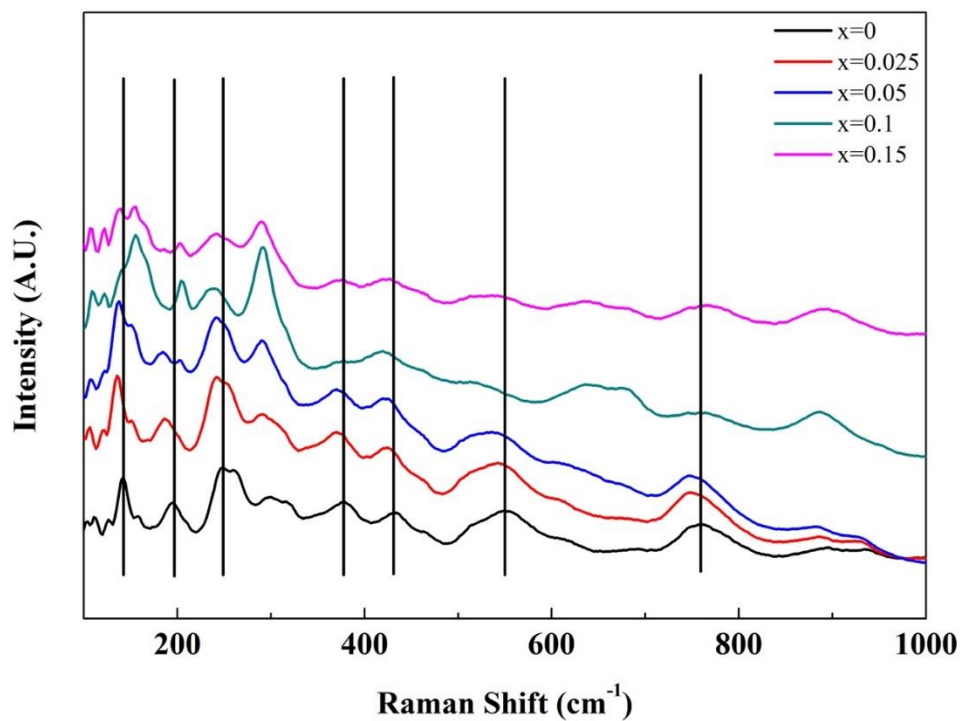


Figure 5.39. Ex-situ Raman analysis of $\text{Na}_4\text{Ti}_{5-x}\text{V}_x\text{O}_{12}$ electrodes after 1000 cycles.

Table 5.4. Raman peak definitions of the Na₄Ti₅O₁₂ system.

<i>Peak (nm)</i>	<i>Bounds</i>	<i>reference</i>
157	O-Ti-O	[138]
196	O-Ti-O	[138]
266	Na-O-Ti	[139]
315	Na-O-Ti	[136]
379	Ti-O-Ti	[137]
415	Ti-O-Ti	[137]
545	Ti-O in TiO ₂	[138]
615	Ti-O-Ti in TiO ₆	[139–141]
650	Ti-O-Na in NaTiO ₂	[140]
696	Ti-O in TiO ₂	[134]
745	Ti-O in TiO ₂	[139], [142]
935	Short Ti-O bond vibration involving non-bridging oxygen coordinated with sodium ions	[143]

Raman spectra of Na₄Ti_{5-x}V_xO₁₂ samples shown in Figure 5.38 and the Raman active modes are presented in Table 5.4. 12 different active modes are observed in the Raman spectra of the pure sample. When Na₄Ti₅O₁₂ is substituted with V a small peak shift is observed in the spectra. Theoretically, the peak shifts originate from the bond expansions as a result of V substitutions. In addition to this, some other significant changes are observed in the spectra depending on V substitutions. The first change at 615 cm⁻¹, which belongs to Ti-O-Ti turning, shifts to ~630 cm⁻¹, which belongs to a singular V-O-V mode. The peak at 650 cm⁻¹, which belongs to Ti-O-Na, shifts to ~700 cm⁻¹, which belongs to V-O-Na bonds vibrations. The second significant change for V substitutions of x = 0.025–0.05 include the new peak at ~860 cm⁻¹ which belongs to anti-symmetric O-V-O bond vibrations. Another significant change for x = 0.1 and x = 0.15 samples is that the peak at 142 cm⁻¹ (due to the V-O-V bonds) shifts to 157 cm⁻¹ and is due to the O-Ti-O bonds. The Raman peak observed at 196 cm⁻¹ for the samples with x = 0.1–0.15 is due to V-O-V bonds and O-Ti-O bonds [145].

Figure 5.39 shows the ex-situ Raman spectra of the electrodes after 1000 cycles of the cell. A deformation is evident at the O-Na-(V-Ti) bonds due to insertion-exertion and formation of impurity phases in the sample.

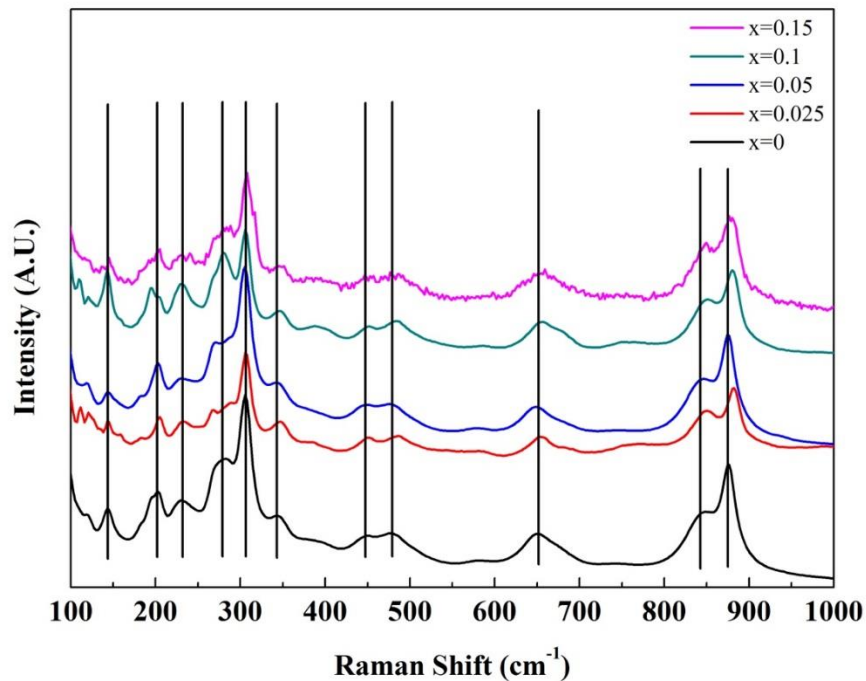


Figure 5.40. Raman analysis of $\text{Na}_2\text{Ti}_{3-x}\text{V}_x\text{O}_7$ powder samples.

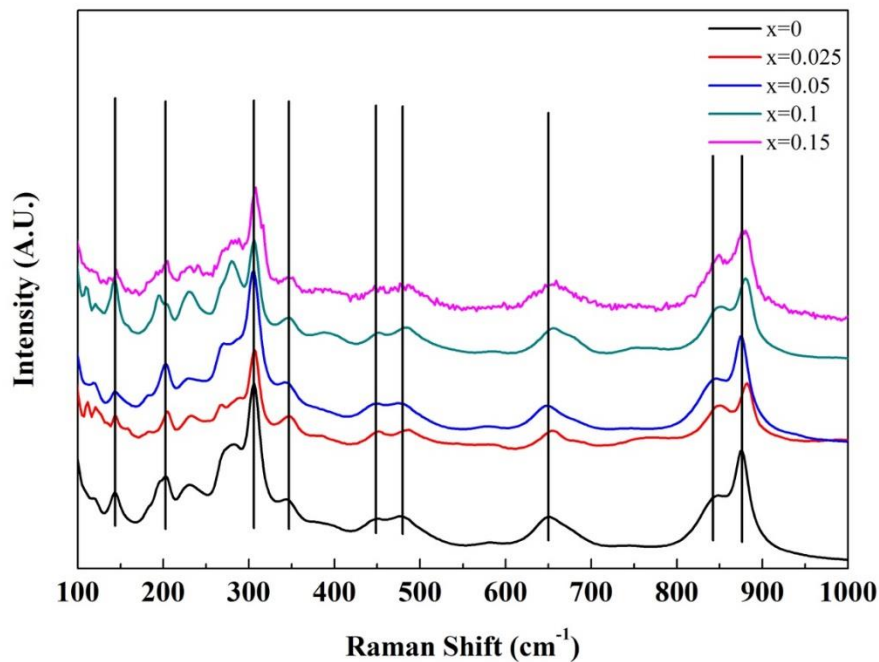


Figure 5.41. Ex-situ Raman analysis of $\text{Na}_2\text{Ti}_{3-x}\text{V}_x\text{O}_7$ electrodes after 1000 cycles.

Table 5.5. Raman peak definitions for the Na₂Ti₃O₇ system

<i>Peak (nm)</i>	<i>Bonds</i>	<i>Reference</i>
155	O-Ti-O	[138]
216	O-Ti-O	[138]
234	Na-O-Ti	[139]
274	Ti-O-Na	[134]
311	Na-O-Ti	[136]
359	Ti-O-Ti	[137]
394	Ti-O-Ti	[137]
459	Ti-O in TiO ₂	[138]
503	Ti-O in TiO ₂	[138]
603	Ti-O-Ti	[136]
668	Ti-O-Ti stretch in edge-shared TiO ₆	[136]
700	Ti-O-Ti stretch in edge-shared TiO ₆	[136]
757	Na-O-Ti	[136]
859	Short Na-O & Ti-O bonds vibration	[136], [143]
896	Short Na-O & Ti-O bonds vibration	[136], [143]

Raman spectra of Na₂Ti_{3-x}V_xO₇ samples are given in Figure 5.40 and the Raman modes of the obtained peaks are given in Table 5.5. When the samples are substituted with vanadium, no new peaks are observed in the spectra. A small peak shift is determined for the V substituted samples and shifts originate from bond expansion upon V substitution.

Figure 5.41 shows the ex-situ Raman spectra of the electrode materials after 1000 cycles of the cell. The intensity of the peaks decrease less when compared to as-prepared samples. It is an evidence for the stronger structural stability of the Na₂Ti_{3-x}V_xO₇ phase compared to that of the other Ti based electrodes.

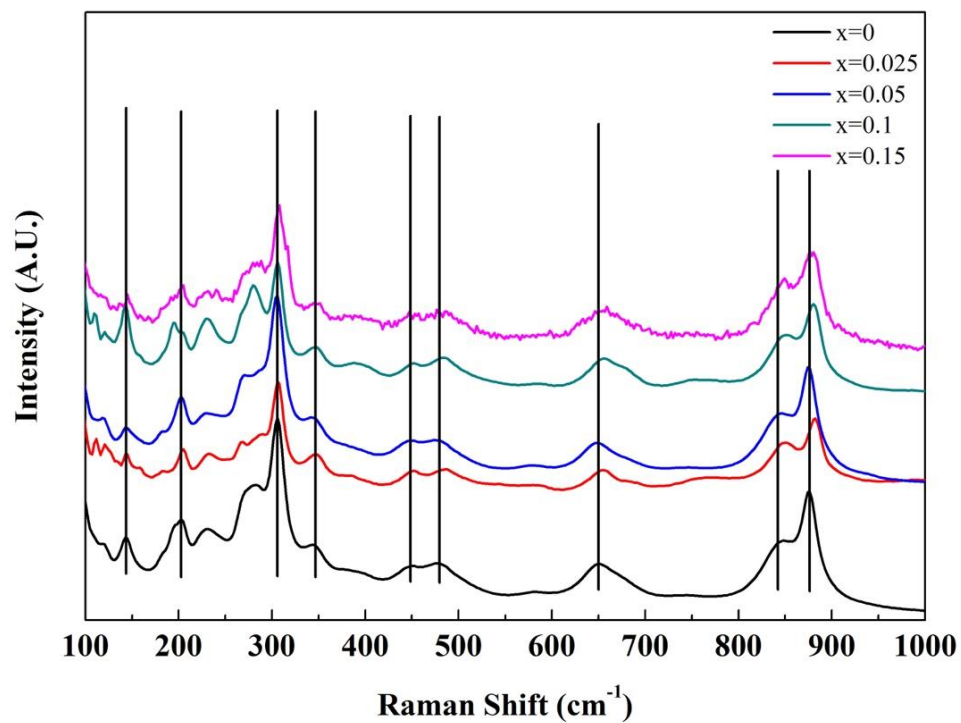


Figure 5.42. Raman analysis of $\text{Na}_2\text{Ti}_{6-x}\text{V}_x\text{O}_{13}$ powder samples.

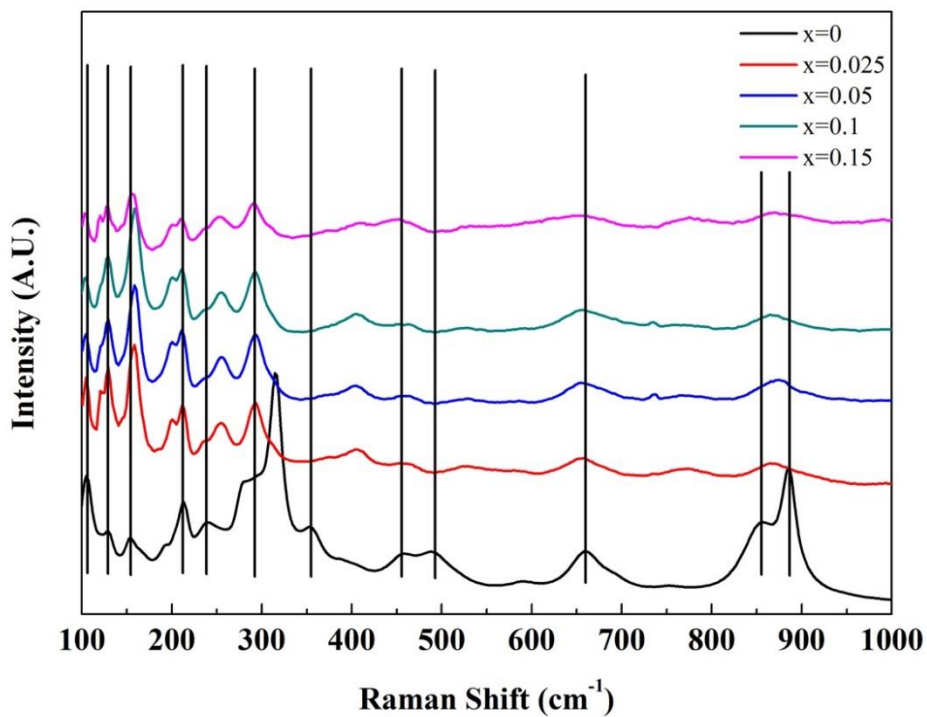


Figure 5.43. Ex-situ Raman analysis of $\text{Na}_2\text{Ti}_{6-x}\text{V}_x\text{O}_{13}$ electrodes after 1000 cycles.

Table 5.6. Raman peak definitions for the $\text{Na}_2\text{Ti}_6\text{O}_{13}$ system.

<i>Peak (nm)</i>	<i>Bonds</i>	<i>Reference</i>
155	O-Ti-O	[138]
195	O-Ti-O	[138]
205	Na-O-Ti	[139]
239	Ti-O-Na	[136]
284	Na-O-Ti	[136]
354	Ti-O-Ti	[137]
369	Ti-O-Ti	[137]
414	Ti-O in TiO_2	[138]
494	Ti-O in TiO_2	[138]
618	Ti-O-Ti	[136]
693	Ti-O-Ti stretch in edge-shared TiO_6	[136]
758	Short Na-O & Ti-O bonds vibration	[136], [143]
798	Na-O-Ti	[136]
888	Ti-O-Ti stretch in edge-shared TiO_6	[136]

Raman spectra of unprocessed $\text{Na}_2\text{Ti}_{6-x}\text{V}_x\text{O}_{13}$ samples are given in Figure 5.42 and the observed peaks are presented in Table 5.6. There are 14 different peaks in the Raman spectra of the pure sample; nine of them are due to Ti-O vibration modes and the remaining five are due to Na-O-Ti vibrations in the samples. When V ions are substituted into the sample, the intensity of the peaks change and a peak shift is observed. The peak at 618 cm^{-1} (due to Ti-O-Ti) shifts to $\sim 630\text{ cm}^{-1}$ (due to singular V-O-V bonds); the peak at 650 cm^{-1} , which is related to Ti-O-Na vibrations, shifts to $\sim 700\text{ cm}^{-1}$ and is caused by V-O-Na bonds vibrations.

Figure 5.43 shows the ex-situ Raman spectra of the electrodes after 1000 cycles. A decrease in the peak intensities is observed due to the deformation of the bond structure of Ti-O-Ti, V-O-V, and O-Na-(V-Ti). The deformation is related to the ion insertion-exertion process during charge-discharge, and to impurities in the structure.

5.5. Resistivity Analysis

The resistivity of the battery cell is related to its lifetime and performance since non-conducting electrodes cannot perform good intercalation and deintercalation during charge-discharge of the cell. Although the electrode materials have high resistivity (above 1 k Ω /cm), the conductivity of the electrodes is increased by the addition of materials such as super carbon (SC), carbon black (CB) or carbon based conducting materials. The basic principle of the battery is electron and ion transfer during the charge and discharge processes. Movement of the charged particles strongly depend on the electric field applied between the two electrodes of the cell. Therefore, the conducting properties of the electrode should be investigated as part of the cell characterization process.

The resistivity of the as-prepared samples of $\text{Li}_4\text{Ti}_{5-x}\text{V}_x\text{O}_{12}$ are given in Table 5.7; the materials have high resistivity values and when V is added, the resistivity of the samples increase. Ti ions in $\text{Li}_4\text{Ti}_5\text{O}_{12}$ have a valence state of 4+ and the valence state of V ions is known as V^{5+} . We predicted that V^{5+} doping in p-type $\text{Li}_4\text{Ti}_5\text{O}_{12}$ can cause an increase of the resistivity due to the decrease in the number of the charge carriers.

Table 5.7. Resistivity measurement results for $\text{Li}_4\text{Ti}_{5-x}\text{V}_x\text{O}_{12}$.

Phase	Active Material ($\Omega\cdot\text{cm}$)	Electrode		
		Before cycling ($\Omega\cdot\text{cm}$)	After 1 cycle ($\Omega\cdot\text{cm}$)	After 1000 cycles ($\Omega\cdot\text{cm}$)
$\text{Li}_4\text{Ti}_5\text{O}_{12}$	1.8×10^4	0.55	0.860	2.872
$x = 0.025$	1.8×10^4	0.57	0.882	2.981
$x = 0.05$	1.805×10^4	0.63	0.93	3.016
$x = 0.1$	1.807×10^4	0.82	0.98	3.189
$x = 0.15$	2.23×10^4	1.35	-----	-----

We measured the resistivity of the electrodes after a certain cycling number in order to investigate the change in the conducting mechanism of the electrodes. The battery cells were taken apart to get the electrodes in the glove box. We found that increasing the cycle number causes an increase in the resistivity of the electrodes. Similar results are also

obtained for the V substituted samples. The increase in resistivity can be explained as being due to SEI layers and impurity phase formation during the charge-discharge process.

Table 5.8 shows the results of resistivity measurements for the $\text{Li}_2\text{Ti}_{3-x}\text{V}_x\text{O}_7$ system. According to these results, the resistivity value of pure $\text{Li}_2\text{Ti}_3\text{O}_7$ is lower than that of the $\text{Li}_4\text{Ti}_5\text{O}_{12}$ phase. It can be regarded as a characteristic feature of two different materials the same as band structure, carrier density, etc. V substitutions cause an increase in the resistivity value and we observed that the resistivity values for $x \geq 0.05$ are almost the same. The electrodes which were fabricated using CB, PVDF, and active materials have similar values compared to the $\text{Li}_4\text{Ti}_5\text{O}_{12}$ phase. Cycling causes an increase in resistivity. Increasing resistivity in the cell leads to the emergence of a heating problem. As stated before, SEI layers and impurity phases, which form during cycling of the battery, are the main reasons for the resistivity increase.

Table 5.8. Resistivity measurements for $\text{Li}_2\text{Ti}_{3-x}\text{V}_x\text{O}_7$.

Phase	Active Material ($\Omega\cdot\text{cm}$)	Electrode		
		Before cycling ($\Omega\cdot\text{cm}$)	After 1 cycle ($\Omega\cdot\text{cm}$)	After 1000 cycles ($\Omega\cdot\text{cm}$)
$\text{Li}_2\text{Ti}_3\text{O}_7$	3.4×10^3	0.484	0.415	1.862
$x = 0.025$	3.52×10^3	0.567	0.583	2.915
$x = 0.05$	3.43×10^3	0.503	0.521	2.154
$x = 0.1$	3.42×10^3	0.492	0.507	2.273
$x = 0.15$	3.42×10^3	0.497	0.518	2.334

Table 5.9 shows the resistivity measurements of the $\text{Li}_2\text{Ti}_{6-x}\text{V}_x\text{O}_{13}$ system. The resistivity of the pure sample is the highest among the Li-Ti-O anode materials in this study. The electrodes before cycling have a resistivity of $0.63 \Omega\cdot\text{cm}$ and it increases with increasing V content. The obtained resistivity value of the V substituted electrodes before cycling is above $4.7 \Omega\cdot\text{cm}$, but no battery properties are obtained. We suggest that battery features are prevented by high resistivity of the electrodes above $0.7 \Omega\cdot\text{cm}$.

Table 5.9. Resistivity measurements for $\text{Li}_2\text{Ti}_{6-x}\text{V}_x\text{O}_{13}$.

Phase	Active Material ($\Omega\cdot\text{cm}$)	Electrode		
		Before cycling ($\Omega\cdot\text{cm}$)	After 1 cycle ($\Omega\cdot\text{cm}$)	After 1000 cycles ($\Omega\cdot\text{cm}$)
$\text{Li}_2\text{Ti}_6\text{O}_{13}$	2.6×10^4	0,630	0,580	3,652
$x = 0.025$	3.23×10^5	4.721	-----	-----
$x = 0.05$	3.8×10^5	4.957	-----	-----
$x = 0.1$	$3.82.6 \times 10^5$	5.678	-----	-----
$x = 0.15$	4.03×10^5	5.897	-----	-----

The electrical conducting properties of Na-Ti-O batteries with V doping were investigated. Table 5.10 shows the results of the resistivity measurements of the $\text{Na}_4\text{Ti}_{5-x}\text{V}_x\text{O}_{12}$ system. The resistivity value of as-prepared active materials is 4.2×10^5 Ohm.cm which is higher than that of the Li-Ti-O based anode materials. Increasing the V content in the structure causes an increase in the resistivity of the samples, which may be due to changes in the carrier concentration, band structure, and impurity phases. When the active materials are mixed with CB and PVDF in NMP to obtain the electrodes, the resistivity value decreases to 0.083 Ohm.cm. Similarly, the resistivity values of the electrodes with higher V ion content than the pure sample increase.

After one cycle the resistivity of the electrodes decrease with increasing V content of the sample. This situation can be explained from ex-situ SEM results: the SEI layer gets thinner with V substitutions and it should be noted that the important part of the SEI layer is grown during one cycle. On the other hand, after 1000 cycles the resistivity values first decrease and then increases with increasing V content, as observed in other anode materials in this study.

Table 5.10. Resistivity measurements for $\text{Na}_4\text{Ti}_{5-x}\text{V}_x\text{O}_{12}$.

Phase	Active Material ($\Omega\cdot\text{cm}$)	Electrode		
		Before cycling ($\Omega\cdot\text{cm}$)	After 1 cycle ($\Omega\cdot\text{cm}$)	After 1000 cycles ($\Omega\cdot\text{cm}$)
$\text{Na}_4\text{Ti}_5\text{O}_{12}$	4.2×10^5	0.083	2.350	5.689
$x = 0.025$	4.27×10^5	0.092	2.12	4.823
$x = 0.05$	4.46×10^5	0.107	2.05	5.247
$x = 0.1$	5.37×10^5	0.302	1.972	6.982
$x = 0.15$	5.83×10^5	0.428	1.826	8.459

Table 5.11 shows the resistivity values of the $\text{Na}_2\text{Ti}_{3-x}\text{V}_x\text{O}_7$ system for as-prepared samples, before cycling, after one cycle, and after 1000 cycles. We see that V substitution increases resistivity. The measured resistivity of the electrodes before cycling is $0.066 \Omega\cdot\text{cm}$ and it increase to $0.093 \Omega\cdot\text{cm}$ for $x = 0.15$. As with other electrode materials in this study, we saw that the cycling of the battery causes an increase in the electrode resistivity.

Table 5.11. Resistivity measurements for $\text{Na}_2\text{Ti}_{3-x}\text{V}_x\text{O}_7$.

Phase	Active Material ($\Omega\cdot\text{cm}$)	Electrode		
		Before cycling ($\Omega\cdot\text{cm}$)	After 1 cycle ($\Omega\cdot\text{cm}$)	After 1000 cycles ($\Omega\cdot\text{cm}$)
$\text{Na}_2\text{Ti}_3\text{O}_7$	2.3×10^5	0.066	2.150	4.820
$x = 0.025$	2.32×10^5	0.072	2.238	5.183
$x = 0.05$	2.37×10^5	0.077	2.346	5.629
$x = 0.1$	2.43×10^5	0.086	2.654	6.782
$x = 0.15$	2.57×10^5	0.093	2.891	7.437

Table 5.12 shows the resistivity values of the $\text{Na}_2\text{Ti}_{6-x}\text{V}_x\text{O}_{13}$ samples. The pure sample's resistivity is $7.4 \times 10^4 \text{ } \Omega \cdot \text{cm}$ and it increases to 7.89×10^4 for $x = 0.15$. The resistivity values for samples before cycling, after one cycle, and after 1000 cycles show similar behavior as the other active materials, and the increase in resistivity for increasing cycle number can be explained as above.

Table 5.12. Resistivity measurements for $\text{Na}_2\text{Ti}_{6-x}\text{V}_x\text{O}_{13}$.

Phase	Active Material ($\Omega \cdot \text{cm}$)	Electrode		
		Before cycling ($\Omega \cdot \text{cm}$)	After 1 cycle ($\Omega \cdot \text{cm}$)	After 1000 cycles ($\Omega \cdot \text{cm}$)
$\text{Na}_2\text{Ti}_6\text{O}_{13}$	7.4×10^4	0.200	0.720	0,460
$x = 0.025$	7.52×10^4	0.215	1.182	5.272
$x = 0.05$	7.58×10^4	0.218	1.238	5.386
$x = 0.1$	7.81×10^4	0.226	1.296	5.681
$x = 0.15$	7.89×10^4	0.234	1.378	5.825

From the resistivity changes of the V substituted Na-Ti-O and Li-Ti-O samples, some conclusions are now suggested:

- 1- The V doping in Li-Ti-O and Na-Ti-O materials causes an increase in resistivity since the substitution of Ti^{4+} with V^{5+} promotes a decrease in the carrier concentration and causes changes in the band structure.
- 2- Although the resistivity value of the active materials are above $\text{k}\Omega \cdot \text{cm}$ level, when the electrodes are prepared using CB and PVDF, the resistivity drops below $1 \text{ } \Omega \cdot \text{cm}$.
- 3- Cycling of the battery causes an increase in the resistivity value, since the resulting SEI layer and impurity phases can be regarded as contributing to the change of resistivity with increasing cycle number.
- 4- The electrodes which have a resistivity value above $1 \text{ } \Omega \cdot \text{cm}$ did not display the rechargeable battery feature; this should be investigated in more detail.

5.6. Battery Performance Analysis

Ti based anode materials exhibit longer battery life due to their intrinsic properties [147]. The main reason for the long cycle life may be the structural stability of the electrodes during the charge-discharge process. To this end we investigated the battery performance of V substituted Li-Ti-O and Na-Ti-O anode materials systematically. To explain V substitution effects on battery performance, the electrochemical properties of V substituted $\text{Li}_4\text{Ti}_5\text{O}_{12}$, $\text{Li}_2\text{Ti}_3\text{O}_7$, $\text{Li}_2\text{Ti}_6\text{O}_{13}$, $\text{Na}_4\text{Ti}_5\text{O}_{12}$, $\text{Na}_2\text{Ti}_3\text{O}_7$, and $\text{Na}_2\text{Ti}_6\text{O}_{13}$ systems were investigated by CV. Cycling performances were measured for constant C up to 1000 cycles and for different C values. The battery performance measurements were conducted via charge/discharge of the cells at 1C constant current rate up to 1000 cycles. The capacity dependence of the current was recorded for five cycles for C rates of 0.2C, 0.5C, 1C, and 2C.

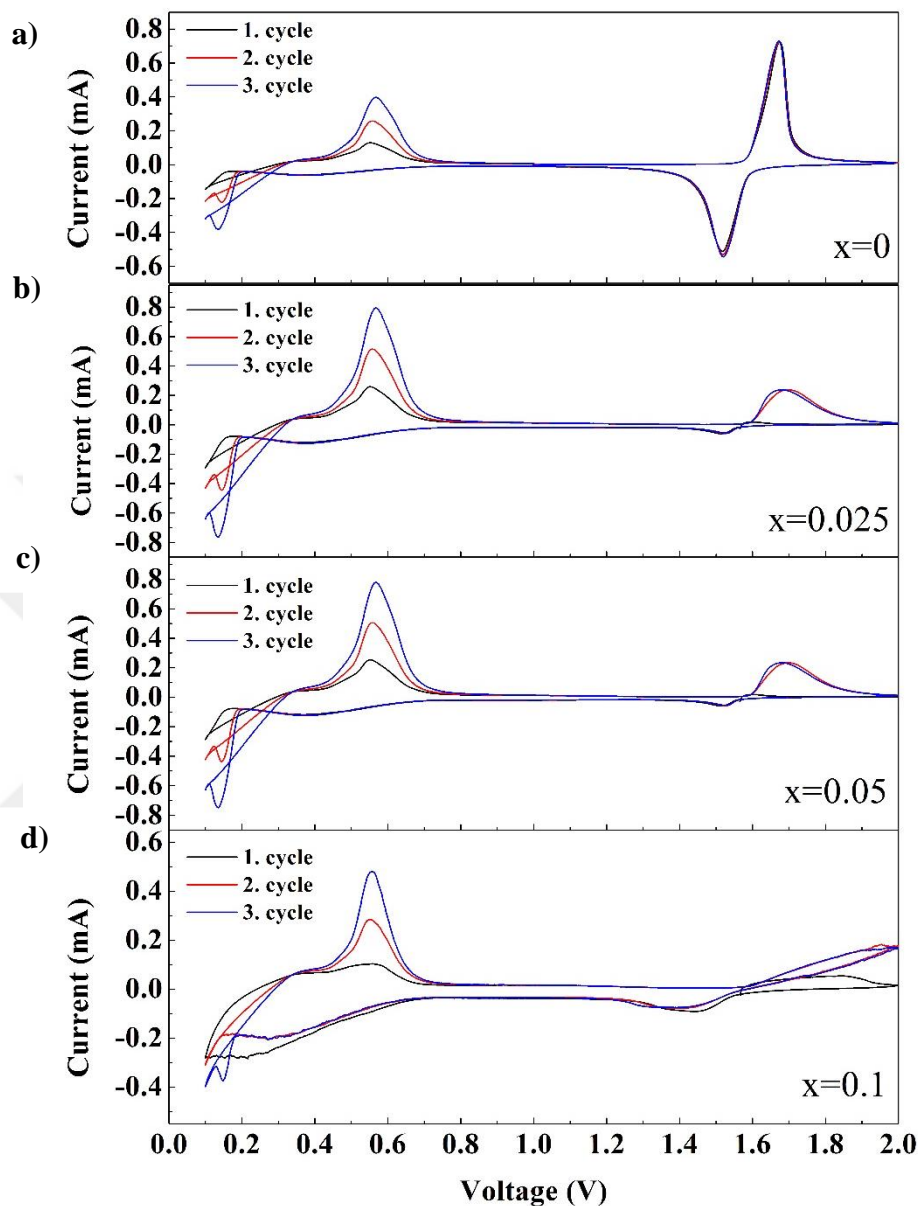


Figure 5.44. CV measurements of the $\text{Li}_4\text{Ti}_{5-x}\text{V}_x\text{O}_{12}$ system. a) $x = 0$, b) $x = 0.025$, c) $x = 0.05$, and d) $x = 0.1$.

CV is a technique in which the intercalation and deintercalation of Li/Na ions for Li/Na-ion batteries are observed as peaks during positive and negative scan rates of the voltage, which is a characteristic feature of the rechargeable batteries. If one of the peaks in the CV is not observed, it can be said that the cell does not have rechargeable properties. The peak in the CV is related to ion-sites and coordination number of Li/Na in the crystal lattice. While the increase of the coordination number of the diffusing ions causes an

increase of the voltage in the CV graph, the intensity of the peak is related to the current value which is obtained in the cell.

The CV measurements were conducted in the 0.1–2 V region (vs Li/Li+) with 0.1 mV/s scanning rate. Figure 5.44 a) to d) shows the CV measurements of $\text{Li}_4\text{Ti}_{5-x}\text{V}_x\text{O}_{12}$ ($x = 0, 0.025, 0.05, \text{ and } 0.1$) cells. During the first three cycles, we observe two redox peaks; the first one is obtained at 1.67 V/1.47 (it shows a cathodic peak/anodic peak) and the other one is seen at 0.6 V/0.12 V. It is known that $\text{Li}_4\text{Ti}_5\text{O}_{12}$ has two Li-ion sites in the lattice. The first has five coordinations in the lattice and the second one has eight. The increasing coordination number can cause an increase in the crystal field and bond strength of Li-ions. So, we predict that the first redox peak is due to the five-coordinated Li-ions and the second is due to the eight-coordinated ones in the crystal structure.

Figures 5.44 b) and c) show the CV graph of the cell, fabricated with $x = 0.025$ which has a similar structure with the unsubstituted sample. The intensity of the second redox peak in the CV graph decreases upon V doping. It can be predicted that V doping prevents the extraction of the eight-coordinated Li ions during the charge-discharge process. It is seen from Figure 5.44 d) that the second redox-cathodic peak is deformed by increasing V content.

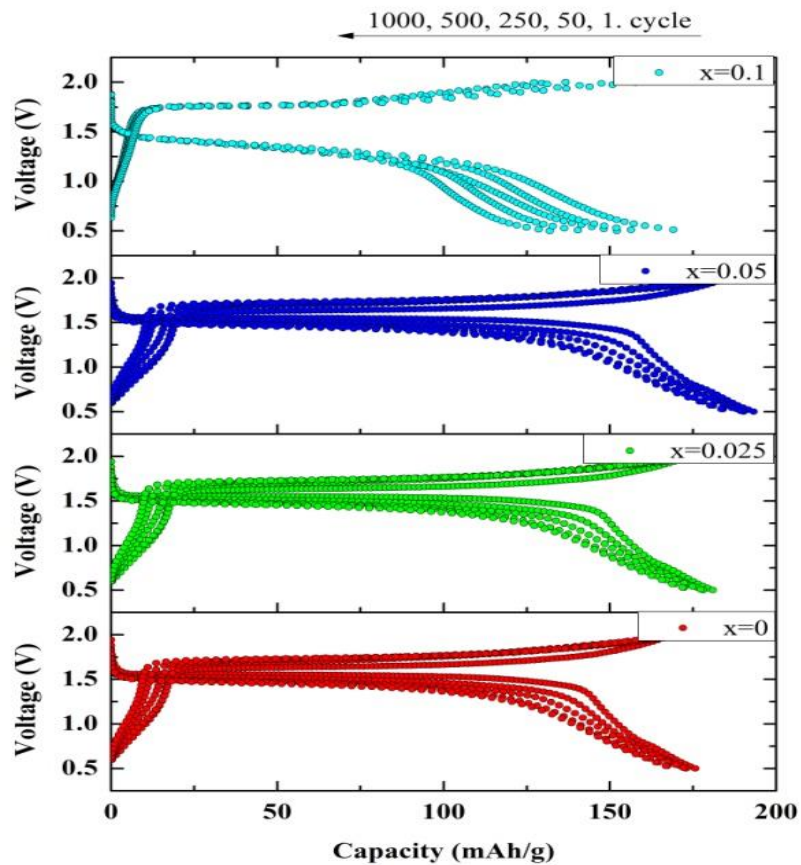
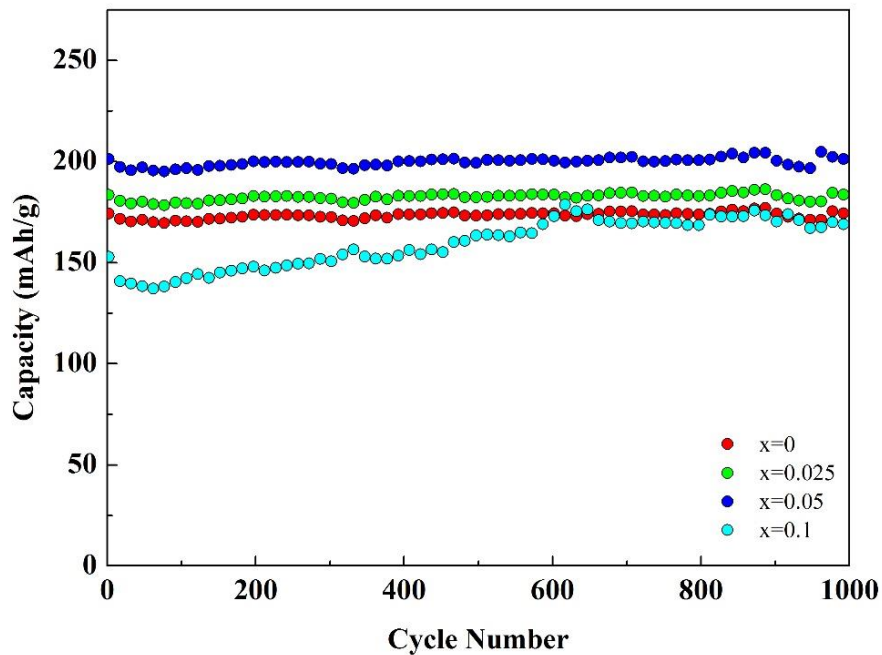


Figure 5.45. Battery performance of the $\text{Li}_4\text{Ti}_{5-x}\text{V}_x\text{O}_{12}$ system over 1000 cycles at 1C constant current.

Figure 5.45 shows the capacity change in $\text{Li}_4\text{Ti}_{5-x}\text{V}_x\text{O}_{12}$ system with increasing cycle number up to 1000 cycles at 1C current rate. The highest capacity is obtained for the cell fabricated using $x = 0.05$ sample. The capacity of the cell for $x = 0.025$ is 184 mAh/g and 180 mAh/g for 1 and 1000 cycles, respectively; the capacity fade is calculated as 0.04% in the cell. The capacity of the cell with $x = 0.5$ is 202 mAh/g and 194 mAh/g for 1 and 1000 cycles, respectively, and the capacity fade is calculated as 0.07%. V doping with $x \leq 0.05$ in $\text{Li}_4\text{Ti}_5\text{O}_{12}$ causes an increase in the capacity of the cell. Further increasing the V content decreases the capacity to a value which is less than that of the unsubstituted sample.

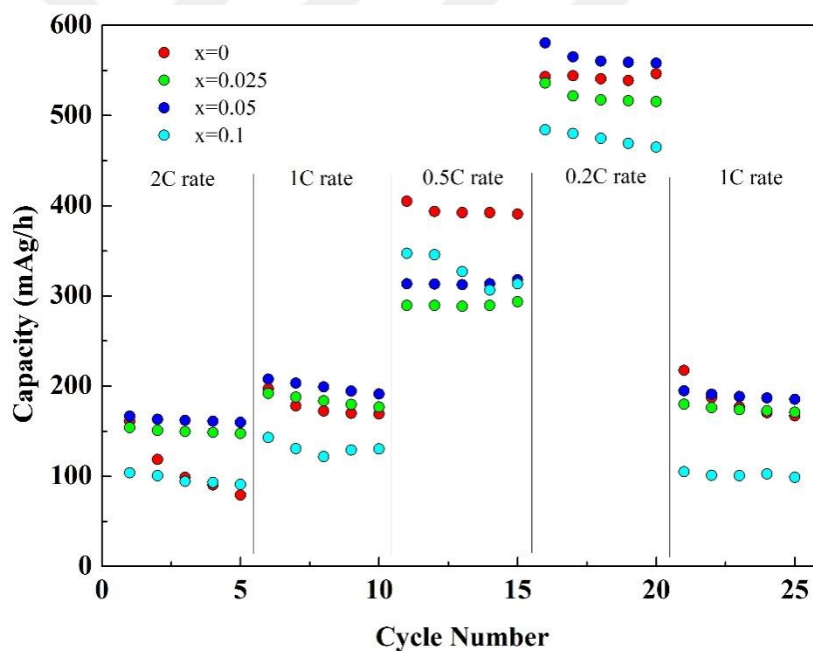


Figure 5.46. Battery performance of $\text{Li}_4\text{Ti}_{5-x}\text{V}_x\text{O}_{12}$ system at different C rates.

Figure 5.46 shows the capacity change of the cell at different C rates. The best battery performance is obtained for the cell with $x = 0.05$ at a 1C rate, which is the standard value for comparison of battery performance as seen in Figure 5.45. To see the different current performances, the cell was measured at different C rates. However, it should be noted that C rates which are higher or lower than 1C can cause different responses in the

cell. We conclude that the differences originate from the voltage fluctuations, inhomogeneity of the electrodes, and the surface roughness.

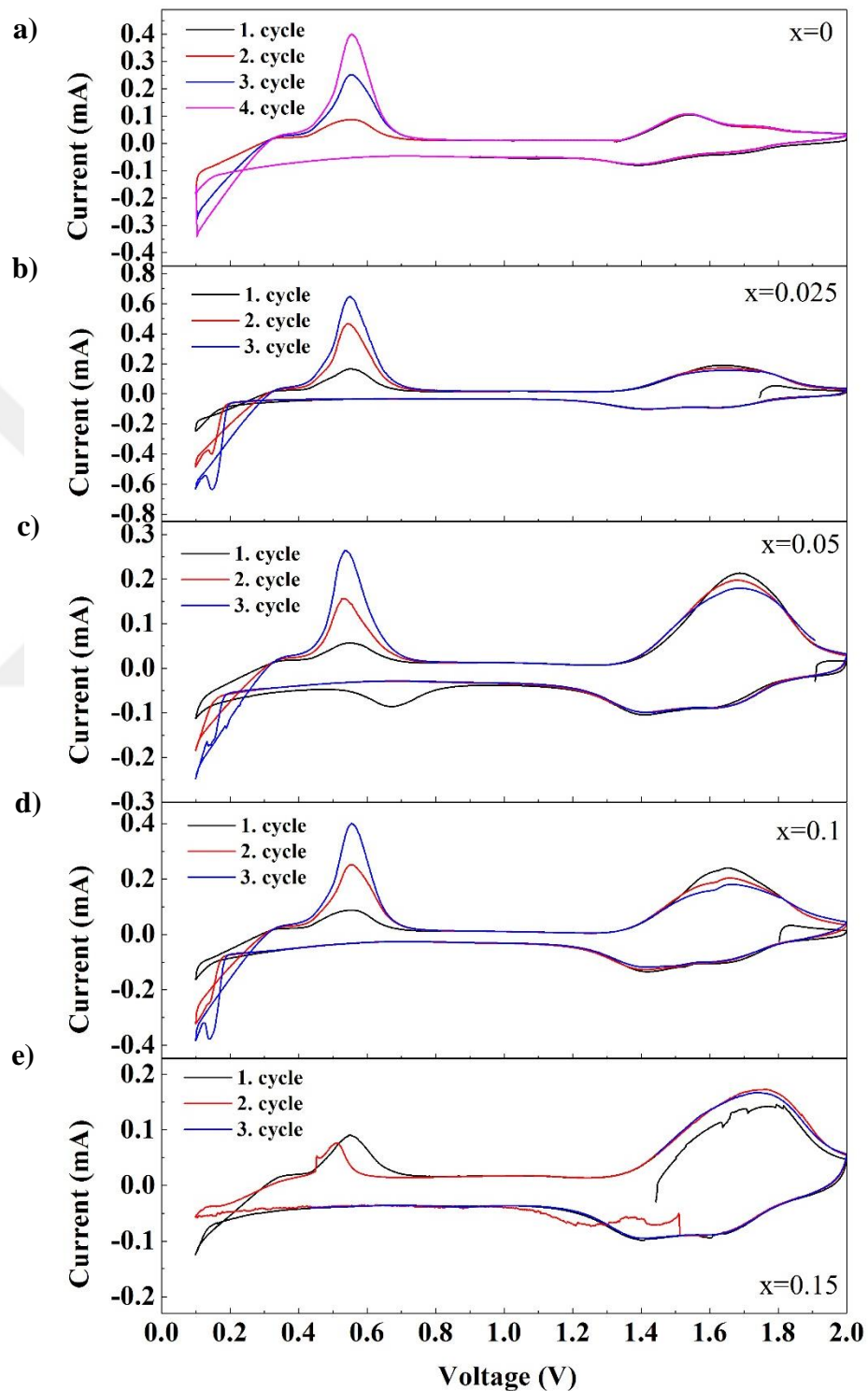


Figure 5.47. CV measurements of $\text{Li}_2\text{Ti}_{3-x}\text{V}_x\text{O}_7$ system where a) $x = 0$, b) $x = 0.025$, c) $x = 0.05$, d) $x = 0.1$, and e) $x = 0.15$.

The V substituted $\text{Li}_2\text{Ti}_3\text{O}_7$ system battery measurement results are given in Figures 5.47–5.49. The CV measurements of $\text{Li}_2\text{Ti}_{3-x}\text{V}_x\text{O}_7$ are performed in the range 0.1–2 V (vs Li/Li+) with a 0.1 mV/s scanning rate; Figure 5.47 a)–e) shows the results of CV measurements. Two redox peaks are observed at 0.6 V/0.15 V and 1.53 V/1.39 V (cathode voltage/anodic voltage) in the CV data. There are two different Li sites in the unit cell of $\text{Li}_2\text{Ti}_3\text{O}_7$. The redox reactions are related to extraction and insertion of Li ions for different lattice sites with different coordination numbers as stated in the previous sections.

When V ions are substituted into the $\text{Li}_2\text{Ti}_{3-x}\text{V}_x\text{O}_7$ system, the peak positions and their intensities change. The redox peaks are obtained at 0.55 V and 1.63 V during the positive voltage scan, and the oxidation peaks are observed at 0.14 V and 1.41 V for $x = 0.025$. The reduction peaks of the $x = 0.5$ cell are obtained at 0.54 V and 1.73 V and the oxidation peaks at 0.14 V and 1.43 V. In the cell with $x = 0.1$, the reduction peaks appear at 0.55 V and 1.8 V and the oxidation peaks are observed at 1.42 V. The reduction peaks are obtained at 0.55 V and 1.67 V and the oxidation peaks are seen at 0.66 V and 1.42 V for $x = 0.15$ substitution. According to CV measurement of the cells, V substitution in $\text{Li}_2\text{Ti}_3\text{O}_7$ causes redox peak expansion and decrease current values. This result can be attributed to the change of the crystal field and coordination of the ions in the structure.

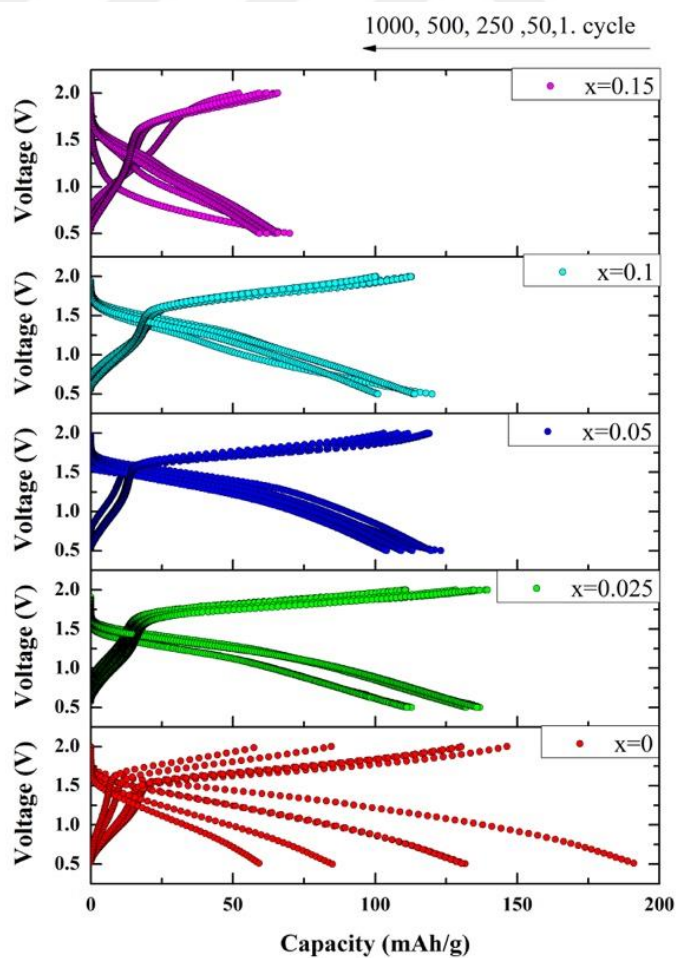
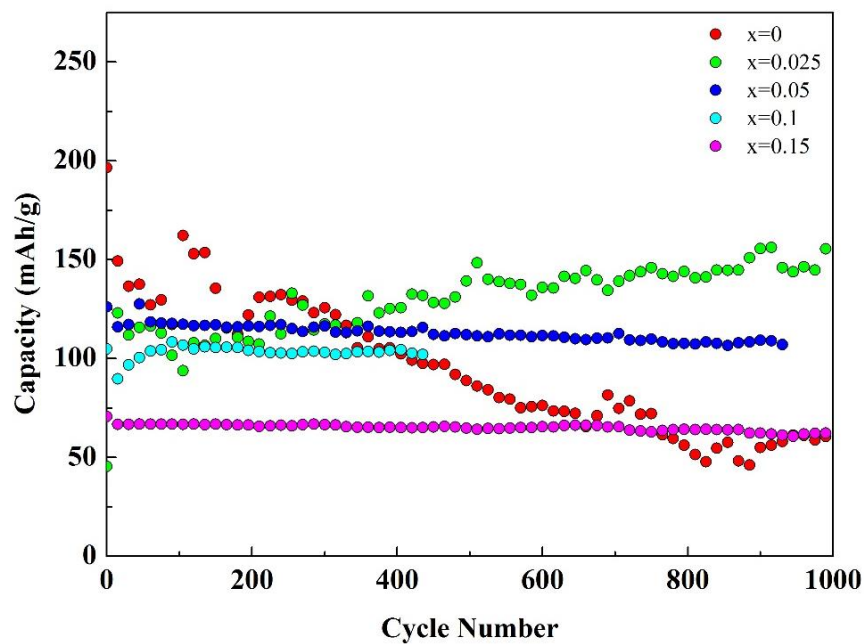


Figure 5.48. Battery performance of the $\text{Li}_2\text{Ti}_{3-x}\text{V}_x\text{O}_7$ system at 1C rate up to 1000 cycles.

Figure 5.48 shows the capacity change with increasing numbers of cycles up to 1000; the highest capacity is obtained for the sample with $x = 0.025$ at 123 mAh/g and 153 mAh/g for 1 and 1000 cycles, respectively. On the other hand, the pure samples have 149 mAh/g and 159 mAh/g for 1 and 1000 cycles, respectively, and the cell with $x = 0.05$ has 125 mAh/g and 107 mAh/g after 1 and 930 cycles, respectively. After 930 cycles the cell lost all battery properties. The cell containing $x = 0.1$ has 104 mAh/g and 101 mAh/g for 1 and 435 cycles, respectively. After the 435th cycle this cell also lost its battery performance. The cell fabricated using $x = 0.15$ vanadium substitution has 70 mAh/g and 61 mAh/g for 1 and 1000 cycles, respectively. As a consequence, although V substitution in $\text{Li}_2\text{Ti}_3\text{O}_7$ increases the stability of the cell, it also causes a decrease in the capacity of the cell.

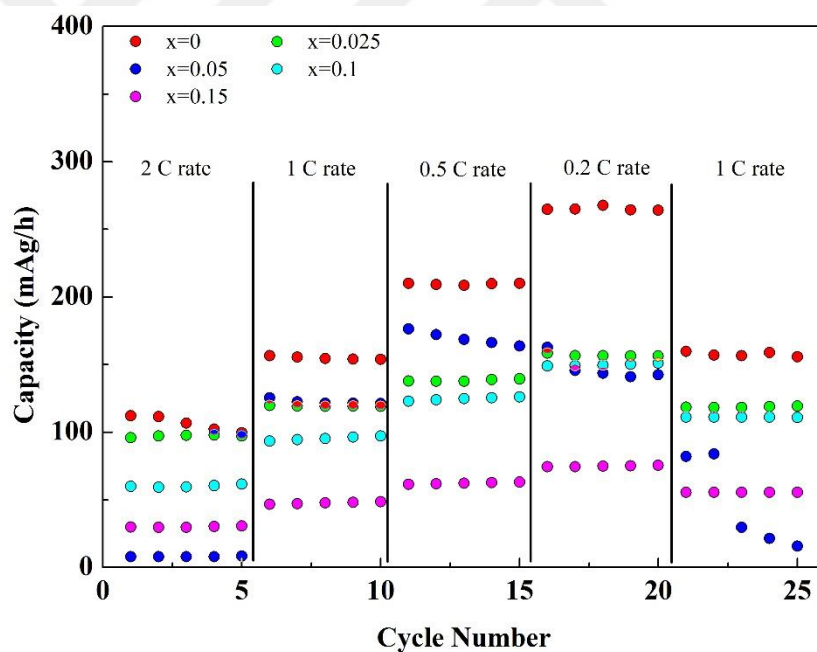


Figure 5.49. Battery performance at different C rates of the $\text{Li}_2\text{Ti}_{3-x}\text{V}_x\text{O}_7$ system.

Battery performance at different C rates is important for commercial applications. Figure 5.49 shows the performance at different C rates. We see that the pure sample shows the highest battery performance of all the C rate results, and that the V substitutions cause different capacity behaviors at different C rates. According to Figure 5.48, the V substitution causes an increase in the stability of the cell after 300 cycles, and the different

C rate measurements were performed for newly fabricated cells. High performance is expected for pure samples, for cycles numbers lower than 300. It is therefore expected that the best performing cells would be the V substituted ones after 300 cycles.

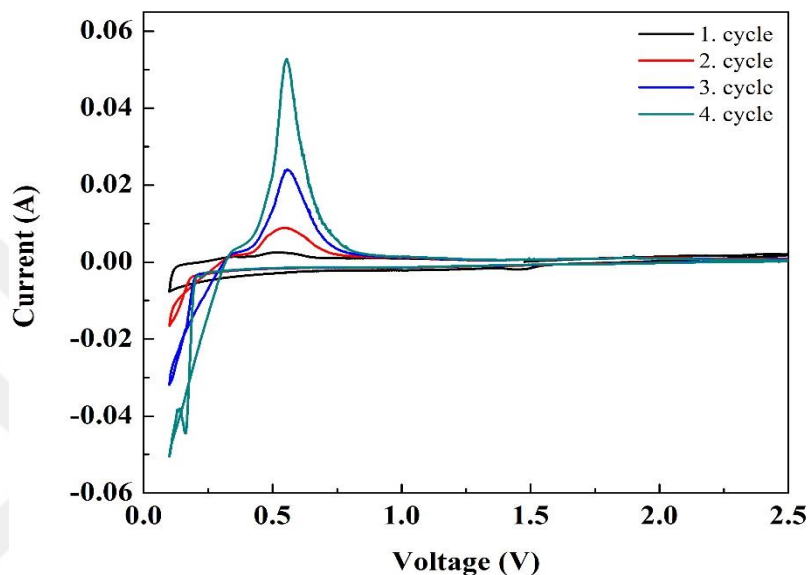


Figure 5.50. CV measurements of the $\text{Li}_2\text{Ti}_6\text{O}_{13}$ system.

The CV measurements were conducted in the 0.1–2.5 V region (vs Li/Li+) with a 0.1 mV/s scanning rate. Figure 5.50 shows the CV graph of pure $\text{Li}_2\text{Ti}_6\text{O}_{13}$ /Li cell; two redox peaks are observed, one is for the cathode at 0.55 V and the other is the anodic peak at 0.16 V. These result show that $\text{Li}_2\text{Ti}_6\text{O}_{13}$ has the lowest ionization voltage among the Li-Ti-O based materials in this study, and shows expected behavior for an anode material. The V substituted samples didn't show any CV or capacity measurements which are the characteristic properties of the rechargeable batteries.

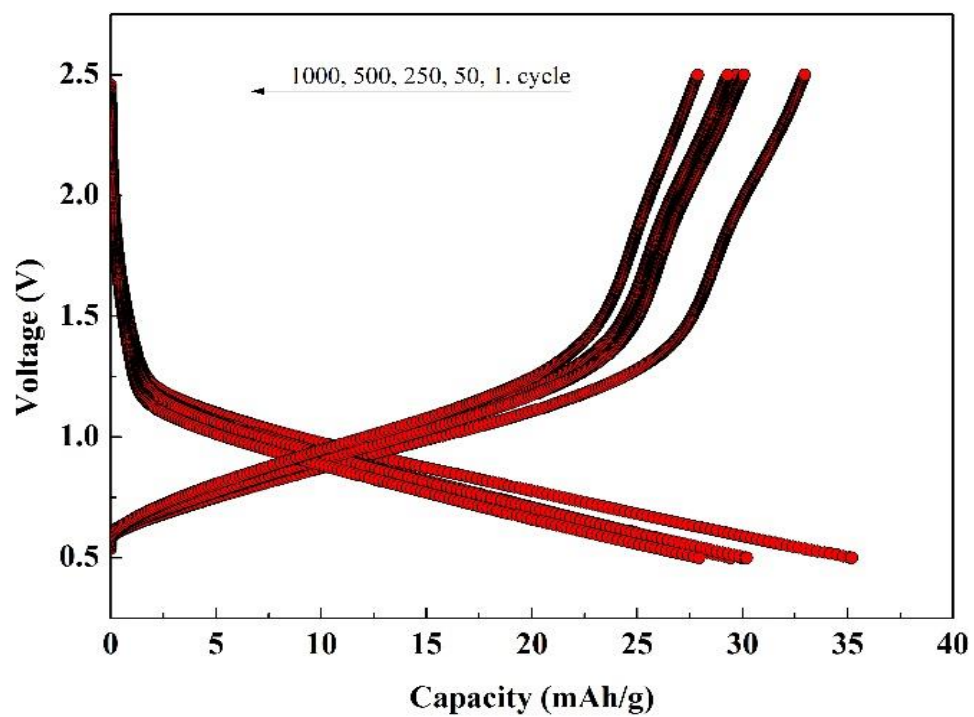
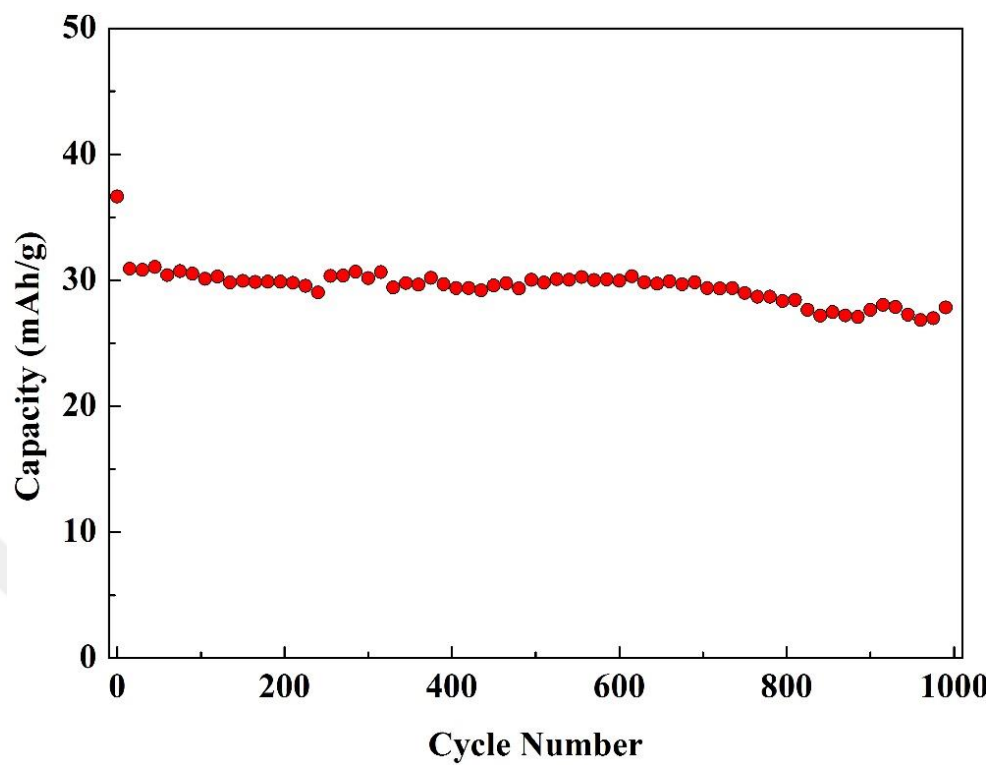


Figure 5.51. The battery performance of the $\text{Li}_2\text{Ti}_6\text{O}_{13}$ system at 1C rate up to 1000 cycles.

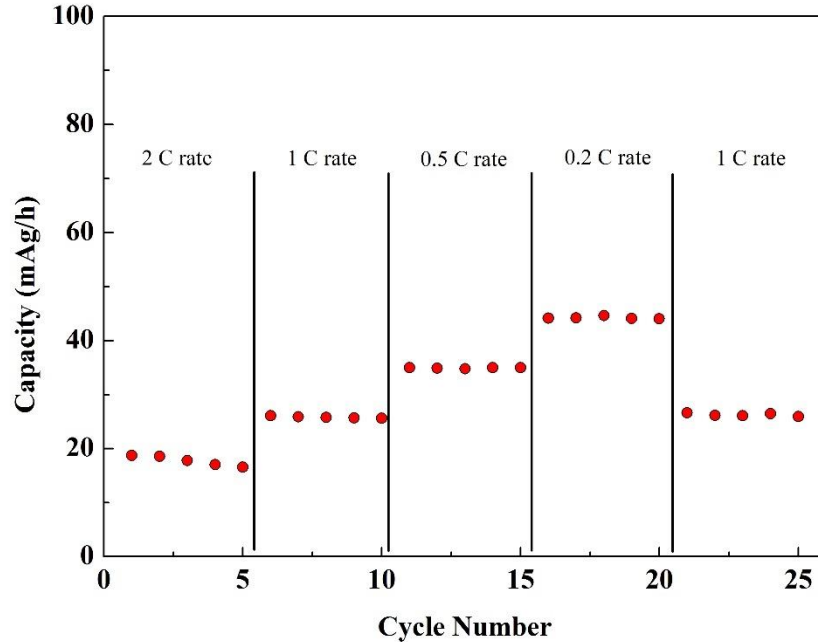


Figure 5.52. Different C rate battery performance of the $\text{Li}_2\text{Ti}_6\text{O}_{13}$ system.

Figure 5.51 shows the capacity change with increasing cycle number of the cell. We see that the capacity value is low, which is an unwanted property in a battery cell. Figure 5.52 shows that the capacity of the cell is 36 mAh/g and 27 mAh/g for 1 and 1000 cycles, respectively. Even if $\text{Li}_2\text{Ti}_6\text{O}_{13}$ has a lower ionization voltage, it has poor capacity values for commercial applications.

The CV measurements of $\text{Na}_4\text{Ti}_{5-x}\text{V}_x\text{O}_{12}$ were conducted in the 0.1–2 V region (vs Na/Na+) with 0.1 mV/s scanning rate. Figure 5.53 a)–e) shows the CV graphs for $x = 0, 0.025, 0.05, 0.1,$ and 0.15 . For the pure $\text{Na}_4\text{Ti}_5\text{O}_{12}/\text{Na}$ cell the CV graph corresponds to a capacitance type cell and we did not observe any redox peaks at all. Although one oxidation peak is observed at 1.03 V during the negative voltage scan for the first cycle, there are no oxidation/reduction peaks at all for $\text{Na}_4\text{Ti}_5\text{O}_{12}$ cell after the first cycle; it acts as hybrid capacitor, and the obtained CV graph exhibits too small capacity for it to act as a good hybrid capacitor.

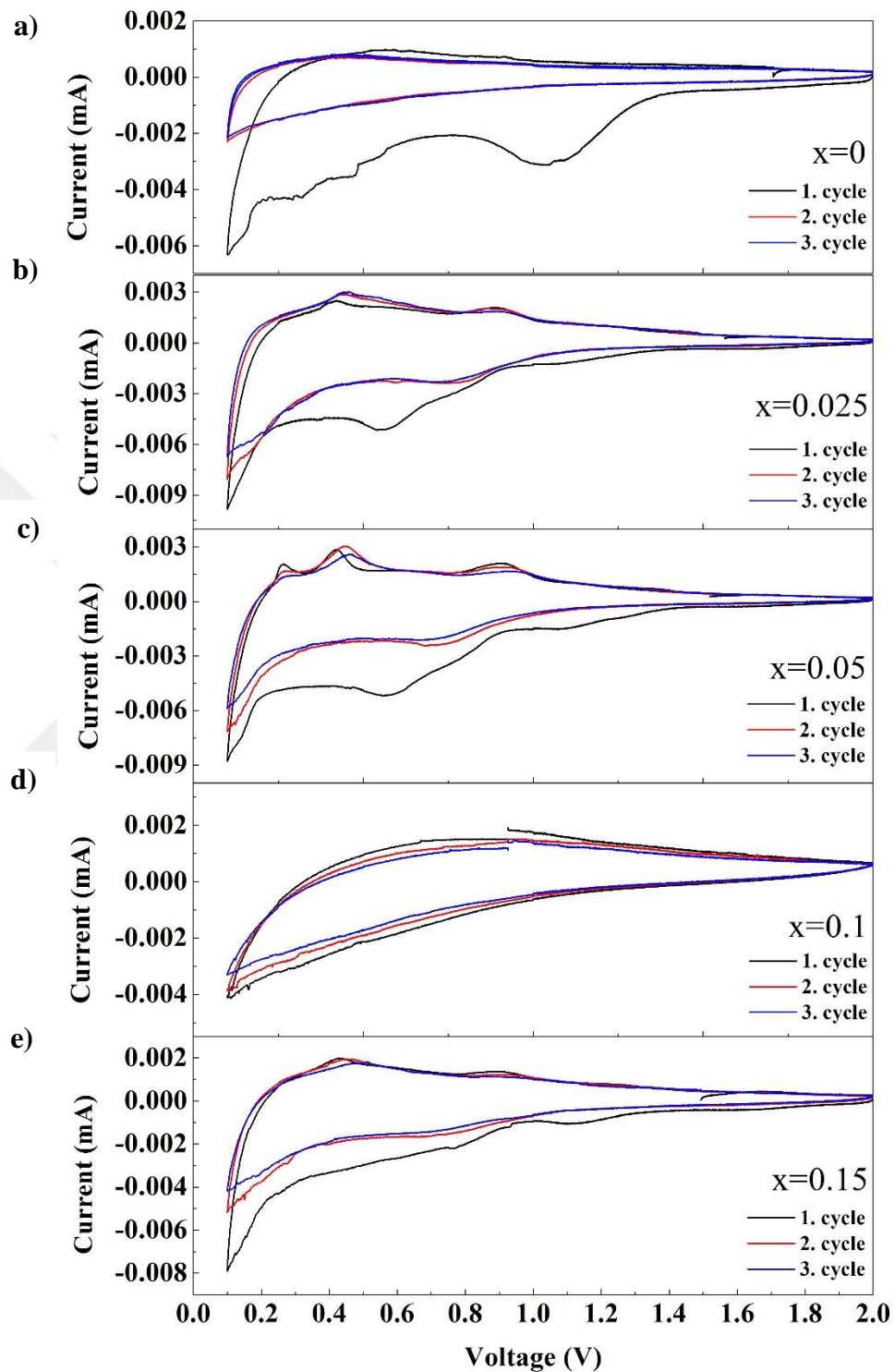


Figure 5.53. CV measurements of the $\text{Na}_4\text{Ti}_{5-x}\text{V}_x\text{O}_{12}$ system where a) $x = 0$, b) $x = 0.025$, c) $x = 0.05$, d) $x = 0.1$, and e) $x = 0.15$.

Figure 5.53 b) shows the CV graph of the cell with $x = 0.025$. Three reduction peaks which are obtained at 0.9 V, 0.41 V, and 0.26 V during the positive scan rate, and the oxidation peak is seen at 0.55 V. During the second and third cycles, the oxidation peak at 0.26 V vanishes and other reduction peaks appears at 0.45 V and 0.89 V. Figure 5.53 c) shows the CV graph of the cell with $x = 0.05$, and reduction peaks appears at 0.26 V, 0.41 V, and 0.9 V and the oxidation peak is obtained at 0.56 V during the first cycle. The reduction peaks are obtained at 0.27 V, 0.45 V, and 0.91 V and the oxidation peak is obtained at 0.71 V for the second and third cycles. It should be noted that there are no redox peaks in the cell with $x = 0.1$ which means that it doesn't have any battery type properties. On the other hand, $x = 0.15$ sub cells show tiny reduction peaks at 0.42 V and 0.91 V during three cycles. The oxidation peaks are obtained at 1.12 V for the first cycle and at 0.74 V for the second and third cycles.

According to the CV graph of $\text{Na}_4\text{Ti}_{5-x}\text{V}_x\text{O}_{12}$, two types of data are observed, one characteristic of batteries and one characteristic of capacitors. The redox peaks observed has lower intensities (below 10 μm) compared to the other materials in this study. Capacitive type CV graphs exhibit hysteresis behavior as observed in Figure 5.53, and we predict that $\text{Na}_4\text{Ti}_{5-x}\text{V}_x\text{O}_{12}$ is not a good material for battery applications.

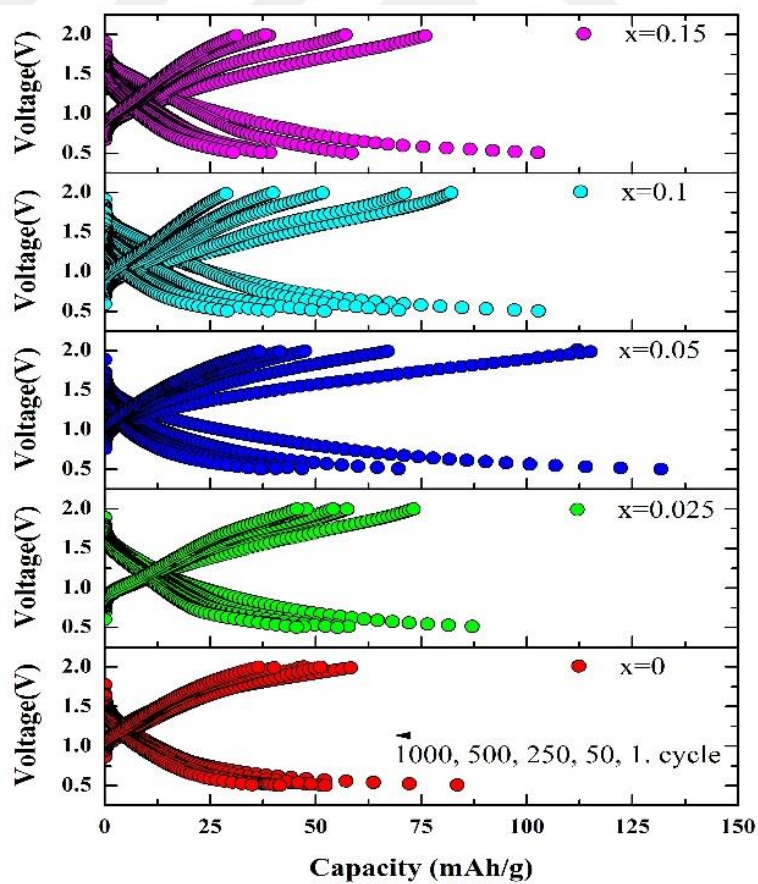
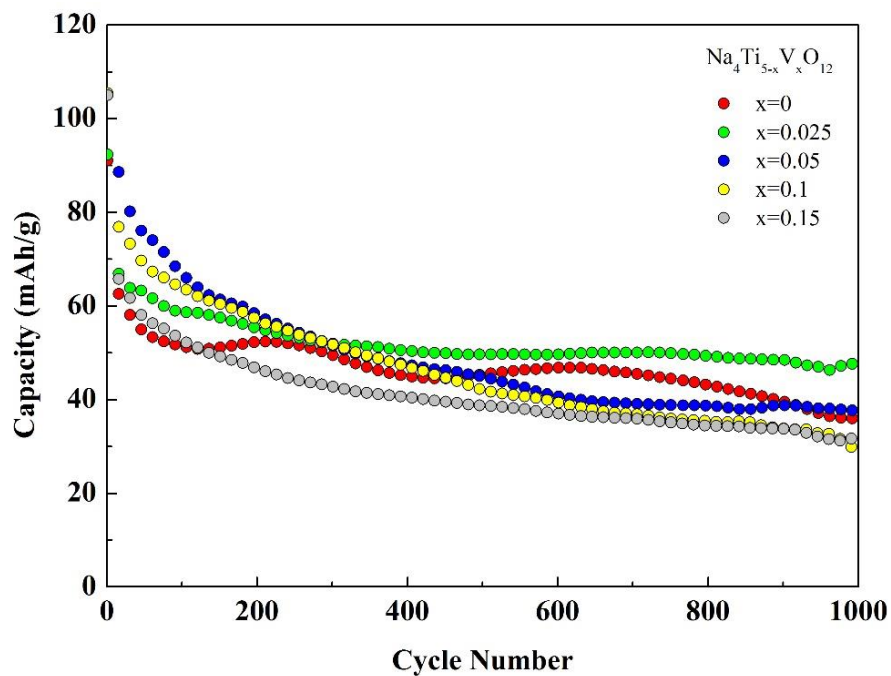


Figure 5.54. Battery performance of the $\text{Na}_4\text{Ti}_{5-x}\text{V}_x\text{O}_{12}$ system for 1C rate up to 1000 cycles.

Figure 5.54 shows the capacity change with increasing cycle number for $\text{Na}_4\text{Ti}_{5-x}\text{V}_x\text{O}_{12}$ samples up to 1000 cycles. The highest capacity is obtained for $x = 0.025$ at 87 mAh/g and 45 mAh/g for 1 and 1000 cycles, respectively. The capacity of the cell with $x = 0.05$ is 131 mAh/g and 37 mAh/g for the first cycle and 1000 cycles, respectively.

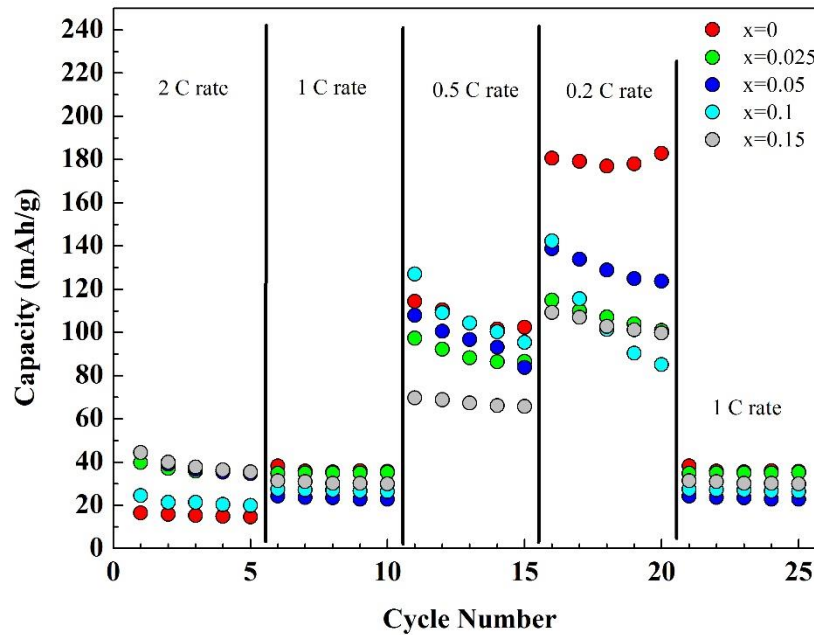


Figure 5.55. Different C rate battery performance of the $\text{Na}_4\text{Ti}_{5-x}\text{V}_x\text{O}_{12}$ system.

Figure 5.55 shows the capacity change with different C rates of the $\text{Na}_4\text{Ti}_{5-x}\text{V}_x\text{O}_{12}$ system. At a 2C rate, the cell with $x = 0.15$ shows a similar capacity performance to those with $x = 0.025$ and $x = 0.05$. The highest value obtained is ~40 mAh/g at a 2C rate for $x = 0.025$ and $x = 0.05$. This can be explained by the impurity phases in these samples. The lower C rate shows higher capacity values than the 1C rate. At 0.5 and 0.2 C rates, the discharge capacity shows better battery performance than other substituted levels. After cycling of 2, 1, 0.5 and 0.2 C rates, we performed cycling of the cell at a 1 C rate and observed a decrease in the capacity of the cell. These results show that the $\text{Na}_4\text{Ti}_5\text{O}_{12}/\text{Na}$ batteries are not promising for battery applications at different C rates..

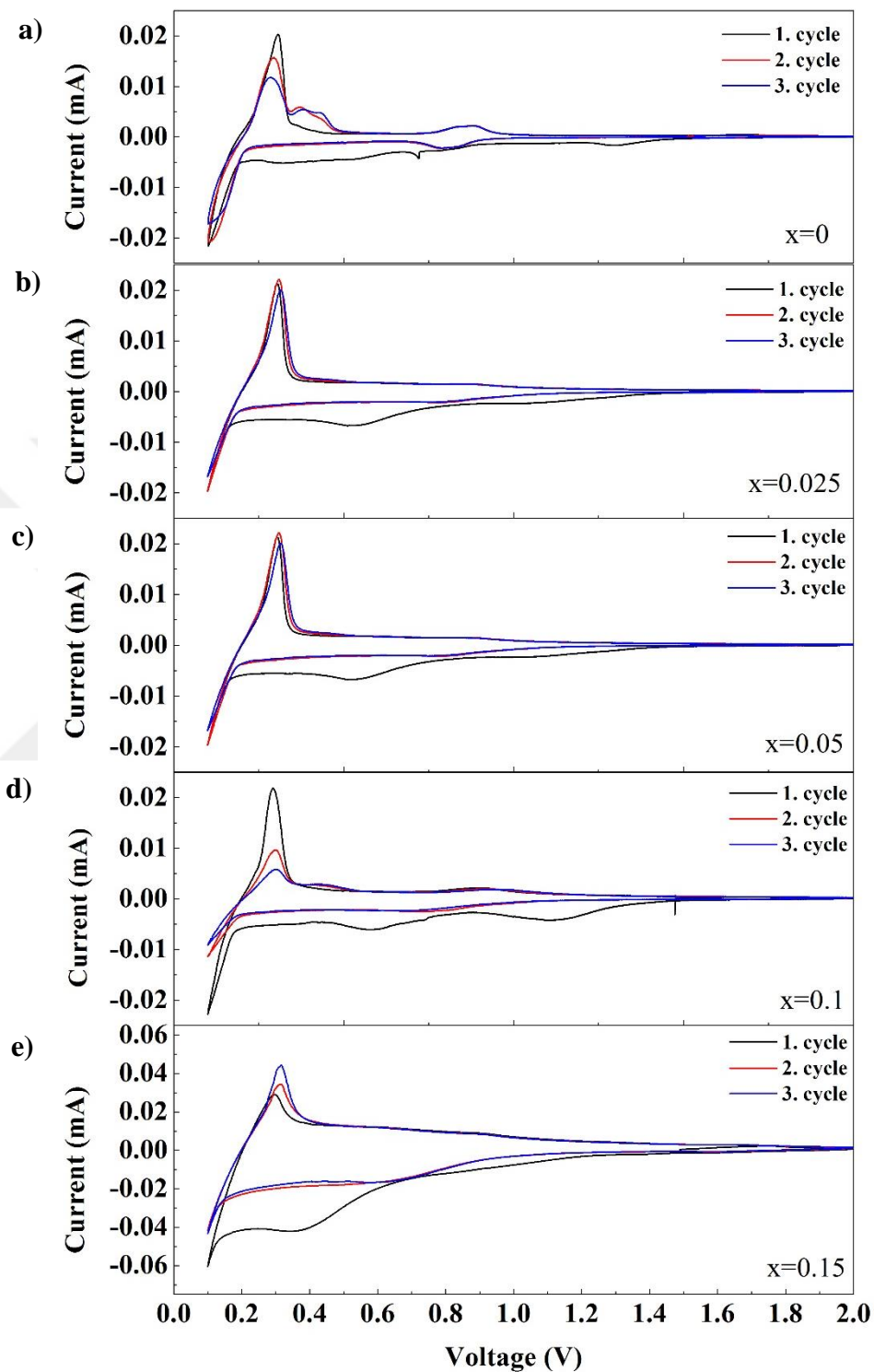
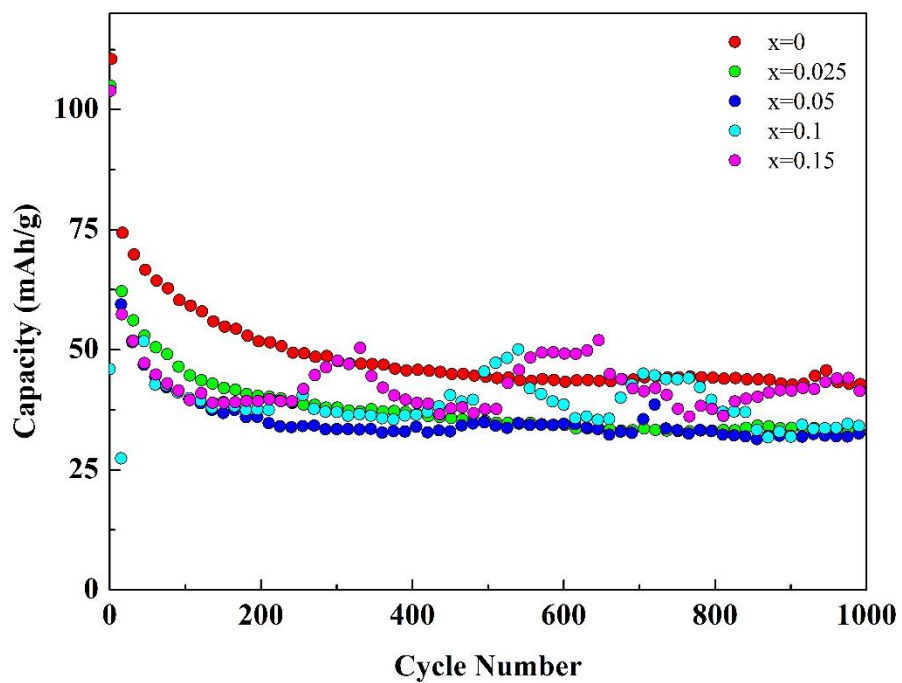


Figure 5.56. CV measurements of $\text{Na}_2\text{Ti}_{3-x}\text{V}_x\text{O}_7$ system where a) $x = 0$, b) $x = 0.025$, c) $x = 0.05$, d) $x = 0.1$, and e) $x = 0.15$.

Figure 5.56 a)–e) shows the CV measurements of $\text{Na}_2\text{Ti}_{3-x}\text{V}_x\text{O}_7$ ($x = 0, 0.025, 0.05, 0.1, \text{ and } 0.15$) cells. Six redox peaks are observed with cathodic peaks at 0.28, 0.4, and 0.86 V and anodic peaks at 0.11, 0.8, and 1.13 V. When V ions are substituted into $\text{Na}_2\text{Ti}_{3-x}\text{V}_x\text{O}_7$, two redox peaks appear for the $x = 0.025$ sample. During the CV measurement, the reduction peak is obtained at 0.29 V and the oxidation peak is obtained at 0.53 V. After the first cycle of the CV measurement, there is only capacitive-like anodic structure in the battery cell. A similar structure is observed for the cell with $x = 0.05$ in that the reduction peak is observed at 0.3 V and the oxidation peak is seen at 0.53 V. Vanadium substitutions and impurity phases in the structure can cause changes in the CV graph such as the redox voltages and the peak intensities. Figure 5.56 d) shows the CV graph of the cell with $x = 0.1$; there are only four redox peaks at 0.29 V and 0.44 V for cathodic peaks, and at 0.53 V and 1.03 V for anodic peaks. In Figure 5.56 e) the number of the redox peaks in the cell decrease to two at 0.3 V and 0.35 V for cathode and anodic peaks, respectively. As a result of Figure 5.56, we conclude that V doping in $\text{Na}_2\text{Ti}_{3-x}\text{V}_x\text{O}_7$ can cause a decrease in the number of redox peaks and convert the behavior to capacitance-like CV data.



1000, 500, 250, 50, 1. cycle

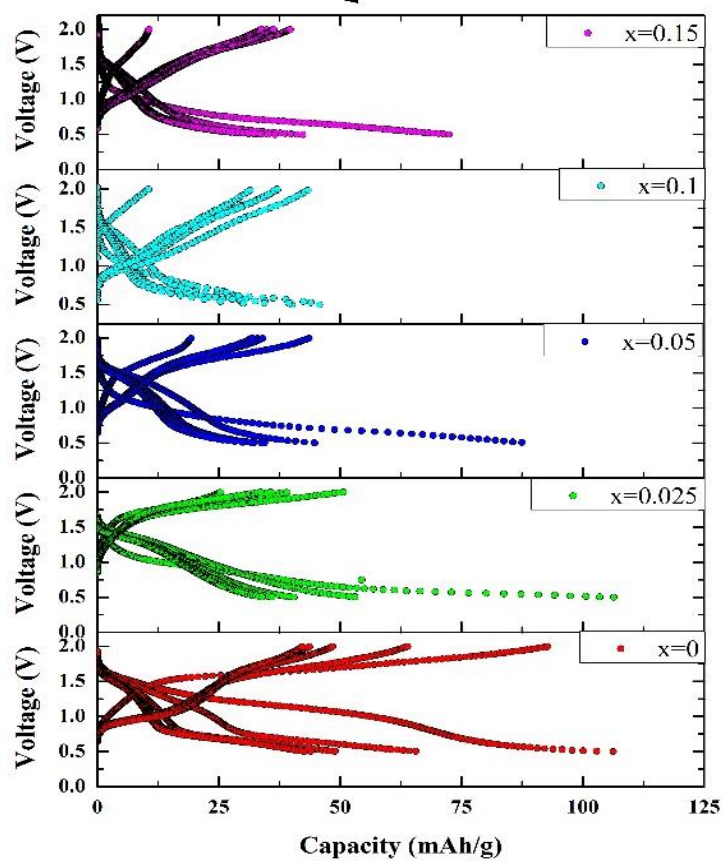


Figure 5.57. The battery performance of the $\text{Na}_2\text{Ti}_{3-x}\text{V}_x\text{O}_7$ system for 1C rate up to 1000 cycles.

Figure 5.57 shows the capacity change with increasing number of charge-discharge cycles for the $\text{Na}_2\text{Ti}_{3-x}\text{V}_x\text{O}_7$ system; it is seen that V substitutions cause a decrease in cell capacity. The pure sample has 81 mAh/g and 43 mAh/g, the sample with $x = 0.0025$ has 72 mAh/g and 32 mAh/g, the sample with $x = 0.05$ has 67 mAh/g and 32 mAh/g, the sample with $x = 0.1$ has 48 mAh/g and 34 mAh/g, and the sample with $x = 0.15$ has 62 mAh/g and 41 mAh/g for 1 and 1000 cycles, respectively.

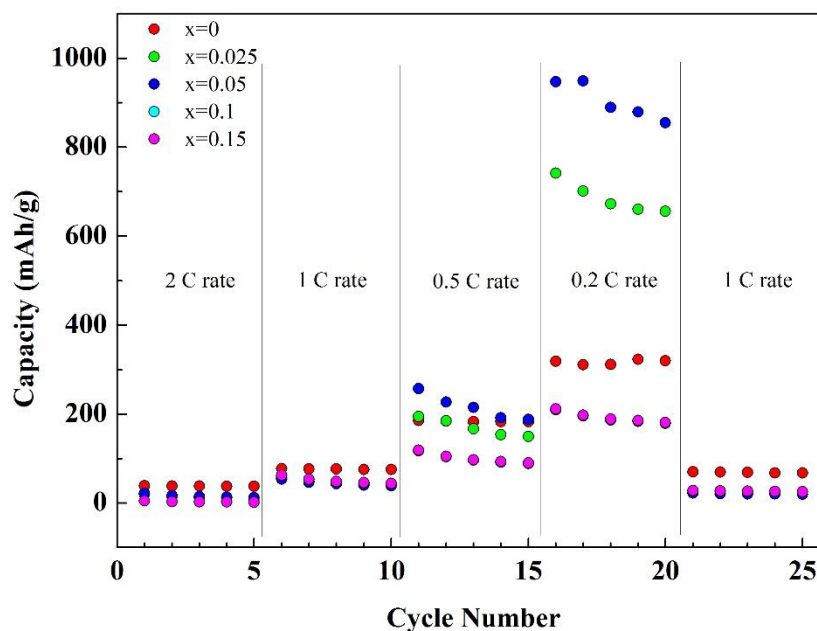


Figure 5.58. Different C rate battery performance of the $\text{Na}_2\text{Ti}_{3-x}\text{V}_x\text{O}_7$ system.

Figure 5.58 shows the capacity changes for different C rates up to 1000 cycles. Although pure and V substituted samples show similar performance behaviors at different C rates, we found that the higher and the lower C rate behaviors are different. The samples containing $x = 0.05$ and 0.025 have higher capacity values than others at 0.2C rate. This may be due to an increase in the chemical potential of the system. However, the highest capacity value is obtained at 947 mAh/g for $x = 0.5$ substitution at a 0.2C rate, and the capacity at 0.5C rate shows a similar increasing trend. High C rate capacity measurements show similar behavior at 1C rate.

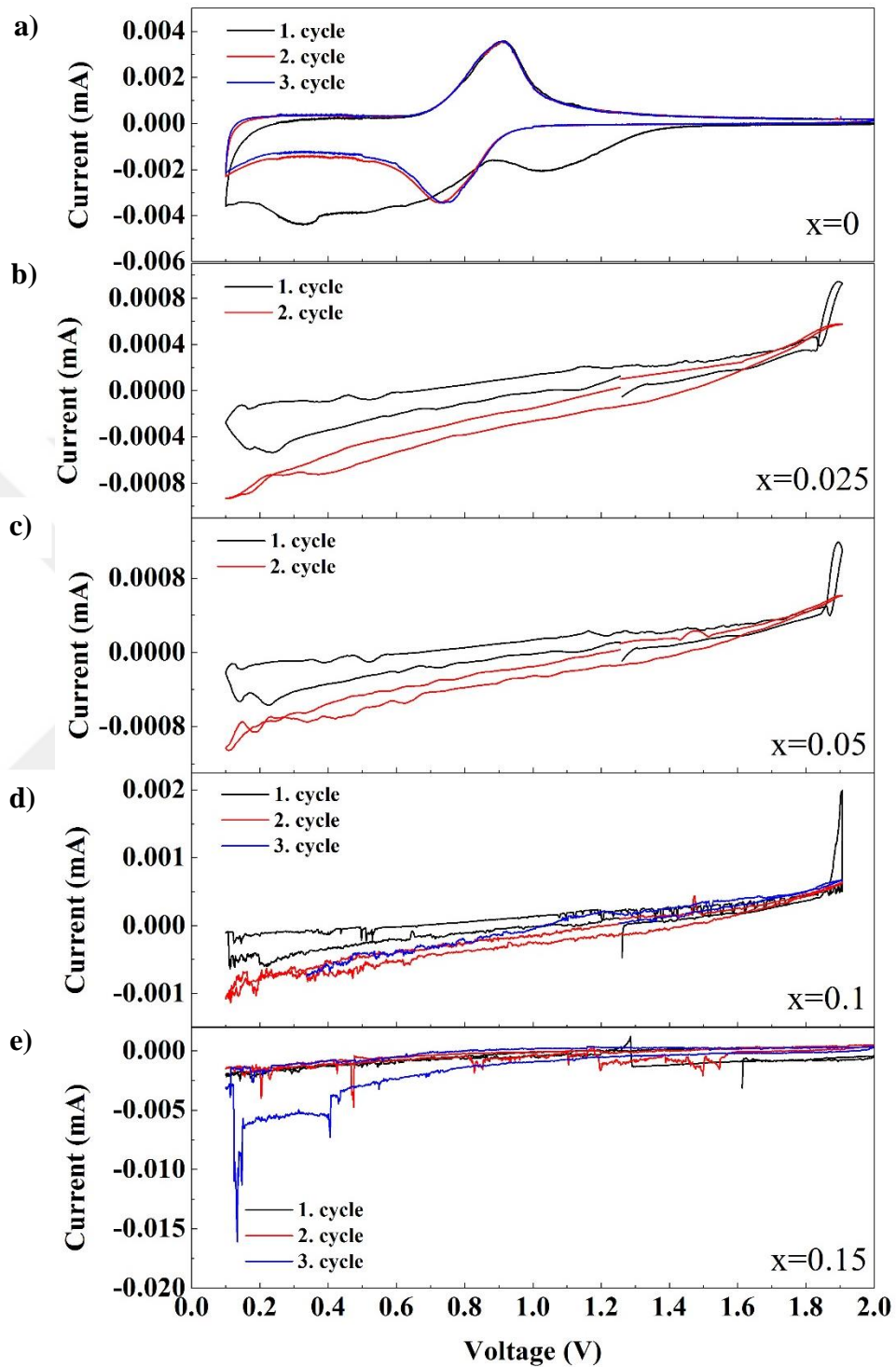


Figure 5.59. CV measurements of the $\text{Na}_2\text{Ti}_{6-x}\text{V}_x\text{O}_{13}$ system where a) $x = 0$, b) $x = 0.025$, c) $x = 0.05$, d) $x = 0.1$, and e) $x = 0.15$.

The CV measurements for $\text{Na}_2\text{Ti}_{6-x}\text{V}_x\text{O}_{13}$ system were conducted at 0.1–2.0 V (vs Na/Na+) with a 0.1 mV/s scanning rate. Figure 5.59 a) shows the CV result for the pure $\text{Na}_2\text{Ti}_6\text{O}_{13}/\text{Li}$ cell. Over three cycles we observed two redox peaks, although for the first cycle the obtained redox peaks are seen at 1.02 V and 0.33 V and the oxidation peaks appear at 0.91 V. After the first cycle, the obtained peaks are at 0.91 V (a reduction cathode peak) and 0.73 V for the oxidation anodic peak. It is predicted that the anomaly in the first cycle is related to the stability of the cell. V substitutions in $\text{Na}_2\text{Ti}_{6-x}\text{V}_x\text{O}_{13}$ cause distortion in system which means there are no battery properties associated with the cell, and the redox peaks vanish as seen in Figure 5.59 b)–e).

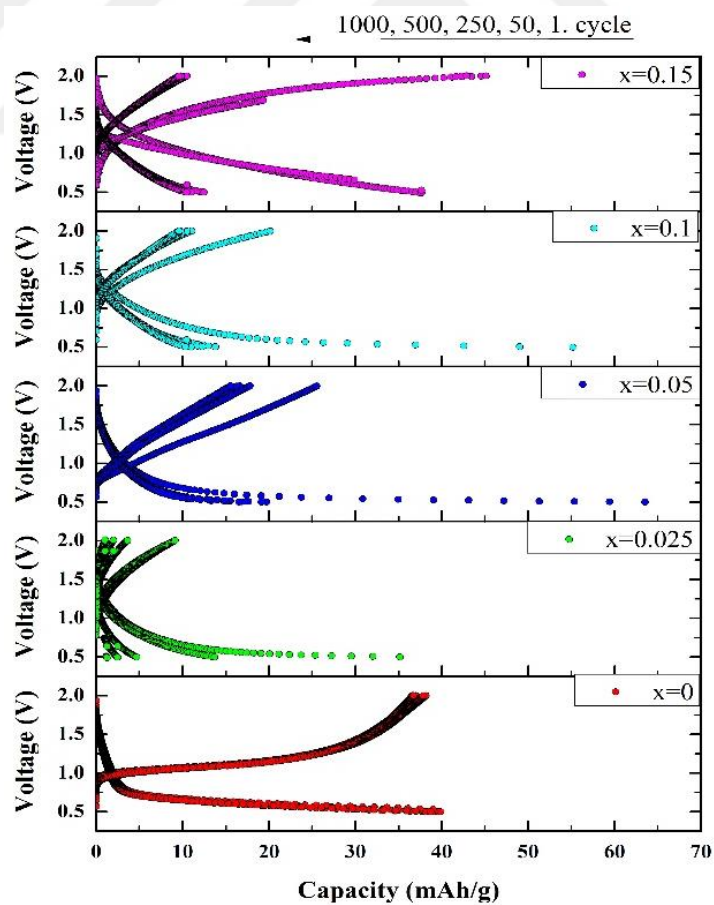
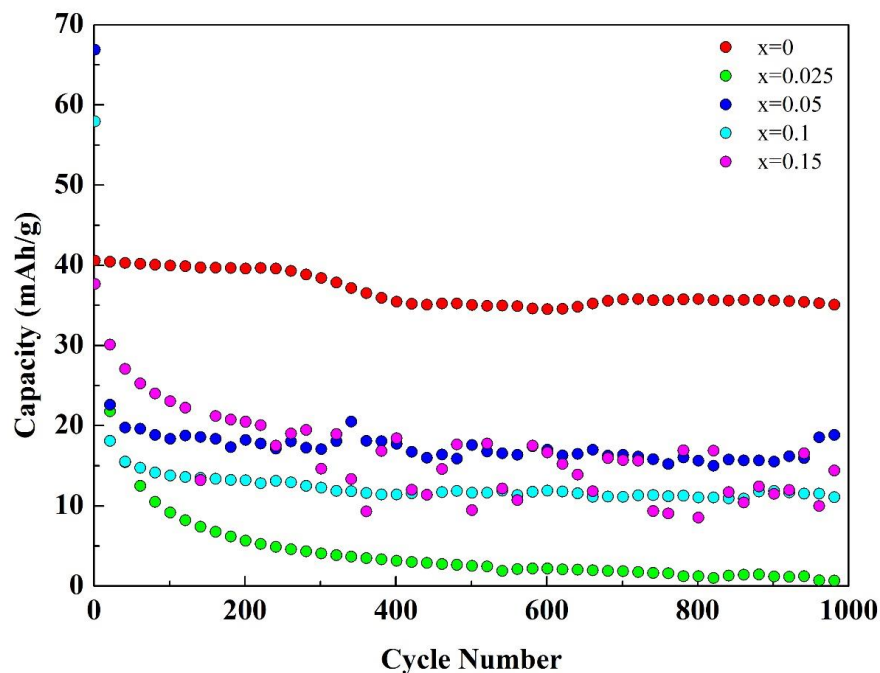


Figure 5.60. Battery performance of the $\text{Na}_2\text{Ti}_{6-x}\text{V}_x\text{O}_{13}$ system for 1C rate up to 1000 cycles.

Figure 5.60 shows the capacity change with increasing cycle number for the $\text{Na}_2\text{Ti}_{6-x}\text{V}_x\text{O}_{13}$ system up to 1000 cycles. We found that V substitutions cause a decrease in battery performance in this system. The capacity values for the V substituted samples are due to capacitive behavior of the cell, and it is concluded that the V substituted $\text{Na}_2\text{Ti}_6\text{O}_{13}$ materials are not suitable for battery applications.

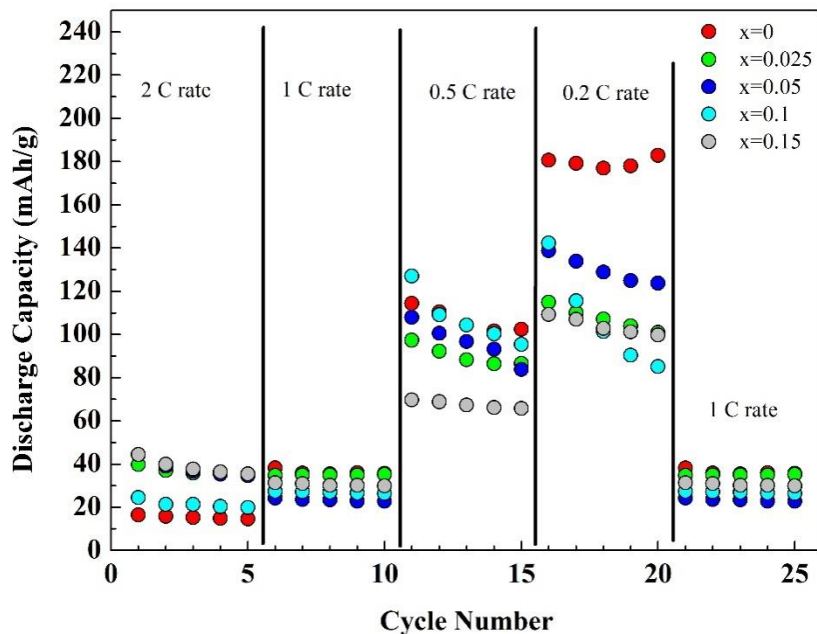


Figure 5.61. Different C rate battery performance of the $\text{Na}_2\text{Ti}_{6-x}\text{V}_x\text{O}_{13}$ system.

Figure 5.61 shows the different C rates battery performances of the cell. At 2C constant current rate, the highest capacity value is found to be ~40 mAh/g and all substitutions levels show better capacity values than pure $\text{Na}_4\text{Ti}_5\text{O}_{12}/\text{Na}$ cell. Lower C rate measurements show higher capacity values than the one measured at 1C rate. At 0.5 and 0.2C rates higher capacities are measured than that of the pure $\text{Na}_4\text{Ti}_5\text{O}_{12}$ samples.

6. CONCLUSION

In the last decade, the need for portable batteries has increased due to increasing numbers of small electronic devices and large systems such as electric cars. The Ti based anode materials for rechargeable batteries have longer battery life compared to the other oxide anode materials. From this point of view, Ti based anode materials for the development and/or improvement of battery properties are one of the hot topics for commercial and scientific studies in rechargeable batteries. The main goal of this study is the investigation of battery performance and lifetime of Ti based anode materials for Li and Na-ion cells via the substitution of Ti^{4+} with V^{+5} ions.

$\text{Li}_4\text{Ti}_{5-x}\text{V}_x\text{O}_{12}$, $\text{Li}_2\text{Ti}_{3-x}\text{V}_x\text{O}_7$, $\text{Li}_2\text{Ti}_{6-x}\text{V}_x\text{O}_{13}$, $\text{Na}_4\text{Ti}_{5-x}\text{V}_x\text{O}_{12}$, $\text{Na}_2\text{Ti}_{3-x}\text{V}_x\text{O}_7$, and $\text{Na}_2\text{Ti}_{6-x}\text{V}_x\text{O}_{13}$ (with $x = 0, 0.025, 0.05, 0.1, \text{ and } 0.15$) anode materials have been fabricated successfully via solid state reaction and ion exchange methods, and their structural and electrochemical properties were investigated in detail. The obtained results were discussed as summarised below.

The XRD results of pure and V substituted $\text{Li}_4\text{Ti}_5\text{O}_{12}$ show that the main phase is protected in all V substitution levels in this study. The impurity phases are observed after $x = 0.1$ level of substitution and they affected the battery performance of the cells. The ex-situ XRD results show that the main phase, $\text{Li}_4\text{Ti}_5\text{O}_{12}$, has been protected and the $\text{Li}_2\text{V}_2\text{O}_4$ impurity phase becomes dominant in the structure after 1000 cycles of the cells. The morphological analysis has shown that the V substitutions cause the formation of larger granular structures. In addition, after 1000 cycles huge levels of SEI layers are coated on all electrodes. Raman analysis show that the V substitutions do not affect the characteristic Li-Ti-O bonds for as-prepared samples. We found that the boundary deformations are the main reason for the decrease in battery performance of the cell by ion intercalation/deintercalation process and impurity phases after 1000 cycles. In addition to this, an increase in the resistivity of the samples is seen upon V doping in the samples. It is stated by Zhong Zhi-Yong et al. [143] that $\text{Li}_4\text{Ti}_5\text{O}_{12}$ shows p-type and n-type conductivity in the structure; the intercalation potential is found as 1.42 V for the p-type conducting mechanism which corresponds to the peak in the CV curve at 1.55 V in

this study. So if V^{5+} is substituted by Ti^{4+} in p-type $Li_4Ti_5O_{12}$, an increase in the resistivity of the samples is expected.

On the other hand, the V substitutions up to the $x = 0.05$ level for $Li_4Ti_5O_{12}$ leads to an improvement in the battery performance. The best capacity at a 1C rate is obtained for $x = 0.05$: 201.37 mAh/g and 200.55 mAh/g for one and 1000 cycles, respectively. According to these values, the capacity fade is calculated as 0.04% for 1000 cycles. It can be predicted that V substitutions at level lower than 0.05 for $Li_4Ti_5O_{12}$ can be used for commercial battery cells.

$Li_2Ti_3O_7$ is one of the important Ti based anode materials in rechargeable batteries. The effect of V doping in $Li_2Ti_3O_7$ on the structural and electrochemical performance of the cell was investigated. The XRD patterns of pure and V substituted $Li_2Ti_3O_7$ show that the main phase does not change for all V substitutions. The change in structural properties after 1000 cycles reveal the main phase of $Li_2Ti_3O_7$ is protected in all samples and that $Li_{0.5}TiO_2$ is the dominant phase for $x = 0.1$ and $x = 0.15$ samples. The morphological analysis show that the V substitutions in the system cause larger grains and a SEI layer is observed after 1000 cycles. The Raman analysis show that the V substitutions affect the characteristic Li-Ti-O bonds for $x \geq 0.1$ and that boundary deformations are observed after 1000 cycles.

The electrical resistivity measurements of $Li_2Ti_3O_7$ show that the V substitutions cause an increase of the resistivity for $x \leq 0.025$ and then a decrease with increasing V content in the structure. The change of resistivity, which depends on the V content, is related to changes in the carrier concentration and the formation of impurity phases. V doping in $Li_2Ti_3O_7$ up to $x = 0.05$ causes an increase in battery performance, which means a decrease of the capacity fade of the cell. The lives of the cells fabricated with $x = 0.05$ and 0.1 V doping are determined as 930 cycles and 435 cycles, respectively. The best capacity results are obtained with an $x = 0.05$ vanadium substitution level, and the pure samples show 149 mAh/g and 159 mAh/g after one and 1000 cycles, respectively. The $x = 0.05$ sample exhibits 125 mAh/g and 107 mAh/g after one and 930 cycles, respectively. As a conclusion of the electrochemical investigation, although V doping in $Li_2Ti_3O_7$

decreases the battery life and the capacity, capacity retention increases upon V doping, which is important for long cycle applications of the batteries.

The last investigated anode material in Li-Ti-O system in this study is $\text{Li}_2\text{Ti}_6\text{O}_{13}$. There is limited information in the literature due to the difficulty of the fabrication techniques such as ion exchange. This material is successfully synthesized in this study by using the exchange of Na ions with Li ions in the starting materials; their structural, electrical, and electrochemical performance were investigated in detail. The XRD data of V substitution in $\text{Li}_2\text{Ti}_6\text{O}_{13}$ show that the main phase is protected for all V substitutions, and that LiVO_3 and LiV_3O_8 impurity phases are observed with increasing V content for $x \geq 0.025$.

The morphological analysis show nanorod formation with V substitution. It is a property of Na-Ti-O based anode materials. We predicted that the substitution of V by Ti causes an increase in nanorod formation, which can be due to flux agent behavior of the high mobility ions (such as Na or Li) in the structure. The Raman analysis show the characteristic Li-Ti-O bonds, implying formation of $\text{Li}_2\text{Ti}_6\text{O}_{13}$ phase. V substitution causes peak shifts due to boundary structure changes, and it begins from the $x = 0.05$ substitution level. Formation of boundary deformation effects in the materials also increase with increasing cycle number of the cell.

The impurity phases reveal that for $x = 0.025$ level substitution battery performance was lost for all V substituted samples. After 1000 cycles the ex-situ XRD results show undefined structural deformations in $\text{Li}_2\text{Ti}_6\text{O}_{13}$ system.

The electrical resistivity measurements show that the V substitutions increases the resistivity for $x \geq 0.025$ levels significantly. As stated above, the increase of the resistivity is related to the decrease in the carrier concentration and the formation of impurity phases in the structure. The reflection of the carriers at grain boundaries is another explanation for the increase in resistivity of the samples.

V substitution in $\text{Li}_2\text{Ti}_6\text{O}_{13}$ causes the disappearance of the battery properties of the materials. The pure sample has 36 mAh/g and 27 mAh/g capacity after one and 1000

cycles respectively. Even if $\text{Li}_2\text{Ti}_6\text{O}_{13}$ has lower ionization voltage and stable capacity values, the battery cell shows poor capacity values for a commercial application.

The other group of Ti based anode materials investigated in this study are the Na based materials. $\text{Na}_4\text{Ti}_5\text{O}_{12}$, $\text{Na}_2\text{Ti}_3\text{O}_7$, and $\text{Na}_2\text{Ti}_6\text{O}_{13}$ phases were fabricated successfully and Ti was substituted by V ions. The structural, electrical, and electrochemical properties of the materials fabricated were investigated.

The $\text{Na}_4\text{Ti}_5\text{O}_{12}$ phase was successfully fabricated by a solid state reaction technique and V substitutions were performed systematically. XRD results of the samples show that the main phase is protected for all V substitution in the system. The impurity phases are observed for $x \geq 0.05$. The ex-situ XRD results show that the main phase ($\text{Na}_4\text{Ti}_5\text{O}_{12}$) is protected after 1000 cycles, and formation of the $\text{Na}_2\text{V}_9\text{O}_{19}$ impurity phase is observed for increasing cycle number. The volume expansion for 1000 cycles is determined as ~15% for the cell with $x = 0.05$.

Nanorod formations are observed in $\text{Na}_4\text{Ti}_5\text{O}_{12}$ system. These have a larger surface area for ion diffusion. We observed an increase in the number of the nanorods with increasing V content in the structure. In addition, the nanorods are deformed after 1000 cycles, which means that the Na-insertion and de-insertion in the nanorods cause deformation of the structure.

The Raman results show that there is a peak shift in the spectra of all V substitutions which originate from bond expansion. On the other hand, deformation of O-Na-(V-Ti) bonds are observed for 1000 cycles. The deformations are attributed to the ion insertion-exertion process during the charge-discharge. The electrical resistivity measurements show that the V substitutions cause an increase in resistivity as obtained for the other electrodes in this study.

According to battery performance results, the capacity of the cell which was fabricated with V substituted electrodes show an increase for the first few cycles and then decrease with increasing cycle number. The capacity of $x = 0.05$ substitution is obtained as 131 mAh/g for the first cycle, and it decreases to 37 mAh/g for 1000 cycles; the capacity fade rate is 9.4%. According to 1000 cycle measurements of the cell, the highest capacity

results are obtained for $x = 0.025$ vanadium, and $x = 0.0025$ substitution shows better battery performance than other samples after ~400 cycles being 87 mAh/g and 45 mAh/g after 1 and 1000 cycles, respectively. According to these values, the capacity fade is calculated as 4.2% for 1000 cycles.

It can be predicted that low level of V doping of the $\text{Na}_4\text{Ti}_5\text{O}_{12}$ structure has a promising outlook for commercial batteries.

Another important anode material for Na-Ti-O type cells is $\text{Na}_2\text{Ti}_3\text{O}_7$. The XRD results of V substituted samples show that the main phase is protected for all V substituted samples. Impurity phases are detected for $x \geq 0.05$ — Ti_3O_5 and $\text{Na}_2\text{Ti}_4\text{O}_9$. After 1000 cycles of the cells, although the main phase of $\text{Na}_2\text{Ti}_3\text{O}_7$ is protected in the structure, the impurity phases are observed for $x \geq 0.1$.

Nanorod formations are observed in the $\text{Na}_2\text{Ti}_3\text{O}_7$ system, and increasing V content cause an increase in the number of nanorods in the samples. According to ex-situ SEM analysis, deformation of the nanorods in the structure is lower than in the $\text{Na}_4\text{Ti}_5\text{O}_{12}$ system.

From Raman measurements of $\text{Na}_2\text{Ti}_3\text{O}_7$ we found that boundary stabilizations occur before cycling and after 1000 cycles. The electrical resistivity measurements show that the V substitutions cause an increase in the resistivity.

The battery performance measurements of the cell show that V substitutions cause a change in the capacity for long cycle measurements. The highest capacity results are obtained for pure samples and are equal to 81 mAh/g and 43 mAh/g after one and 1000 cycles, respectively.

$\text{Na}_2\text{Ti}_6\text{O}_{13}$ is the last material investigated for use as an electrode of a battery cell in this study. We found that the main phase of $\text{Na}_2\text{Ti}_6\text{O}_{13}$ composition is protected for all V substitutions and an impurity phase (such as $\text{Na}_4\text{V}_2\text{O}_7$) is observed for $x \geq 0.025$.

In the ex-situ XRD results after 1000 cycles, the main phase of $\text{Na}_2\text{Ti}_6\text{O}_{13}$ and the impurity phases of $\text{Na}_4\text{V}_2\text{O}_7$ and $\text{Na}_2\text{Ti}_9\text{O}_{19}$ are observed in the structure. The crystal volume changes are in the range from -3 to -1%.

Nanorod formations are seen in $\text{Na}_2\text{Ti}_6\text{O}_{13}$. Vanadium doping in the structure increases the number of nanorods and SEM results show nanorod deformation after 1000 cycles. The Raman results from $\text{Na}_2\text{Ti}_{6-x}\text{V}_x\text{O}_{13}$ compositions show that there are significant changes in boundary structure with V substitution. The ex-situ Raman measurements of 1000 cycled electrodes exhibit boundary deformations of Ti-O-Ti, V-O-V and O-Na-(V-Ti) vibrations. According to electrical resistivity measurements, V substitutions are the cause of an increase in the resistivity of the system.

From 1000 cycle charge-discharge measurements, we found that the V substitutions in the structure cause a decrease in the battery performance of the cell. In addition to this, the first cycles of V have better capacity than that of pure $\text{Na}_2\text{Ti}_6\text{O}_{13}$. $\text{Na}_2\text{Ti}_6\text{O}_{13}$ has ~40 mAh/g and ~35mAh/g capacity values for one and 1000 cycles with 0.05% capacity fade values. As a consequence, the Effects of V doping in Li-Ti-O and Na-Ti-O were investigated in detail. We found that vanadium content in these systems can improve capacity and cycle life for low concentrations of $x \leq 0.05$, such as in $\text{Li}_4\text{Ti}_5\text{O}_{12}$, $\text{Li}_2\text{Ti}_3\text{O}_7$ and $\text{Na}_4\text{Ti}_5\text{O}_{12}$ systems. We hope that they can be used as anode materials in commercial batteries in the near future.

7. REFEEERENCES

- [1] X. Luo, J. Wang, M. Dooner, J. Clarke, *Overview of current development in electrical energy storage technologies and the application potential in power system operation*, **Applied Energy**, 137 (2015) 511-536.
- [2] C. Liu, Z. G. Neale, G. Cao, *Understanding electrochemical potentials of cathode materials in rechargeable batteries*, **Mater. Today**, 19 (2016) 109-123.
- [3] Anonymus. (2017). https://en.wikipedia.org/wiki/Baghdad_Battery (on-line access on 3 June, 2017)
- [4] Anonymus. (2017). <http://thinkingsidewayspodcast.com/wp-content/uploads/2013/12/Baghdad-battery.jpg> (on-line access on 3 June, 2017)
- [5] C. Daniel and J. O. Besenhard, *Handbook of Battery Materials*, Wiley-VCH, Germany (1999)
- [6] M. Piccolino *The bicentennial of the Voltaic battery (1800–2000): the artificial electric organ*, **Trends Neurosci.**, 23 (2000) 147-151
- [7] Anonymus. (2017). <https://tackk.com/fc870m> (on-line access on 3 June, 2017)
- [8] Anonymus. (2017). <http://www.nova.org.au/technology-future/batteries> (on-line access on 3 June, 2017)
- [9] J.-M. Tarascon¹ and M. Armand, *Issues and challenges facing rechargeable lithium batteries*, **Nature**, 414 (2001) 359-367.
- [10] C. A. Vincent and B Scrosati, *MODERN BATTERIES: An Introduction Electrochemical to Power Sources*, Elsevier, Oxford (1984)
- [11] M. Winter, R. J. Brodd, *What Are Batteries, Fuel Cells, and Supercapacitors?* **Chem. Rev.**, 104 (2004) 4245-4270
- [12] T. R Crompton, *Battery Reference Book*, Elsevier, Oxford (1990)
- [13] Anonymus. (2017). https://www.researchgate.net/profile/Pei-Hsing_Huang/publication/283971505/figure/fig18/AS:296597922566161@1447725863598/Figure-4-Schematic-illustration-of-the-lead-acid-battery-chemical-reaction.png (on-line access on 15 June, 2017)
- [14] S. Kassatly, *The lithium-ion battery industry for electric vehicles*, Massachusetts Institute of Technology, 2010.

- [15] C. G.A. Karina, G. R. Pedro, Organic/inorganic hybrid materials based on conducting organic polymers as electrodes for energy storage devices, PhD Thesis. Universitat Autònoma de Barcelona 2004.
- [16] Anonymus. (2017). <http://evbud.com/news/323/> (on-line access on 3 June, 2017)
- [17] J. W. Fergus, *Recent developments in cathode materials for lithium ion batteries*, **J. Power Sources**, 195 (2010) 939-954
- [18] T. Ohzuku and A. Ueda, *Solid State Redox Reactions of LiCoO_2 ($R\bar{3}m$) for 4 Volt Secondary Lithium Cells*, **J. Electrochem. Soc.**, 141 (1984) 2972-2977.
- [19] P. G. Bruce, *Solid-state chemistry of lithium power sources*, Chemical Communications, 19 (1997) 1817-1824.
- [20] Anonymus. (2017). <https://crystallography365.wordpress.com/tag/battery/> (on-line access on 3 June, 2017)
- [21] S. J. Ana, J. Li, C. Daniel, D. Mohanty, S. Nagpure, D. L. Wood III, *The state of understanding of the lithium-ion-battery graphite solid electrolyte interphase (SEI) and its relationship to formation cycling*, **Carbon**, 105 (2016) 52-76.
- [22] S. Demirel, *Sb ve B katkılı $\text{Ca}_3\text{Co}_4\text{O}_9$ bileşiğinin termoelektrik özelliklerinin incelenmesi*, MS Thesis, University of Inonu Turkey, 2013
- [23] K. Mizushima, P. C. Jones, P. J. Wiseman, J. B. Goodenough, *Li_xCoO_2 ($0 < x < 1$): A new cathode material for batteries of high energy density*, **Mater. Res. Bull.**, 15 (1980) 783-789
- [24] C. M. Julien, A. Mauger, K. Zaghib and H. Groult, *Comparative Issues of Cathode Materials for Li-Ion Batteries*, **Inorg.**, 2 (2014) 132-154
- [25] R. Paravasthu, *Synthesis and characterization of lithium-ion cathode materials in the system $(1-x-y)\text{LiNi}_{1/3}\text{Mn}_{1/3}\text{Co}_{1/3}\text{O}_2 \cdot x\text{Li}_2\text{MnO}_3 \cdot y\text{LiCoO}_2$* , PhD Thesis Colorado State University USA, 2012
- [26] P. Nie, L. Shen, H. Luo, H. Li, G. Xu, X. Zhang, *Synthesis of nanostructured materials by using metal-cyanide coordination polymers and their lithium storage properties*, **Nanoscale**, 5 (2013) 11087-11093
- [27] X. Dai, A. Zhou, J. Xu, Y. Lu, L. Wang, C. Fan, and J. Li, *Extending the High-Voltage Capacity of LiCoO_2 Cathode by Direct Coating of the Composite*

- Electrode with Li₂CO₃ via Magnetron Sputtering*, **J. Phys. Chem. C**, 120 (2016) 422-430
- [28] J-H. Shim, N-H. Cho, S. Lee, *Synthesis and characterization of Mg₂TiO₄-coated LiCoO₂ as a cathode material for lithium ion batteries*, **Electrochim. Acta**, 243 (2017) 162-169
- [29] A. Konarov, S-T. Myung, and Y-K. Sun, *Cathode Materials for Future Electric Vehicles and Energy Storage Systems*, **ACS Energy Letters**, 2 (2017) 703-708
- [30] R.S. Ledwaba, M.G. Matshaba and P.E. Ngoepe, *Molecular dynamics simulations of spinels: LiMn₂O₄ and Li₄Mn₅O₁₂ at high temperatures*, **IOP Conf. Series: Materials Science and Engineering**, 80 (2015) 012024
- [31] K. Hoang, *Understanding the electronic and ionic conduction and lithium overstoichiometry in LiMn₂O₄ spinel*, **J. Mater. Chem. A**, 2 (2014) 18271-18280
- [32] W. Sun, H. Liu, Y. Liu, G. Bai, W. Liu, S. Guo, X. Z. Zhao, *A general strategy to construct uniform carbon-coated spinel LiMn₂O₄ nanowires for ultrafast rechargeable lithium-ion batteries with a long cycle life*, **Nanoscale**, 7 (2015) 13173-13180
- [33] M. S. Islam and C. A. J. Fisher, *Lithium and sodium battery cathode materials: computational insights into voltage, diffusion and nanostructural properties*, **Chem. Soc. Rev.**, 43 (2014) 185-204
- [34] Y. Tang, Y. Zhang, W. Li, B. Ma and X. Chen, *Rational material design for ultrafast rechargeable lithium-ion batteries*, **Chem. Soc. Rev.**, 44 (2015) 5926-5940
- [35] M. M. Thackeray, W. I. F. David, P. G. Bruce, J. B. Goodenough, *Lithium insertion into manganese spinels*, **Mater. Res. Bull.**, 18 (1983) 461-472.
- [36] H-L. Zhang and N. Xiang, *Structural and Electrochemical Investigation of Li_{1.02}Mn_{1.92}Al_{0.02}Fe_{0.02}Cr_{0.02} (x=0,0.08) Synthesized by Solid-State Method*, **Adv. Mater. Sci. Eng.**, 2013 (2013) 137032-137038
- [37] T. Dong, S. Zhang, L. Zhang, S. Chen and X. Lu, *Improving Cycling Performance of LiMn₂O₄ Battery by Adding an Ester-Functionalized Ionic Liquid to Electrolyte*, **Aust. J. Chem.**, 68 (2015) 1911-1917

- [38] S. Demirel, E. Oz, S. Altin, A. Bayri, E. Altin and S. Avci, *Enhancement of battery performance of LiMn_2O_4 : correlations between electrochemical and magnetic properties*, **RCS Adv.**, 6 (2016) 43823-43831
- [39] A. Choudhury and H. Y. Asl, *New Iron-Based Polyanion Compounds As Low-Cost Cathode Materials for Rechargeable Alkali-Ion Batteries*, **ECS Meeting Abstracts**, Abstract MA2016-01 501 (2016)
- [40] M. S. Whittingham, *Lithium Batteries and Cathode Materials*, **Chem. Rev.** 104 (2004) 4271–4301
- [41] J. B. Goodenough, A. K. Padhi, K. S. Nanjundaswamy, C. Masquelier, *Cathode materials for secondary (rechargeable) lithium batteries*, US Patent, US 08/840,523 (1996)
- [42] C. M. Julien, A. Mauger, J. Trottier, K. Zaghbi, P. Hovington and H. Groult, *Olivine-Based Blended Compounds as Positive Electrodes for Lithium Batteries*, **Inorg.**, 4 (2016) 17-
- [43] D. Su, *Development of Novel Electrode Materials for Li-ion Batteries and Na-ion Batteries*, PhD Thesis, University of Technology Sydney, 2013
- [44] Anonymus. (2017). http://medicpdf.com/images/pdf/dev.laptop.org1-3_2.png (on-line access on 3 June, 2017)
- [45] C. Liu, Z. G. Neale. G. Cao, *Understanding electrochemical potentials of cathode materials in rechargeable batteries*, **Mater. Today** 19 (2016) 109-123
- [46] N. Nitta, F. Wu, J. T. Lee, G. Yushin, *Li-ion battery materials: present and future*, **Mater. Today** 18 (2015) 252-264
- [47] J. Barker, *Lithium ion electrochemical cell*, US Patent, US 5744264 A (1998)
- [48] Anonymus. (2017). <http://www.bbc.co.uk/staticarchive/0bc701c5f64b900a3e55a1433182402c4aef3a74.gif> (on-line access on 3 June, 2017)
- [49] M. Armand, J. M. Tarascon, *Building better batteries*, *Nature* 451 (2008) 652–657.
- [50] J. Cabana, L. Monconduit, D. Larcher, M. R. Palacín, *Beyond intercalation-based Li-ion batteries: the state of the art and challenges of electrode materials reacting through conversion reactions*, **Adv. Mater.** 15(2010) E170-92.

- [51] G.-N. Zhu, Y.-G. Wang and Y.-Y. Xia, *Ti-based compounds as anode materials for Li-ion batteries*, **Energy Environ. Sci.**, 5 (2012) 6652-6667.
- [52] L. Gao, D. Huang, Y. Shen and M. Wang, *Rutile-TiO₂ decorated Li₄Ti₅O₁₂ nanosheet arrays with 3D interconnected architecture as anodes for high performance hybrid supercapacitors*, **J. Mater. Chem. A** 46 (2015) 23570-23576.
- [53] T.-F. Yi, L.-J. Jiang, J. Shu, C.-B. Yue, R.-S. Zhu, H.-B. Qiao, *Recent development and application of Li₄Ti₅O₁₂ as anode material of lithium ion battery*, **J. Phys. Chem. Solids** 71 (2010) 1236-1242.
- [54] V. Augustyn, P. Simon and B. Dunn, *Pseudocapacitive oxide materials for high-rate electrochemical energy storage*, **Energy Environ. Sci.** 7 (2014) 1597-1614.
- [55] C. Zhang, Y. Zhang, J. Wang, D. Wang, D. He, Y. Xia, *Li₄Ti₅O₁₂ prepared by a modified citric acid sol-gel method for lithium-ion battery*, **J. Power Sources** 236 (2013) 118-125.
- [56] W. W. Lee and J.-M. Lee, *Novel synthesis of high performance anode materials for lithium-ion batteries (LIBs)*, **J. Mater. Chem. A** 2 (2014) 1589-1626
- [57] X. Sun, P. V. Radovanovic and B. Cui, *Advances in spinel Li₄Ti₅O₁₂ anode materials for lithium-ion batteries*, **New J. Chem.**, 39 (2015) 38
- [58] B. Zhao, R. Ran, M. Liu, Z. Shao, *A comprehensive review of Li₄Ti₅O₁₂-based electrodes for lithium-ion batteries: The latest advancements and future perspectives*, **Mater. Sci. Eng. R** 98 (2015) 1-71
- [59] H. Ge, L. Chen, W. Yuan, Y. Zhang, Q. Fan, H. Osgood, D. Matera, X.-M. Song, G. Wu, *Unique mesoporous spinel Li₄Ti₅O₁₂ nanosheets as anode materials for lithium-ion batteries*, **J. Power Sources** 297 (2015) 436-441
- [60] T. Zeng, X. Hu, P. Ji, Q. Peng, B. Shang, S. Gong, *General synthesis of nano-M embedded Li₄Ti₅O₁₂/C composites (M = Sn, Sb and Bi) with high capacity and good cycle stability*, **Electrochim. Acta** 217 (2016) 299-309
- [61] M. V. Tran, N. L. T. Huynh, T. T. Nguyen, D. T. C. Ha, and P. M. L. Le, *Facile Solution Route to Synthesize Nanostructure Li₄Ti₅O₁₂ for High Rate Li-Ion Battery*, **J. Nanomater.** 10.1155/2016/4261069 (2016)

- [62] B. Tang, A. Li, Y. Tong, H. Song, X. Chen, J. Zhou, Z. Ma, *Carbon-coated $\text{Li}_4\text{Ti}_5\text{O}_{12}$ tablets derived from metal-organic frameworks as anode material for lithium-ion batteries*, **J. Alloys Comp.** 708 (2017) 6–13.
- [63] J. Liu, M. Hou, Y. Shen, L. Chen, Y. Wang, Y. Xia, *Electrochemical Performance of $\text{Li}_4\text{Ti}_5\text{O}_{12}$ Nanowire/ Fe_3O_4 Nanoparticle Compound as Anode Material of Lithium Ion Batteries*, **Electrochim. Acta** 241 (2017) 179–188.
- [64] M. V. Thournout, L. Monconduit, C. Villevieille, J. Olivier-Fourcade, J.-C. Jumas, C. Tessier, *High voltage negative active material for a rechargeable lithium battery*, US Patent US8628694 B2 (2014)
- [65] A. Orera, M. T. Azcondo, F. García-Alvarado, J. Sanz, I. Sobrados, J. Rodríguez-Carvajal and U. Amador, *Insight into Ramsdellite $\text{Li}_2\text{Ti}_3\text{O}_7$ and Its Proton-Exchange Derivative*, **Inorg. Chem.** 48 (2009) 7659–7666
- [66] D. Wiedemann, S. Nakhal, A. Franz, M. Lerch, *Lithium diffusion pathways in metastable ramsdellite-like $\text{Li}_2\text{Ti}_3\text{O}_7$ from high-temperature neutron diffraction*, **Solid State Ionics** 293 (2016) 37-43
- [67] K. Chiba, N. Kijima, Y. Takahashi, Y. Idemoto, J. Akimoto, *Synthesis, structure, and electrochemical Li-ion intercalation properties of $\text{Li}_2\text{Ti}_3\text{O}_7$ with $\text{Na}_2\text{Ti}_3\text{O}_7$ -type layered structure*, **Solid State Ionics** 178 (2008) 1725-1730.
- [68] M. V. Thournout, M. Womes, J. Olivier-Fourcade, J.-C. Jumas, *Effect of the substitution Ti/(Fe,Ni) on the electrochemical properties of $\text{Li}_2\text{Ti}_3\text{O}_7$ as electrode materials for Li-ion accumulators*, **J. Phys. Chem. Solids** 67 (2006) 1355-1358.
- [69] S. Ma and H. Noguchi, *High temperature electrochemical behaviors of ramsdellite $\text{Li}_2\text{Ti}_3\text{O}_7$ and its Fe-doped derivatives for lithium ion batteries*, **J. Power Sources** 161 (2006) 1297-1301
- [70] C. Villevieille, M. V. Thournout, J. Scoyer, C. Tessier, J. Olivier-Fourcade, J.-C. Jumas, L. Monconduit, *Carbon modified $\text{Li}_2\text{Ti}_3\text{O}_7$ ramsdellite electrode for Li-ion batteries*, **Electrochim. Acta** 55 (2010) 7080-7084.
- [71] X. Gan, G. Yang, Y. Yao, Y. Dai, *Synthesis of spinel $\text{Li}_4\text{Ti}_5\text{O}_{12}$ -ramsdellite $\text{Li}_2\text{Ti}_3\text{O}_7$ composites under vacuum and their electrochemical properties*, **J. Alloys Comp.** 637 (2015) 178-182.

- [72] G. Ali, A. Mehmood, H. Y. Ha, J. Kim, and K. Y. Chung, *Reduced graphene oxide as a stable and high-capacity cathode material for Na-ion batteries*, **Sci. Reports** 7 (2017) 40910.
- [73] K. Kataoka, J. Awaka, N. Kijima, H. Hayakawa, K.-i. Ohshima, and J. Akimoto, *Ion-Exchange Synthesis, Crystal Structure, and Electrochemical Properties of $\text{Li}_2\text{Ti}_6\text{O}_{13}$* , **Chem. Mater.** 23 (2011) 2344–2352.
- [74] J. C. Pérez-Flores, A. Kuhn, F. García-Alvarado, *Synthesis, structure and electrochemical Li insertion behaviour of $\text{Li}_2\text{Ti}_6\text{O}_{13}$ with the $\text{Na}_2\text{Ti}_6\text{O}_{13}$ tunnel-structure*, **J. Power Sources** 196 (2011) 1378-1385.
- [75] X. K. Zhang, J. J. Yuan, H. J. Yu, X. R. Zhu, Z. Yin, H. Shen, Y.M. Xie, *Synthesis, conversion, and comparison of the photocatalytic and electrochemical properties of $\text{Na}_2\text{Ti}_6\text{O}_{13}$ and $\text{Li}_2\text{Ti}_6\text{O}_{13}$ nanobelts*, **J. Alloys Comp.** 631 (2015) 171-177
- [76] K. Kataoka, J. Awaka, N. Kijima, H. Hayakawa, K-i. Ohshima, and J. Akimoto, *Ion-Exchange Synthesis, Crystal Structure, and Electrochemical Properties of $\text{Li}_2\text{Ti}_6\text{O}_{13}$* **Chem. Mater.** 23 (2011) 2344–2352.
- [77] J.C. Pérez-Flores, A. Kuhn, F. García-Alvarado, *Synthesis, structure and electrochemical Li insertion behaviour of $\text{Li}_2\text{Ti}_6\text{O}_{13}$ with the $\text{Na}_2\text{Ti}_6\text{O}_{13}$ tunnel-structure*, **J. Power Sources** 196 (2011) 1378-1385.
- [78] G-A. Nazri, *Lithium Batteries: Science and Technology* (first published), New York, Philadelphia: Springer (2003)
- [79] C. Delmas, I. Saadoune *Electrochemical and physical properties of the $\text{Li}_x\text{Ni}_{1-y}\text{Co}_y\text{O}_2$ phase*” **Solid State Ionics** 370 (1992) 53-56
- [80] R. J. Gummow, M. M. Thackeray, *Characterization of LT- $\text{Li}_x\text{Co}_{1-y}\text{Ni}_y\text{O}_2$ Electrodes for Rechargeable Lithium*, **J. Electrochem. Society** 140 (1993) 3365
- [81] R. Yazami, N. Lebrun, M. Bonneau, M. Molteni, *High performance LiCoO_2 positive electrode material*, **J. Power Sources** 54 (1995) 389-392.
- [82] T. Ohzuku, Y. Makimura, *Layered Lithium Insertion Material of $\text{LiNi}_{1/2}\text{Mn}_{1/2}\text{O}_2$: A Possible Alternative to LiCoO_2 for Advanced Lithium-Ion Batteries*, **Chem. Lett.** 30 (2001) 744.

- [83] N. Yabuuchi, M. Kajiyama, J. Iwatate, H. Nishikawa, S. Hitomi, R. Okuyama, R. Usui, Y. Yamada, S. Komaba, *P2-type $\text{Na}_x[\text{Fe}_{1/2}\text{Mn}_{1/2}]\text{O}_2$ made from earth-abundant elements for rechargeable Na batteries*, **Nature Mater.** 11 (2012) 512-517
- [84] B. Jean-Jacques, D. Claude, F. Claude, H. Paul, *Comportement electrochimique des phases Na_xCoO_2* , **Mater. Res. Bull.** 15 (1980) 1797-1804.
- [85] S. Kikkawa, S. Miyazaki, M. Koizumi, *Electrochemical aspects of the deintercalation of layered AMO_2 compounds*, **J. Power Sources** 144 (1985) 231-234.
- [86] J. M. Tarascon, G.W. Hull, *Sodium intercalation into the layer oxides $\text{Na}_x\text{Mo}_2\text{O}_4$* , **Solid State Ionics** 22 (1986) 85-96.
- [87] F. Claude, M. Guy, R. Jean-Maurice, H. Paul, *Sur de nouveaux bronzes oxygénés de formule Na_xCoO_2 (χ 1). Le système cobalt-oxygène-sodium*, **J. Solid State Chem.** 6 (1973) 532-537.
- [88] M. M Doeff, Y. Ma, S. J. Visco, L. C. De Jonghe, *Electrochemical insertion of sodium into carbon*, **J. Electrochem. Soc.** 140 (1993) L169-L170.
- [89] R. Berthelot, D. Carlier & C. Delmas, *Electrochemical investigation of the $\text{P2-Na}_x\text{CoO}_2$ phase diagram*, **Nature Mater.** 10 (2011) 74–80.
- [90] N. Yabuuchi and S. Komaba, *Recent research progress on iron- and manganese-based positive electrode materials for rechargeable sodium batteries*, **Sci. Tech. Adv. Mater.** 15 (2014) 043501.
- [91] M. M. Thackeray, *Manganese oxides for lithium batteries*, **Prog. Solid State Chem.** 25 (1997) 1-71.
- [92] M. Xu, Y. Niu, Y. Li, S. Bao and C. M. Li, *Synthesis of sodium manganese oxides with tailored multi-morphologies and their application in lithium/sodium ion batteries*, **RSC Advances** 4 (2014) 30340-30345
- [93] A. Urban, D.-H. Seo and G. Ceder, *Computational understanding of Li-ion batteries*, **npj Comp. Mater.** 2 (2016) 16002

- [94] J. Dahn, U. Von Sacken, C. Michal, *Structure and electrochemistry of $Li_{1+y}NiO_2$ and a new Li_2NiO_2 phase with the $Ni(OH)_2$ structure*, **Solid State Ionics** 44 (1990) 87-97.
- [95] P. Moreau, D. Guyomard, J. Gaubicher, F. Boucher, *Structure and Stability of Sodium Intercalated Phases in Olivine $FePO_4$* , **Chem. Mater.** 22 (2010) 4126–4128.
- [96] R. W. Abigail, E. R. Paul, J. D. Francis, *Powerful oxidizing agents for the oxidative deintercalation of lithium from transition-metal oxides*, **J. Solid State Chem.** 81 (1989) 203-207
- [97] K. Zaghib, J. Trottier, P. Hovington, F. Brochu, A. Guerfi, A. Mauger, C. M. Julien, *Characterization of Na-based phosphate as electrode materials for electrochemical cells*, **J. Power Sources** 196 (2011) 9612-9617
- [98] S. Y. Hong, Y. Kim, Y. Park, A. Choi, N.-S. Choi and K. T. Lee, *Charge carriers in rechargeable batteries: Na ions vs. Li ions*, **Energy Environ. Sci.** 6 (2013) 2067-2081.
- [99] A. Saracibar, J. Carrasco, D. Saurel, M. Galceran, B. Acebedo, H. Anne, M. Lepoitevin, T. Rojo, M. Casas Cabanas, *Investigation of sodium insertion-extraction in olivine Na_xFePO_4 ($0 \leq x \leq 1$) using first-principles calculations*, **Phys. Chem. Chem. Phys.** 14 (2016) 13045-51.
- [100] V. Chevrier, G. Ceder, *Challenges for Na-ion Negative Electrodes*, **J. Electrochem. Soc.** 158 (2011) A1011.
- [101] R. Alcantara, J. M. Jimenez-Mateos, P. Lavela, J. L. Tirado, *Carbon black: a promising electrode material for sodium-ion batteries*, **Electrochem. Comm.** 3 (2001) 639-642.
- [102] R. Alcantara, P. Lavela, G. F. Ortiz, J. L. Tirado, *Carbon Microspheres Obtained from Resorcinol-Formaldehyde as High-Capacity Electrodes for Sodium-Ion Batteries*, **Electrochem. Solid State Lett.** 8 (2005) A222-A225.
- [103] D. A. Stevens, J. R. Dahn, *High Capacity Anode Materials for Rechargeable Sodium- Ion Batteries*, **J. Electrochem. Soc.** 147 (2000) 1271-1273.

- [104] R. Asher, *A lamellar compound of sodium and graphite*, **J. Inorg. Nuc. Chem.** 10 (1959) 238-2249.
- [105] P. Ge, M. Foulletier, *Electrochemical intercalation of sodium in graphite*, **Solid State Ionics** 28 (1988) 1172-1175.
- [106] D. Stevens, J. Dahn, *The Mechanisms of Lithium and Sodium Insertion in Carbon Materials*, **J. Electrochem. Soc.** 148 (2001) A803-A809.
- [107] J. Sangster, *C-Na (Carbon-Sodium) System*, **J. Phase Equilibria Diffus.** 28 (2007) 571.
- [108] M. M. Doeff, Y. Ma, S. J. Visco, L. C. De Jonghe, *Electrochemical Insertion of Sodium into Carbon*, **J. Electrochem. Soc.** 140 (1993) L169-L170.
- [109] S. I. Park, I. Gocheva, S. Okada, J.-i Yamaki, *Electrochemical Properties of $\text{NaTi}_2(\text{PO}_4)_3$ Anode for Rechargeable Aqueous Sodium-Ion Batteries*, **J. Electrochem. Soc.** 158 2011 A1067-A1070.
- [110] S. Il Park, I. Gocheva, S. Okada, and J.-i. Yamaki, *Electrochemical Properties of $\text{NaTi}_2(\text{PO}_4)_3$ Anode for Rechargeable Aqueous Sodium-Ion Batteries*, **J. Electrochem. Soc.**, 158 (2011) A1067-A1070.
- [111] Y. Ni, R. Zheng, X. Tan, W. Yue, P. Lv, J. Yang, D. Song, K. Yu, W. Wei, *A fluorophosphate glass-ceramic electrolyte with superior ionic conductivity and stability for Na-ion batteries*, **J. Mater. Chem A** 3 (2015) 17558-17562
- [112] D. Hamani, M. Ati, J.-M. Tarascon, P. Rozier, *Na_xVO_2 as possible electrode for Na-ion batteries*, **Electrochem. Comm.** 13 2011 938-941.
- [113] Y. L. Cao, L. F. Xiao, W. Wang, D. W. Choi, Z. M. Nie, J. G. Yu, L. V. Saraf, Z. G. Yang, J. Liu, *Reversible Sodium Ion Insertion in Single Crystalline Manganese Oxide Nanowires with Long Cycle Life*, **Adv. Mater.** 23 (2011) 3155-3160.
- [114] V. Palomares, M. Casas-Cabanas, E. Castillo-Martínez, M. H. Han, T. Rojo, *Update on Na-based battery materials. A growing research path*, **Energy Environ. Science** 6 (2013) 2312-2337.

- [115] P. J. P. Naeyaert, M. Avdeev, N. Sharma, H. B. Yahia, and C. D. Ling, *Synthetic, Structural, and Electrochemical Study of Monoclinic $\text{Na}_4\text{Ti}_5\text{O}_{12}$ as a Sodium-Ion Battery Anode Material*, **Chem. Mater.** 26 (2014) 7067-7072.
- [116] S. H. Woo, Y. Park, W. Y. Choi, N.-S. Choi, S. Nam, B. Park and K. T. Lee, *Trigonal $\text{Na}_4\text{Ti}_5\text{O}_{12}$ Phase as an Intercalation Host for Rechargeable Batteries*, **J. Electrochem. Soc.** 159 (2012) A2016-A2023.
- [117] A. D. Tevar, J. F. Whitacre, *Relating synthesis conditions and electrochemical performance for the sodium intercalation compound $\text{Na}_4\text{Mn}_9\text{O}_{18}$ in aqueous electrolyte*, **J. Electrochem. Soc.** 157 (2010) A870-A875.
- [118] H. Pan, X. Lu, X. Yu, Y.-S. Hu, H. Li, X.-Q. Yang, L. Chen, *Sodium Storage and Transport Properties in Layered $\text{Na}_2\text{Ti}_3\text{O}_7$ for Room-Temperature Sodium-Ion Batteries*, **Adv. Energy Mater.** 3 (2013) 1186–1194
- [119] H. Zhanga, X. P. Gaoa, G. R. Lia, T. Y. Yana, H. Y. Zhu, *Electrochemical lithium storage of sodium titanate nanotubes and nanorods*, **Electrochim. Acta** 53(2008) 7061-7068.
- [120] X. Man, K. Wang, R. Chen, L. Li, F. Wu, *A facile route to synthesize sheet-like $\text{Na}_2\text{Ti}_3\text{O}_7$ with improved sodium storage properties*, **Chem. Res. Chinese Universities** 31 (2015) 443–446
- [121] Z. Zhou, H. Xiao, F. Zhang, .X. Zhang, Y. Tang, *Solvothermal synthesis of $\text{Na}_2\text{Ti}_3\text{O}_7$ nanowires embedded in 3D graphene networks as an anode for high-performance sodium-ion batteries*, **Electrochim. Acta** 211(2016) 430-436.
- [122] C. Ding, T. Nohira, R. Hagiwara, *Electrochemical performance of $\text{Na}_2\text{Ti}_3\text{O}_7/\text{C}$ negative electrode in ionic liquid electrolyte for sodium secondary batteries*, **J. Power Sources** 354 (2017) 10–15.
- [123] A. Rudola, K. Saravanan, S. Devaraj, H. Gong, P. Balaya, *$\text{Na}_2\text{Ti}_6\text{O}_{13}$: a potential anode for grid-storage sodium-ion batteries*, **Chem. Comm. (Cambridge)** 28 (2013) 7451-7453
- [124] D. Maurya, M. Murayama, S. Priya, *Synthesis and Characterization of $\text{Na}_2\text{Ti}_6\text{O}_{13}$ Whiskers and their Transformation to $(1-x)\text{Na}_{0.5}\text{Bi}_{0.5}\text{TiO}_3-x\text{BaTiO}_3$ Ceramics*, **J. Am. Ceram. Soc.** 94 (2011) 2857–2871.

- [125] K. Shen and M. Wagemaker, *Na_{2+x}Ti₆O₁₃ as Potential Negative Electrode Material for Na-Ion Batteries*, **Inorg. Chem.** 53 (2014) 8250–8256.
- [126] P. Li, P. Wang, S. Qian, H. Yu, X. Lin, M. Shui, X. Zheng, N. Long, J. Shu, *Synthesis of Na₂Ti₆O₁₃ nanorods as possible anode materials for rechargeable lithium ion batteries*, **Electrochim. Acta** 187 (2016) 46–54.
- [127] A. Rambabu, B. Kishore, N. Munichandraiah, S. B. Krupanidhi, and P. Barpanda, *Na₂Ti₆O₁₃ thin films as anode for thin film sodium ion batteries*, **AIP Conf. Proceed.** 1832 (2017) 080059.
- [128] ASM Handbook, ASM International, Materials, OH (1992)
- [129] T. Reddy, *Linden's Handbook of Batteries, 4th Edition (Electronics)*, McGraw-Hill Education: New York (2011)
- [130] A. Maxim, K. Andrei, *Low-temperature Na₄Ti₅O₁₂ from X-ray and neutron powder diffraction data*, **Acta Cryst. C** 56 (2000) e539–e540
- [131] S. Andersson, A. D. Wadsley, *The crystal structure of Na₂Ti₃O₇*, **Acta Cryst.** 14 (1961) 1245–1249
- [132] L. Aldon, P. Kubiak, M. Womes, J. C. Jumas, J. Olivier-Fourcade, J. L. Tirado, J. I. Corredor, C. P. Vicente CP, *Chemical and Electrochemical Li-Insertion into the Li₄Ti₅O₁₂ Spinel*, **Chem. Mater.** 16 (2004) 5721–5725.
- [133] R. Baddour-Hadjean, J.-P. Pereira-Ramos, *Raman Microspectrometry Applied to the Study of Electrode Materials for Lithium Batteries*, **Chem. Rev.** 110 (2010) 1278–1319.
- [134] G. Yan, H. Fang, H. Zhao, G. Li, Y. Yang, L. Li, *Ball milling-assisted sol–gel route to Li₄Ti₅O₁₂ and its electrochemical properties*, **J. Alloys Comp.** 470 (2009) 544–547.
- [135] A. Laumann, H. Boysen, M. Bremholm, K. T. Fehr, M. Hoelzel, M. Holzapfel, *Lithium Migration at High Temperatures in Li₄Ti₅O₁₂ Studied by Neutron Diffraction*, **Chem. Mater.** 23 (2011) 2753.
- [136] L. Hongwei, Y. Dongjiang, Z. Zhanfeng, K. Xuebin, W. Eric, Z. Huaiyong and L. Ray, J. Frost, *A Raman spectroscopic and TEM study on the structural*

- evolution of Na₂Ti₃O₇ during the transition to Na₂Ti₆O₁₃*, **J. Raman Spec.** 41 (2010) 1331–1337.
- [137] Z. Zhang, J. B. M. Goodall, S. Brown, L. Karlsson, R. J. H. Clark, J. L. Hutchison, I. U. Rehman and J. A. Darr, *Continuous hydrothermal synthesis of extensive 2D sodium titanate (Na₂Ti₃O₇) nano-sheets*, **Dalton Trans.** 39 (2010) 39 711-714.
- [138] F.D. Hardcastle, *Raman Spectroscopy of Titania (TiO₂) Nanotubular Water-Splitting Catalysts*, **J. Ark. Aca. Sci.** 65 (2011).
- [139] B. C. Viana, O. P. Ferreira, A. G. Souza Filho, J. M. Filho and O. L. Alves, J. Braz., *Structural, Morphological and Vibrational Properties of Titanate Nanotubes and Nanoribbons*, **Chem. Soc.** 20 (2009) 167-175.
- [140] M. Shirpour, J. Cabana and M. Doeff, *New materials based on a layered sodium titanate for dual electrochemical Na and Li intercalation systems*, **Energy Environ. Sci.** 6 (2013) 2538-2547.
- [141] T. Gao, H. Fjellvåg and P. Norby, *Crystal Structures of Titanate Nanotubes: A Raman Scattering Study*, **Inorg. Chem.** 48 (2009) 1423-1432.
- [142] F. Miyaji, T. Yoko, H. Kozuka and S. Sakka, *Structure of Na₂O·₂TiO₂ glass*, **J. Mater. Sci.** 26 (1991) 248.
- [143] H. M. Kim, F. Miyaji and T. Kokubo, *Effect of heat treatment on apatite-forming ability of Ti metal induced by alkali treatment*, **J. Mater. Sci.: Mater. Med.** 8 (1997) 341.
- [144] S. Demirel, E. Oz, E. Altin, S. Altin, P. Kaya, S. Turan, S. Avci, S. Avci, *Growth Mechanism, Magnetic and Electrochemical Properties of Na_{0.44}MnO₂ Nanorods as Cathode Material for Na-ion Batteries*, **Mater. Charact.** 105 (2015) 104-112.
- [145] Ch. V. Subba Reddy, K.-I. Park, S.-i. Mho, I.-H. Yeo, and S.-M. Park, *Simple Preparation of V₂O₅ Nanostructures and Their Characterization*, **Bull. Korean Chem. Soc.** 29 (2008) 2061-2064.

- [146] Z. Zhi-Yong, N. Zheng-Xin, D. Yan-Lan, O. Chu-Ying, S. Si-Qi and L. Min-Sheng, *Ab initio studies on n-type and p-type $Li_4Ti_5O_{12}$* , **Chi. Phys. B** 18 (2009) 2492-2506.
- [147] T. Nordh, *Lithium titanate as anode material in lithiumion batteries*, Bachelor Thesis, Uppsala University (2015).



RESUME

Name & Surname : Serkan DEMIREL

Address : Saray Mah. Sinema Cad. Kutsal Apt. No:64/3 Malatya-TURKEY

E-mail : demirel.srkn@gmail.com

BS : **University of Firat** Science Faculty Physics Department (2006-2010)

Master : **University of Inonu** Graduate School of Natural and Applied Sciences Physics Department (2011- 2013)

Professional Experience

USA – (Visiting Scholar) - University of Illinois at Urbana-Champaign Materials Science and Engineering (2016-2017)

Awards

TUBITAK 2214-A International Scholarship Program-2016

TUBITAK Publication award –2013, 2014, 2015, 2016, 2017

The European Union NMI3 Programs Scholarship Program - 2013

TUBITAK PTI Scholarships – 2013

Publications

- **S. Demirel**, E. Oz, S. Altin, A. Bayri, O. Baglayan, E. Altin, S. Avci, “Structural, Magnetic, Electrical and Electrochemical properties of $\text{SrCoO}_{2.5}$, $\text{Sr}_9\text{Co}_2\text{Mn}_5\text{O}_{21}$ and SrMnO_3 compounds” *Ceramics International*, DOI: 10.1016/j.ceramint.2017.07.230 (2017)
- E. Oz, **S. Demirel**, E. Altin, S. Altin, A. Bayri, S. Avci, “Electrochemical performance improvement of LiCoO_2 system via Quench” *Electrochimica Acta* DOI: 10.1016/j.electacta.2017.07.147 (2017)
- **S. Demirel**, E. Oz, S. Altin, A. Bayri, E. Altin, S. Avci, “Enhancement of battery performance of LiMn_2O_4 : Correlations between electrochemical and magnetic properties” *RSC Advances* 6, 2016

- E. Oz, **S. Demirel**, S. Altin, A. Bayri, S. Avci, “Synthesis of ultra-thin nanobristles of Na-Mn-O compounds and their magnetic and structural properties” *Ceramics International* 42(15) 2016
- E. Oz, **S. Demirel**, S. Altin, “Fabrication and electrochemical properties of $\text{LiCo}_{1-x}\text{Ru}_x\text{O}_2$ cathode materials for Li-ion Battery” *Journal of Alloys and Compounds* 671, 2016
- E. Oz, **S. Demirel**, S. Altin “Electrochemical effects and magnetic properties of B substituted LiCoO_2 : Improving Li-battery performance” *Journal of Alloys and Compounds* 657 2016
- E. Altin, **S. Demirel** “Applications of Infrared Sensors in Field of Health“ *T.C.İnönü Üniversitesi Sağlık Hizmetleri Meslek Yüksekokulu Dergisi*, 5 2016
- H. Kamalak, E. Oz, **S. Demirel**, S. Altin “The mechanical and heat conducting properties of dental composites“*Biointerface Research in Applied Chemistry*, 6 2016
- H. Kamalak, M. Erdem, E. Altin, **S. Demirel**, E. Oz, S. Altin, “Giant Dielectric Constant and Mechanical, Heat Conducting and Structural Properties of Dental Composites by Adding Ca Ions” *Journal of Dentistry and Orofacial Surgery* 01(03) 2016
- H. Kamalak, **S. Demirel**, E. Oz, S. Altin, “ The Leakage Study Between Restorative and Pulp Capping Materials and Diffusion Analysis by Fick Laws” *Biointerface Research in Applied Chemistry*, 6 2016.
- **S. Demirel**, E. Oz, E. Altin, S. Altin, A. Bayri, P. Kaya, S. Turan, S. Avci, “Growth mechanism and magnetic and electrochemical properties of $\text{Na}_{0.44}\text{MnO}_2$ nanorods as cathode material for Na-ion batteries” *Materials Characterization*, 105, 104-112, 2015
- E. Altin, E. Oz, **S. Demirel**, A. Bayri, “Magnetic and thermoelectric properties of B-substituted NaCoO_2 ” *Applied Physics A-Materials Science & Processing*, 119, 3, 1187-1196, 2015
- **S. Demirel**, E. Oz, A. Bayri, S. Altin, “Magnetic and microstructural properties of $\text{LiCrO}_2\cdot\text{Cr}_2\text{O}_3$ system by doping of the boron ions”, *Journal of Materials Science Materials in Electronics* 26(11) 2015
- **S. Demirel**, E. Altin, E. Oz, S. Altin, A. Bayri, “An enhancement ZT and spin state transition of $\text{Ca}_3\text{Co}_4\text{O}_9$ with Pb doping”, *Journal of Alloys and Compounds*, 627, 430-437, 2015

- E. Altin, E. Oz, **S. Demirel**, M. Erdem, “Thermal and mechanical properties of La–Al–Sb alloys” *Journal of Materials Science: Materials in Electronics*, 25, 5331-5337, 2014
- E. Altin, E. Oz, M. Erdem, **S. Demirel**, Y. Aydogdu, S. Altin, “Thermoelectric and mechanical properties of Mg–Al–Sb alloys” *Journal of Materials Science: Materials in Electronics*, DOI 10.1007/s10854-014-2500-3
- E. Altin, D. Gokhfeld, **S. Demirel**, E. Oz, F. Kurt, S. Altin, M. E. Yakinci, “*Vortex pinning and magnetic peak effect in $\text{Eu}(\text{Eu},\text{Ba})_{2.125}\text{Cu}_3\text{O}_x$* ”, *Journal of Materials Science: Materials in Electronics*, 25, 1466-1473, 2014
- S. Altin, A. Bayri, **S. Demirel**, M. A. Aksan, “*Thermal conductivity and magnetic properties of the B substituted $\text{Ca}_3\text{Co}_4\text{O}_9$* ”, *Current Applied Physics*, 14, 590-595, 2014
- **S. Demirel**, S. Avci, E. Altin, S. Altin; M. E. Yakinci, “*Enhanced thermoelectric properties induced by chemical pressure in $\text{Ca}_3\text{Co}_4\text{O}_9$* ”, *Ceramics International*, 40, 5217-5222, 2014
- Z. D. Yakinci, D. M. Gokhfeld, E. Altin, S. Altin, F. Kurt, **S. Demirel**, M. A. Aksan and M. E. Yakinci, “*Jc enhancement and flux pinning of Se substituted YBCO Compound*”, *Journal of Material Science Materials in Electronics*, 24, 12, 4790-4797, 2013
- **S. Demirel**, S. Altin, M. A. Aksan, “*High Temperature thermoelectric properties of the $\text{Ca}_{3-x}\text{B}_x\text{Co}_4\text{O}_9$ system*” *Journal of material Science Materials in Electronics*, 10.1007/s10854-013-1417-6, 2013
- **S. Demirel**, S. Altin, M. A. Aksan, “*Low Temperature Magnetic Behavior of $\text{Ca}_3\text{Co}_4\text{O}_x$ Polycrystalline Material*”, *Journal of Superconductivity and Novel Magnetism*, 26, 1617-1620, 2013 (**Impact Factor: 1.180**)
- **S. Demirel**, M. A. Aksan, S. Altin, “*Low Temperature electrical and thermal transport properties of $\text{Ca}_{3-x}\text{Sb}_x\text{Co}_4\text{O}_9$ system*”, *Journal of Materials Science: Materials in Electronic*, 23, 12, 2251-2256, 2012